Fakultät für Mathematik und Naturwissenschaften
Fachgruppe Physik
Fachrichtung Theoretische Chemische Physik

BERGISCHE
UNIVERSITÄT
WUPPERTAL

From Microscopic Interactions to Macroscopic Mechanical Properties of Filled Elastomers

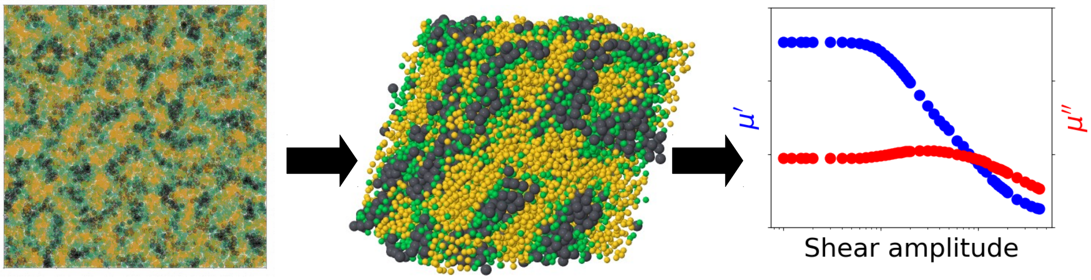

Dissertation zur Erlangung des akademischen Grades eines
Doktors der Naturwissenschaften (Dr. rer. nat.)
vorgelegt von

Mariia Viktorova

Acknowledgment

I would like to thank all the people who helped me in completing this thesis.

Firstly, I would like to emphasize my sincere gratitude to my supervisor, Prof. Dr. Reinhard Hentschke for being an excellent mentor and a great person. His patience, support and suggestions helped me a lot during my PhD. I appreciate the numerous discussions we had, which were beneficial for me from both scientific and personal points of view.

Special thanks go to Dr. Hossein Ali Karimi-Varzaneh for accepting to be one of the reviewers of my PhD thesis and for his valuable ideas, comments and suggestions, which defined to a large extent the course of my research.

I would like to thank Prof. Dr. Knechtli and Prof. Dr. Scherf for reading my thesis and agreeing to be part of the examination committee.

Next I would like to thank Continental AG and, especially, Dr. Frank Fleck, Dr. Fereshte Taherian, Dr. Corrina Prange, Dr. Carla Recker, Dr. Jorge Lacayo-Pineda, Dr. Thomas Müller-Wilke and Dr. Peter Zmolek for the productive collaboration and scientific discussions including important feedback.

For the friendly atmosphere in the research group of Theoretical Chemical Physics I would like to thank my colleagues Dr. Norman Gundlach, Susanne Christ, Paul Lucas and Björn Lindhauer.

Finally, I would like to express my deepest gratitude to my family for their support and to my husband Aleksandr for his unconditioned love and believing in me at the moments when even I did not believe in myself. Thank you!

Abstract

Elastomers play an important role in our everyday life. Their mechanical properties can be enhanced by addition of active fillers – usually carbon black or silica. The filler particles, which are initially well dispersed in the polymer matrix, in the post-mixing stages tend to form agglomerates and filler networks in a process called flocculation. The mechanical properties of the resulting products depend on the properties of the filler network, while the latter are strongly affected by the chemical composition. One of the most important effects in this context is the so-called Payne effect or the pronounced decrease in the dynamic moduli with increasing strain amplitude in filled elastomers under cyclic loading. Up to now, it is unclear, what is the main source of the Payne effect, i.e., the polymer-filler or filler-filler interactions. Therefore, finding a relation between the chemical composition and the mechanical properties of filled rubbers is an important problem from both scientific and manufacturing points of view. To the best of our knowledge, to date, there is no theoretical model relating the chemical composition of a filled elastomer on the microscopic scale to its macroscopic mechanical properties. This work presents a simulation approach combining two models. The first one is an extension of previous work, which presents a coarse-grained simulation approach to filler flocculation based on the Metropolis Monte Carlo simulation. This algorithm, called the morphology generator, minimizes the free enthalpy of the system, while the interactions between different components are described via the experimental interface free energies. The second model, based on the assumption of local equilibrium, performs shear of the systems obtained via the morphology generator in order to obtain storage and loss moduli as well as their ratio – the loss tangent or damping. This simulation mimics dynamic mechanical analysis, or DMA, which is widely used in laboratories to measure the mechanical performance of tire materials. Hence, the model provides a connection between the chemical composition characterized by the experimental surface free energies and the mechanical properties of the material. The focus of this work is on the model parameterization and on studying the properties of filled pure polymer systems and filled polymer blends consisting of natural rubber, styrene-butadiene rubber and different types of fillers, such as carbon black, silica or surface modified silica. We find that the typical relaxation in the polymer-filler interface is much slower than the related relaxation in the bulk polymer or in the filler-filler interface. One important implication is that this leads to a realistic form of the loss tangent in the low frequency/high temperature regime, i.e., the regime commonly associated with rolling resistance. We propose an approach which ties the surface energies, used in the morphology generator, to the force constants, describing interactions in the shear simulation, by making the latter being proportional to the interface tension. We study reversible bond breaking and bond relaxation as functions of different parameters such as filler dispersion, frequency, strain amplitude and filler content. Furthermore, we consider contributions of polymer-filler and filler-filler interactions to the Payne effect in filled elastomers. In addition, we study local strain and stress distributions in the polymer matrix surrounding the filler and in the interfaces between polymer and filler, as well as between filler particles. We find that both the local stresses and the local strains, aside from being dependent on the macroscopic strain amplitude, do depend on frequency. Low excitation frequencies, allowing the local stresses and strains to relax differently, can lead to large differences between the local and the global quantities in certain parts/interfaces of the system. This phenomenon, which is also strongly influenced by filler dispersion, is likely to be of significance to fatigue and fracture in rubber composites.

Contents

Chapter 1

Introduction

Elastomer materials are essential in construction, wearables as well as in mobility. The biggest segment in the latter market are tires. The tire industry continuously requires new materials, combining improved sustainability with higher performance. However, tires have been around for more than 100 years [1], and thus it may be surprising to the laymen that tire materials are the subject of current research and that this research indeed still leads to better products. The reason is the extraordinary complexity of elastomer composites. Physico-chemical processes on the scale of nanometres govern product performance over tens of thousands of kilometres. Processes in the frequency domain of molecular vibrations may determine what happens during one as well as after one million tire revolutions. There is no exact theory for any of this. And often, even after many decades, certain basic concepts – like reinforcement by particulate fillers – can be understood differently by different researchers. But there is one tool, which, by comparison, is a recent addition to the tool chest of elastomer research. This tool is computer modelling. It is relatively recent because the computer power needed is significant and has been available only in the past 15 to 20 years. A comprehensive review on computer simulation of elastomer nanocomposites can be found in [2]. This thesis describes a novel modelling approach, which is intermediate between finite element and atomistic force field calculations. With the former it shares the ability to access the macroscopic spatial (here μm) and temporal scales. With the latter it shares the ability to include chemical detail.

The mechanical performance of filled polymers is strongly affected by the properties of filler particles, which are widely used to reinforce the elastomer materials [3–9]. During the mixing process, the filler particles, which are at this stage broken down to the aggregates consisting of primary particles, are dispersed in the polymer matrix. However, in the post-mixing stages the filler tends to re-agglomerate forming larger structures – agglomerates and, at sufficiently large concentrations, filler networks. This process is called filler flocculation, and it has a strong impact on the dynamic mechanical and other physical properties of filled elastomers [10–17]. The filler dispersion in the elastomer matrix occurs on different levels, so that one can distinguish between visual, macro- and micro-dispersion. In this work, we focus on the latter, i.e., the dispersion in the range from primary particles to the filler network on the scale of up to several μm.

There exist several approaches to modelling of filler dispersion in the polymer matrix. For instance, Stöckelhuber et al. propose a game theory-based algorithm, which uses experimental surface tensions of the material components [18]. Another approach is based on local equilibrium thermodynamics [19–21]. The morphology generator, used in this work, is an extension of the latter, where the filler flocculation is modelled based on a combination of local equilibrium thermodynamics with experimental interface tensions. The surface/interface tensions serve as a measure of the interaction strength between different components. The impact of the surface tensions on the filler dispersion and the material's properties was also established experimentally [22–26].

One of the main laboratory techniques used for measuring the performance of elastomer materials is dynamic mechanical analysis or DMA [27–30]. During the analysis, a specimen of a material under study is subjected to the sinusoidal stress (or strain) and the strain (stress) in the material is determined. These quantities are then used to calculate the loss and storage moduli of the material. The storage modulus is a measure of the energy stored in the material, while the loss modulus is proportional to the energy dissipated during deformation. The ratio of the loss modulus to the storage modulus is called the loss tangent, $\tan\delta$ or damping. Plotted vs. temperature, it is widely used for estimating tire performance parameters such as rolling resistance, wet or ice grip [31]. One of the key effects in this context is the Payne effect, i.e., the decrease in the storage modulus with increasing strain amplitude in filled rubbers under cyclic deformation [32–36]. As the Payne effect is not observed in unfilled rubbers, it is caused by the processes occurring due to rubber-filler and/or filler-filler interactions. The question, which kind of interactions provide the main contribution into the Payne effect, has been until now not resolved [37].

In order to relate the molecular composition to the dynamic moduli, one needs not only the information on the morphology of the filler network as a whole, but also how the external load is distributed in the material. In this context, a concept of the load bearing paths, discussed in [38, 39], can be helpful. According to the scaling model, the distribution of the minimal load bearing paths is crucial for understanding the Payne effect. On the other hand, the information on the load distribution is also essential to study the initiation and propagation of damage in the material. Some authors believe that the material's strength and modulus reinforcement in general are the result of distribution of the applied load between matrix and filler, where filler particles bear a disproportionately higher portion of the load [40].

The research on the properties of filled elastomers has attracted many scientists that have developed numerous theoretical models and simulation approaches. One of the most interesting questions in this context is the effect of filler. As an example, in [41] the authors used molecular dynamics simulations to predict the properties of unfilled and silica-filled elastomers. The inclusion of nanoparticles increased the glass transition temperature and the elastic modulus. In addition, under the tensile deformation, the formation of microcavities was observed at the elastomer-nanoparticle interfaces. Lauke et al. performed a modelling of structure evolution of filled elastomers under uniaxial elongation [42]. The filler network was represented by spherical particles of different sizes randomly distributed in a prismatic volume. Stretching of the material resulted in a change of the distances between originally neighbouring nodes, which exceeded the macroscopic elongation by several times. In [43] computer simulations of filled polymer networks were performed. The coarse grained dissipative particle dynamics model was used, where the stiff and spherical particles were either well dispersed or aggregated. Oscillatory shear was applied to the system to study the nonlinear viscoelastic behaviour of the material, which, however, had different characteristics than the Payne effect. In [44] the authors used a finite element computational model to study the effect of microstructure morphology in filled elastomers on their macroscopic large deformation behaviour. This research follows the same idea of the connection between the microscopic structure and macroscopic properties as in the present work, although the main focus is on the Mullins effect. Long et al. developed and studied a force equilibrium approach [45, 46]. The polymer was simulated as a network of viscous springs. Filler particles were modelled in a similar fashion with additional breakable bonds at the polymer-filler interface. The entire system was then subject to cyclic strain. The Payne and Mullins effects were related to the yield and formation of glassy bridges around the fillers. In [47] the same authors used reverse Monte Carlo simulations to obtain the filler pair correlation function. The mechanical properties were studied using oscillatory shear experiments. It was found that the Payne effect can be correlated with the average number of immobilized polymer bridges between particles. Li at el. investigated the effect of the chemical coupling between polymer and nanoparticles on the viscoelastic properties of polymer nanocomposites using coarse-grained molecular dynamics simulations [48]. They were able to calculate the dynamic moduli and the loss tangent and study their changes as functions of strain amplitude. In addition, they explored the effects of temperature, frequency and the interfacial physical interaction between nanoparticles and polymers. Termonia in [49] used Monte Carlo simulations to study the effect of particle radius and volume fraction, trying to give a molecular explanation of the Payne effect. In [50] the authors combined experimental DMA measurements with constitutive modelling and FEM simulations to study the strain induced effects of filler reinforced elastomers with respect to the Payne effect. Wang and colleagues used molecular dynamics simulations to explore the effect of the nanoparticle network and its state, i.e., from the aggregated to the uniform dispersed one, on the tensile mechanical behaviour and the Payne effect [51]. In [52] a molecular dynamics simulation study was presented, which allowed to observe a change in the elastic modulus as a function of strain. Two typical distribution states of nanoparticles – aggregated and dispersed – were considered. In both cases, the Payne effect was observed, whereas the modulus of the aggregated case was more sensitive to the imposed strain. The authors postulated that the underlying mechanism of the Payne effect was different for different filler dispersions. While in the aggregated case the main effect was the disintegration of the nanoparticle network of clusters formed through direct contacts, in the dispersed case the non-linear behaviour was attributed to the destruction of the nanoparticle network of clusters formed through the bridging of adsorbed polymer segments. Davris and colleagues presented in [53] experimental and simulation insights into the mechanisms of reinforcement. They studied the impact of polymer-filler interactions on the nanocomposite microstructure and its macroscopic dynamic mechanical properties. Based on non-equilibrium molecular dynamics simulations, Chen et al. were able to reproduce the Payne effect in model cross-linked elastomers containing spherical nanoparticles [54]. The magnitude of the Payne effect was found to depend on the polymer-particle interaction and the filler loading, while the rigid polymer shell around nanoparticles and the polymer-shell-bridged filler network were the main contributions to reinforcement. In [55] the authors performed molecular dynamics simulations, both on the coarse-grained and the chemistry-specific levels, to study the impact of morphology on the mechanical properties. They studied the effect of different parameters, such as filler size, shear flow, filler-filler interaction strength and heterogeneity of the filler surface, on the Payne effect. As the last reference, we mention [56], where the authors used a machine learning approach to predict the surface energies of the polymers and fillers, which are then correlated with the nanofiller dispersion morphology and filler/matrix interface properties. The latter allowed predicting the thermomechanical properties of nanofilled polymer composites.

The main goal of this work is a development of a modelling approach relating the filler structure, based on the experimental surface energies of individual components, to the mechanical properties of macroscopic materials, which can serve for a laboratory prediction of material performance parameters. The first step is the morphology generator – a coarse grained model, which simulates the filler flocculation process in filled elastomers. The algorithm utilizes a nearest neighbour node-exchange Metropolis Monte Carlo algorithm together with experimental interface tensions characterizing the interactions between the components. The model allows varying the chemical composition and the temperature of the flocculation, and can be used to study the compatibility between various polymers and fillers. The morphologies are then mapped onto a topologically identical model, which performs a virtual DMA analysis – cyclic shearing of the system with a subsequent determination of the dynamic moduli. A general idea of cyclic shear simulations based on the assumption of local equilibrium is originally formulated in [57, 58]; in this work we further develop and elaborate it. In this part of the model, the interactions are described via viscous springs, which can reversibly break depending on the interaction type. This form of the interaction potential is motivated by the Jump-In-Jump-Out model – a model considering the behaviour of two filler aggregates under external load [59–61]. The resulting dynamic moduli, obtained during the shear simulation, can be computed as functions of either frequency or strain amplitude. The focus in this work is on filled polymer blends of NR (natural rubber) and SBR (styrene butadiene rubber). In terms of fillers, the model can be used to simulate an arbitrary type of filler, but here we concentrate on CB (carbon black), silica and surface modified silica. The main aspect of the connection of the two models is finding a mapping between the morphology generator and the shear simulation, as the interactions in the models are described differently. Therefore, a parameterization of the model is especially important for a potential prediction of mechanical properties. In addition, an attempt was made to tie the values of the spring constants, used to describe the interactions in the DMA part, to the interface tensions, that are a measure of interaction strength in the morphology generator.

We model different types of systems, starting from pure polymers over systems containing two components – a polymer and a filler – to filled polymer blends and describe their properties. In addition, we study reversible bond breaking and the Payne effect. Furthermore, we look at the local strain and stress and their dependence on strain amplitude, frequency and filler dispersion. At low frequencies, the local stresses and strains relax differently, which can lead to large differences between the local and the global quantities in certain parts of the system. This phenomenon can be of special significance in studying the initiation of damage and fatigue in filled elastomer systems.

1.1 Outline of the Thesis

This thesis consists of 9 Chapters and 3 Appendices.

Chapter 2 provides theoretical background on elastomer materials. It is explained how the mechanical testing of such materials is done. In addition, main dynamic properties of unfilled and filled elastomers are discussed. Chapter 3 discusses the morphology generator algorithm, which is based on local equilibrium thermodynamics and experimental interface tensions. Chapter 4 is devoted to the basics of computer simulation of dynamical mechanical analysis. This chapter explains the simulation of shear based on the local equilibrium approach. Chapter 5 discusses the parameterization of the model, i.e., how to choose and adjust the simulation parameters for different systems (pure polymers, filled one polymer systems, unfilled and filled blends). Chapter 6 presents the simulation results for systems comprising pure polymer plus filler. On the basis of filled natural rubber systems, we compare different fillers, their compatibility with the polymer and their tendency to form agglomerates. Additionally, we show why the polymer-filler interface plays an important role in the mechanical properties of filled elastomers. Chapter 7 addresses filled polymer blends consisting of natural rubber, styrene-butadiene rubber and different fillers. We discuss the preferential distribution of fillers in the two polymer subphases, and the impact of filler dispersion on the dynamic mechanical properties of filled blends. In Chapter 8 we study the contributions of polymer-filler and filler-filler bond breaking to the energy loss in the system and, subsequently, to the Payne effect. In addition, we consider the stress and strain distributions in the system under load. Finally, Chapter 9 combines the conclusion with an outlook.

Appendix A provides theoretical basics of surface energies and surface tensions. It explains main terms, such as the contact angle and the work of adhesion, and gives an overview over experimental techniques for measuring surface energies. Appendix B contains the theoretical background of the theory of elasticity. It introduces essential terms like strain, stress and shows the relation between the loss modulus and the energy loss. Appendix C compiles all the simulation parameters significant for the model.

Chapter 2

Elastomer Materials

This chapter gives an introduction into elastomers and their mechanical properties. The first part of the chapter provides the chemical basics of elastomer materials and explains the most important definitions in the context of rubber compounds. In the second part of the chapter, we discuss how these materials are tested in laboratories and what are typical mechanical properties of filled and unfilled elastomers. The theoretical review in this chapter is based on [7, 19, 61–67].

2.1 Elastomers

An elastomer is a polymer exhibiting viscoelastic, i.e., both viscous and elastic, properties during deformation [66]. A polymer is a macromolecule consisting of repeating units called monomers bonded together by covalent bonds. Under specific conditions, the monomer molecules form a polymer during a process called polymerization. Polymer materials are usually classified as being thermoplastic, thermosetting or elastomer. Thermoplastic materials are typically branched and linear polymers, which melt when heated and solidify upon cooling, and therefore, may be reshaped. Unlike thermoplastics, thermosets can be characterized by a close-meshed three-dimensional network, where polymer chains are coupled together by chemical bonds called cross-links. Cross-links drastically change properties of the polymers, so that the resulting materials cannot be melted and they decompose upon heating. Most elastomers are thermosets having wide-meshed cross-linking, but there exist thermoplastic elastomers as well, which combine both thermoplastic and elastomeric properties. Usually, elastomers are cross-linked polymers, where polymer chains are connected by relatively weak intermolecular forces and are stretched when external stress is applied. These viscoelastic properties strongly depend on the cross-link density and the functionality of the junction units, and found a broad application in the industry. Especially significant in this context and the most famous elastomer is natural rubber (NR) or *cis*-1,4-polyisoprene. The natural rubber, as used by industry, mainly comes from the rubber tree (*Hevea brasiliensis*) or others. Its monomer unit is 2-methyl-1,3-butadiene or isoprene, which is depicted in Fig. 2.1.

Another important type of polymer, which is widely used in the tire industry, is styrene-butadiene rubber (SBR). Its structural formula is presented in Fig. 2.2. SBR is a synthetic rubber produced as a copolymer of styrene and butadiene. The

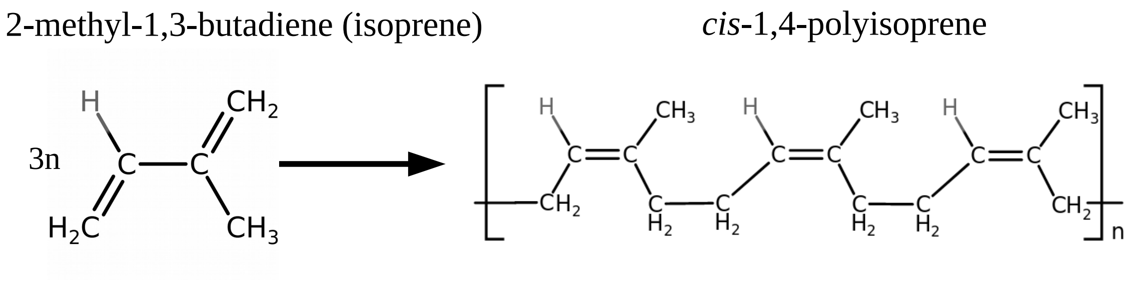

Figure 2.1: 2-methyl-1,3-butadiene or isoprene is a monomer unit of *cis*-1,4-polyisoprene. The latter is the main component of natural rubber.

ratio between styrene and butadiene strongly affects properties of the final product, i.e., rubbers with a low styrene content exhibit less hardness and higher elasticity. High styrene contents result in a higher density and a higher glass transition temperature, i.e., the range of temperatures over which the transition from a polymer melt (amorphous state) to a polymer glass (solid state) occurs.

Elastomer elasticity is a result of a change in the conformation entropy of the polymer segments between cross-links during deformation [68]. Cross-links are needed if one wants to tie conformation changes of polymer segments to external forces. When external stress is applied, the number of available microstates reduces and thus the entropy decreases. When the stress is removed, the elastomer returns to its original state, and the entropy increases again. In contrast, a simple liquid, where the molecules move independently, does not change its entropy in response to a change in the shape of its container. Cross-linking is used in the rubber industry to enhance the physical properties of rubber. There are two main types of cross-links: physical cross-links and chemical cross-links. Physical cross-links are always present and are formed by entanglements between polymer chains. These interactions are weaker than the chemical bonds, and the domains that act as cross-links are reversible. Chemical cross-links are formed in chemical reactions; in this case, the resulting modification of mechanical properties strongly

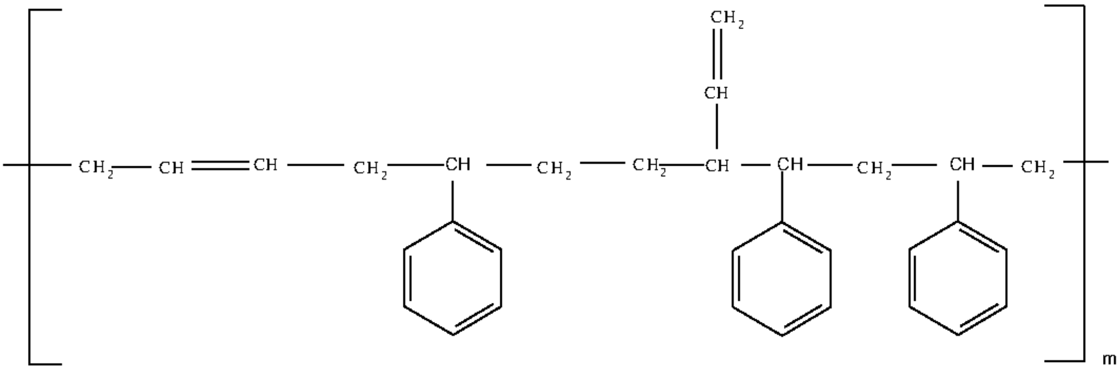

Figure 2.2: Structural formula of styrene-butadiene rubber or SBR.

depends on the cross-link density. As the main quantities characterizing the mechanical properties of elastomers in this work, we consider storage and loss moduli. The former describes the energy stored during deformation, while the latter is a measure of the dissipated energy. Low cross-link densities result in increased viscosities of polymer melts and, consequently, in a higher loss modulus. At very high cross-link densities, the material becomes very rigid or glassy, which increases its storage modulus and makes the material less deformable. The desired elastomeric properties are obtained at intermediate cross-link densities [67]. In terms of the number of monomers per cross-link, this would roughly correspond to 150-210 at the cross-link densities between 3.4 and $5.0 \cdot 10^{-5}$ mol/g [69]. Chemical cross-links are typically covalent bonds, which are formed during a special chemical process called vulcanization or curing. Curing systems in common use include sulphur, peroxides, metallic oxides (e.g., ZiO) and acetoxysilanes. The most broadly used polymers in the tire industry, NR and SBR, are also subjected to vulcanization due to a large number of unsaturated bonds [70]. During vulcanization, polymers are heated together with a curing system and additional reagents that can modify the kinetics and chemistry of the process. When sulphur is used, the sulphur atoms form the so-called sulphur bridges between the polymer chains; the sulphur bridges can contain one or several sulphur atoms. The underlying reaction mechanism is still not completely understood [71].

The simplest model used to qualitatively describe linear polymers is an ideal chain model. It neglects the interactions between monomers separated by large distances. Independent of this assumption we can always define $\vec{R}$ - the total end-to-end vector via

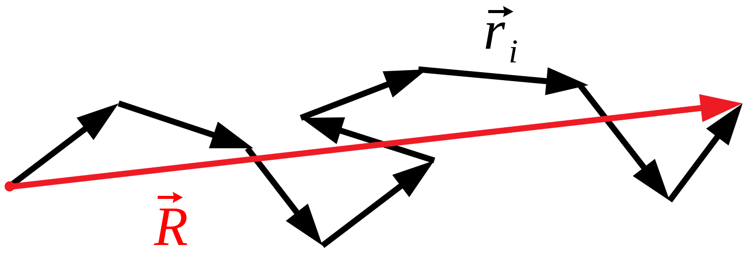

Figure 2.3: End-to-end vector of a polymer $\vec{R}$ consists of bond vectors $\vec{r_i}$.

$$\vec{R} = \sum_{i=1}^{n} \vec{r_i}, \tag{2.1}$$

where $\vec{r_i}$ is the $i-$th segment or the bond vector and n is the number of segments. The end-to-end vector is depicted in Fig. 2.3. If the chain is in its completely stretched form, then the end-to-end vector is equal to the contour length of the chain. In the freely jointed chain model, the polymer consists of freely jointed bond vectors which have the same length $|\vec{r_i}| = l$. The model assumes no correlations between bond vectors, and a polymer simply is random walk. The mean square end-to-end distance is then given by

$$< R^2 > = nl^2. \tag{2.2}$$

In a typical polymer chain, however, only a limited range of values for the bond angle is possible, which implies the correlations between neighbouring bond vectors. These constraints are accounted for in the freely rotating chain model, which assumes that a bond vector is free to rotate on a cone with a fixed cone angle, where the main axis of the cone is defined by the preceding bond angle. In this context, Flory introduced a quantity which is called a characteristic ratio defined via

$$C_n = \frac{< R^2 >}{nl^2}. \tag{2.3}$$

In a given ideal chain model, the characteristic ratio can be considered as a measure of the polymer's stiffness. The characteristic ratio depends on the number of bond vectors n, but for long chains it reaches a constant value C_∞. It is worth mentioning that there exist other quantities characterizing the polymer size, such as the Kuhn length, persistence length and radius of gyration [65]. The former is used for chains much longer than the range of correlation and is obtained by rescaling a given chain into a freely jointed chain, such that the neighbouring segments do not correlate. The Kuhn length is the length of the obtained segments and characterizes the stiffness of the chain. The persistence length is defined as the length over which correlations in the direction of the tangent are lost. It is considered to be one half of the Kuhn length and is more appropriate than the latter for persistent flexible polymers such as DNA. The radius of gyration is used for describing branched or ring polymers, where the mean-square end-to-end distance cannot be well-defined.

2.2 Filler Particles

The main aim of using filler particles is to get significant reinforcement of the mechanical properties of elastomers [4]. In the tire industry, the most widely used fillers are carbon black and silica. Using the filler particles helps to achieve strong modification of the elastic properties due to the complex filler structure. Fillers consist of primary particles which tend to establish rigid aggregates. Aggregates are the smallest filler structures which cannot be broken down during the mixing process. At high concentrations these aggregates form filler agglomerates which are less weakly coupled than the aggregates. It is also possible that the agglomerates build a continuous filler network. If the filler is conductive, like, for instance, carbon black, this causes a sharp step-like increase in electrical conductivity, signalling filler percolation [72]. This also indicates that at and beyond the percolation threshold neighbouring filler particles may be close, i.e., their separation is a few Å or less. The location of the percolation threshold depends on the particle size, where it usually increases for larger particles. The reinforcement is achieved via two main effects: the interaction between filler particles and surrounding polymer and the formation of the filler network. Thus, reinforcement is a complex multiscale problem.

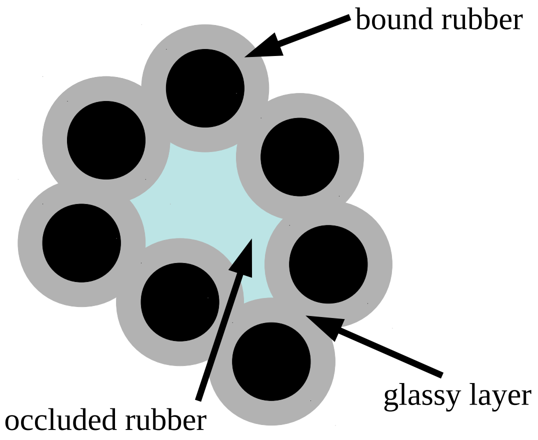

Figure 2.4: Different types of constrained rubber in the vicinity of the filler surface.

Reinforcement requires that the components, forming the rubber, are well mixed. To achieve this, rubber mixing consists of several steps. In the first step, a filler is subdivided into smaller structures, allowing the incorporation into a rubber matrix, which takes place in the next step. The incorporation is followed by mixing. During mixing, the filler agglomerates are broken down to aggregates and distributed throughout the compound. The dispersion in this step occurs on different levels, so we can distinguish between visual, macro- and micro-dispersion [73]. In the post-mixing production stages, the initially dispersed filler tends to reagglomerate or flocculate. The resulting filler dispersion is modelled by the Monte Carlo morphology generator described in Chapter 3.

Adhesion between filler and polymer plays an important role in determining mechanical properties of composites. The interaction between filler and elastomer is very complex and is based on several types of forces. These forces can be divided into dispersion and polarization forces. Dispersion or London forces act between all atoms and molecules and usually exceed the induction and orientation forces, providing the main contribution to long-range van der Waals forces. Polarization or polar interactions include Keesom (dipole-dipole or orientation) interactions and Debye (dipole-induced dipole or induction) interactions. Chemical bonds, acid-base (e.g., hydrogen bonding) and capillary forces can affect the filler-elastomer interaction as well. All these possible types of forces are responsible for adhesion[74]. The process of adhesion in general, and how it can be described in terms of surface tensions, is discussed in Appendix A.

There exist several models describing the contribution of rubber to reinforcement [75]. This contribution may also be different depending on the filler type [31]. For highly polar fillers the filler networking mainly takes place due to direct contacts between aggregates, e.g., hydrogen bonds, because of incompatibility with low polar hydrocarbon rubbers [24]. For fillers with a high affinity toward rubber, the network could be formed by a different mechanism. Due to strong polymer-filler interactions, there is a fraction of rubber which is adsorbed on the filler surface and cannot be extracted by the polymer solvent. This rubber is called the bound rubber, and in this rubber shell the mobility of the polymer segments is reduced. In the filler network, two filler aggregates interact via these rubber shells, forming glassy layers. During the formation of the filler network, fillers can also trap some rubber in the void of the filler aggregates. This immobilized rubber, which is shielded from deformation, is called trapped or occluded rubber. The immobilized rubber chains act as rigid filler particles, increasing the effective filler loading. A schematic presentation of a filler cluster with the adjacent rubber is shown in Fig. 2.4.

Some authors believe that the bound rubber consists of two phases with different molecular mobility. The molecules that are attached to the filler surface form a tightly bound phase, where the molecular mobility is strictly constrained. In a loosely bound phase, the molecules are slightly more constrained than those in the unfilled rubber. A filler-rubber interface model for CB-reinforced elastomer, based on stress analysis, was proposed in [76]. The model consists of double polymer layers with different molecular mobility: the inner glassy hard layer and the outer sticky hard layer. The former has a thickness of about 2 nm, while the latter possesses a thickness of 3-8 nm. The glassy hard layer increases the effective diameter of a CB particle. When the filler volume content is above 0.2-0.25, the sticky hard layers surrounding two adjacent carbon black particles overlap and form a network of oriented molecules. Another model, including glassy layers around filler particles, is put forward by Merabia et. al in [46]. This model considers reinforcement as the result of overlapping of glassy layers between filler particles. At small volume fractions and/or low temperatures, the glassy layers do not overlap, and the only effect is an increase in the effective filler volume fraction. When the filler content and/or temperature is high, then the glassy layers overlap, forming glassy bridges between fillers. As a result, a strong reinforcement effect is observed. Additionally, it was found, that the properties of the elastomer matrix itself change due to presence of glassy domains and a glass transition temperature shift of the matrix in the vicinity of fillers [77, 78]. The thickness of the layer, where the polymer chain dynamics is significantly reduced, depends on the temperature and can be found via [77, 79]

$$e(T) = \delta_m \left(\frac{T_g}{T - T_g} \right),$$

where δ_m is the ability of the filler surface to reduce the polymer mobility, and T_g is the glass temperature. This equation holds for temperatures far from the glass transition ($T > T_g + 50$ K).

On the other hand, there are also studies reporting no significant effect of fillers on the local segmental dynamics of a polymer and the glass transition of the latter. Robertson showed in [14] that in silica-filled SBR the bulk modulus was mainly unchanged by silanes. The silanes increased the bound rubber, but the glass transition of this bound rubber was similar to the bulk SBR. The modification of the polymer-filler interface had almost no influence on the segmental dynamics of polymer chains proximate to filler particles. Huang et al. found that in silica and carbon black-filled NR, a bulk change in the glass transition temperature does not occur in the presence of filler particles [80]. Thus, the issue of the existence of glassy layers remains unresolved, and no finite conclusions can be drawn regarding this problem.

2.2.1 Carbon Black

Carbon black is a result of incomplete combustion of petroleum products, and it is most commonly used as a reinforcing filler in car tires or as a colour pigment in inks, paints and plastics. Carbon black usually consists of spherical particles with a rough surface, which form rigid aggregates with a fractal structure. Agglomeration of the aggregates leads to the formation of a filler network at high concentrations. The primary particles in the case of carbon black have a diameter of 5-100 nm depending on the production process, while aggregates have dimensions of 100-500 nm. The aggregates form agglomerates due to van der Waals forces; their dimension is about 1-40 μm. There exists a broad variety of carbon black types depending on the particular parameters required in production. The reinforcement effect depends on the specific surface and the structure of primary aggregates. The former is defined by the size of the primary particles and varies between 10 m^2/g and 200 m^2/g [7]. According to ASTM D1765-21, carbon black types are typically classified using a special code consisting of 3 digits (e.g., N339), where the first one gives information on the average surface area, while the last two are assigned arbitrarily. The diameter of carbon black primary particles largely affects blackness and dispersibility. Generally, smaller particles possess higher blackness and higher surface area but poorer dispersion due to an increase in coagulation forces. The same applies to larger carbon black structures – aggregates and agglomerates. Hence, blacks with larger particles provide lower reinforcement in comparison to blacks with smaller particles.

One way to classify carbon black aggregates, based on their shape, was proposed in [81]. The authors used 4 shape categories to describe the carbon black structures: spheroidal, ellipsoidal, linear and branched. Spheroidal types are found in a significant concentration only in thermal blacks, whereas the other shapes are presented in all other types of carbon blacks. It was found that highly reinforcing tread-grade carbon blacks, having a small particle size, also usually form branched aggregates. Thus, the authors concluded that the branched aggregate percentage has the greatest effect on the modulus. The ratio of branched aggregates decreased for semi-reinforcing blacks and was the smallest for the largest particles. The latter had mostly ellipsoidal and spherical aggregates, while spherical ones were often presented by single particles.

Recently, environmental concerns have promoted an increase in the production of high-performance and 'green' tires, where carbon black is replaced by silica as a filler. Using silica in car tires reduces CO_2 emission and increases fuel efficiency. Nevertheless, carbon black still finds application in the products, where tensile strength and abrasion resistance are of great importance.

2.2.2 Silica

Nowadays, silica has become the filler of choice in car tires production due to a better relation between the tire performance parameters in comparison to carbon black. The improved rolling resistance, wet and ice grip make silica the best available filler for winter tires as well. Silica is used in conjunction with compatibilizing agents for better dispersion. The chemical structure of these agents, their concentration on the particle surface and the type of bonding to the surface as well as to the polymer offer additional 'degrees of freedom' to the developer.

Silica is silicon dioxide, which has the chemical formula SiO_2. In nature it is most commonly found as quartz and is the major component of sand. However, natural forms of silica are difficult to process, and they are often harmful to health. Therefore, silica is generally produced using synthetic chemical processes. A good overview of the manufacture of colloidal silica is given in [82]; here we focus on two methods: fumed or pyrogenic synthesis and precipitated synthesis.

The fumed synthesis starts with a vaporization of silicon tetrachloride in a hydrogen and oxygen flame at temperatures between 1100 and 1800 °C and proceeds via polymerization and/or oxidation of $SiCl_4$:

$$\mathrm{SiCl_4 + 2H_2 + O_2 \rightarrow SiO_2 + 4HCl.}$$

Silica forms molten nuclei, which grow during the reaction into larger aggregates. Then the fumed silica is extracted from HCl and purified. Varying concentration, temperature and reaction time allows to control the particle size, size distribution and surface area. The primary particle size of the fumed silica is 5-50 nm, the surface area is 50-600 m^2/g. Additives may also be used during or after the process to alter the surface properties, e.g., produce hydrophilic or hydrophobic silica. The main advantage of this method is using $SiCl_4$, which is a pollutant by-product of the polysilicon industry. The main drawback is a large energy consumption of the process. Fumed silica is currently used in many industries, especially where a high degree of purity is required, such as medical applications and electrical insulation. However, because of its high cost in comparison to, for example, precipitated silica, fumed silica is rarely used in the tire industry. Major global manufacturers of fumed silica are Evonik (the trademark Aerosil), Wacker Chemie (HDK) and Cabot (Cabosil).

The precipitated silica method is the most widely used method for manufacturing colloidal silica. It is based on the neutralization reaction of a soluble silicate with an acid. As a result, a silicic acid forms at high concentrations, leading to its polymerization and precipitation from the solution. In industry, precipitated silica is produced mainly from sodium silicate and sulphuric acid

$$\mathrm{Na_2O \cdot 2.6SiO_2 + H_2SO_4 \rightarrow 2.6SiO_2 + Na_2SO_4 + H_2O.}$$

Sulphuric acid is added to a heated solution of sodium sulfate; simultaneously, additional components can be added to alter the properties of the final product. During the reaction time, an intermittent stirring is used to prevent the formation of a gel. After the reaction is finished, the silica is filtered, washed, dried and milled. The mean particle size of the precipitated silica is 5-100 nm and the specific surface area 5-100 m^2/g. The properties of the final product are affected by variations in pH, temperature, concentrations of the components and stirring rate. The precipitated silica is less pure than the fumed one, but the costs and energy consumption of the method are less than in the case of the fumed synthesis. Due to their high cost-effectiveness, precipitated silica is widely used not only in the rubber industry, but also as absorbents and catalytic supports. Major manufacturers

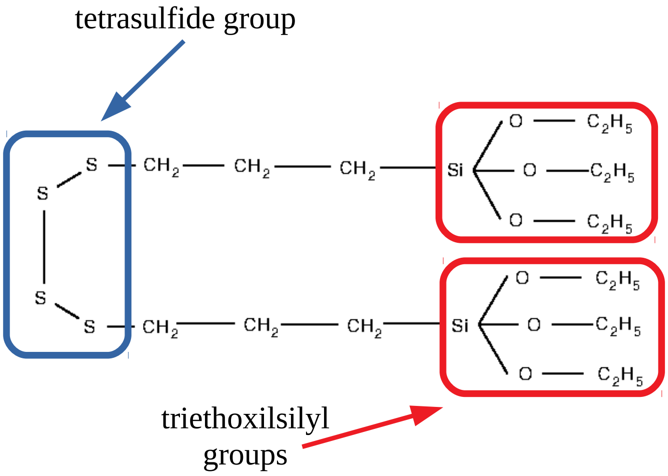

Figure 2.5: Functional groups of TESPT.

of precipitated silica are Evonik (Ultrasil), Solvay(Zeosil), Gujarat Multi Gas Base Chemicals (Mansil) and IQE (Ibersil).

Fumed silica has a lower tendency to aggregate and to form agglomerates than precipitated silica because of its lower surface density of silanol groups, which results in a lower bulk density [83]. In general, however, silica has a stronger tendency to flocculate than carbon black due to its high polar component of the surface energy. The hydrogen bonding interactions between polar groups (siloxane, silanol) on the silica surface are stronger than the interactions between the silica surface and an elastomer. Therefore, a hydrophobic modification of the silica surface is required to improve the compatibility of elastomer and silica. This is usually done using silanes and will be discussed next.

Surface Modification of Silica

Surface modification of silica by a coupling agent is done to increase the interaction strength between polymer and filler. The latter is a necessary condition for obtaining products with required mechanical properties. The most common way of silica surface treatment is silanization – the process of chemical adsorption of silanes. The most widely used compound in this context is TESPT – bis-(triethoxysilylpropyl) tetrasulfide, also known as Si69 [15, 60, 84–86]. TESPT has triethoxysilyl groups, which react with the silanol groups on the silica surface. The tetrasulfide group of the silane, in turn, forms covalent bonds with the methyl groups of the polymer. The functional groups of TESPT are shown in Fig. 2.5. Thus, TESPT permanently binds the polymer to the filler surface.

The silanization is usually performed in situ, when silanes are added to the mixture after silica at elevated temperatures [16, 87]. The addition of silanes changes the silica surface energy, decreasing its polar part and increasing the dispersive component, and, consequently, strongly affects properties of the final product. For example, the storage modulus as a function of strain amplitude for S-SBR filled with 40 phr silica drops with an increase in the spacer length (the number of CH_2 groups in the aliphatic chain) [88]. The authors in [88] also showed, that higher

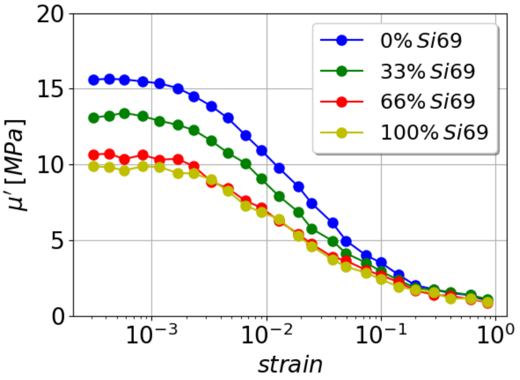

Figure 2.6: The storage modulus vs. strain amplitude for S-SBR filled with 40 phr silica. The concentration of Si69 used for the silica surface modification is varied. Data is taken from [88].

concentrations of Si69 lead to a drop in the storage modulus as well (see Fig. 2.6). The difference between unmodified and modified silica can also be seen when one compares Ultrasil VN3 (precipitated silica) and Coupsil 8113 (the same silica, but prereacted with Si69) [22]. The silane addition promotes a decrease in the storage modulus, which can be observed in both flocculation and dynamic mechanical measurements.

2.3 Quantities in the Rubber Industry

In the rubber industry, the quantities of different components required for production of a particular rubber compound are usually given in special units – parts per hundred rubber or phr. For instance, a filled elastomer with the filler loading equal to 40 phr of filler contains 40 g of the filler per 100 g of the polymer. Using the units of phr is especially convenient in the mixing process, because the only information needed for the right mixing is the masses of the components. In simulations, however, another quantity is typically used – the volume fraction of a component ϕ. In order to find the volume contents of the components, based on their amount in phr, the following relation can be used

$$\phi_i = \frac{V_i}{V_{total}} = \frac{\frac{phr_i}{\rho_i}}{\sum_i \frac{phr_i}{\rho_i}}. \tag{2.4}$$

Here V_i and ρ_i are the volume and density of the i-th component, respectively. It is worth noting that different types of fillers have different densities, and, consequently, different filler volume contents, although the amounts in phr may be the same. At the same time, mechanical properties of filled elastomers depend on the filler volume content. Therefore, without information on the filler densities, a direct comparison of mechanical properties observed for systems filled with different fillers is often impossible.

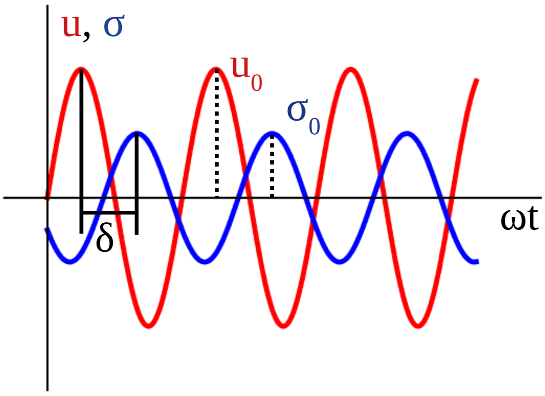

Figure 2.7: Strain u with the strain amplitude u_0 is applied to a sample in a DMA run. The resulting stress function σ with the stress amplitude σ_0 has the same form, but it is shifted by the phase shift δ.

2.4 Mechanical Testing of Elastomers

In the case of elastomers it is their mechanical performance which is the most important. Polymers are special in this context because they combine elastic and viscous properties in both the fluid and the solid state, so they are generally called viscoelastic materials. For measuring the mechanical performance, several laboratory methods can be used. A detailed description can be found in [27, 64], and the basics given in this section are also based on these sources. The description of the mechanics of polymers requires basic knowledge on the theory of elasticity. The terms strain, stress and relations between them are described in Appendix B.

A basic method to study the viscoelastic properties of a sample is the creep testing. It involves loading of a sample followed by a measurement of the strain as a function of time. Recovery tests look at the material's relaxation once the external load is removed. The tests can be done separately, but provide more useful information when combined. Creep and creep-recovery tests are useful in the cases, when low shear rates or frequencies are applied, as well as when the test times are very long. The test cycles can be repeated several times at different temperatures, allowing to mimic real conditions. The stress relaxation test is the inverse of the creep experiment: a material is held at a constant strain and the induced stress is measured as a function of time. These measurements often provide important information which complements creep data. The third common test method includes an application of a dynamic force to a sample and is called the dynamic mechanical analysis. In this work, one of the main steps is to simulate the dynamic mechanical analysis, therefore, in the next section we will focus on the theory of this method.

2.4.1 Dynamic Mechanical Analysis

Dynamic Mechanical Analysis or DMA is one of the main testing methods applied to elastomers in the rubber industry [27, 28, 68, 89]. Typically, during the analysis a sinusoidal stress σ is applied to a material and the resulting strain u is measured, but it can also be the other way around. Schematically, this is illustrated in Fig. 2.7. For a perfectly elastic solid, the resulting strain and the stress will be perfectly in phase, i.e., $\delta = 0$. For a purely viscous fluid, there will be a 90 degree phase shift of the strain with respect to the stress, i.e., $\delta = \pi/2$. Viscoelastic materials have the characteristics in between, where some phase shift $\delta \in (0, \pi/2)$ occurs during DMA tests [90]. This behaviour of elastomers can be modelled mechanically by combinations of springs and dashpots, where springs model the elastic contribution and dashpots represent the viscous contribution (see Fig. 2.8).

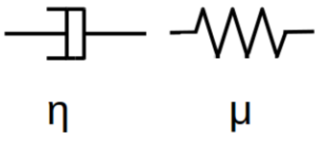

Figure 2.8: Elements representing the elastic and viscous contributions. Left: the dashpot characterized by a viscosity coefficient η; right: the harmonic spring characterized by its modulus μ.

The mathematical form of these elements:

$$\sigma_\mu = \mu u_\mu \tag{2.5}$$

$$\sigma_\eta = \eta \dot{u}_\eta. \tag{2.6}$$

Here u is the shear strain, σ is the shear stress, μ is the (shear) modulus, $\dot{u}$ is the strain rate, η is the viscosity coefficient. The first equation describes the elastic contribution, while the second one represents the dissipative contribution. These basic elements can then be combined into simple models. One possible combination is the Kelvin-Voigt model, which consists of a parallel connection of a spring and a friction pot (Fig. 2.9).
In this case

$$\sigma = \sigma_\mu + \sigma_\eta \qquad u = u_\mu = u_\eta, \tag{2.7}$$

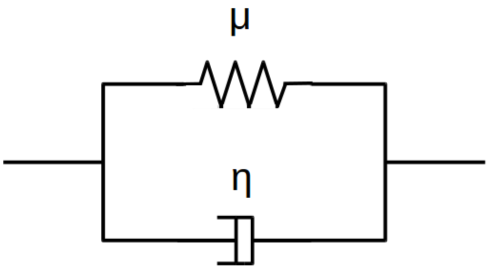

Figure 2.9: The Kelvin-Voigt model.

where σ is the total stress, u is the total strain. Using Eq. (2.5) and (2.6), we obtain

$$\sigma = \mu u + \eta \dot{u}. \tag{2.8}$$

We assume that the shear strain is harmonic. Then the shear stress should also be harmonic, but with a different amplitude and a phase shift:

$$u = u_0 \sin(\omega t), \tag{2.9}$$

$$\sigma = \sigma_0 \sin(\omega t + \delta). \tag{2.10}$$

The phase shift is caused by the energy dissipation in the system. By inserting this to (2.7) and using

$$\sin(\omega t + \delta) = \cos(\delta)\sin(\omega t) + \sin(\delta), \cos(\omega t),$$

we get

$$\mu' = \frac{\sigma_0}{u_0}\cos(\delta) = \mu, \tag{2.11}$$

$$\mu'' = \frac{\sigma_0}{u_0}\sin(\delta) = \omega\eta, \tag{2.12}$$

$$\tan\delta = \tau_K \omega, \tau_K = \eta/\mu. \tag{2.13}$$

Here τ_K is a relaxation time, which describes the strain relaxation. Note that the first '='-sign in (2.11) and (2.12) define μ' and μ'' in general, while the second '='-sign in each equation is true for the particular model (in this case, the Kelvin-Voigt model). The relaxation time can also be seen as the time required to reduce the strain to $1/e$ of its initial value. The quantity μ' is the storage modulus and μ'' is the loss modulus, and they are the quantities measured in experiments. The storage modulus measures the stored energy, representing the elastic part, and the

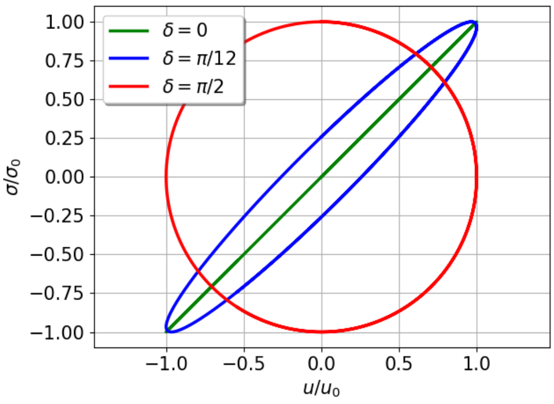

Figure 2.10: Hysteresis in the $\sigma - u$-plane for different values of δ. Note that the area enclosed by the curves gives the dissipated work w_{loss}.

loss modulus is a measure of the energy dissipated as heat, representing the viscous part. Note that the equations (2.11)-(2.12) are obtained under the assumption of harmonic stress and strain, which does not always hold, especially in the case of filled systems. Nevertheless, the discussion of most experimental data is based on this linear or one-coefficient Fourier analysis, even for highly non-linear systems. In this work we use this approach as well.

The combination of the storage and the loss moduli gives the complex modulus of a sample:

$$\mu^* = \mu' + i\mu''. \tag{2.14}$$

The quantity $\tan\delta$ is the loss tangent, and it is equal to the ratio of the loss modulus to the storage modulus $\tan\delta = \mu''/\mu'$. The loss tangent is also called damping and is widely used in the rubber industry as a direct indicator for properties like rolling resistance and wet grip. It shows how efficient the material is in terms of energy lost to internal friction and molecular rearrangements. One important property of the loss tangent is that it is independent of geometry because the sample dimensions cancel when the ratio of the moduli is taken. In addition, some earlier instruments recorded only the phase angle and therefore the early literature uses the $\tan\delta$ as a measure for many properties [27]. Thus, by calculating the amplitudes σ_0, u_0 and the phase shift δ, we can determine the storage and the loss moduli and the loss tangent. However, in experiments we often do not have the pure sine strain and stress, so we require a different way for estimating the moduli. We can, for instance, calculate the work dissipated by a system during one shear cycle (see also B.3):

$$w_{loss} = \oint_{u(0)}^{u(T)} \sigma du = \int_0^T \sigma \frac{du}{dt} dt = \pi\mu'' u_0^2, \tag{2.15}$$

where $T = \frac{2\pi}{\omega}$ is a period. If we know the dissipated work w_{loss} and the phase shift δ between the strain and the stress, we can calculate the loss and the storage moduli by

$$\mu'' = \frac{w_{loss}}{\pi u_0^2}, \tag{2.16}$$

$$\mu' = \frac{\mu''}{\tan\delta}. \tag{2.17}$$

Equations (2.16) – (2.17) can be used for determining loss and storage moduli, even if the form of the strain and stress is far away from a sine function. Fig. 2.10 shows w_{loss} in the $\sigma - u$-plane for different values of δ. The area enclosed by the curves is the respective w_{loss}. In particular, $\delta = 0$ yields $w_{loss} = 0$, which corresponds to a purely elastic system (from Eq. (2.5): $\sigma = \mu u \Longrightarrow \sigma_0 \sin(\omega t + \delta) = \mu u_0 \sin\omega t \Longrightarrow \delta = 0$), whereas $\delta = \pi/2$ gives the maximum w_{loss} and corresponds to a purely viscous case (from Eq. (2.6): $\sigma = \eta\dot{u} \Longrightarrow \sigma_0 \sin(\omega t + \delta) = \eta u_0 \cos\omega t \Longrightarrow \delta = \pi/2$). The behaviour observed when $\delta > 0$ is called hysteresis.

The next model is called the Maxwell model, and it is presented in Fig. 2.11. The model consists of a spring and a dashpot in series. The model can be mathematically

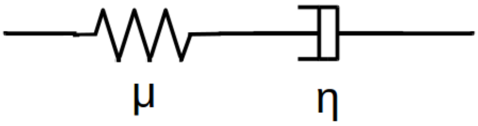

Figure 2.11: The Maxwell model.

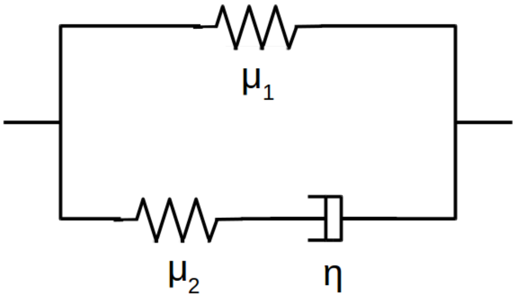

Figure 2.12: The Zener model.

described by the following set of equations:

$$\sigma = \sigma_\mu = \sigma_\eta \qquad u = u_\mu + u_\eta. \tag{2.18}$$

Using the aforementioned approach, we obtain

$$\mu'/\mu = \frac{\tau_M^2 \omega^2}{\tau_M^2 \omega^2 + 1} \tag{2.19}$$

$$\mu''/\mu = \frac{\tau_M \omega}{\tau_M^2 \omega^2 + 1} \tag{2.20}$$

$$\tan\delta = \frac{1}{\tau_M \omega}, \tag{2.21}$$

where $\tau_M = \eta/\mu$.

As the Kelvin-Voigt and the Maxwell models are not applicable in the full frequency range, we require another model. The next model is called the Zener model, and it consists of a spring with a spring constant μ_1 in parallel to a spring with a spring constant μ_2 and a dashpot with a friction coefficient η in series (Fig. 2.12). Hence, the Zener model is a combination of the Kelvin-Voigt and the Maxwell models. The mathematical description of this model is

$$\begin{aligned} \sigma &= \sigma_1 + \sigma_M \\ \sigma_M &= \sigma_2 = \sigma_\eta \\ u &= u_1 = u_M \\ u_M &= u_2 + u_\eta. \end{aligned} \tag{2.22}$$

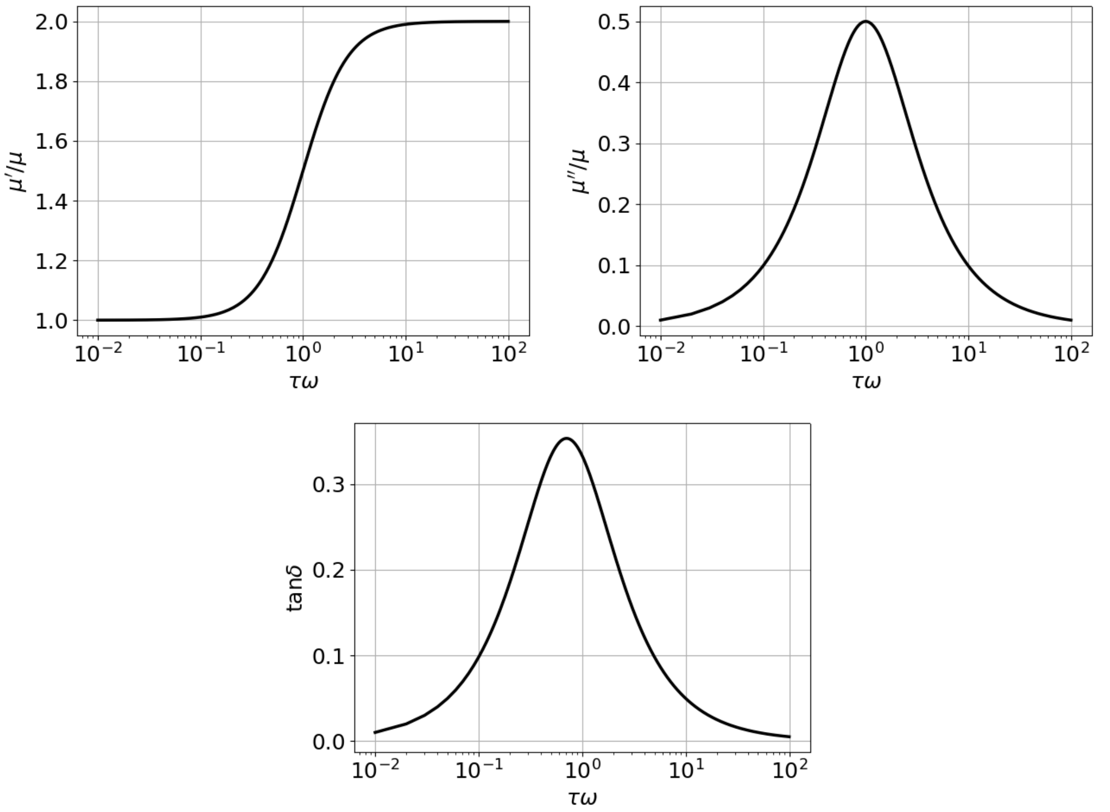

Figure 2.13: Results of the Zener model.

The indices 1 and 2 refer to μ_1 and μ_2. We solve this system of equations using (2.5) and (2.6), and get

$$\sigma + \frac{\eta}{\mu_2}\dot{\sigma} = \mu_1 u + \eta\Big(1 + \frac{\mu_1}{\mu_2}\Big)\dot{u}. \tag{2.23}$$

Using (2.9)-(2.10), we obtain

$$\mu' = \mu_1 \frac{\tau^2\omega^2/\theta + 1}{\tau^2\omega^2 + 1}, \tag{2.24}$$

$$\mu'' = \mu_2 \frac{\tau\omega}{\tau^2\omega^2 + 1}, \tag{2.25}$$

$$\tan\delta = \frac{1-\theta}{\theta}\frac{\tau\omega}{\tau^2\omega^2/\theta + 1}, \tag{2.26}$$

where $\tau = \eta/\mu_2$ and $\theta = \mu_1/(\mu_1+\mu_2)$. The quantity τ is again a relaxation time and describes the stress relaxation at a constant strain. If $u(t=0) = u_0$ and $\dot{u}(t) = 0$, then

$$\sigma(t) = \Big(\mu_1 + \mu_2 e^{-t/\tau}\Big)u_0. \tag{2.27}$$

The value of frequency ω at the maximum of μ'' is called a characteristic frequency, and it is equal to

$$\omega_0 = \frac{1}{\tau} = \frac{\mu_2}{\eta}. \tag{2.28}$$

The moduli and the loss tangent as functions of frequency, obtained for the Zener model, are shown in Fig. 2.13. The shape of the curves is a result of the elements used in the model, i.e., the dashpot and elastic springs. At low frequencies we observe an increase in the $\tan\delta$, which means that the friction element follows the strain $u(t)$. This is realized in the Kelvin-Voigt model because the amplitudes in the two branches are coupled. At high frequencies the decrease in $\tan\delta$ requires the decoupling of the friction elements from the excitation, so the spring takes over the strain from the friction element, which is included into the Maxwell model. The Zener model as a combination of the models combines both behaviours [68]. Note that while the aforementioned models are useful in a qualitative sense on a macroscopic level, it is not clear how they relate to polymer networks on a microscopic level.

One of the most important uses of the DMA is studying the relaxation processes and transitions in a polymer. Here we can distinguish between time and temperature runs. If a polymer is kept at a set frequency, while the temperature increases, then a temperature scan is performed. During a time run, the specimen is held at a constant temperature and changing of properties over time is studied. In this context, temperature control is of special importance, especially for large sample sizes. Poor temperature control can lead to differences in the temperature across the sample, resulting in anomalies such as two glass transition peaks[1] in a single polymer [27]. Thus, large samples require very slow heating rates. As materials are stiff at low temperatures and soft near the melting temperature, sometimes multiple runs may be needed using different conditions and/or different geometries. Possible geometries for the DMA analysis will be discussed later in this chapter.

Time Mapping

To compare simulation results with experimental ones, we need a link between the experimental time and the temperature and the ones used in the model. A possible way to link the two scales is discussed in [57]. The $\tan\delta$-curve in the Zener model is given by (see Eq. 2.26)

$$\tan\delta = \frac{1-\theta}{\theta}\frac{\tau_2\omega}{(\tau_2\omega)^2/\theta + 1},$$

where $\theta = \mu_1/(\mu_1+\mu_2)$ and $\tau_2 = \eta/\mu_2$. In order to find the value of $\tan\delta$ at maximum, we take a derivative of 2.26 with respect to $\tau_2\omega$ and set it to zero. Thus, we obtain

$$\tan\delta|_{max} = \frac{1-(\tau_2\omega_{max})^2}{2\tau_2\omega_{max}}. \tag{2.29}$$

---

[1] Glass transition and other temperature-related processes in a polymer are discussed in Section 2.5.

The Zener model describes the $\tan\delta$ vs. ω qualitatively correct. Assuming that we know $\tan\delta$ vs. ω for an experimental system at a certain temperature T, we can calculate (2.29) to obtain the value of $\tau_2^{exp}\omega_{max}^{exp}$ using the height of the $\tan\delta$ peak at maximum. Then we repeat the same procedure for $\tan\delta$ vs. ω obtained from the simulation and find the numerical value for $\tau_2^{sim}\omega_{max}^{sim}$. We require $1/\omega_{max}^{sim} = 1/\omega_{max}^{exp}$, i.e., $\tau_2^{sim} = \tau_2^{exp}$, which relates the simulation unit of time to the experimental unit of time. For instance, if we have a simulation frequency ω^{sim} which we want to convert, then the corresponding experimental frequency is given by $\omega^{exp} = \omega^{sim}(\omega_{max}^{exp}/\omega_{max}^{sim})$. Note that this conversion of time units holds only for one particular temperature. The conversion obtained using a pure rubber system is assumed fixed independent of the filler content, i.e., for filled systems we use the same time unit conversion.

Instrumentation for DMA

There exists a broad variety of instrumentation for DMA measurements. In this section a short introduction to the topic is given, which is mainly based on [27].

Force resonance analysers are the most common DMA analysers nowadays. They force a sample to oscillate at a fixed frequency and can scan material properties across a temperature range. The analysers include different parts responsible for controlling the temperature, deformation, sample geometry and environment.

Depending on the type of the load control, the analysers can be divided into two main groups: strain- and stress-controlled analysers. The former move the sample a set distance and measure the stress. They usually have a better time response for low viscosity materials and can perform stress relaxation experiments as well. The stress-controlled analysers are cheaper; in stress control, a set force is applied to the sample and the strain is measured. While the applied force remains the same when temperature, time or frequency varies, the stress in the material may be different. The constant stress is more natural in many cases since it can mimic real-life conditions and is often more sensitive to sample changes. This type of analyser allows to more easily perform long relaxation times or long creep experiments. Both types of analysers give the same results as long as the DMA measurements are run at very low strains to keep the sample within its linear region. However, in the non-linear region the difference becomes large, as the linear relation between stress and strain does not hold any more.

DMA analysers usually apply stress or strain in two ways. One of them is torsional deformation, when force is applied in a twisting motion. Torsion deformation is mainly used for testing of liquids and melts, but solid samples can also be studied in such a manner. Most of torsional analysers also can perform creep-recovery, stress-relaxation and stress-strain measurements. Another possible type of deformation is axial. Axial analysers apply a linear force to the sample and are typically used for solid materials. These analysers often perform flexure, tensile and compression tests, but can also be adapted to liquid samples and to do shear. In addition to measurements that torsional analysers can run, axial analysers can do thermal mechanical analysis (TMA) and study materials with a large modulus. It is worth noting that there exists a considerable overlap between the analysers and by a correct choice of the sample geometry both types can test similar samples.

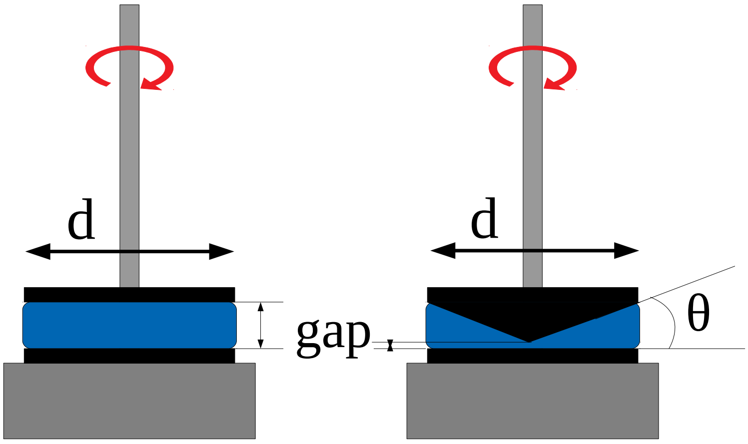

Figure 2.14: Plates geometries. Left: parallel plates, right: cone and plates. Here *d* is a diameter, θ is a cone angle. The gap between plates is defined by the sample. The figure is done in style of Fig. 4.11 from [27].

Sample geometry is one of the key factors affecting the dynamic moduli values. Each of the geometries uses different equations to calculate stress and strain, and the moduli obtained in various testing geometries are always different. In those cases, special geometric factors are used to transfer the force and deformation into the stress and strain. The most common geometries for axial and torsion analysers are listed in Table 2.1. Due to the importance of the shear mode for this work, we limit ourselves to considering the geometries allowing to apply shear deformation to the sample.

Table 2.1: Sample geometries for DMA

Axial analysers	Torsion analysers
Bending (3-Point and 4-Point) Cantilever (Dual and Single) Parallel Plate and its Variants Shear Plates and Sandwiches Bulk Tensile	Parallel Plate Cone-and-Plate Torsional Beam Couette

The most common approach to measuring shear in an axial analyser is the use of the shear sandwich fixtures. During the test, a sliding plate moves between two samples which should be maximally close to identical. One of the restrictions of the technique is a limited range of temperatures due to thermal expansion of the fixture.

In torsional shear, the simplest geometry is two parallel plates with a set gap height for a spherical sample. The gap height is determined by the sample viscosity.

The main disadvantage of this geometry is inhomogeneity of strain: the material at the centre barely moves, while at the edge the movement is much larger. This drawback can be partially overcome in the cone-and-plate geometry, which uses a cone of a given angle instead of the top plate. Both geometries are shown in Fig. 2.14. In the cone-and-plate geometry, at small cone angles the strain is homogeneous across the material. This geometry is the most widely used one for testing non-Newtonian fluids. Both parallel plates and cone-and-plate geometries are inappropriate at very high shear rates due to failure of the material, which reaches a critical edge velocity. Another way to overcome the inhomogeneity problem is using two opposite cones instead of cone-plate or plate-plate geometries.

2.5 Mechanical Properties of Unfilled Elastomers

The aforementioned complex viscoelastic behaviour of polymers implies that their mechanical properties strongly depend on temperature. This limits a range of useful temperatures which differ for various polymers. In a DMA temperature run, one can distinguish between three main regions on the temperature scale: the rubbery region, the transition region and the glassy region. All these regions correspond to different transition processes in a polymer, which can be described by either free volume changes or relaxation times. Both descriptions, however, are equivalent. A simple model describing transition processes in a polymer is the crankshaft model, where the molecule is represented as a series of jointed segments. The model and the variety of transition processes in polymers seen on a DMA scan can be found in [27]; here we limit ourselves to the most important ones.

Fig. 2.15 shows an example of a DMA temperature run for SBR, both unfilled and filled with carbon black N234 at various concentrations. It can be seen that the general behaviour of unfilled and filled systems is very similar. The lowest temperature range corresponds to the glassy region, where the polymer exhibits glass-like properties. In this region, the storage modulus remains large and constant, while the loss modulus is low, making the loss tangent being close to zero. As the temperature increases, the material expands and the free volume increases. This enables localized bond movements such as stretching and bending, as well as side chain movements. This process, which occurs in the glassy state and thus is not shown in Fig. 2.15, is called the gamma transition T_γ.

At higher temperatures there is a transition region, where a glassy solid polymer turns into a melt-like material or, if cross-linked, into rubber. In this region, large segments of the chain start moving, the loss modulus and the loss tangent have a maximum, while the storage modulus drops by 2-3 orders of magnitude. The range of temperatures, where the glass transition occurs, and where the loss tangent reaches its highest value, is called the glass transition temperature T_g [30]. As the glass transition is the main transition for most polymers, it is also called the alpha transition T_α. The glass transition temperature typically defines the operating range of a polymer. For polymers used in their glassy state, T_g represents the upper temperature limit, while for rubbers it gives the lower operating temperature. T_g strongly depends on the functional groups presented in a polymer. For instance, if

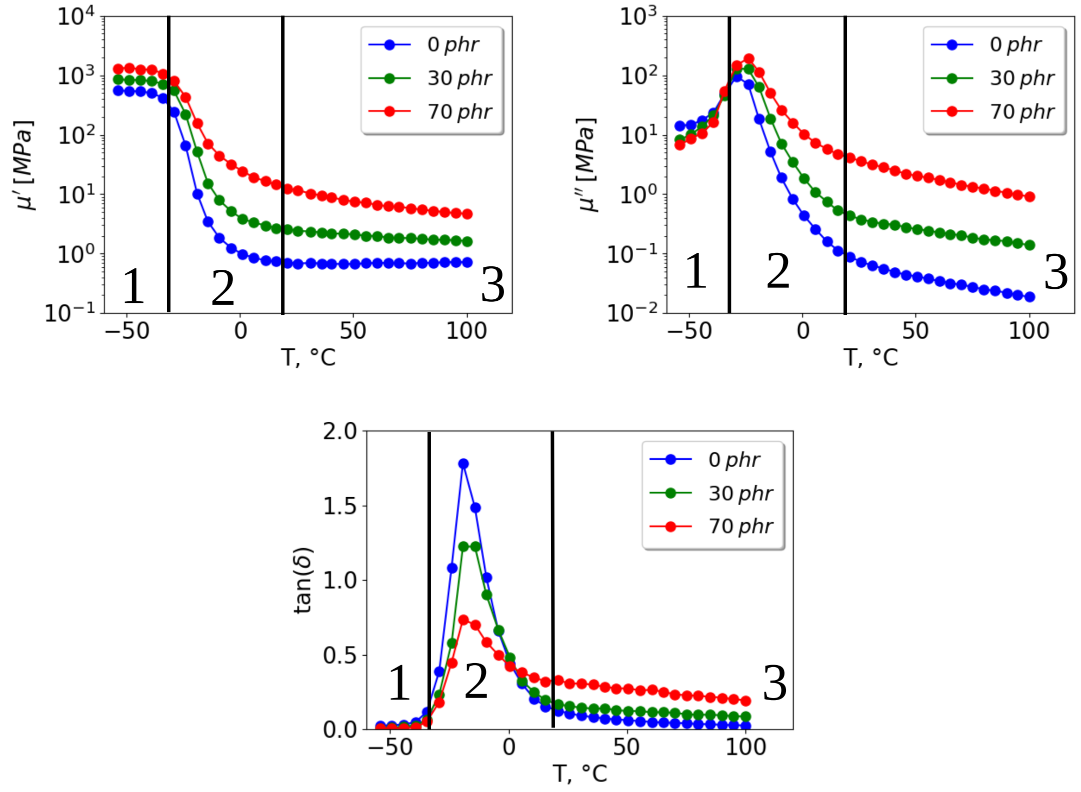

Figure 2.15: The storage modulus, the loss modulus and the loss tangent as functions of temperature for SBR filled with different loadings of CB N234 at 10 Hz and the strain amplitude of 5%. The marked regions are: 1 - glassy region, 2 - transition region, 3 - rubbery region. Data is taken from [31].

a polymer contains a lot of benzene rings (e.g., SBR with a large styrene content), the movements of its chain segments are hindered, and higher T_g is observed.

In the so-called rubbery region, at temperatures above T_g, the elastic properties of rubber dominate. The storage modulus at these temperatures is almost constant, but the values are lower than in the glassy region. The loss tangent in this region does not change much as well. The length of the rubbery plateau and the modulus depend on the number of cross-links or, equivalently, the chain length between cross-links. Hence, increased cross-linking will be indicated in DMA results by increasing T_g and μ'.

At high temperatures, a polymer starts to melt and flow. In this region, which is also called the terminal region, large-scale chain slippage occurs, the storage modulus decreases and the elastic properties cannot be seen any more. The temperature, at which the transition from the rubbery state to the melt state happens, is called the melt temperature T_m. The ability to flow depends on the molecular weight of the polymer and the cross-link density. Polymers possessing large molecular weights melt at higher temperatures, while the ones with very high cross-link densities do not melt at all.

Many commercial elastomers contain additional polymers as a blend or as a copolymer[2]. Polymer blending often affects the DMA results. Typically, for block copolymers and immiscible blends two different T_gs will be seen, each corresponding to an individual component. For miscible polymer blends and random copolymers one single T_g will be observed, which position will depend on the polymer ratio in the mixture.

The behaviour of a polymer over the temperature scale is quite similar to the one observed when frequency changes. At low temperatures, a material is more rigid, and its elastic behaviour dominates. As temperature increases, the material becomes softer and at some point starts to flow. On the other hand, at low frequencies the material has time to relax and respond to stress, therefore, in the low-frequency range viscous or flow behaviour dominates. The same happens if the material is stressed over a long period of time, as frequency is the inverse of time. When frequency increases, the material has less time to relax and becomes more elastic. Thus, by changing the frequency a polymer experiences the same transitions as when one changes the temperature, while low frequencies correspond to high temperatures and vice versa. This principle is often referred to as the time-temperature superposition. It is frequently applied when one wants to obtain data outside the available frequency range of an instrument. In this case, a series of frequency runs is performed at different temperatures. Then the curves are shifted relative to a curve obtained at a reference temperature, giving the so-called master curve, which covers a larger range of frequencies than each of the original runs. The shift factors a_T are usually defined according to the Williams-Landel-Ferry (WLF) model [91]

$$\log a_T = \frac{-C_1(T - T_r)}{C_2 + (T - T_r)}. \tag{2.30}$$

Here C_1 and C_2 are material constants, T is a run temperature, T_r is the reference temperature – the temperature to which the data will be shifted. The materials obeying the time-temperature superposition are called rheologically simple materials. Natural rubber, for example, is a rheologically simple material, therefore, the time-temperature superposition principle is often used in the rubber industry. It is worth noting that the principle is based on several assumptions, e.g., that all relaxation times within the sample are equally affected by temperature. In addition, mechanisms of changing the sample and their rates must be the same at all temperatures. This is not always true, especially in the case of filled elastomers and polymer blends, and care must be taken when applying the principle.

2.6 Mechanical Properties of Filled Elastomers

Addition of filler particles leads to reinforcement of cross-linked polymer systems, which significantly changes their mechanical properties. This happens, however, only at a specific concentration called percolation threshold, where the filler content is sufficient to form a filler-filler network. Filled elastomer systems with the

---

[2] The former term refers to a physical mixture of components, while the latter – to a chemical mixture.

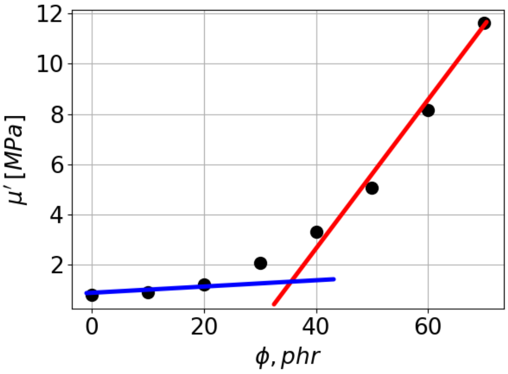

Figure 2.16: Experimental storage modulus vs. filler volume fraction in phr for SBR filled with CB N234 at 70°C and 0.2% strain. The reinforcement slope y is calculated based on the last four points and is equal to 2.4. The percolation threshold is determined as an intersection of the red and blue lines plotted over initial and last points, and in this case is at approx. 35 phr ($\approx 15\%$). The data is taken from [31].

filler concentrations below and above the percolation threshold possess significantly different thermal [92], electrical [29], rheological [93] and mechanical [94] properties, therefore it can be important to determine the position of the percolation threshold. In this section we will discuss changes in the mechanical properties of filled elastomers beyond the percolation threshold.

Fig. 2.16 shows the experimental storage modulus at different filler volume contents for SBR filled with CB N234. Initially, the storage modulus does not increase considerably. But at concentrations above approximately 35 phr, which roughly corresponds to 15% vol. according to (2.4), a power-law increase $\mu' \propto \phi^y$ can be observed. Here y is called a reinforcement slope, and it is typically between 3 and 4, based on the assumption of self-similarity of the filler network [7]. But what are the consequences of adding a filler in terms of other parameters, such as temperature or strain amplitude?

Based on Fig. 2.15, one can see that the storage modulus increases with the filler volume content throughout the temperature range. Larger μ' means that the stiffness and the strength of the material increase, when more filler is added. The loss modulus increases in the range of high temperatures, but does not change significantly at temperatures below the glass transition. Larger μ'' assumes that the energy dissipation in filled systems is also larger than in unfilled ones at high temperatures. Due to the aforementioned factors, the loss tangent, as the ratio of the moduli, plotted vs. temperature demonstrates a complex behaviour. At the glass transition temperature, $\tan\delta$ drops for larger filler volume contents (region 2 in Fig. 2.15). However, the order of the curves corresponding to different filler contents changes in the rubbery region, i.e., at temperatures above the glass transition the higher filled systems exhibit larger values of the loss tangent. In the glassy region, the loss tangent does not change significantly because the values of the storage modulus are large for both, filled and unfilled, systems. According to Fig. 1 in [31],

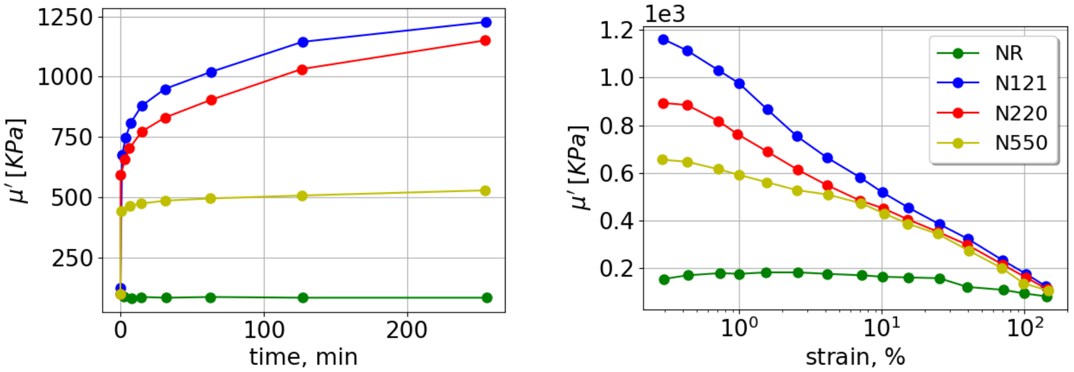

Figure 2.17: Left: flocculation curves for NR melts filled with 50 phr of carbon black with different grades. Right: the attendant Payne effect. The data is taken from [13].

$\tan\delta$ plotted vs. temperature can be used as a laboratory indicator for ice grip (between -40 and -20 °C), wet grip (roughly between -10 and 20 °C) and rolling resistance (between approx. 30 and 80 °C). An ideal material should demonstrate significant values of the loss tangent at low temperatures to achieve the high skid resistance and wet grip. At the same time, it has to possess a low $\tan\delta$ value at high temperatures to reduce the rolling resistance. Based on Fig. 2.15, it is clear, that the addition of filler improves the wet grip but also increases the rolling resistance.

It is well known that filler, which initially is finely dispersed in the polymer matrix during mixing, in the post-mixing stages tends to form larger structures – agglomerates and filler networks [10, 11, 15, 17]. This process is called filler flocculation, and it considerably changes the mechanical properties of filled rubbers. The filler flocculation can be monitored by studying the changes of the small-strain storage modulus of a filled system in time. The left panel of Fig. 2.17 gives an example of such an experiment for natural rubber melts filled with different carbon black grades, taken from [13]. The curves in the left panel of Fig.2.17 are also called flocculation curves, and the attendant experiments are called flocculation tests. Initially, the storage modulus increases rapidly, but levels out after some time. The change in μ' depends on the primary aggregate size; the sample with the smallest CB particles (N121) shows the largest increase in the storage modulus, while the sample containing larger particles (N550) exhibits almost no change in the value of μ'. The authors also found that while the initial increase in μ' is related to the primary particle size, at longer time scales the flocculation kinetics depends on the structure of carbon black and polymer macromolecules. Flocculation tests can also provide information on the quality of microdispersion. In [95], it was found that samples with smaller, well-distributed primary aggregates flocculate less than samples with poor microdispersion. Other factors, affecting the storage modulus, include filler loading, filler surface properties and mixing conditions [31, 95].

Under large deformation, the filler network, formed during flocculation, breaks down, and the storage modulus drops to values which are close to the values obtained for the unfilled system. This can be seen in the right panel of Fig. 2.17 as well.

This effect is called the Payne effect, and it denotes the pronounced decrease in the complex modulus with increasing strain amplitude in filled rubbers under cyclic loading [38]. The effect was named after Payne, who investigated it in the 1960s [32, 96–101]. The Payne effect is observed in both carbon black [102–104] and silica [105] reinforced rubbers. An example of the Payne effect for SBR, filled with CB at different filler loadings, is shown in Fig. 2.18. It can be seen, that not only μ' for the filled system changes with the strain amplitude, but also μ'' exhibits a maximum when plotted vs. strain.

Generally, one can distinguish between different contributions to the storage modulus of a filled system (see Fig. 2.19). The interactions due to the polymer network are present in both, filled and unfilled, systems and define the storage modulus of the latter. This part of the storage modulus does not depend on the strain amplitude, as well as the contribution due to hydrodynamic reinforcement. Originally, Einstein found that the viscosity of a Newtonian fluid η_0 changes to η, if one adds a small amount of rigid spherical particles with volume fraction ϕ according to [106]

$$X = \frac{\eta}{\eta_0} = 1 + 2.5\phi. \tag{2.31}$$

Here X is called the hydrodynamic amplification factor. Later Smallwood [107] found the same equation for the shear modulus in the case of rigid spherical particles embedded in an incompressible linear elastic matrix

$$X = \frac{\mu}{\mu_0} = 1 + 2.5\phi. \tag{2.32}$$

In (2.32) μ_0 is the shear modulus of the elastic matrix. The equations (2.31) and (2.32) hold only for small ϕ, assume no interactions between spheres and are true only in the linear case, i.e., for a Newtonian liquid or a linear elastic material [108].

The Payne effect is not observed in unfilled rubbers, therefore it can be related to either filler-filler or polymer-filler contacts (or a combination of both). However, until now, it has been debated what kind of interactions play a predominant role in the Payne effect. Different models have been proposed in the literature to explain the Payne effect. One of the most well-known theories assumes the breakdown of the filler-network being the main reason of the Payne effect [17, 35, 109–111], as shown in Fig. 2.19. Payne assumed as well that the non-linear behaviour of filled vulcanizates is caused by the breakdown of the carbon black network structure. In [37] the authors found that the drop of the storage modulus vs. strain amplitude similar to the Payne effect in filled rubbers occurs in CB-filled paraffin oil. This strongly suggests the deformation-induced breaking of the filler network to be the main cause for the Payne effect. But the polymer matrix was found to play a significant role in the temperature dependence of the Payne effect. Other possible explanations of the Payne effect include filler deagglomeration in the framework of self-similarity [112] or assume a more important role of the polymer-filler interface, such as polymer debonding from the filler surface [36, 113] or strain softening of the polymer shell around filler aggregates [114]. Ouyang proposed a network junction model, which focuses on the rubber behaviour near the filler network junctions [33, 34].

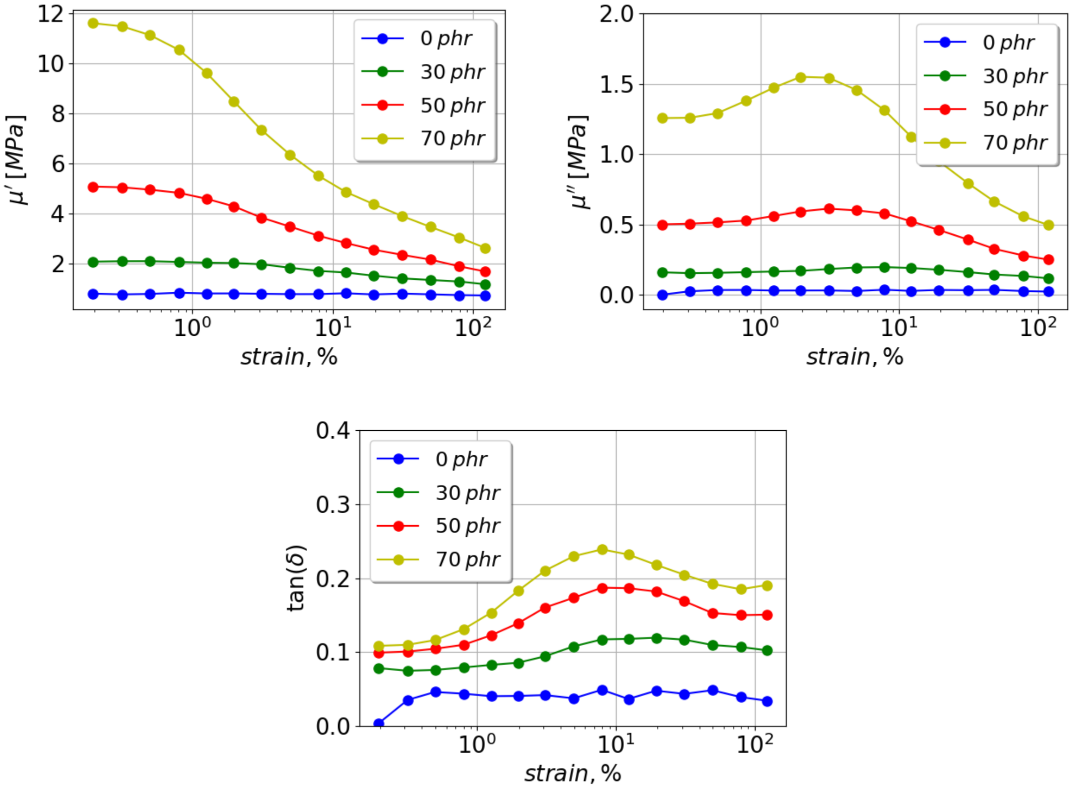

Figure 2.18: The storage modulus, the loss modulus and the loss tangent as functions of strain amplitude for SBR, filled with different loadings of N234, at 10 Hz and 70 °C. The data is taken from [31].

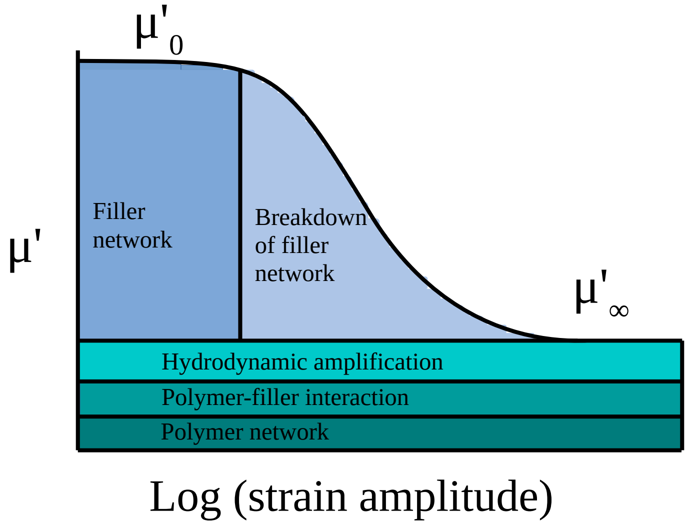

Figure 2.19: Contributions of different effects to the storage modulus of a material. The figure is done in style of [7].

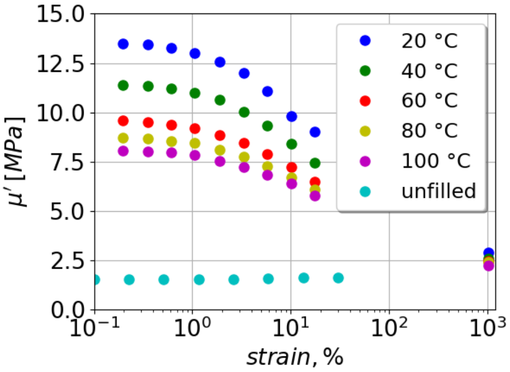

Figure 2.20: Storage modulus as a function of strain amplitude for SBR filled with 40 phr Aerosil 200 at different temperatires. Data is taken from [22].

The dynamic properties of filled elastomers in general, and the Payne effect in particular, depend on temperature and filler morphology, while the latter depends on the surface area and particle size. As the Payne effect is believed to be closely related to the filler network structure, all the parameters affecting the filler network will also affect the Payne effect. An example of the temperature dependence of the Payne effect in SBR filled with Aerosil 200 (a special type of fumed silica) is shown in Fig. 2.20. At low strains, the storage modulus of the filled system drops when the temperature increases. For the unfilled SBR, no dependence on the strain amplitude can be observed. At large strain amplitudes, the values of the storage modulus for the filled system drop and become close to the values obtained for the unfilled SBR. As another parameter affecting the Payne effect, filler surface modifications can be named. For instance, covering the silica surface with TESPT reduces the storage modulus and, consequently, the Payne effect (cf. Fig. 2.6).

Another important effect observed in filled rubbers is the Mullins effect, or the pronounced stress softening [115, 116]. While the Payne effect is observed under dynamic loading at small strain amplitudes between 0.1 and 20%, the Mullins effect can be seen under quasi-static deformations at much larger strains. Depending on the strain history, the material exhibits permanent changes in the elastic properties and the hysteresis, or the area under the curve in the stress-strain plain, increases. Most of the effect can be seen in the first deformation cycle, and after a few cycles the material reaches a steady state, when its stress-strain behaviour does not change any more. Although the micromechanical origin of the Mullins effect has not been fully understood, it reflects damage in the material caused by the previous loading. The stress softening is observed in unfilled systems as well, but the effect is much more pronounced in elastomers containing high filler concentrations. In the literature, the Mullins effect has been attributed to a breakdown or slippage [117] of bonds between filler and polymer, a strain-induced crystallization-decrystallization [118] or hydrodynamic reinforcement of the rubber matrix by filler clusters that irreversibly break during the first deformation cycle [119].

Chapter 3

Monte Carlo Morphology Generator

The general idea of the morphology generator was initially developed in [20, 21] and is also thoroughly discussed in the PhD thesis of Norman Gundlach [19]. The morphology generator combines a coarse-grained description of the components with measured interface or surface tensions. The terms 'interface tension', 'surface tension' or 'surface energy' and experimental methods for their determination are discussed in Appendix A. The 'old' morphology generator utilizes a cubic lattice, and therefore cannot generate input morphologies to the mechanical analysis (DMA) part of the model developed in this work. In this chapter, it is explained how the cubic lattice is replaced by a neighbour list scheme. This removes any lattice symmetry from the generated morphologies, ensuring isotropy and homogeneity. In addition, the same neighbour list can also be used to force-couple the nodes, i.e., polymer volume elements and filler particles, during the DMA.

3.1 Monte Carlo Flocculation

In this section, the set up of the morphology generator will be explained. The section also describes the cell index method, which can be used for constructing neighbour lists in systems with a large number of particles.

3.1.1 Basic Idea

Basic elements of the model are nodes, which can be either filler particles, i.e., non-breakable aggregates, or polymer volume elements. The nodes can have any spatial arrangement, i.e., they can be located on a lattice, or they can be distributed randomly. A node possesses a property 'filler' with probability ϕ, where ϕ is the filler volume content. There are $n = \phi \cdot N$ filler nodes in the system, where N is the total number of nodes. The particle type for the remaining $N - n$ nodes is set to 'polymer'. For simulations of polymer blends, we can also use more than just one polymer. In a binary blend, we assign the properties 'polymer A' and 'polymer B' randomly, with probabilities given by the blend ratio. The binary blends in this work consist of natural rubber (NR), styrene-butadiene rubber (SBR) plus, if they are filled, carbon black or silica. It is convenient, but not essential, to initially place the nodes on a lattice (usually an FCC-lattice). To ensure the system isotropy, the

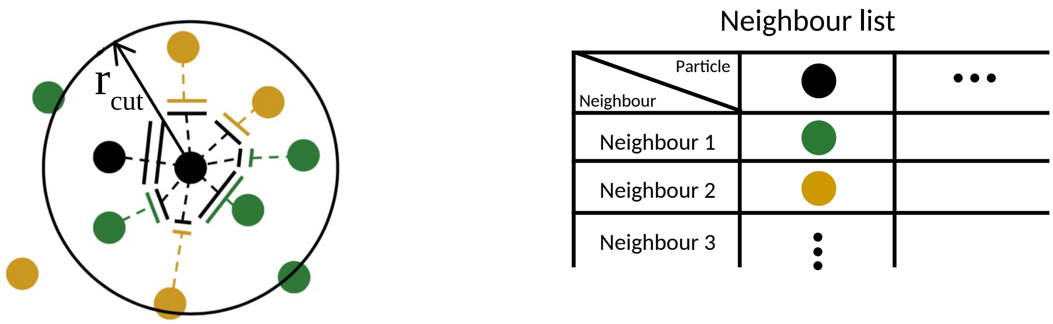

Figure 3.1: Left: a cutoff radius r_{cut} determines the nodes which have a common interface with a given node. Golden and green dots indicate volume elements occupied by different types of polymer. Black circles are filler nodes. Common interfaces are shown by the lines orthogonal to the dotted lines connecting the nodes. Right: construction of a neighbour list based on r_{cut}.

lattice nodes are subsequently displaced by adding $\delta\vec{r}_i$ to their initial positions. The vector components $\delta r_{i,\alpha}$ depend on d, where d denotes the initial distance between nearest neighbours. In the following, d is the smallest linear scale in the system, which corresponds to the center-to-center separation of two filler particles. Hence, d sets the unit of length in the system. It is worth noting that this system preparation is not essential for the simulation of filler flocculation, as it was shown in [20] on the basis of the cubic lattice, but it is important for the subsequent shear simulation. Note that the node distribution is fixed after the aforementioned randomization and remains unchanged throughout all subsequent modelling steps.

We identify the quantity d with the diameter of the smallest non-breakable filler aggregate. The size of these aggregates is typically larger than the size of primary particles by a factor of two to three [120]. In experiments, the size of the smallest non-breakable aggregates can be estimated by studying the attendant TEM images. Then the simulated TEM images can be scaled, so that the unit of length d in the simulation corresponds to the size of the smallest non-breakable aggregates in the experimental system. There exists, however, no such direct correspondence for polymer, and we define d as the linear dimension of a polymer volume element. Note, however, that the typical separation between two cross-links in usual tire rubbers is of the same order as the size of the smallest non-breakable aggregate [65]. Assuming $n = 200$ monomers between cross-links (see also Section 2.1), one has for their separation roughly $\sqrt{< R^2 >} = b\sqrt{C_\infty n}$, where b is the monomer's length. Taking $b \sim 0.8$ nm and C_∞ (NR) ~ 5 [7], we obtain $\sqrt{< R^2 >} \sim 25$ nm, which has the same order of magnitude as the particle size.

We assign surface free energies to each node depending on its type. Every node possesses a number of neighbouring sites, and we assume that the interactions between them can be described via the interface free enthalpy $\gamma_j a$. Here γ_j is the interface tension of the particular node-node-pair j and a is a certain interaction area. Then we define a list of neighbours for each node using a cutoff radius r_{cut}, as shown in Fig. 3.1. The green and yellow colours in Fig. 3.1 correspond to NR

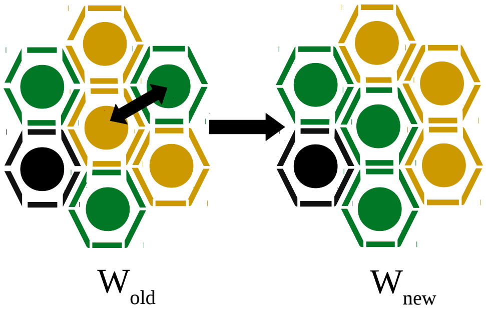

Figure 3.2: An example of the Monte Carlo node exchange move.

and SBR respectively, while the black circles represent filler aggregates. Once the list of neighbours has been constructed, we no longer need the information on the initial lattice or the random spatial distribution of nodes, because the Monte Carlo algorithm operates solely on the neighbour list.

The filler flocculation is simulated via a single type of site-exchange Monte Carlo move. The Monte Carlo move consists of the nearest-neighbour node exchange of a randomly chosen node with its random neighbour from the neighbour list. To save the computational time, this is realized by exchanging the attendant nodes' types. An example of this Monte Carlo move is depicted in Fig. 3.2. Initially the central node has the type 'polymer B', while its neighbour in the upper right corner is 'polymer A'. After the Monte Carlo move, the nodes exchange their types, and the central node becomes 'polymer A', whereas its neighbour in the upper right corner is now 'polymer B'. Each Monte Carlo move is followed by checking the Metropolis criterion, i.e.,

$$\exp[\beta\Delta W] \geq \xi, \tag{3.1}$$

where $\beta^{-1} = k_B T$, k_B is the Boltzmann's constant, T is the temperature, $\xi = RND[0,1]$ is a random number between 0 and 1. If this condition is satisfied, then the respective move will be accepted. The quantity ΔW is related to the free enthalpy change of the system dG.

Consider the equilibrium free enthalpy G of the system

$$G = \frac{\sum_i G_i e^{-\beta G_i}}{\sum_i e^{-\beta G_i}}. \tag{3.2}$$

Here G_i are the free enthalpies at fixed configurations i. At equilibrium

$$dG|_{T,P,N_k} = \gamma_j dA_j, \tag{3.3}$$

where P is the pressure, N_k is the number of nodes of type k, γ_j is the interface tension of a pair of type j and $A_j = n_j a$ denotes the attendant total area of j-type interfaces in the system. To keep things simple, we follow [19] and assume that the effective contact area between nodes a is the same for all j. In general, however,

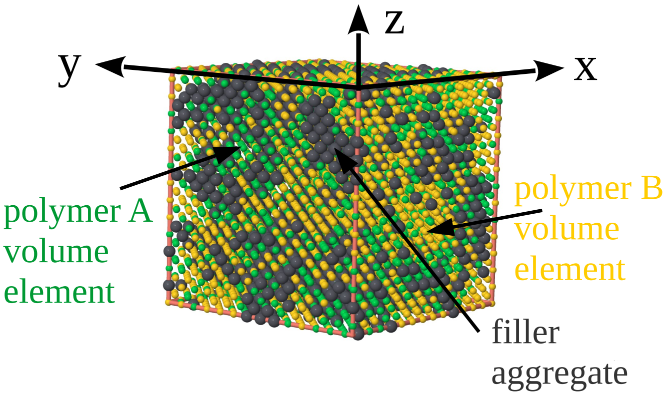

Figure 3.3: Face-centered cubic lattice. Green and yellow nodes represent the polymer A and B volume elements respectively, black nodes are filler aggregates.

this is not true, especially in randomized systems, where the contact area between nodes can be different depending on the distance between them.

For a system developing towards equilibrium under NPT-conditions, we have $\Delta W = -\gamma_j \Delta A_j$, or,

$$\exp[\beta \Delta W] = \exp[-\beta \gamma_j a \Delta n_j]. \tag{3.4}$$

The system configurations generated by using (3.4) satisfy (3.2) on average. Hence, the algorithm will drive the system towards the lowest possible free enthalpy G. Since the site-exchange Monte Carlo moves are local, their number will be a rough measure of time. The last assumption is based on local equilibrium and the local nature of Monte Carlo moves.

3.1.2 Initial Lattices

In [20] filler aggregates and polymer volume elements are modelled as cubic cells on an attendant cubic lattice. As in this work we perform the Monte Carlo simulation based on neighbour lists, we are not limited to any particular lattice type. Therefore, different types of lattices can be tested, and the effect of the initial node distribution in space on filler morphology can be studied. Note, that in this case we have to recalculate the value of the contact area between nodes a, because the number of nearest neighbours is different for each lattice type. In a simple cubic lattice, the number of nearest neighbours is equal to 6, whereas the number of the nearest neighbours in our system is defined by the cutoff radius r_{cut}. The corrected value of the contact area is calculated via $a' = 6a/\bar{n}_n$, where $\bar{n}_n$ is the average number of nearest neighbours in the system, and 6 is the number of nearest neighbours in the cubic lattice. For instance, if $\bar{n}_n = 12$, then $a' = a/2$, i.e., in the face-centered cubic lattice, shown in Fig. 3.3, the contact area between nearest neighbours is two times smaller than the contact area in the cubic lattice. The face-centered cubic lattice, however, has a regular structure and cannot adequately represent rubber. Note that

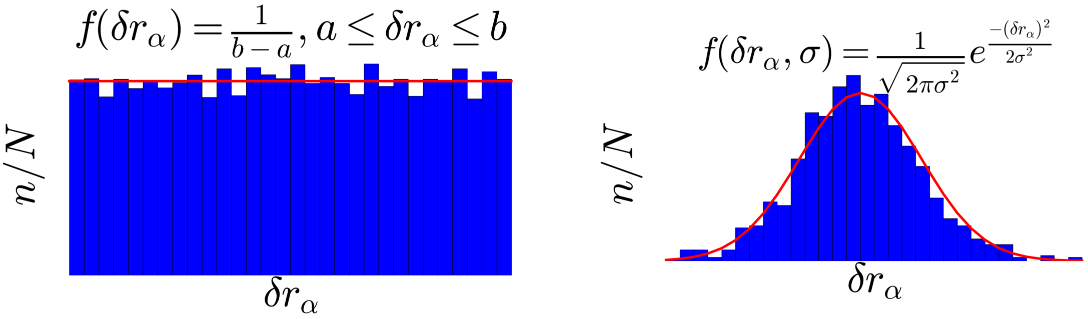

Figure 3.4: Possible distributions of the displacement δr_α. Left – uniform distribution, right – Gaussian distribution.

rubber is an isotropic material and has two elastic constants, while the FCC crystal has three different ones. To make the system isotropic, we randomly displace nodes from their initial positions on a lattice by a displacement δr_α, where $\alpha = x, y, z$. We use two different distributions of the displacement: the uniform distribution and the Gaussian distribution, which are shown in Fig. 3.4. In the uniform distribution the displacement depends on the minimum and maximum values a and b. Typically, the minimum value a is set to zero. The width of the Gaussian distribution depends on the variance, which also can be varied. Generally, larger values of the variance lead to a broader peak. Another possible initial configuration is a random one. In this case, coordinates of each node are set randomly within the simulation box length, i.e., $x \in [0, L]$, $y \in [0, L]$, $z \in [0, L]$. Using the aforementioned randomized systems allows avoiding undesirable effects due to irregularity of the lattice and ensures isotropy of the simulated system. A common drawback of these systems is that the number of neighbours of a node and the distance between them are arbitrary, and thus, the contact area may vary significantly throughout the system.

3.1.3 Cell Index Method

The Monte Carlo morphology generator algorithm operates on systems containing approximately 1.4 million nodes. Finding nearest neighbours and constructing a list of neighbours in systems of such size is time and memory consuming. Note that the usual double-loop implementation to find the neighbouring nodes scales as $O(N^2)$, where N is the total number of nodes. In fact, with a finite cutoff radius r_{cut}, a particle has only a limited number of neighbours equal to $\sim 4\pi/3\, r_{cut}^3(N/V)$ in a general case, where V is the volume of the simulation box. An alternative method of keeping track of neighbours for large systems is the cell index method [121]. The cubic simulation box is divided into a regular lattice of cells. The edge length of each cell is $l = L/s$, where $s = \lfloor L/r_{cut} \rfloor$ and L is the simulation box length. Here $\lfloor x \rfloor$ is the floor function, returning the largest integer that is less than or equal to x. Next, the list of nodes in each cell is created. A node in a cell interacts only with other nodes in the same cell and its 26 neighbouring cells. The number of cells to accommodate all these nodes is $s \times s \times s$, where $s = L/l$. We identify a cell with a vector cell index

$$\vec{c} = (c_x, c_y, c_z)(0 \leq c_x \leq s-1; 0 \leq c_y \leq s-1; 0 \leq c_z \leq s-1),$$

and a serial cell index

$$c = c_x s^2 + c_y s + c_z$$

or

$$\begin{aligned} c_x &= c/(s^2), \\ c_y &= (c/s) \mod s, \\ c_z &= c \mod s. \end{aligned}$$

A node with the coordinate $\vec{r}$ belongs to a cell with the vector cell index

$$c_\alpha = \lfloor r_\alpha / l \rfloor \ (\alpha = x, y, z).$$

The cost of this method scales with $O(N)$ rather than $O(N^2)$ in the case of the double-loop implementation, which allows to significantly speed up the determination of neighbours and decrease the simulation time.

3.1.4 Simulation Algorithm

Based on the information above, we can write down a simulation algorithm for modelling of filler flocculation:

- Based on the lattice type, set initial coordinates of nodes and randomize them, if needed.
- For each node, select the node type 'filler' at random with the probability ϕ_f. The rest of nodes has the type 'polymer'.
- Using the cell index method, find the nearest neighbours and construct a neighbour list.
- Repeat the Monte Carlo step while $n_{\text{current step}} < n_{\text{MC steps}}$:
  - Select a node at random.
  - Choose a random neighbour of the given node.
  - If the particles types are the same, then $\Delta W = 0$.
  - If the particle types are different, calculate $W_{old,local}$.
  - Swap the particle types.
  - Calculate $W_{new,local}$ and $\Delta W = W_{new,local}$ - $W_{old,local}$.
  - Generate $\xi = RND[0,1]$.
  - Check the Metropolis criterion $\exp[\beta \Delta W] \geq \xi$.

  - If the inequality is satisfied, accept the step. If not, return the initial particle types.

Note that during each MC step, we need to consider only the two nodes chosen initially and their respective neighbours from the neighbour list. As ΔW is the only quantity in the Metropolis criterion which can change, and all these changes are local, we do not require to calculate contributions to W from other nodes. This provides the opportunity to significantly reduce the simulation time and makes the algorithm computationally efficient. For instance, performing 70 million MC steps (50 MC steps per node on average and 1.4 million nodes) using the programming language C++ takes several minutes only (on a Dell PowerEdge R7525 Server using the AMD 7452 processor).

3.2 Screening Methods

In order to analyse filler morphologies simulated by the morphology generator and to compare them with experimental data, we require additional screening methods. These methods include the wetting-envelope – work of adhesion plots and transmission electron microscopy (TEM). The first method is independent of simulation and provides information on the compatibility between filler and polymer based on their surface energies. Simulated TEM images allow visualizing filler dispersion in a single polymer or in polymer blends and the time evolution of filler morphology.

3.2.1 Wetting-Envelope – Work of Adhesion Plots

Wetting envelopes are a helpful tool for analysing the compatibility between filler and polymer. They are derived from the wetting-envelope equation. This equation is obtained from (A.7) together with (A.5), when $\alpha = s$ and $\beta = l$:

$$(\gamma_l^d + \gamma_l^p)\frac{\cos\theta + 1}{2} = \sqrt{\gamma_s^d \gamma_l^d} + \sqrt{\gamma_s^p \gamma_l^p}. \tag{3.5}$$

The equation is then solved for fixed values of the surface tensions of the liquid and the solid and a contact angle θ [123]. For solving this equation, we use an approach described in [19]. We define the dispersive and the polar parts of the surface tensions via polar coordinates for the liquid

$$\gamma_l^d = R\cos\psi \qquad \gamma_l^p = R\sin\psi,$$

or for the solid

$$\gamma_s^d = R'\cos\psi' \qquad \gamma_s^p = R'\sin\psi'.$$

Solving for R and R', we get

$$R(\psi,\theta) = \left(\frac{\sqrt{\gamma_s^d \cos\psi} + \sqrt{\gamma_s^p \sin\psi}}{\cos\psi + \sin\psi}\right)^2 \frac{4}{(\cos\theta + 1)^2},$$

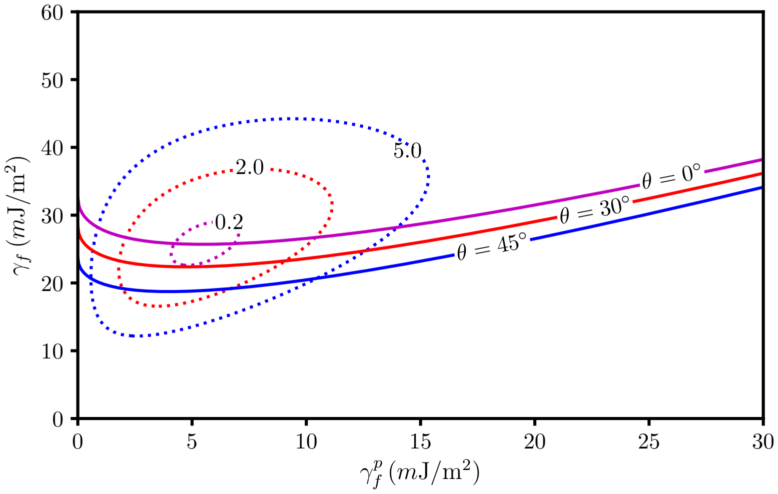

Figure 3.5: Wetting-envelope – work of adhesion plot for natural rubber ($\gamma_p^d = 20.2$ mJ/m^2 and $\gamma_p^p = 5.5$ mJ/m^2). Surface tension values are obtained by sessile drop technique and taken from [122]. The solid lines correspond to the constant values of the contact angle θ, and dashed lines show the constant values of the difference in work of adhesion ΔW. Fillers above $\theta = 0°$ are perfectly wetted by the polymer. Fillers outside the largest loop have the strongest tendency to flocculate. The plot is made in style of [19].

$$R'(\psi', \theta) = \left(\frac{\gamma_l^d + \gamma_l^p}{\sqrt{\gamma_l^d} \cos \psi' + \sqrt{\gamma_l^p} \sin \psi'} \right)^2 \frac{(\cos \theta + 1)^2}{4}.$$

Then we obtain the following expressions for the surface tension of the liquid

$$\gamma_l^d = R(\psi, \theta) \cos \psi \qquad \gamma_l^p = R(\psi, \theta) \sin \psi,$$

and for the surface energy of the solid

$$\gamma_s^d = R'(\psi', \theta) \cos \psi' \qquad \gamma_s^p = R'(\psi', \theta) \sin \psi'.$$

Both parts of the surface energy must be non-negative, which implies $\psi \in [0, \pi/2]$ and $\psi' \in [0, \pi/2]$. Then for a fixed value of θ the attendant dispersive and the polar parts of the surface tension can be obtained. A natural choice is to consider the polymer (p) as the liquid and the filler (f) as the solid. An example solution of the wetting-envelope equation for a filler using the surface tension of NR is presented in Fig. 3.5. The solid lines in the plot are obtained for the fixed values of θ and are called iso contact angle lines. Lower values of θ correspond to higher wettability. The dashed lines in the plot show areas with the constant difference in work of adhesion – iso ΔW. The value of ΔW is given by

$$\Delta W_a = W_{a,pp} + W_{a,ff} - 2W_{a,pf}, \tag{3.6}$$

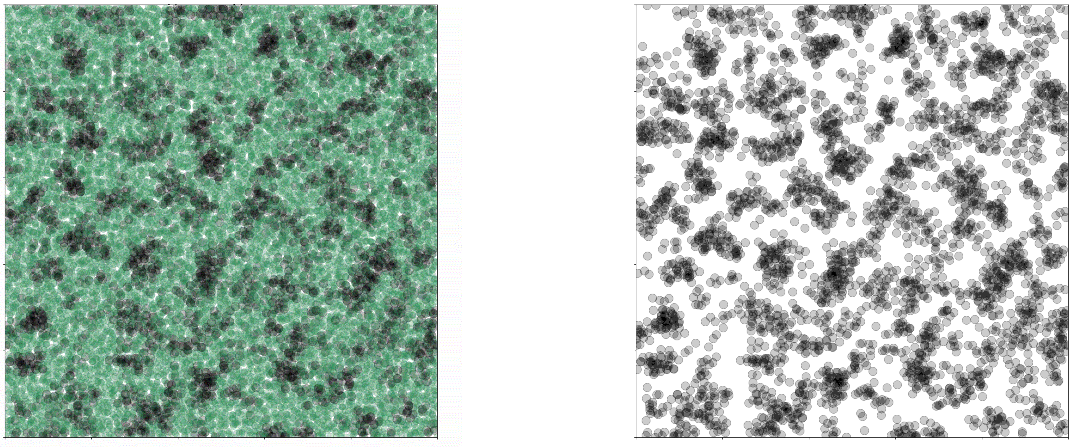

Figure 3.6: Simulated TEM images obtained for the NR system filled with carbon black ($\gamma_p^d = 20.24$ mJ/m^2, $\gamma_p^p = 5.46$ mJ/m^2, $\gamma_f^d = 20$ mJ/m^2, $\gamma_f^p = 0$ mJ/m^2). The thickness is $5d$, the size is $50d\times$ $50d$, where d is the node diameter. The TEM images are extracted after 50 MC moves per node on average. Left: green – polymer nodes, black – filler nodes; right: the same as left but only filler nodes are shown.

or

$$\Delta W_a = 2\left(\sqrt{\gamma_f^d} - \sqrt{\gamma_p^d}\right)^2 + 2\left(\sqrt{\gamma_f^p} - \sqrt{\gamma_p^p}\right)^2. \tag{3.7}$$

The difference in work of adhesion is the quantity used in the Metropolis criterion (Eq. (3.4)) and denotes the Gibbs free energy change for separating a unit $f-$ p- interface from contact to infinity [124]. It tends to zero when the polar and the dispersive parts of the surface energies of filler and polymer are equal and is essential for filler flocculation [31, 125]. Larger values of ΔW correspond to a stronger tendency for a filler to flocculate. Filler particles, which have the same surface properties as the surrounding polymer, do not tend to form agglomerates at all. Consequently, different filler surface modifications may be essential in order to change the flocculation behaviour and improve the material's performance.

3.2.2 TEM Images

Transmission electron microscopy is a helpful method to study the properties of polymer nanocomposites. Aside from small angle X-ray scattering (SAXS), TEM is the only method allowing to 'look' into a rubber sample. Typically, experimental samples have to be cut into slices with a thickness less than 100 nm [126]. The simulated TEM images are also obtained by cutting slices through the system and can be helpful in visualizing the flocculation process. They can also be used to qualitatively compare the simulation results with experiments. The cuts are usually extracted after a certain number of MC steps and have a fixed size and thickness. The nodes in these images are shown as circles with a unit diameter and the attendant colour corresponding to the node type. An example is presented in Fig. 3.6. The TEM images in this figure correspond to the NR system filled with the CB-type

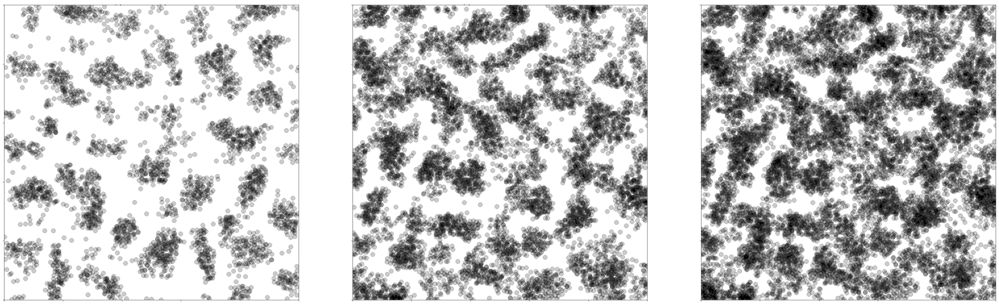

Figure 3.7: Simulated TEM images with different thicknesses (from left to right: $5d$, $10d$, $15d$). The system is NR filled with carbon black ($\gamma_f^d = 20$ mJ/m^2, $\gamma_f^p = 0$ mJ/m^2). The morphologies are extracted after 1000 MC steps per node on average.

filler. The underlying lattice is a face-centered cubic crystal, with the subsequent random displacement of nodes according to the uniform distribution with $\delta r_{\alpha,max} = 0.3d$. On the left-hand side, polymer nodes (green) are shown together with filler nodes (black). This kind of representation allows to obtain the information on filler distribution. The filler distribution is particularly important for polymer blends consisting of immiscible polymers, where the polymers can form different phases. On the right-hand side of this figure, only filler nodes are shown. The darker shades are the result of stacking several particles along the line of sight. In this image the filler network can be clearly seen, so this kind of visualization can be helpful in studying the flocculation process itself and the filler network evolution with time. It can also be used for determining the filler agglomerate size and for comparison studies of the filler dispersion obtained for different fillers. The most information on the filled systems can be obtained by combining both types of representation.

Note that when comparing the simulated TEM pictures with experimental ones, not only the linear size should be considered, but also the slices' thickness. In Fig. 3.7 three TEMs obtained for the same system are presented, which have different thicknesses, namely, $5d$, $10d$ and $15d$. Although the system is the same, the morphologies look quite differently, so it is essential to compare the slice's thickness with the experimental one. Notice, that in the latter case, the thickness may vary significantly depending on the experimental conditions.

3.3 Examples

In this section, some examples obtained via the MG algorithm will be discussed. Firstly, we will compare filler morphologies obtained for different lattice types. Secondly, we will study the effect of changing the cutoff radius r_{cut} on the average number of nearest neighbours and, hence, on the number of interfaces in the system. Therefore, we will also compare the morphologies modelled using various values of r_{cut}.

Fig. 3.8 shows simulated TEM images obtained for different lattice types. The last image in the bottom row corresponds to a random placement of nodes into the simulation box, while the first picture in the upper row is obtained for a regular FCC

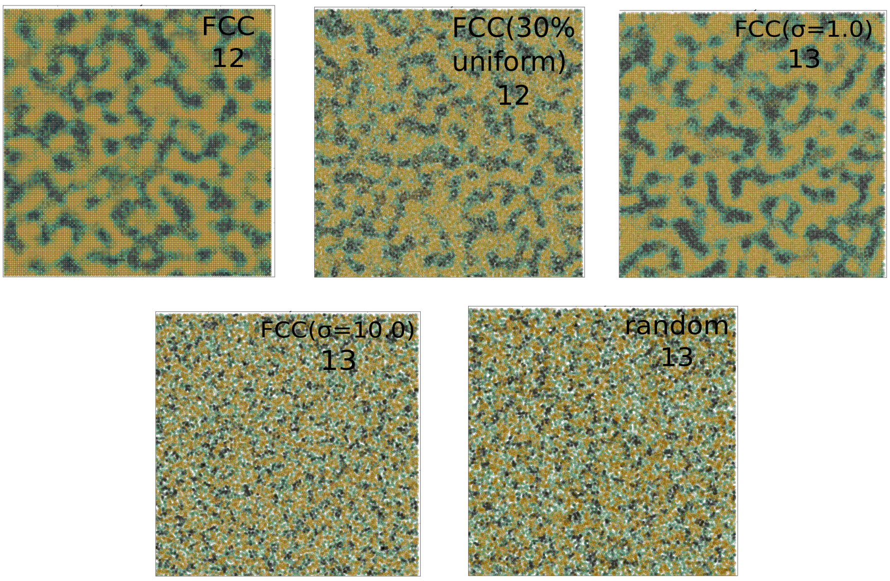

Figure 3.8: Simulated TEM pictures obtained for different lattice types. The number in each panel is equal to the average number of neighbours in the system. The cutoff radius r_{cut} is equal to 1.3.

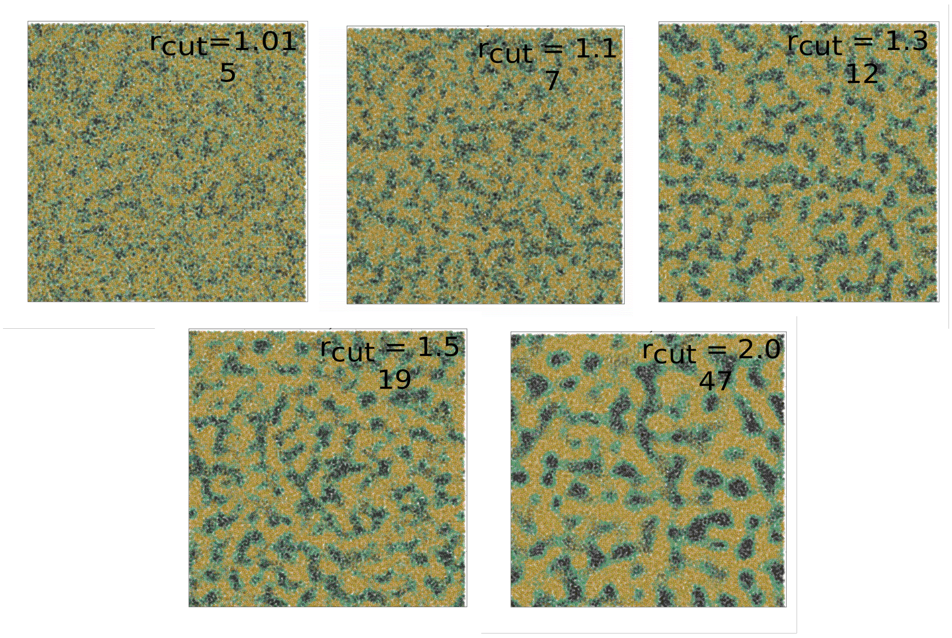

Figure 3.9: Simulated TEM pictures obtained using different values of the cutoff radius r_{cut}. The number in each panel is equal to the average number of neighbours in the system. The underlying lattice is an FCC randomized using the uniform distribution of the displacement.

lattice. All other images represent randomized FCC lattices, where the displacement distribution and the distribution parameters are varied (from left to right, from top to bottom: the uniform distribution of the displacement and $\delta r_{\alpha,max} = 0.3d$; Gaussian distribution with $\sigma = d$; Gaussian distribution with $\sigma = 10\ d$, where d is the node's diameter). In the upper right corner of each panel, the average number of nearest neighbours in the respective system is given. The system is a 50/50 blend consisting of NR ($\gamma_p^d = 20.24$ mJ/m^2, $\gamma_p^p = 5.46$ mJ/m^2) and SBR ($\gamma_p^d = 29.91$ mJ/m^2, $\gamma_p^p = 1.64$ mJ/m^2) plus filler ($\gamma_f^d = 20$ mJ/m^2, $\gamma_f^p = 10$ mJ/m^2). The TEM images are extracted after 1000 MC moves per node on average, the thickness is $5d$, and the size is $100d\times\ 100d$. The number of nodes in each system is approximately $1.4\times\ 10^6$. If the size of the smallest non-breakable aggregate is about 60 nm, which is typical for carbon black (for instance, the size of these aggregates for N234 is 66 nm [120]), then the resulting linear size of these images is in μm-range (≈ 6 μm, assuming that the polymer volume elements are of the same size as the filler nodes). Note that generally the images look similar, i.e., the polymer blend tends to separate forming two subphases consisting of NR and SBR. The filler typically concentrates in the NR subphase and forms agglomerates. However, the size of the filler agglomerates is different depending on the underlying lattice structure. The largest filler agglomerates are observed for the regular FCC or when randomizing displacements are small. In addition, in these cases the lattice structure can be clearly seen. When randomizing displacements are large, e.g., for the images in the bottom row, the filler agglomerates are small and can be hardly seen. The pictures in the upper row are visually comparable, although the average number of the nearest neighbours in these systems is slightly different. The system with the uniform distribution of the displacements has an intermediate agglomerate size and does not exhibit the regular lattice structure, i.e., it can be considered as isotropic. Additionally, the average number of neighbours in this system is the same as in the common FCC, which implies that the average contact area between nodes is the same.

The cutoff radius r_{cut} determines the number of neighbours of a given node, i.e., when the cutoff distance is varied, the average number of interfaces in the system changes. We use the 30 % uniformly displaced FCC as our standard lattice and simulate filler flocculation using different values of the cutoff distance r_{cut}. The resulting TEM images are shown in Fig. 3.9. The simulation parameters, surface energy values and procedure for obtaining the TEM pictures are the same as above. The average number of nearest neighbours in each system is given as well in the upper right corner of each panel. Note that the general tendency is similar to the one shown in the previous figure, i.e., the polymers form two subphases consisting of NR and SBR, and the filler concentrates in the NR subphase. Simultaneously, the cutoff distance strongly affects the obtained morphologies. The system with 5 interfaces on average looks more dispersed and homogeneous in comparison to the system with 47 neighbours on average, although the value of the contact area between nodes was corrected in each case. The filler agglomerate size also increases with r_{cut}. This might happen due to a more efficient site exchange, when the number of neighbours is large, and Monte Carlo steps are accepted with a larger probability. On the other hand, in real systems, we cannot expect a filler aggregate having 47 different interfaces with its surrounding. Therefore, we consider $r_{cut} = 1.3$ to be the standard value in our simulations because it corresponds to 12 nearest neighbours (or interfaces) on average for one node – the value one would also expect from a liquid-like packing of spheres.

Chapter 4

Dynamic Mechanical Analysis via Simulation

Dynamic mechanical analysis is a frequently used experimental technique to investigate the mechanical properties of elastomers. In order to study the dynamic characteristics of systems created by the morphology generator, discussed in the preceding chapter, we shear the virtual morphologies and compute their attendant dynamic moduli. During shear simulations, we apply sinusoidal strain to the system and measure the resulting microscopic stress. The definitions of stress and strain refer to the theory of elasticity, and they can be found in Appendix B. In this chapter, we present the basics of DMA simulations. We also discuss the setup of the system, the simulation algorithm and how the interactions are defined, as well as computer techniques used to model DMA.

4.1 Set Up

The Monte Carlo morphology generator, discussed in Chapter 3, typically operates on systems containing approximately 1.4×10^6 nodes. The dynamic simulation, however, updates the positions, the velocities and the forces for all nodes during each step. Hence, we must store these variables for at least 2 steps: the previous and the newly calculated ones. This large number of variables, which are updated during each step, effects significantly the computational time. Therefore, for investigating the dynamic properties, we consider subsystems of the original morphology. The linear dimension of the subsystems is five times smaller than that of the original morphology, which is $L = 100d$. To keep results consistent, we cut several subsystems from different places of the original system. The final result is then obtained by averaging over these subsystems.

In the morphology generator, the interfaces between nodes are characterized by the surface tensions of the components. In the DMA simulations, interactions between nodes are modelled via springs. Generally, there exists no particular algorithm for determining the form of the microscopic elastic forces based on the surface energies. Here we apply the idea illustrated in Fig. 4.1. In the MG, each node has a particular number of nearest neighbours, and it shares a common interface with each neighbour. In the DMA simulation part, the interface tensions

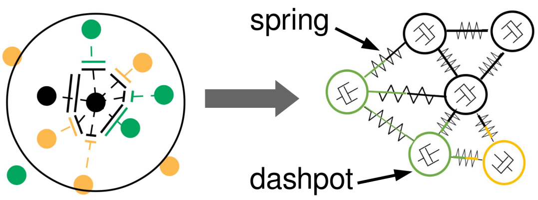

Figure 4.1: Left: the original spacial distribution of nodes generated by the morphology generator; right: nodes are connected to their neighbouring nodes via attendant springs. Note that thin lines indicate springs which are harmonic independent of their strain, while thick lines and lines composed of both line types indicate springs which can reversibly break depending on strain.

are replaced by attendant springs, with the force constant depending on the type of nodes. The parametrization of the springs, describing the interactions in the system, is discussed in Section 4.3 of this chapter.

4.2 Simulation Algorithm

We assume local equilibrium in the system, which implies that the sum of the forces acting on a given node i, consisting of the friction and interaction forces, is zero:

$$\vec{F}_{fric,i} + \vec{F}_{nn,i} = 0. \tag{4.1}$$

Here $\vec{F}_{fric,i}$ is the friction force and $\vec{F}_{nn,i}$ is the force due to interactions with neighbouring nodes. Due to the balance of forces, each node moves uniformly without acceleration. During shearing, the friction force acting on a particular node is given by

$$\vec{F}_{fric,i} = -m_i \gamma (\vec{v}_i - \dot{\vec{u}}_i), \tag{4.2}$$

where m_i is the mass of node i, γ is a friction coefficient, $\vec{v}_i$ is the velocity of node i and $\dot{\vec{u}}_i$ is the shear velocity profile at node i. Note that the friction force is determined not by the absolute velocity of node i, but by the difference of the absolute velocity of i compared to the velocity of the shear profile at the position i. The node will experience a drag-force trying to adjust its velocity to the motion of the shear profile. Combining equations (4.1) and (4.2) and using $m_i = 1$, we obtain

$$\vec{F}_{nn,i}(t) - \gamma(\vec{v}_i(t) - \dot{\vec{u}}_i(t)) = 0. \tag{4.3}$$

Now we can use the Taylor expansion of the position of the i-th node:

$$\vec{r}_i(t + \delta t) = \vec{r}_i(t) + \vec{v}_i(t)\delta t + O(\delta t^3). \tag{4.4}$$

Here, δt is a time step. Note that the error is of the order δt^3 due to the balance of forces, which implies that the acceleration is zero. Using (4.3) and (4.4), we obtain the following algorithm:

$$\vec{v}_i(t) = \frac{1}{\gamma}\vec{F}_i(t) + \dot{\vec{u}}_i(t) \tag{4.5}$$

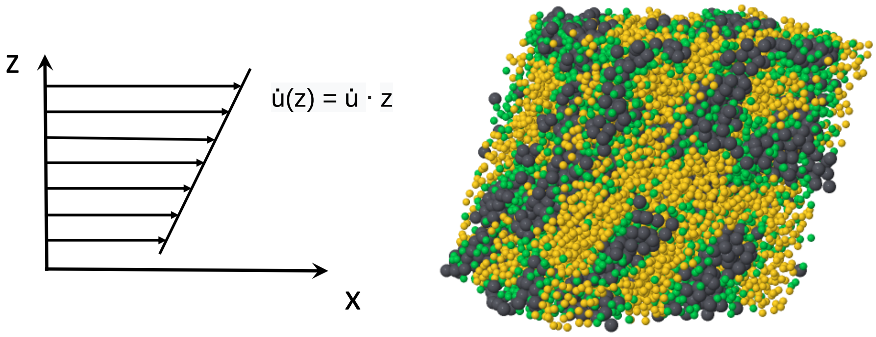

Figure 4.2: Left: shear velocity profile, where $\dot{u}$ is the macroscopic shear rate; right: simulation snapshot of a filled binary polymer system under shear deformation.

$$\vec{r}_i(t+\delta t) = \vec{r}_i(t) + \vec{v}_i(t)\delta t, \tag{4.6}$$

which is implemented as follows:

- Update the shear strain $u(t) = u_0 \sin(\omega t)$ and the shear rate $\dot{u}(t) = u_0 \omega \cos(\omega t)$.
- Calculate the forces $\vec{F}_i(t)$ based on the coordinates from the previous step.
- Calculate the velocity profile $\dot{\vec{u}}_i(t)) = \dot{u}(t) \cdot z_i(t)$.
- Calculate the velocities $\vec{v}_i(t)$.
- Calculate new coordinates $\vec{r}_i(t+\delta t)$.

Note that the shear velocity profile $\dot{\vec{u}}_i$ is calculated for every node because it depends on the position of a node in the z-direction, as shown in the left panel of Fig. 4.2. In the right panel of this figure, a snapshot of a filled binary polymer system under shear deformation is depicted. The system's morphology was extracted after 1000 MC steps per node on average and represents a 50-NR/50-SBR blend with 20% vol. filler ($\gamma_f^d = 20$ mJ/m^2, $\gamma_f^p = 20$ mJ/m^2) at 20% strain amplitude.

To apply the aforementioned simulation algorithm, we also have to define the initial conditions. At time $t = 0$, the shear u is zero:

$$u(t=0) = u_0 \sin(\omega t) = u_0 \sin(\omega \cdot 0) = 0,$$

whereas the shear rate u_0 is maximal and equal to

$$\dot{u}(t=0) = u_0 \omega \cos(\omega t) = u_0 \omega \cos(\omega \cdot 0) = u_0 \omega.$$

4.3 Interactions

Combining the morphology generator with the shear simulation requires a justification of the form of the interactions. Note that there exists no exact procedure

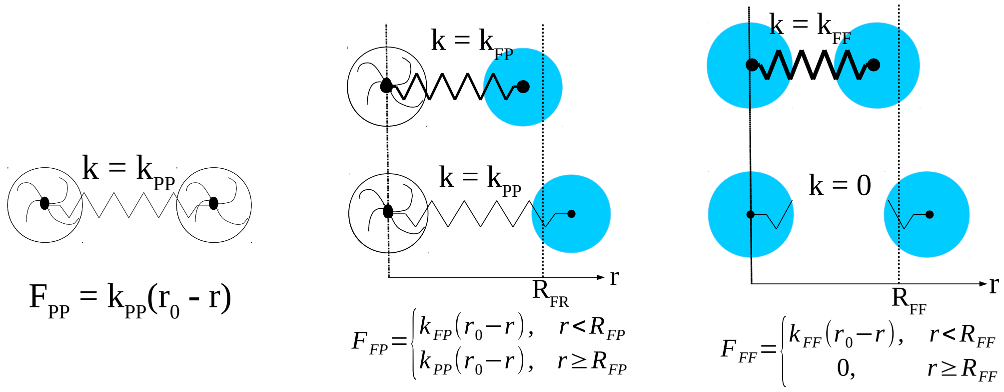

Figure 4.3: Basic types of interactions in the system and their respective forces. From left to right: polymer-polymer, filler-polymer, filler-filler interactions. The blue spheres represent filler particles, white – polymer volume elements.

allowing to estimate the internal forces from the surface tensions. In the DMA simulation part, we model all types of interactions in the system via springs:

$$\vec{F}_{nn,i} = \sum_{j=1}^{n_i} k_{ij}(r_{ij,0}\frac{\vec{r}_{ij}}{r_{ij}} - \vec{r}_{ij}). \tag{4.7}$$

Here n_i is the number of neighbours of node i, k_{ij} is a spring constant between nodes i and j, $\vec{r}_{ij}$ is the vector between i and j, r_{ij} is the distance between i and j and $r_{ij,0}$ is the equilibrium distance between i and j assigned originally by the morphology generator. Hence, the pair interaction potentials can be described by

$$u_{ij} = \frac{1}{2}k_{ij}(r_{ij,0} - r_{ij})^2. \tag{4.8}$$

Basic types of interactions in the system are presented in Fig. 4.3. The interaction between polymer nodes is a simple harmonic spring with the strength k_{PP}. This is valid for all interactions between polymer nodes, despite the polymer type. The filler-filler interaction is also harmonic, with the strength $k_{FF} >> k_{PP}$ within the distance R_{FF}; beyond R_{FF} the filler-filler interaction is set to zero. Therefore, the parameters k_{FF} and R_{FF} model both the stiffness and the interaction range. The interaction between polymer and filler nodes also depends on the node-to-node separation: the spring constant k_{PF} is used at distances less than the bond-breaking distance for the polymer-filler interaction R_{PF}. Beyond this cutoff distance, the polymer-filler interaction can be characterized by the spring constant k_{PP}. This is again true for both polymers. This setup of springs mimics the reversible breaking of filler-filler and polymer-filler bonds. The motivation for this type of interactions is shown in Fig. 4.4 and is based on the Jump-in-Jump-out model for the interaction between filler particles embedded in a polymer matrix. The model is thoroughly discussed in [127, 128].

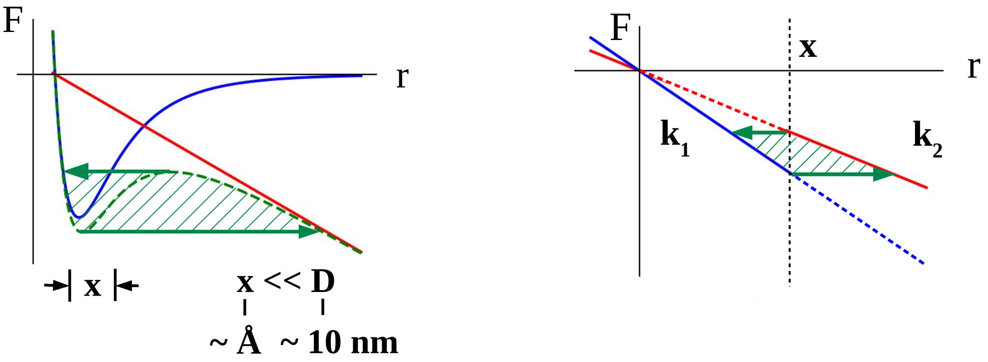

Figure 4.4: Forces acting between two filler aggregates (or particles) in a polymer matrix. Left: the red line corresponds to the harmonic restoring force due to the elastic matrix when two neighbouring particles are separated by a distance r. The direct short range interaction between the particles is depicted by the blue line. Finally, the dashed green line is the sum of the two forces. The arrows indicate the relative motion of the particles trying to establish a stable equilibrium while being separated (right arrow; bond breaking) and upon relaxation of the outside force causing the separation (left arrow; bond closing). Right: the spontaneous transition from a strong spring constant to a weak spring constant at $r = x$ mimics the reversible bond breaking and causes energy dissipation or hysteresis (green shading). The hysteresis here is akin to the analogous hysteresis depicted in the more detailed sketch on the left.

We assume that two nearest neighbour filler aggregates in a polymer matrix interact mainly via short range forces (the left panel of Fig. 4.4). An example for such a force can be a hydrogen bond between silica particles. But a contact between carbon black particles also has a short range component. The range of this interaction is x, and x is between 1 Å and 1 nm, while the typical aggregate size d is usually about 50-100 nm [120]. Therefore, we can expect that $x/d \sim 10^{-2}$ or even less [129].

The importance of the short range interactions in tire tread materials can be justified if we consider the onset of the Payne effect, which is typically observed at less than 1% strain. For sake of simplicity we consider a necklace model, which represents an elastomer nanocomposite in one dimension as a set of filler aggregates separated by narrow gaps filled with polymer. Under deformation, the polymer-filled gaps must accommodate all the strain, since filler does not deform. Therefore, the local strain in the gaps is amplified by the ratio d/d_g, where d_g is the gap width (see also [38]). The early onset of the Payne effect implies that x/d is small, i.e. ~ 0.01 or even less. When the distance between aggregates exceeds x, the reversible breaking in the filler network occurs. Hence, reasonable values of bond breaking distances R should be between $1.01 r_{ij,0}$ and $1.001 r_{ij,0}$, where $r_{ij,0}$ is an equilibrium distance between nodes i and j. Fig. 4.5 represents the idea of the strain amplification in the context of our model.

The total interaggregate force is the sum of two contributions, the aforementioned direct particle-particle force and the linear restoring force due to the elastic

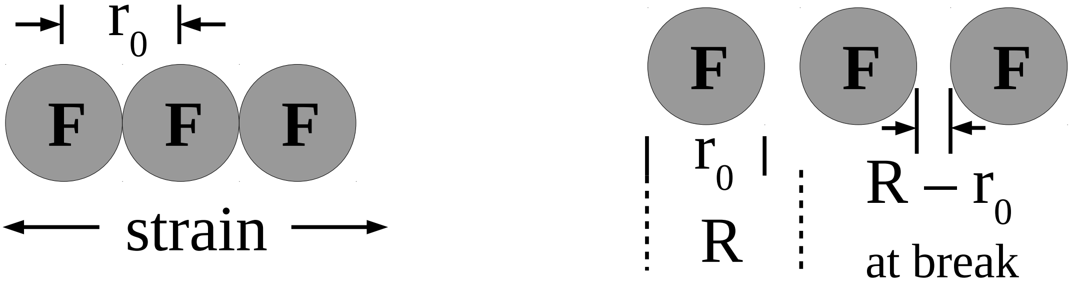

Figure 4.5: Necklace model. Left: filler aggregates separated by narrow gaps in one dimension before deformation. Right: Under deformation, the distance between the aggregates exceeds the bond breaking distance R and the reversible breaking occurs. Here r_0 is an equilibrium distance between two nodes.

properties of the surrounding polymer matrix. Both forces depend on the distance between the aggregates r. An external force would result in a vertical shift of the force curve. When the applied external force is cyclic, the resulting path in the $F - r-$plane would produce spontaneous 'jumps' due to the loop in the force, shown in the Fig. 4.4 by green arrows. During opening and closing of the contact between two aggregates (jump-out-jump-in), the loop in the $F - r-$plane produces hysteresis and the energy dissipation, shown in the Fig. 4.4 as the green shaded area [61, 130].

The right panel of Fig. 4.4 illustrates energy dissipation due to the aforementioned reversible bond breaking, and how it can be modelled in terms of springs. The plot shows the force vs. distance behaviour for two springs with the force constants k_1 and k_2, where $k_1 > k_2$. Note that even if k_2 is set to zero, there is always some restoring force due to the surrounding polymer matrix, and in reality k_2 is never equal to 0. When external deformation is applied, the spring constant is initially equal to k_1. At $r = x$ the spring spontaneously weakens (this is what happens when the bond reversibly breaks) and the stretching continues with k_2. The path in the $F - r-$plane, however, follows the green arrows because at each step the system is in its force equilibrated state. Thus, the path in the $F - r-$plane during cyclic deformation leads to hysteresis (green shaded area) and dissipation of energy. This dissipation mechanism, which occurs between real filler aggregates as well, was studied in detail using atomistic molecular dynamic simulations [60, 131].

4.4 Boundary Conditions

In computer simulations, we cannot simulate a macroscopic system because of memory and speed constraints. However, by choosing periodic boundary conditions, we can let a system with a small number of particles look as if it has macroscopic dimensions. The particles are placed in a central simulation box, which is surrounded by infinitely many image simulation boxes due to periodic boundaries. These simulation boxes form a lattice, and every lattice cell contains the same number of particles at the same positions (see Figure 4.6). If a particle leaves the original sim-

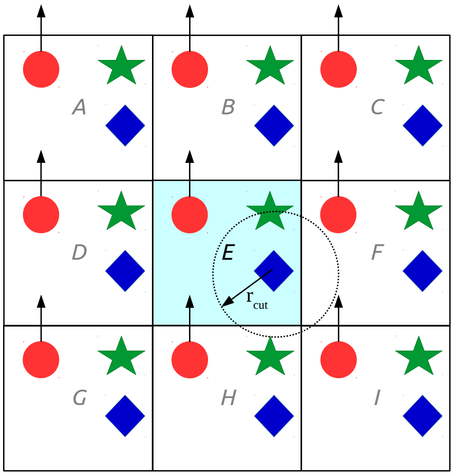

Figure 4.6: Periodic boundary conditions. The central blue cell is the original simulation box surrounded by image cells. The circle with the radius r_{cut} determines the distance of interactions.

ulation box, it reappears from the opposite face. A particle can interact not only with real particles, but also with images of the real particles, none of which needs to be stored in the computer's memory. The distance of interactions is typically set by a cutoff radius r_{cut}. Because the original and the image cells are identical, it is not necessary to save the positions of all images, but the positions of real particles in the central simulation cell. If $\vec{r}_i$ are the positions of real particles in the original simulation box, we can easily determine the positions of atoms in the periodic images by

$$\vec{r}_i^{\,image} = \vec{r}_i^{\,real} + k\vec{a}_x + l\vec{a}_y + m\vec{a}_z \tag{4.9}$$

$$\vec{a}_x = \Big[L, 0, 0\Big], \vec{a}_y = \Big[0, L, 0\Big], \vec{a}_z = \Big[0, 0, L\Big], \tag{4.10}$$

where L is the simulation box length, k, l, m are integers.

We can implement periodic boundary conditions by using the so-called minimum image convention. We consider only interactions between particle pairs ij satisfying the condition $r_{ij} < r_{cut}$. For particle i at position $\vec{r}_i = [x_i, y_i, z_i]$ and particle j at position $\vec{r}_j = [x_j, y_j, z_j]$, $i \neq j$, the minimum distance r_{ij} is

$$(r_{ij}^{min})^2 = (x_{ij}^{min})^2 + (y_{ij}^{min})^2 + (z_{ij}^{min})^2, \tag{4.11}$$

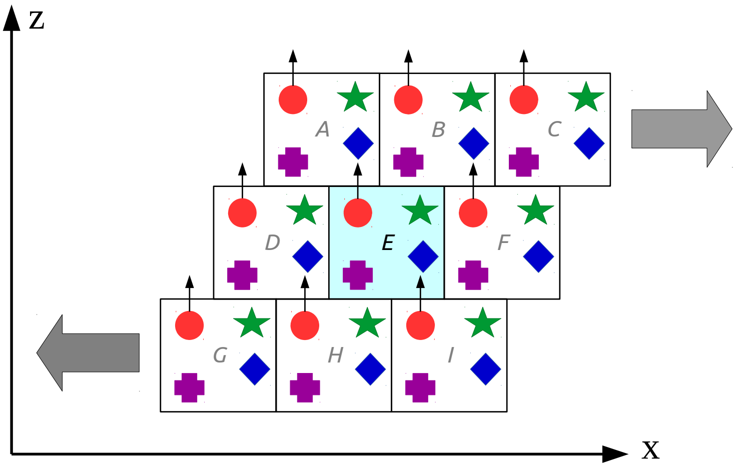

Figure 4.7: Shear boundary conditions.

where

$$x_{ij}^{min} = x_{ij} - L\ Round\left[\frac{x_{ij}}{L}\right],$$
$$y_{ij}^{min} = y_{ij} - L\ Round\left[\frac{y_{ij}}{L}\right],$$
$$z_{ij}^{min} = z_{ij} - L\ Round\left[\frac{z_{ij}}{L}\right].$$

Here $x_{ij} = x_i - x_j$, $y_{ij} = y_i - y_j$, $z_{ij} = z_i - z_j$, and L is the length of the simulation box. The function $Round[a]$ rounds a to the nearest integer.

4.4.1 Shear Boundary Conditions

Applying shear requires a modification of the periodic boundary conditions. The method for shear boundary conditions was first proposed by Lees and Edwards in [132]. The algorithm we use here is described in [121]. The simulation box and its images centred at $(x, z) = (\pm L, 0)$, $(\pm 2L, 0)$, etc., i.e., the boxes D, E and F in Fig. 4.7 are taken to be stationary. Boxes in the layer above, $(x, z) = (0, L)$, $(\pm L, L)$, $(\pm 2L, L)$, etc., i.e., A, B and C, are moving at a speed $\dot{u}(t)L$ in the positive x-direction. Here $\dot{u}(t)$ is the shear rate, or strain rate and L is the simulation box length. Boxes in the layer below, $(x, z) = (0, -L)$, $(\pm L, -L)$, $(\pm 2L, -L)$, etc., i.e., G, H and I, move at the same speed in the negative x-direction. In this case, the minimum image correction should be

$$x_{ij} = x_{ij} - u(t) \cdot L\ Round\left[\frac{z_{ij}}{L}\right],$$

where $L \cdot u(t) = \Delta x(t)$ is a current value of the displacement between the boxes in different layers, $u(t)$ is the dimensionless strain, $x_{ij} = x_i - x_j$, L is the length of the simulation box. Hence, we apply an additional correction to the x-component, which depends on the distance between the particles in the z-direction. The new periodic boundary conditions are

$$\begin{aligned} x_{ij} &= x_{ij} - u(t) \cdot L\,Round\left[\frac{z_{ij}}{L}\right], \\ x_{ij}^{min} &= x_{ij} - L\,Round\left[\frac{x_{ij}}{L}\right], \\ y_{ij}^{min} &= y_{ij} - L\,Round\left[\frac{y_{ij}}{L}\right], \\ z_{ij}^{min} &= z_{ij} - L\,Round\left[\frac{z_{ij}}{L}\right], \end{aligned} \tag{4.12}$$

where $y_{ij} = y_i - y_j$, $z_{ij} = z_i - z_j$.

In order to avoid a substantial difference between the positions of the central simulation box and its images, we can keep replacing particles in the central box, as they cross the boundaries, by using additional equations. When a particle leaves the simulation box, its position is not the same as in the case of usual boundary conditions because the images are shifted. Therefore, we use the following corrections

$$x = x - u(t) \cdot L\,Round\left[\frac{z}{L}\right] \tag{4.13}$$

for the x-coordinate of the particle and

$$v_x = v_x - \dot{u}(t) \cdot L\,Round\left[\frac{z}{L}\right] \tag{4.14}$$

for its velocity. Here $\dot{u}(t)$ is again the shear rate and $\dot{u}(t) \cdot L$ is the difference of the velocities between different layers. Then we apply the following equations to return the particle back into the original simulation box

$$\begin{aligned} x &= x - L\,Round\left[\frac{x}{L}\right], \\ y &= y - L\,Round\left[\frac{y}{L}\right], \\ z &= z - L\,Round\left[\frac{z}{L}\right]. \end{aligned} \tag{4.15}$$

Fig. 4.8 presents a more detailed picture of the calculation of distances between particles in the case of shear. The blue diamond interacts with an image of the red circle in the original simulation box, while the real red circle is several boxes away. Initially, we make a correction to the shear in the x-direction by $x = x - L\,Round\left[\frac{z}{L}\right]u(t)$ (blue arrow). Then we return the red circle to the central layer of the simulation boxes by $z = z - L\,Round\left[\frac{z}{L}\right]$ (purple arrow). Later, we use $x = x - L\,Round\left[\frac{x}{L}\right]$ to move the red circle into the original simulation box (green arrow). If there is a difference in the y-coordinate, we repeat the procedure. After applying these equations, both particles will be in the original simulation box, and

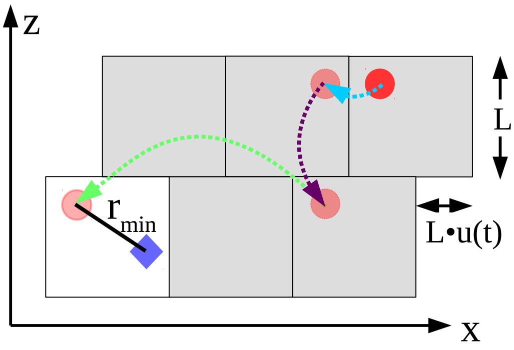

Figure 4.8: Calculation of distances between particles for the shear boundary conditions.

the distance between them can be calculated easily.

Remark: During the runs, it was found that the DMA simulation fails at strain amplitudes above $\approx 45\%$. The reason for such a behaviour is unclear, but as systems fail at shear boundaries, it probably may be caused by the shear boundary conditions, which require additional modifications for the case of large strains. In the following, most of the curves for the dynamic moduli and the loss tangents are terminated at $u_0 = 20\%$. Selected results may include larger strains up to 40%, but no strain amplitudes beyond 45% have been included.

4.5 Stress Calculation

During simulation, homogeneous oscillatory shear strain with amplitude u_0 and frequency ω is applied to the $xz-$plane in the $\pm x-$direction via $u = u_0 \sin(\omega t)$ using the shear boundary conditions discussed above. The $xz-$component of the microscopic stress tensor is computed via

$$\sigma_{xz} \approx \frac{1}{2V} \sum_{\substack{i,j \\ i \neq j}} \frac{x_{ij} z_{ij}}{r_{ij}} F_{ij}. \tag{4.16}$$

Here $x_{ij} = x_i - x_j$ and $z_{ij} = z_i - z_j$ are the distances between nodes i and j in the x- and z-direction respectively, r_{ij} is the total distance between i and j, and F_{ij} is the magnitude of the total force between nodes i and j. A more detailed discussion of this equation can be found in Appendix B.2. As in Section 2.4.1, we assume that the resulting stress obeys the sine function with the same frequency as the applied strain, but with a different amplitude and a phase shift. Therefore, the stress data is fitted via $\sigma = \sigma_0 \sin(\omega t + \delta)$, where σ_0 and δ are adjustable parameters. The loss modulus μ'' can be obtained via the work dissipated during one shear cycle (see

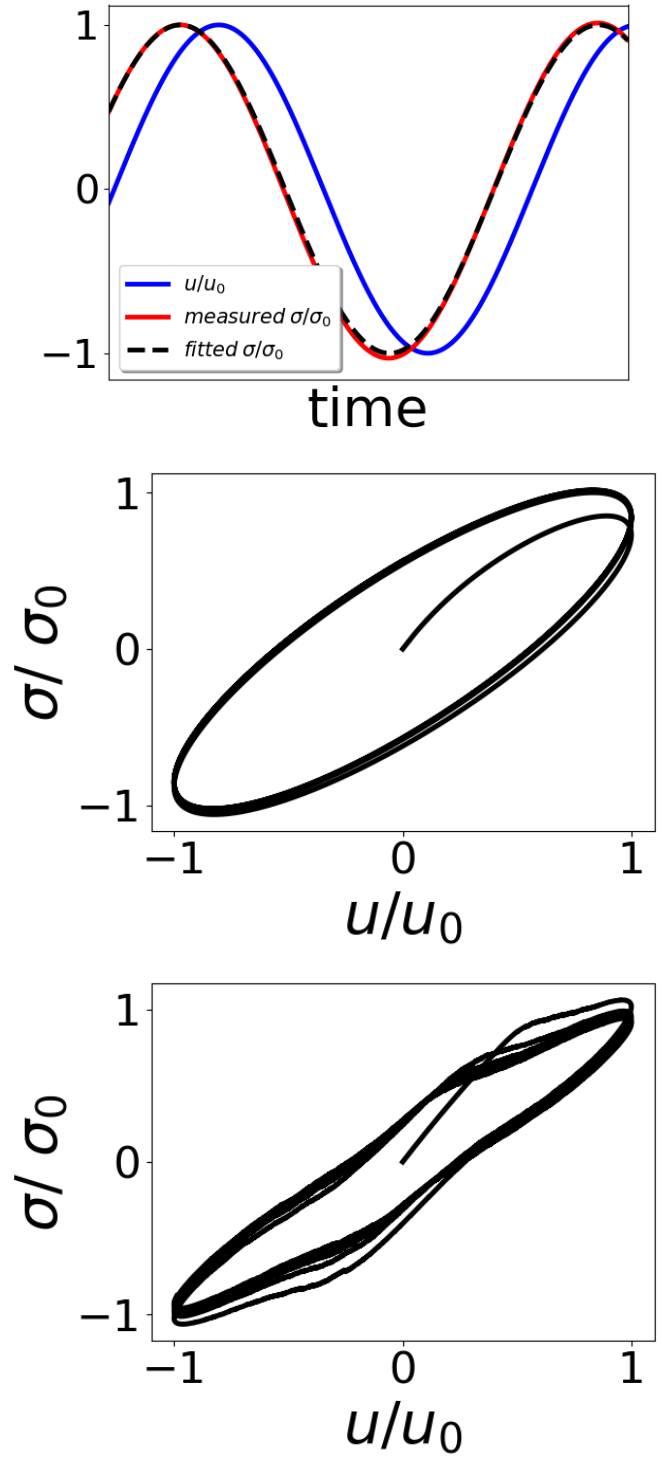

Figure 4.9: Top: a general form of the strain and stress functions; middle: hysteresis of stress and strain for an unfilled system; bottom: hysteresis of stress and strain for a filled system.

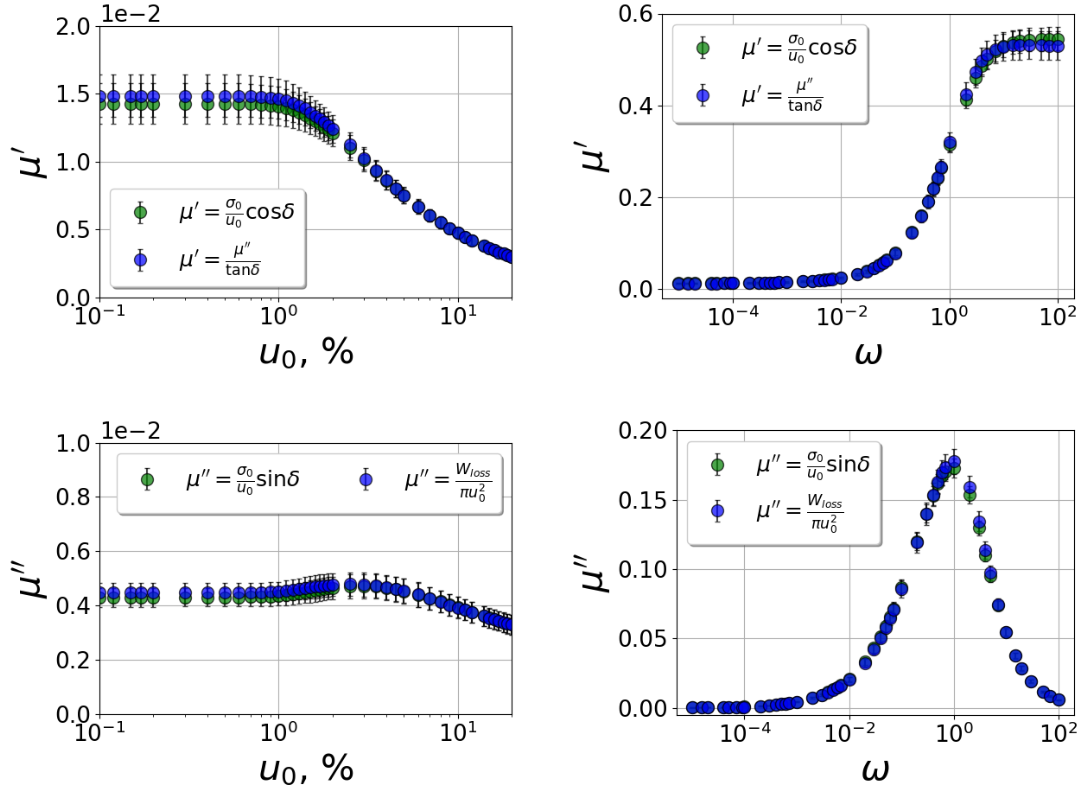

Figure 4.10: Storage and loss moduli vs. strain amplitude u_0 (left) and frequency ω (right) obtained for a 20% filled NR system ($\gamma_f^d = 20$ mJ/m^2, $\gamma_f^p = 10$ mJ/m^2) using Eq. (2.11) – (2.12) (green) and Eq. (2.15) (blue).

also (2.15))

$$W = \oint \sigma du = \pi\mu'' u_0^2.$$

Note that the dissipated work in the above equation is a well defined quantity even in a highly non-linear composite. Applying linear analysis, we obtain the storage and the loss moduli using (2.11) and (2.12), i.e.,

$$\mu' = \frac{\sigma_0}{u_0}\cos(\delta),$$

$$\mu'' = \frac{\sigma_0}{u_0}\sin(\delta).$$

If we plot the resulting stress versus the applied strain, we can observe the hysteresis, which is typical for a viscoelastic material. An example of simulated stress-strain curves is shown in Fig. 4.9. In the top panel of this figure, a general form of the applied strain (blue curve) and the obtained stress (red curve) is shown, as well as the fitted stress according to $\sigma = \sigma_0 \sin(\omega t + \delta)$ (black dotted curve). The phase shift between these functions gives δ, and the tangent of this phase shift is the loss tangent. In the next two panels, the stress-strain curves for both unfilled (middle panel) and filled systems (bottom panel) are presented. Both trajectories start initially at the origin and then after several cycles each system reaches its steady state. For the unfilled system, the standard elliptical shape can be observed, which is similar to the experimental one and to the result obtained in the discussion of the Zener model in Section 2.4.1. The case of the filled system is, however, more complicated. The shape of the curve is highly non-linear, which is also consistent with experiments, and the system requires more time to establish a stable trajectory. The loss during the first cycle is larger than during the following ones. This is also in agreement with experimental data, and a possible explanation might be that during the first shear cycle the number of broken bonds is larger than during the subsequent ones. Note that even though the bonds in this model are reversibly broken, it may take significant time for them to reform. If the local deformation persists, this may never happen. Overall, the shape of the curves allows to calculate the area enclosed by the curve and get the value of the dissipated work. Based on this value, the dynamic moduli can be calculated.

It is worth noting that (2.15) is based on (2.11) and (2.12) in conjunction with $\sigma = \sigma_0 \sin(\omega t + \delta)$. This implies that the loss moduli values obtained via (2.12) and (2.15) have to be the same. Fig. 4.10 provides an example showing the storage and the loss moduli as functions of strain amplitude and frequency obtained using the two approaches. The blue curves are calculated based on the value of the dissipated work, whereas the green curves are obtained using (2.11) – (2.12). The error bars are calculated based on five independent subsystems extracted from the final configuration of a filled NR system. It can be observed, that the error bars showing the differences between subsystems are larger than the numerical difference in the approaches to the calculation of the moduli. Overall, the two approaches provide sufficiently close results. The linear one-coefficient Fourier analysis is commonly used in experiments, even for highly non-linear systems. In our model, it is also helpful in terms of reducing the number of simulation parameters. Therefore, in the remainder of the work, we will follow this experimental approach and will use (2.11) and (2.12) to calculate the dynamic moduli. Eq. (2.15) will be used as a cross-check for the obtained moduli values.

Chapter 5

Model Parameterization

A coarse-grained modelling approach, like the one developed in this thesis, is similar to the design of phenomenological forcefield models for atomistic simulations (e.g., [133]). The latter contain a large number of parameters, which must be adjusted in a development step called parameterization using so-called training sets. A training set is a set of experimental systems, which is small but representative for the range of applications for which the forcefield is intended. Experiments on the training set are carried out, and the results are matched to the model by variation of the parameters. Generally, this is a lengthy undertaking, requiring a sizeable group of people. This of course is not possible in the present case. Instead, the purpose of this section is to explain how the parameterization of the coarse grained model can be developed and, if necessary, generalized to a larger set of polymers and fillers. The results presented in this chapter have also been published and can be found in [129].

5.1 Morphology Generator

We focus on systems consisting of three main components: two polymers – NR and SBR plus filler. These components can be characterized by the respective surface tension values, which are compiled in Table 5.1. The values of the surface tensions for the polymers are fixed, whereas the filler surface energy is variable. By varying the filler surface energy, we can mimic different fillers, such as carbon black and silica. The attendant morphologies, obtained for different fillers, can also be compared to each other or to experimental ones. Subsequently, any filler morphology can be tied to the mechanical characteristics of the system via the DMA simulation.

In Chapter 3 we discussed the effect of the lattice type and the cutoff radius on the resulting morphologies using some selected examples. Throughout this chapter, we use the displaced FCC lattice with $\delta r = 0.3d$ (chosen according to the uniform distribution) with $r_{cut} = 1.3d$. At these conditions, the average number of nearest neighbours in the system is close to 12. We study systems with the linear dimension $L \approx 100$ (in units of d), which yields for the number of nodes $n = 4\left(\frac{100}{d\sqrt{2}}\right)^3 \approx 1.4 \cdot 10^6$. Here d is the nearest neighbour distance and 4 is the number of nodes per unit cell in the FCC crystal. The parameters used for the simulation of flocculation are

Table 5.1: Surface tension values of the components. The values of the surface tensions of the polymers are taken from [122].

Component	γ^d [mJ/m^2]	γ^p [mJ/m^2]	γ_{total} [mJ/m^2]
NR	20.24	5.46	25.70
SBR	29.91	1.64	31.55
filler	10, 20, 30	0, 5, 10, 20	10, ..., 50

Table 5.2: Parameterization of the morphology generator.

Parameter	Value
lattice type	randomized FCC
maximum random displacement	$0.3\,d$
simulation box linear dimension	$\approx 100\,d$
number of direct neighbours	8 to 18
average number of direct neighbours	≈ 12
number of nodes	$\approx 1.4 \cdot 10^6$
cutoff radius	$1.3\,d$
reduced inverse temperature[1]	$a/(k_B T) = 0.421$ m^2/mJ

compiled in Table 5.2.

The morphology generator brings the system towards the lowest possible Gibbs free energy. In real systems, however, the lowest possible Gibbs free energy cannot be achieved due to kinetic and spacial constrains. Therefore, for the validation of the morphology generator and for the estimation of the number of Monte Carlo steps required for a similar filler morphology, the simulated TEM images can be compared to experimental ones. In addition, small angle scattering intensities for a different number of MC steps can be computed and compared to experimental measurements, as shown in [20, 21]. However, this a very time-consuming procedure, which here was not possible. The experiments require synchrotron radiation, and thus the data for specific systems are not always available.

The simulation initially starts in a system with randomly distributed nodes and, thus, allows to observe the filler network development with the number of MC steps. The morphologies can be extracted out of the simulation after an arbitrary number of simulation steps. If filler agglomerates are present, their typical size can be compared to the experimental one observed for the same fillers, polymers and processing conditions. An example of the filler network development in time is presented in Fig. 5.1, where only filler nodes are shown. The morphologies in this picture correspond to a filled NR system with 20 vol. % filler and filler surface tension values $\gamma_f^d = 20$ mJ/m^2 and $\gamma_f^p = 0$ mJ/m^2; the thickness of the images is $5 \times d$. The average number of MC steps per node is given above each of the simulated TEM images. Note that the initial distribution of filler nodes is random and, as the simulation time increases, the filler tends to form agglomerates, which

---

[1] Corresponds to $T_{exp} = 140$°C.

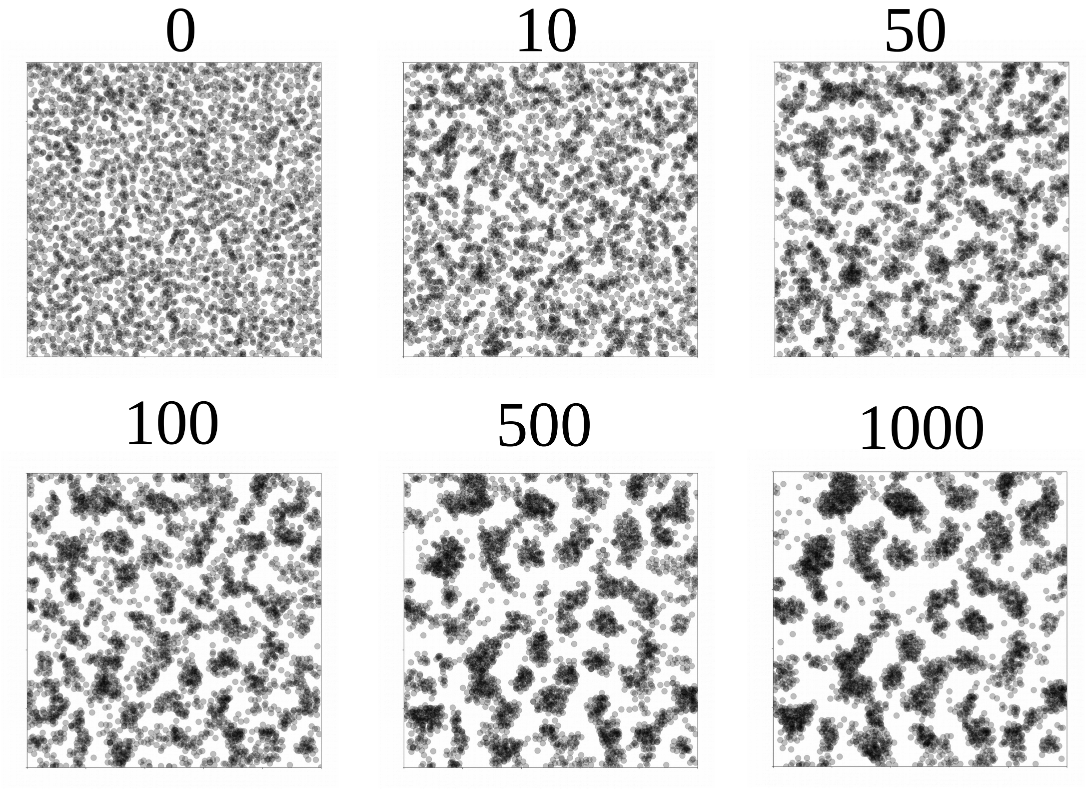

Figure 5.1: Example of the filler network development with the number of MC steps. The number above each panel shows the average number of MC steps per node. Only filler nodes are present.

become larger with the number of MC steps. Notice also the loss of connectivity between agglomerates between 100 and 500 MC steps.

Fig. 5.2 shows a simulated TEM image in comparison to an experimental TEM image obtained for SBR with 20% of CB N330 taken from [134]. The simulated TEM image has a thickness of $5 \times d$ and is scaled, so that the size of the circles in this TEM image matches the size of agglomerates in the experimental TEM image. In addition, the TEM image is extracted after an average of 50 MC steps per node. Notice, that the typical size of agglomerates in the simulated TEM image is similar to the typical agglomerate size in the real TEM image. Increasing the number of MC steps, as was shown above, leads to the loss of connectivity between agglomerates in the simulated TEM image, which does not happen in real systems. Therefore, 50 MC steps per node is a reasonable value to get the agglomerate size being close to the experimentally observed one.

5.2 DMA Simulation

In the DMA part of the model, one has to find the proper values for the parameters used during shear simulation. Initially, we will fix the parameter values for unfilled polymers. The next step is then to find how polymer blends can be modelled. We will continue by adding filler to the system, mimicking filled elastomer systems.

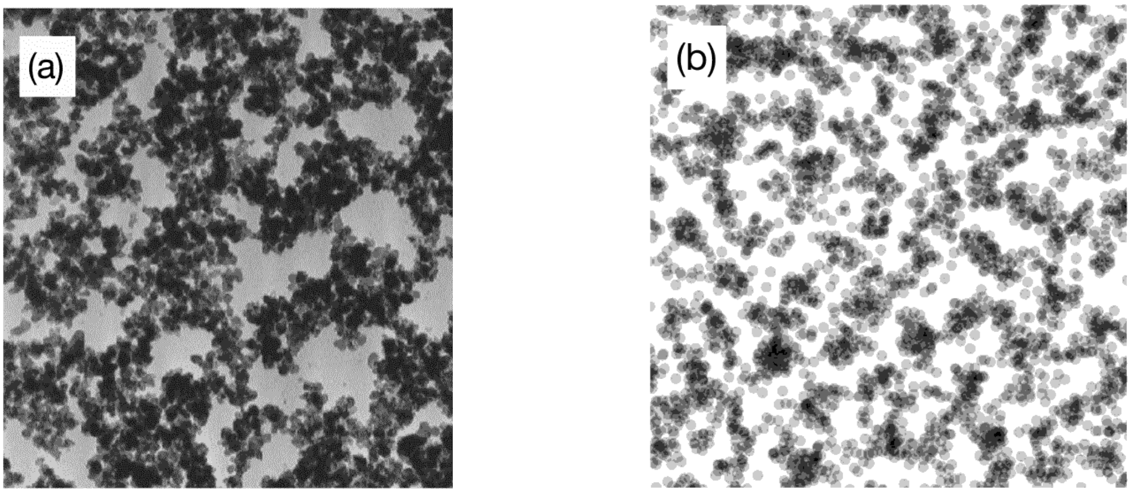

Figure 5.2: Left: experimental TEM picture taken from [134]. Right: simulated TEM image extracted after 50 MC steps per node on average. The thickness of the simulated image is $5 \times d$. Darker regions are the result of stacking of several particles along the line of sight.

Table 5.3: Basic parameters for DMA simulation.

Parameter	Symbol	Value	Comments
number of nodes	n	$1.1 - 1.3 \cdot 10^4$	
friction coefficient	γ	1.0	
number of strain cycles		≈ 5	
strain amplitude	u_o	0.1 to 20 %	
time step	δt	depends on ω	e.g. $5 \cdot 10^{-4}$ for $\omega = 0.2$

In the latter case, the parameter values describing filler-filler and polymer-filler interactions have to be established.

5.2.1 Unfilled Pure Polymer

Before we start with filled elastomer systems, we need to adjust our model for the case of pure polymer systems. Our general motivation is to obtain the simulated $\tan\delta$ curves comparable to the experimental ones for the same polymers. Subsequently, we can use these results to model a system with filler. At this point, there is no need to use the morphology generator because pure polymer systems consist of a single component. The basic parameters used for the shear simulation are compiled in Tab 5.3.

There is only one type of interaction in unfilled systems, i.e., the interaction between neighbouring polymer nodes, which can be described via a simple harmonic spring k_{PP}. In a system consisting of a network of harmonic springs, the only source of loss is the friction loss between nodes. The left panel of Fig. 5.3 shows the experimental loss tangents for natural rubber (NR) and styrene-butadiene rubber

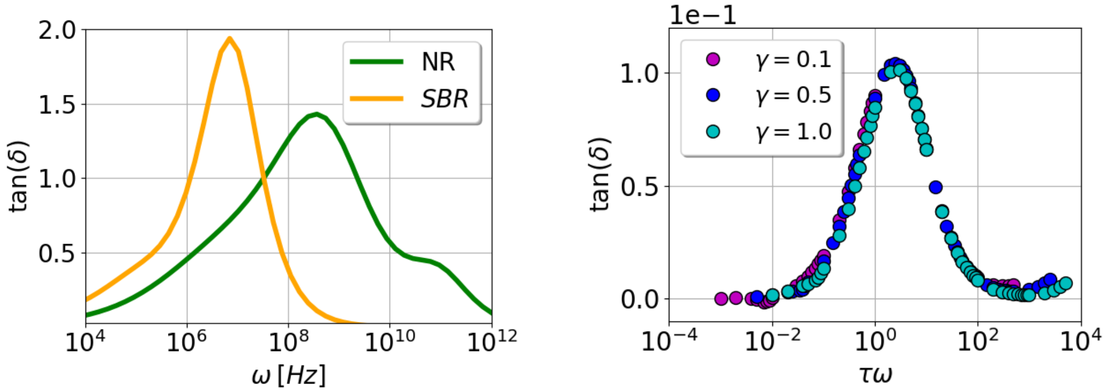

Figure 5.3: Left: the experimental $\tan\delta$ for NR and SBR vs. experimental frequency ω taken from [135]. Right: the simulated loss tangent $\tan\delta$ for $k_{PP} = 0.001$ and various friction coefficients γ vs. $\tau\omega$; here $\tau = \gamma/k_{PP}$, ω is the simulation frequency.

(SBR) vs. frequency ω. In the right panel of this figure, the simulated loss tangents $\tan\delta$ vs. $\tau\omega$ for a pure polymer system with $k_{PP} = 0.001$ and various friction coefficients γ are presented. Here $\tau = \gamma/k_{PP}$, i.e., changing the friction coefficient γ only affects the position of the $\tan\delta$ peak, but not its height. The same is true for k_{PP}. Note that the experimental $\tan\delta$ peak height in pure polymer systems lies between 1 and 2, whereas the simulated $\tan\delta$ is about one order less. To be able to adjust the height and the position of the $\tan\delta$ peak, we require additional model parameters.

Bimodal Distribution of Springs

A simple model that mimics dynamic mechanical properties of pure polymers is the Zener model, discussed in Section 2.4.1. The Zener model consists of a spring μ_1 in parallel to another spring μ_2 and a dashpot η in series. The $\tan\delta$ curve in the Zener model is given by (see also (2.26))

$$\tan\delta = \frac{1-\theta}{\theta}\frac{\tau_2\omega}{(\tau_2\omega)^2/\theta + 1},$$

where $\theta = \mu_1/(\mu_1+\mu_2)$ and $\tau = \eta/\mu_2$. Setting $\mu_1 \approx \mu_2$ yields $\tan\delta|_{max} \approx 0.35$ (see also Fig. 2.13), which is too small compared to the experimental results. However, by varying θ, i.e., the ratio between these two spring constants, we can adjust the peak height of the loss tangent. The results for $\tan\delta$ vs. $\tau\omega$, obtained for different values of θ, are shown in Fig. 5.4. The lowest $\tan\delta$ corresponds to $\theta = 0.8$, while $\theta = 0.1$ leads to the loss tangent peak being close to 1.5. Following this idea, we model each polymer via two springs with significantly different values $k_<$ and $k_>$. The subscripts $>$ and $<$ refer to a *strong* and a *weak* bond, respectively. Note that the terms *weak* and *strong* reflect only the values of spring constants, i.e., both weak and strong bonds are not breakable in any sense. Within each polymer, the values of spring constants $k_<$ and $k_>$ are assigned randomly, but according to a given ratio

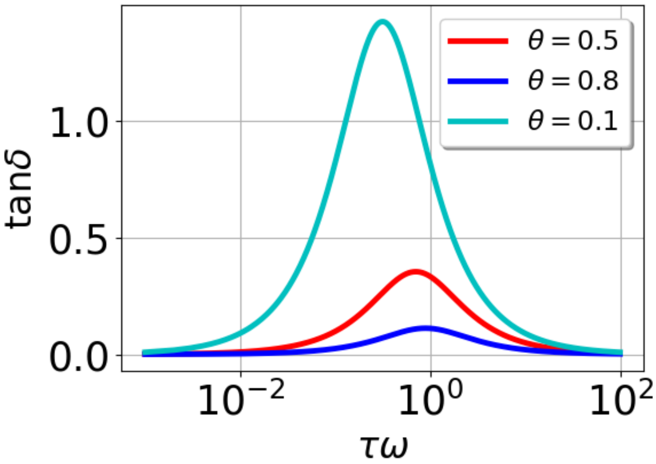

Figure 5.4: $\tan\delta$ obtained for the Zener model using different values of θ.

Table 5.4: Compilation of DMA parameters for pure polymers.

Parameter	Symbol	Value	Comments
NR-NR	$k_<^{NR-NR}$	10^{-3}	weak spring constant
NR-NR	$k_>^{NR-NR}$	0.2	strong spring constant
	$x_<^{NR}$	0.7	fraction of weak springs in NR
SBR-SBR	$k_<^{SBR-SBR}$	10^{-5}	weak spring constant
SBR-SBR	$k_>^{SBR-SBR}$	0.1	strong spring constant
	$x_<^{SBR}$	0.56	fraction of weak springs in SBR

$x_<$. The value $x_<$ is the ratio of weak springs in the system, i.e., the number of weak springs divided by the total number of bonds. The values $k_<$, $k_>$ and $x_<$ allow to adjust the $\tan\delta$ peak position and height, as will be explained below.

We start with adjusting the peak positions using the experimental data for NR and SBR (see Fig. 5.3). Note that the experimental peak position for SBR is located at a lower frequency than the peak for NR, and they are separated by approximately 2 orders of magnitude in units of Hz. Fig. 5.5 shows the result of a variation of $k_<$, $k_>$ and $x_<$ in a pure polymer system. The friction coefficient γ is equal to 1.0. Notice that smaller values of $k_<$ shift the $\tan\delta$ peak position to lower frequencies and increase the peak height, while changing of $k_>$ and $x_<$ affects mainly the peak height and barely its position. We choose the values $k_< = 10^{-5}$ for SBR and $k_< = 10^{-3}$ for NR as the standards. The reason is that for all values $k_< > 10^{-3}$ no peak height adjustment is possible because the peak height remains the same regardless of $k_<$ and $x_<$. On the other hand, the values $k_< < 10^{-5}$ require significantly smaller time steps, which increase the computational effort.

After setting the positions of the simulated peaks for NR and SBR using different values of $k_<$, the next step is to adjust the peak heights according to the

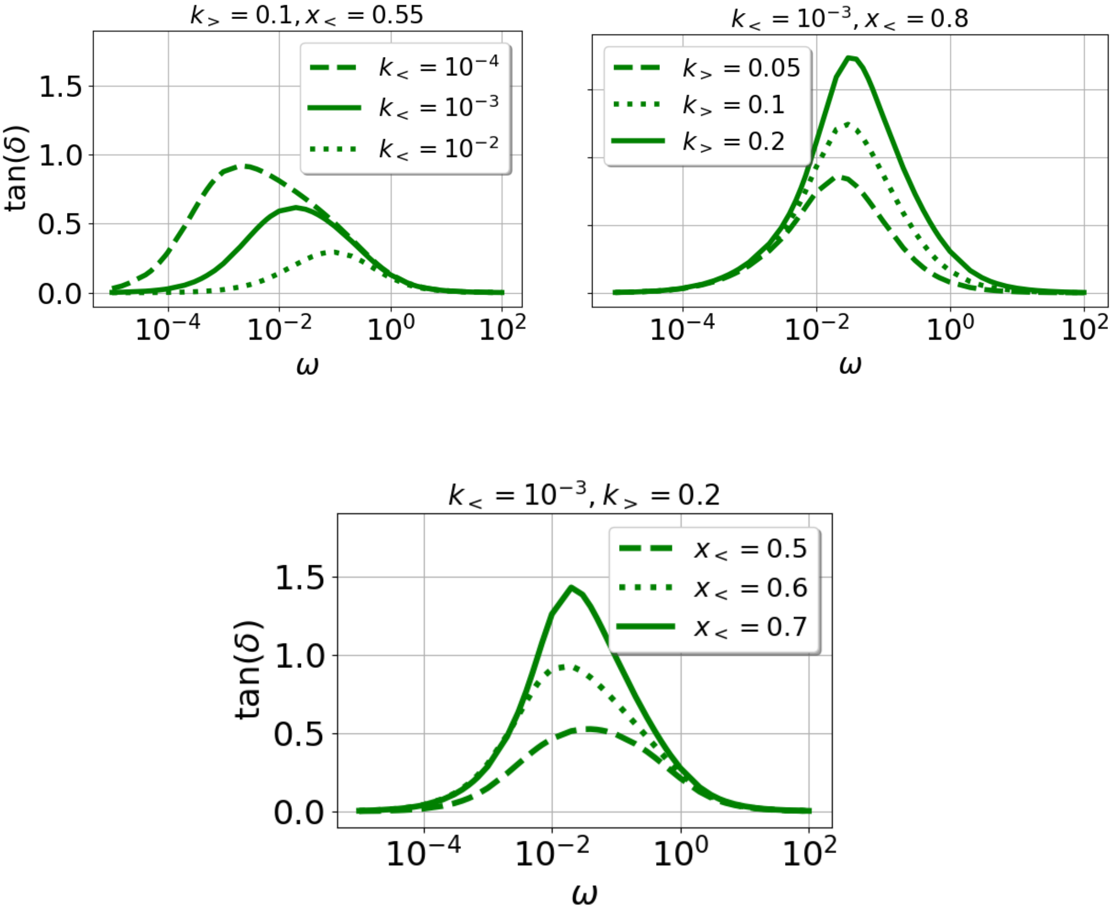

Figure 5.5: The loss tangent vs. simulation frequency ω for a systematic variation of $k_<$, $k_>$, and $x_<$ in a pure polymer system.

experimental data. To achieve that, we vary the values of $k_>$ and $x_<$ for both polymers. Increasing $k_>$ leads to a higher $\tan\delta$ peak, when $k_<$ is kept constant. This is consistent with the Zener model, where $\tan\delta$ depends on $\theta = \mu_1/(\mu_1+\mu_2)$, i.e., larger θ values yield a higher $\tan\delta$ peak. The same is true, when the ratio of weak bonds in the system $x_<$ rises.

The final result of the adjustment together with the experimental curves is presented in Fig. 5.6. Note that not only the peak heights are reasonably well modelled, but also the separation between the peaks. The simulated peak widths, however, differ from the experimental ones. They depend to some extent on the ratio between $k_<$ and $k_>$, but cannot be adjusted based on this set of parameters. Note that the presented model is not suited for describing the detailed dynamics of unfilled elastomers, since it neglects the polymer network structure. Nevertheless, we are able to obtain results for the loss tangents in qualitative agreement with experiments. The mapping of the simulation frequency to the real temperature can be done based on the time-temperature superposition $\log\omega \sim 1/T$ [136]. In addition, we can use the peak positions of simulated $\tan\delta$ curves to relate the simulation time unit to the experimental time unit, as described in Section 2.4.1. For instance, the experimental peak position for SBR is at roughly $\omega_{exp} = 10^7$ Hz, while the simulation frequency at the peak ω_{sim} for the same polymer is about 10^{-4}. This mapping remains a basis for any conversion as long as simulation parameters are fixed. The values of the force constants for pure polymers are compiled in Table 5.4.

5.2.2 Polymer Blends

In polymer blends, we have to deal with one additional interaction type, i.e., the mixed interaction between two different polymers. If polymers tend to separate (see, for instance, the examples in Section 3.3, where NR and SBR form two subphases), the interface between the polymers can significantly affect the mechanical properties. Therefore, the main problem in modelling unfilled blends is finding the proper values of the force constants describing the polymer interface.

To limit the number of additional parameters, we express the interaction between two different polymers as a function of force constants for pure polymers. The *strong* and *weak* spring constants in the interface can be then approximated via the following mixing rules

$$k_>^{P_1P_2} = \sqrt{k_>^{P_1P_1} k_>^{P_2P_2}}, \tag{5.1}$$

$$k_<^{P_1P_2} = \sqrt{k_<^{P_1P_1} k_<^{P_2P_2}}. \tag{5.2}$$

Here P_1 and P_2 refer to the polymers 1 and 2. The remaining adjustable quantity is $x_<^{\text{interface}}$. The upper left panel of Fig. 5.7 shows experimental loss tangents vs. frequency ω in Hz for NR (green), SBR (yellow) and their 50/50 (red) and 70/30 (purple) blends. All other panels present the simulation results for $\tan\delta$ as a function of simulation frequency ω. Note that the error bars are calculated based on five independent simulations. Note also that the simulation includes an

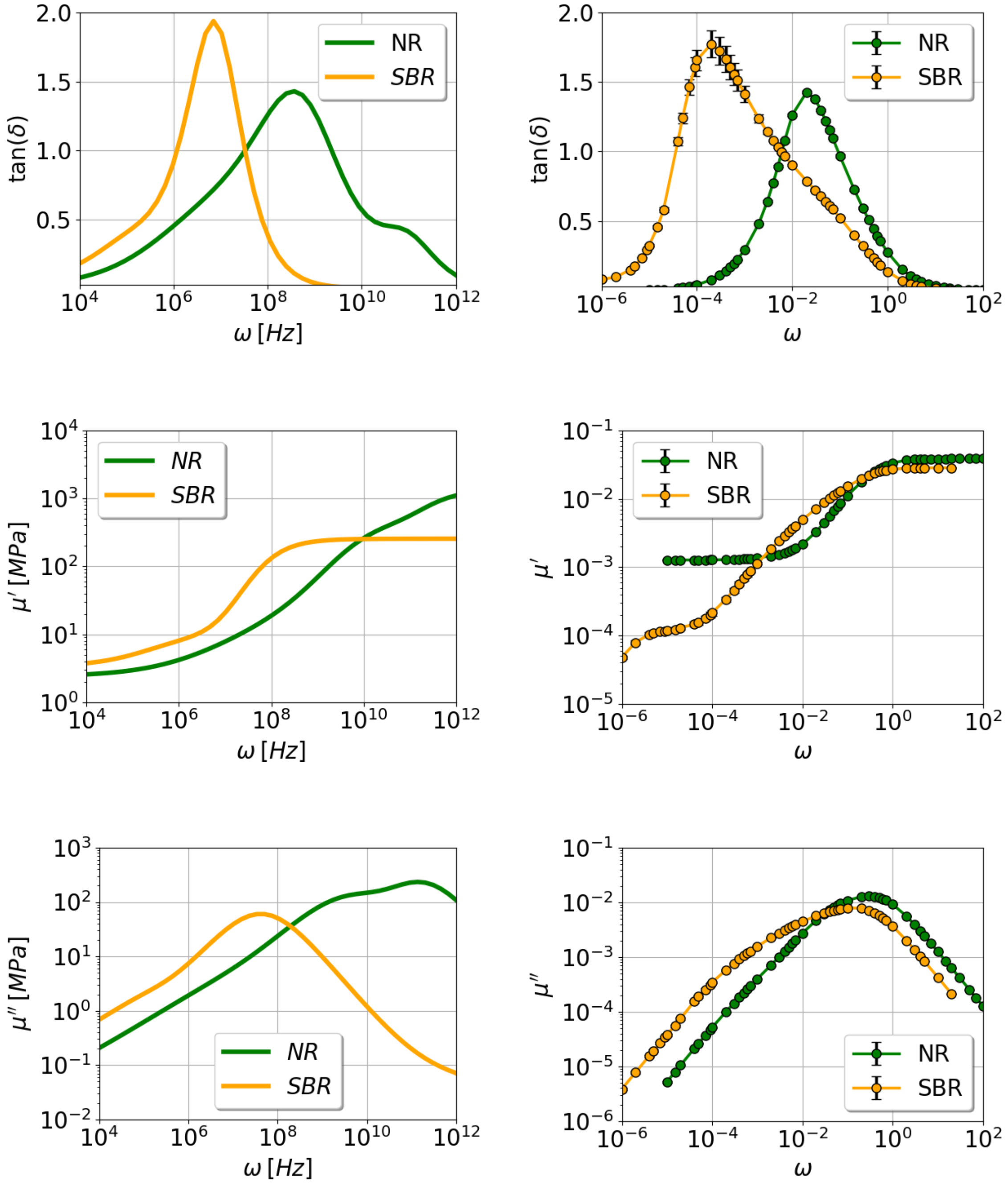

Figure 5.6: The experimental (left) and simulation (right) loss tangents, storage and loss moduli (from top to bottom) vs. frequency ω for NR and SBR. The experimental data is taken from [135].

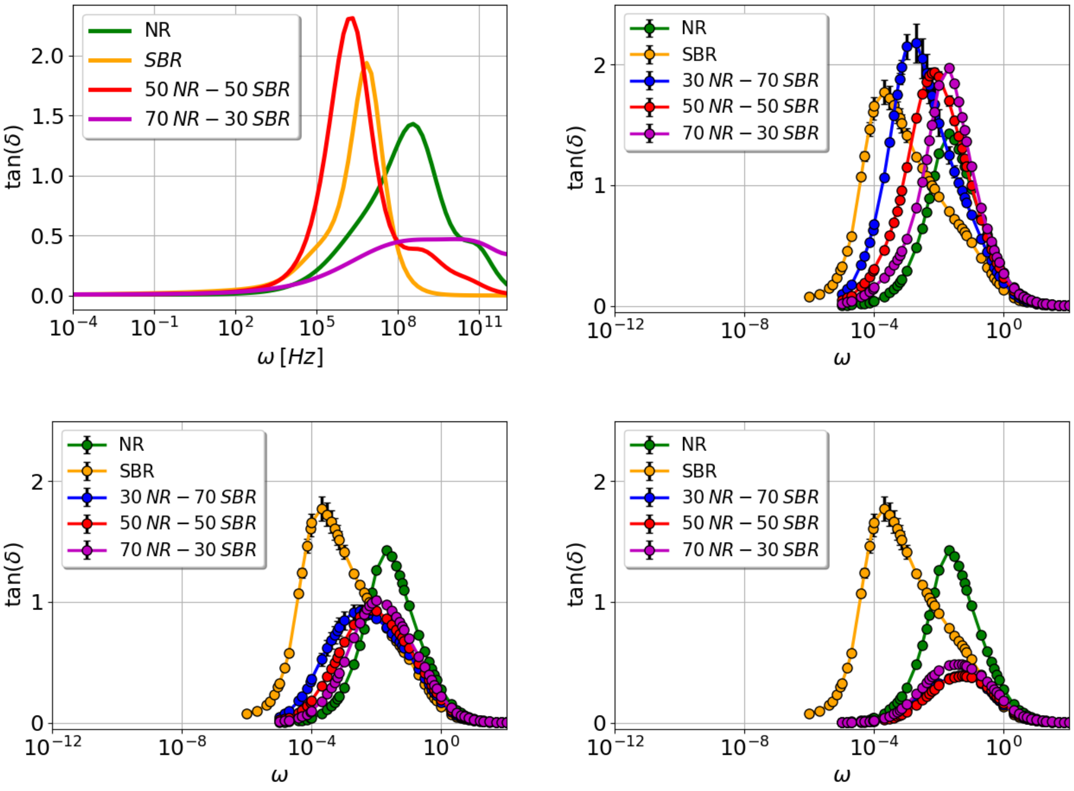

Figure 5.7: Upper left: experimental $\tan\delta$ vs. frequency for NR, SBR and their blends. All other plots are obtained from simulation and show $\tan\delta$ vs. simulation frequency ω. The simulation results are averages over five independent simulations. From the upper right in counter-clockwise order: $x_{<}^{\text{interface}} = 1.0$, 0.5 and 0.0. Note that simulation results include an additional 30/70 blend.

additional 30/70 blend. The value of $x_<^{\text{interface}}$ in the simulation was varied, and it is equal to 1.0, 0.5 and 0.0 from left to right and from bottom to top. Notice that the value of $x_<^{\text{interface}}$ significantly affects the loss tangent peak height. The value of $x_<^{\text{interface}}$ equal to 1.0, i.e., when all springs in the interface between the polymers are weak, leads to the highest $\tan\delta$. When $x_<^{\text{interface}}$ decreases, the loss tangent peak height also drops. The positions of the peaks for the blends, however, do not depend on $x_<^{\text{interface}}$. The order of the peaks corresponds to the experimentally observed one, i.e., a blend peak shifts to a pure polymer peak position, when the attendant polymer ratio in the blend increases. Hence, this 'peak shift' for different polymer blends can be reproduced by the model. The peak height is a more complex parameter to adjust. In experiments, the peak height of the 70/30 blend is much lower than the ones of pure components, while the peak height of the 50/50 blend is higher than the latter. In simulations, depending on $x_<^{\text{interface}}$, the peaks of the blends are either higher or lower than the respective peaks of pure components. For instance, the simulated $\tan\delta$ peak for the 70/30 blend is in good agreement with the experiment when $x_<^{\text{interface}} = 0$. For the 50/50 blend, the closest to the experiment loss tangent peak is observed at $x_<^{\text{interface}} = 1$. Overall, there is no uniform value of $x_<^{\text{interface}}$ allowing to obtain the peak heights similar to the experimental ones for all presented blends. For the later analysis we use $x_<^{\text{interface}} = 1.0$ because this value provides the possibility to distinguish the blends in terms of their peak positions.

5.2.3 Filled Systems

At this point, we can include filler into the system. The springs between filler nodes as well as between filler and polymer nodes can break reversibly. Thus, in addition to the friction loss, which provides the main contribution to the loss modulus in unfilled systems, we introduce loss in the filler-filler and filler-polymer interfaces due to reversible breaking of bonds. The parameterization in this case includes the adjustment of the filler-filler and the filler-polymer spring constants and the bond breaking distances. One way to find the values of the spring constants is to consider the change of the storage modulus with an increasing filler content. Beyond the percolation threshold, one can observe a power-law dependence of the storage modulus on the filler content, i.e., $\mu' \propto \phi^y$, where $3 < y < 4$. This follows from both the experimental findings and theoretical considerations [7]. Therefore, we have to find such values of the force constants, that the simulated storage modulus has a similar power law increase.

Fig. 5.8 shows filler morphologies for the silica filled NR ($\gamma_f^d = 20$ MJ/m^2, $\gamma_f^p = 16$ mJ/m^2) with different ϕ, given in the plot titles. Based on the filler morphologies, we can expect the percolation threshold to be at $\approx 15\%$ filler, as at this concentration the filler starts to form the filler network.

Initially, we choose $k_{FF} = k_{PF} = 1.0$. Then, by making alterations and by comparing with the experimental data, we can find the values allowing the model to reproduce the main experimental findings. On the left-hand side of Fig. 5.9, the simulated loss tangents vs. frequency ω are shown obtained for different filler loadings (0, 10, 20 and 30%). Note that, due to addition of filler, the peak drops and becomes broader, but the peak position does not change significantly. This

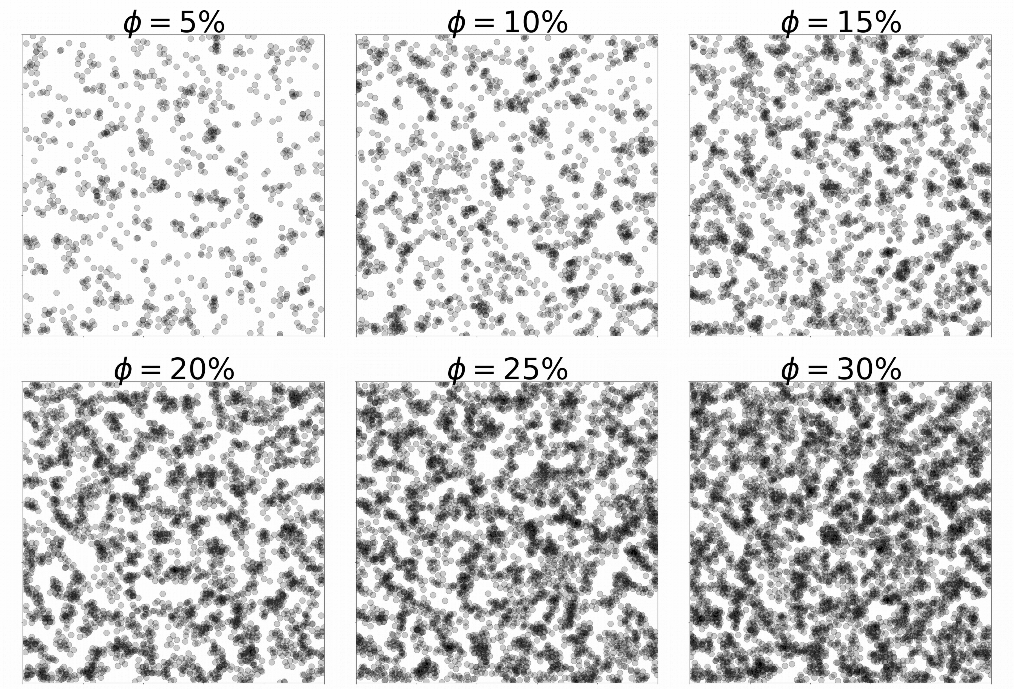

Figure 5.8: Simulated TEM images obtained for NR filled with silica (($\gamma_f^d = 20$ MJ/m^2, $\gamma_f^p = 16$ mJ/m^2) at different filler volume contents, given in the title of each TEM. The images are extracted after 50 MC steps per node on average, $L = 50$.

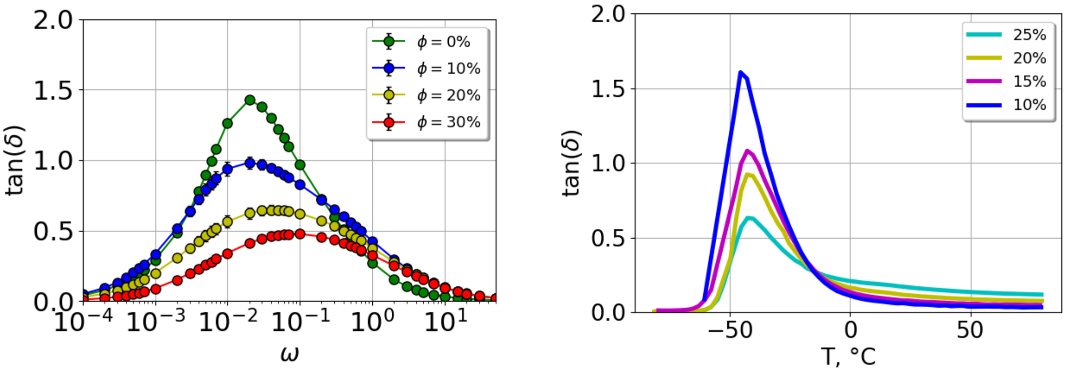

Figure 5.9: Left: The simulated $\tan\delta$ vs. ω at different filler contents given in the legend. The system is filled NR, $\gamma_f^d = 20$ mJ/m^2 and $\gamma_f^p = 0$ mJ/m^2. In addition, $u_0 = 1\%$. $R_{FF} = R_{PF} = 1.01 r_{ij,0}$, $k_{FF} = k_{PF} = 1.0$. Right: the experimental loss tangent vs. temperature for NR filled with CB at $\omega = 10$ Hz and $\phi = 10$, 15, 20 and 25%.

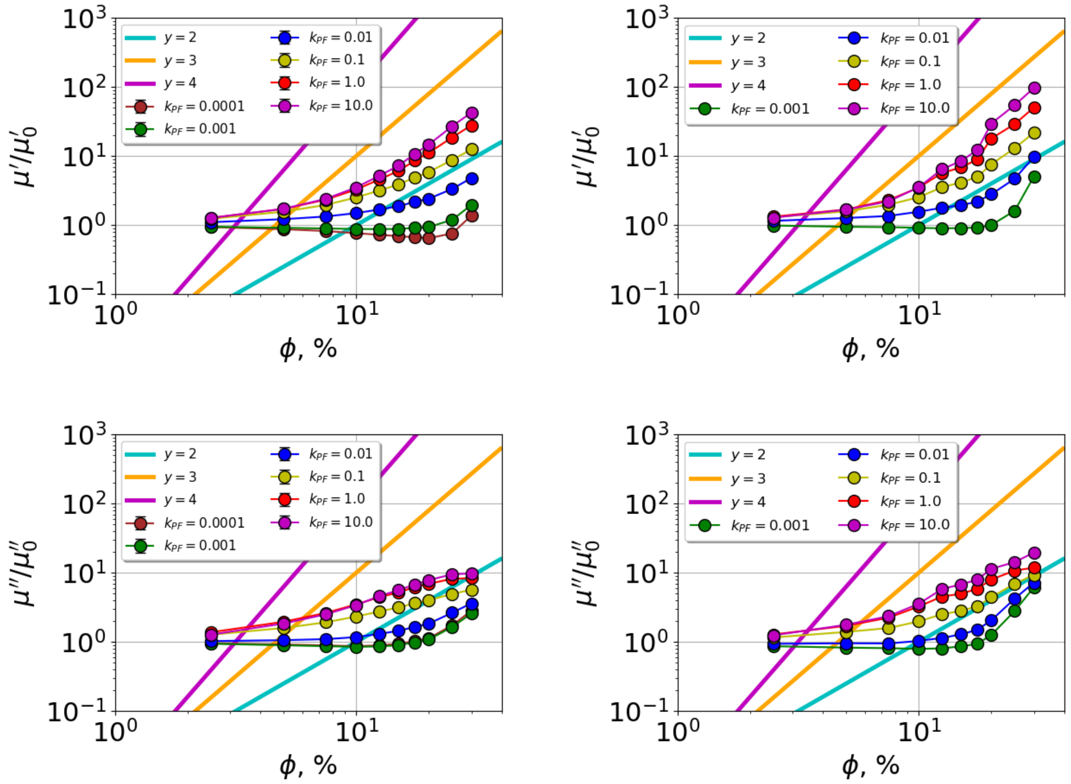

Figure 5.10: Variation of the force constant for the polymer-filler interaction k_{PF} in terms of the reduced storage μ'/μ'_0 and loss μ''/μ''_0 moduli vs. filler volume fraction ϕ. The values μ'_0 and μ''_0 refer to the unfilled NR. The left panel corresponds to $k_{FF} = 1$; in the right panel, $k_{FF} = 10$. The strain amplitude $u_0 = 1\%$ and frequency ω is 0.002. Straight lines show different power law exponents, i.e., $y = 2$, 3 or 4.

effect of filler on the loss tangent is typical in experimental systems and is well reproduced by the model. An example of experimental $\tan\delta$ curves as functions of temperature for NR filled with different filler contents of CB at $\omega = 10$ Hz is shown on the right-hand side of Fig. 5.9. Filler increases the 'strength' of the material, and thus, the storage modulus. The loss modulus, however, is a more complicated quantity. On the one hand, we can expect the loss reduction due to occluded polymer in the polymer-filler interface. On the other hand, the filler-filler and filler-polymer interactions, which are not present in unfilled systems, increase the dissipation and, consequently, the loss. The loss tangent, as the ratio of these two quantities, depends on many processes taking place in filled systems, where some of them have opposite effects. But since the $\tan\delta$ peak height drops with the filler content, one can assume that at the peak position the rise in the storage modulus overcomes the increase in the loss modulus. The low frequency (or high temperature) side of the $\tan\delta$ peak is particularly interesting in light of the rolling resistance measurements. In experimental systems, at high temperatures the order of the $\tan\delta$ curves, corresponding to systems with different filler contents, is reversed in comparison to what one observes at the peak. Notice that in the simulation, the curve for the unfilled system undercuts the curve for $\phi = 10\%$, and subsequently the curve for $\phi = 20\%$, as the frequency decreases. The $\tan\delta$ value for $\phi = 30\%$, however, remains the smallest at the lowest measured frequency $\omega = 10^{-4}$.

Next, we consider the effect of the spring constant strength on the reduced storage $\mu'(\phi)/\mu'(\phi = 0)$ and loss $\mu''(\phi)/\mu''(\phi = 0)$ moduli as functions of filler content ϕ. In Fig. 5.10 we vary the value of the force constant for the polymer-filler interaction k_{PF}, keeping the value of k_{FF} fixed and equal to 1.0 (left panel) and 10.0 (right panel). The other system parameters are the same as above. The simulation frequency ω is 0.002, i.e., the results refer to the low frequency (or high temperature) side of the loss tangent peak. At low filler contents, the moduli values for filled systems are close to the ones for the unfilled system. When filler is added, the moduli start to rise, and at about 10-15% filler the percolation threshold can be reached in most cases. Note that smaller values of k_{PF} at the same k_{FF} shift the percolation threshold to higher filler contents and, simultaneously, increase y, especially when $k_{FF} = 10$. A small k_{PF} yields a weak interaction between polymer and filler, such that, considerably more filler is required to increase the strength of the material. Based on the above observations, we can roughly relate k_{PF} to the filler particle size. Typically, small filler particles have a larger surface area, which corresponds to a stronger overall coupling between polymer and filler. Since the model does not explicitly include the particle size (other than d), we can incorporate the particle size into the model using different k_{PF}, where smaller particles can be characterized by larger k_{PF}. The values of y lie in the range between 2 and 3, when $k_{FF} = 1$ and between 3 and 4 when $k_{FF} = 10$. Notice that when $k_{PF} \geq k_{FF}$, the overall increase of the moduli is larger than for smaller values of k_{PF}, and in some cases can reach 100 at $\phi = 30$ % for the reduced storage modulus. The reduced loss modulus does not exhibit a similar increase and reaches at most 20 when $k_{PF} = k_{FF} = 10$ and $\phi = 30\%$.

The next figure, Fig. 5.11, shows the impact of the bond breaking distances on the reduced storage and loss moduli. In the left panel R_{FF} is varied, while

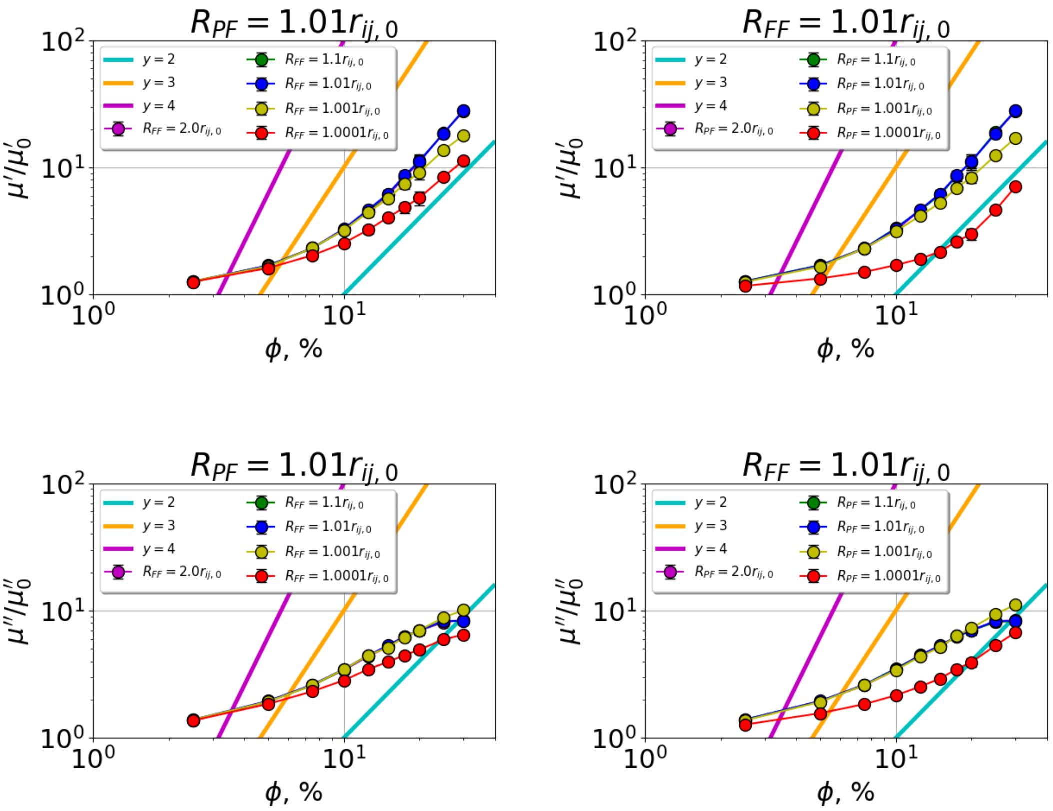

Figure 5.11: Variation of the bond-breaking distances in terms of the reduced storage μ'/μ'_0 and loss μ''/μ''_0 moduli vs. filler volume fraction ϕ. The values μ'_0 and μ''_0 refer to the unfilled NR. Left: variation of R_{FF} at constant $R_{PF} = 1.01\ r_{ij,0}$, right: variation of R_{PF} at constant $R_{FF} = 1.0\ r_{ij,0}$. The strain amplitude is 1% and frequency is 0.002. Straight lines show different power law exponents, i.e., $y =$ 2, 3 or 4.

R_{PF} is kept constant, and the right panel is obtained for different R_{PF} at fixed R_{FF}. Notice that the two largest breaking distances lead to the same values of the reduced storage modulus. The reason is that, on the one hand, the strain amplitude is small. On the other hand, the breaking distance is too large, so no bond breaking can be observed. Reducing the bond breaking distance leads to a decrease in the reduced storage modulus. A small bond breaking distance value yields weak bonds, which can break at a relatively short node-to-node distance. These weak bonds considerably reduce the strength of the composite and, therefore, the storage modulus. The value of R_{PF} has a stronger effect on the dynamic moduli than R_{FF} due to the number of polymer-filler bonds, which significantly exceeds the number of filler-filler bonds. The loss modulus is less sensitive to the variation of the bond breaking distances, and the overall increase with the filler content is smaller than for the storage modulus.

In Fig. 5.12 experimental data from [31] for tan δ vs. ϕ at two temperatures (0°C (blue) and 70°C (red)) are compared with simulation results at two frequencies ($\omega =$

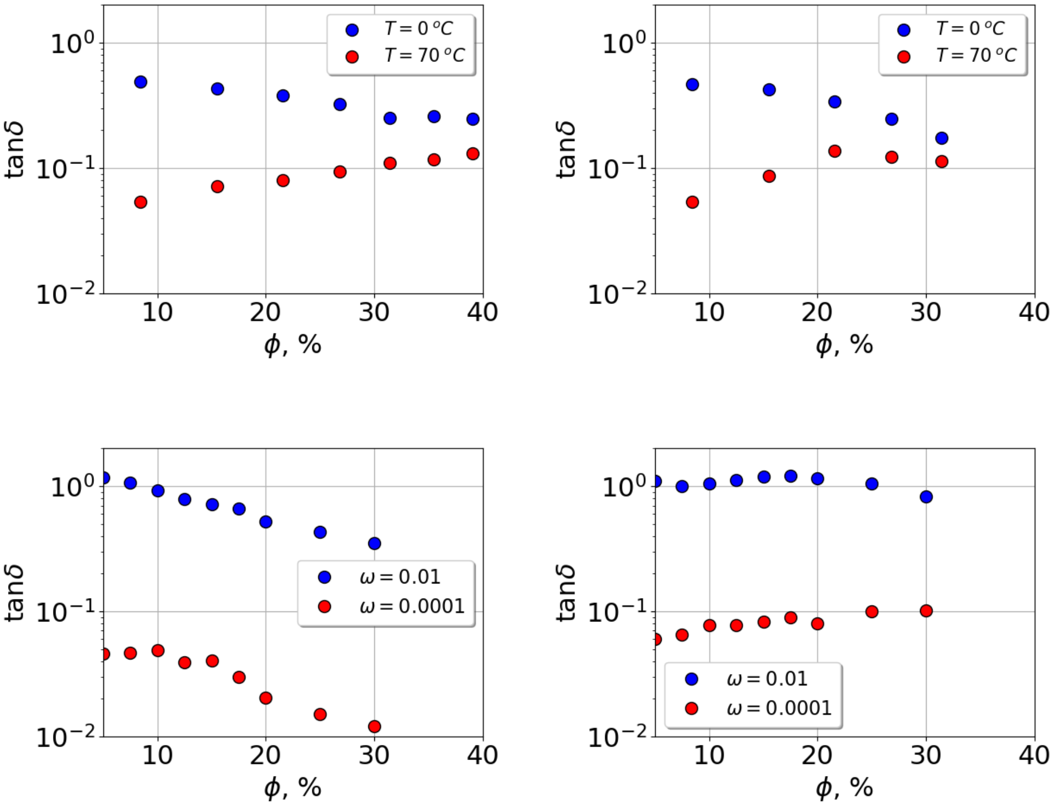

Figure 5.12: Top: the experimental loss tangent for N234 (left) and silica HiSil233 (right) in Duraden 715 at 1% strain, 10 Hz, 0°C (blue) and 70°C (red); bottom: simulation results for $\omega = 0.01$ (blue) and $\omega = 0.0001$ (red). The filler surface tension values: γ_f^d= 20 mJ/m^2 and $\gamma_f^p = 0$ mJ/m^2, the strain amplitude is 1%. Left: $k_{FF} = k_{PF} = 1.0$; right: $k_{FF} = 10$, $k_{PF} = 0.1$, $\gamma_F = 15$. Experimental data is taken from [31].

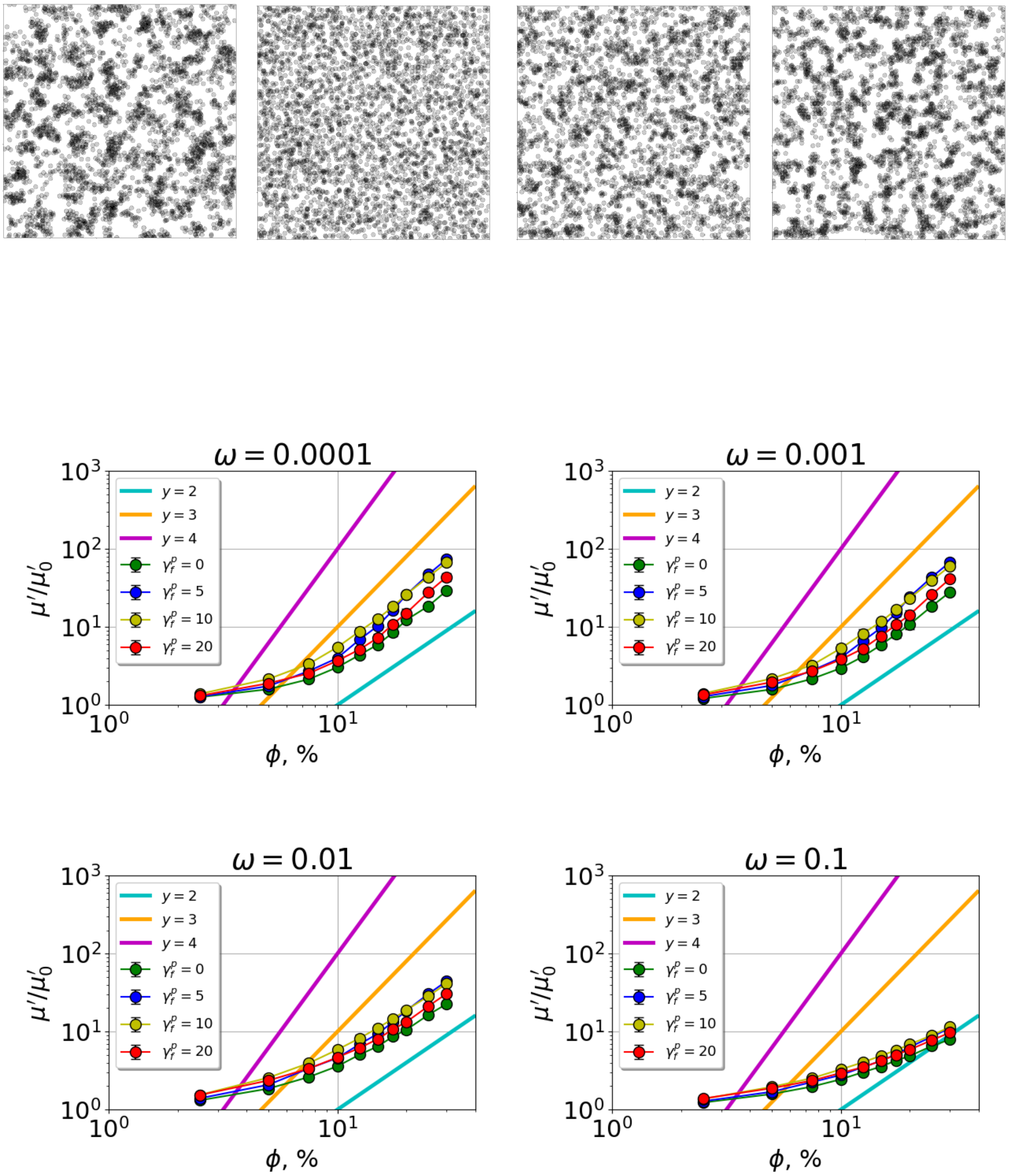

Figure 5.13: Top: simulated TEM images obtained for filled NR systems. The filler surface tension $\gamma_f^d = 20$ mJ/m^2 and $\gamma_f^p = 0$, 5, 10 and 20 mJ/m^2 (from left to right). Only filler nodes are shown. Bottom: the reduced storage modulus at different frequencies for the filled NR systems shown above, where μ'_0 refers to the unfilled NR. The strain amplitude is 1%, $k_{FF} = k_{PF} = 1$.

0.01 (blue) and $\omega = 0.0001$ (red)). Both temperature and frequency are taken from the low frequency/high temperature side of the loss tangent peak. The experimental results are obtained for N234 (top left) and silica (top right) in Duraden 715. The simulated system is filled NR, where $\gamma_f^d = 20$ mJ/m^2 and $\gamma_f^p = 0$ mJ/m^2, $k_{FF} = k_{PF}$ = 1.0 (bottom left). Note that at $T = 0$°C the loss tangent drops with the increasing filler content for both fillers. A similar decrease can be observed for the simulated system at $\omega = 0.01$, i.e., there is a qualitative agreement between the simulation and the experiment. This drop is mainly contributed by the aforementioned effects. The behaviour of the loss tangent at 70°C is different. For the carbon black filled system, one can see a continuous rise of the $\tan\delta$ at large filler contents. At this temperature, the dissipation due to reversible bond breaking plays an essential role in the system, and this rise of the loss overcomes the increase in the material's strength. We can conclude that beyond the percolation threshold the loss modulus must obey the power law with at least the same exponent y as the storage modulus. The silica filled system is more complicated, and the loss tangent in this case has a maximum at the filler content near the percolation threshold. In the simulated system, however, $\tan\delta$ drops beyond the percolation threshold, i.e., the increase in dissipation is smaller than the attendant increase in the storage modulus. Hence, the model with this particular set of force constants ($k_{FF} = k_{PF} = 1.0$) underestimates the loss due to reversible breaking of bonds, and additional parameters are required to increase the loss in the system.

Fig. 5.13 shows the reduced storage moduli as functions of filler volume content for four systems with different filler dispersions ($\gamma_f^d = 20$ mJ/m^2, γ_f^p is varied between 0 and 20 mJ/m^2) at various frequencies given in the title. The respective TEM images are given in the top row, where their length is equal to $50d$ and the thickness is $5d$. When the simulation frequency increases, the amplitude of the storage modulus drops and the dependence on the filler concentration becomes more linear, i.e., the power governing the storage modulus beyond the percolation threshold decreases. Nevertheless, the order of the curves does not significantly depend on frequency, e.g., the system with $\gamma_f^p = 5$ mJ/m^2 (blue) exhibits the largest storage modulus, whereas the system with the non-polar filler (green) – the smallest. When compared to the respective TEMs, it is clear that the storage moduli are inverse to the size of filler agglomerates, which is not in line with experimental observations.

Polymer-Filler Interface

Increasing loss in the system requires changing of the force constants involved in the reversible breaking process, i.e., the constants for the filler-filler and the polymer-filler interactions. So far, these spring constants are equal to each other. But by looking at Fig. 5.10, it is clear, that large k_{FF} and small k_{RF} at the same time provide the required loss modulus, which has at least the same power law exponent y as the storage modulus beyond the percolation threshold. On the left-hand side of Fig. 5.14, the loss tangent as a function of frequency is presented, when k_{FF} = 10.0 and k_{PF} = 0.1. This significant difference in the force constants for the polymer-filler and the filler-filler interactions leads to a second peak of the $\tan\delta$ at high frequencies. Note that the $\tan\delta$ at the peak in the Zener model depends on the

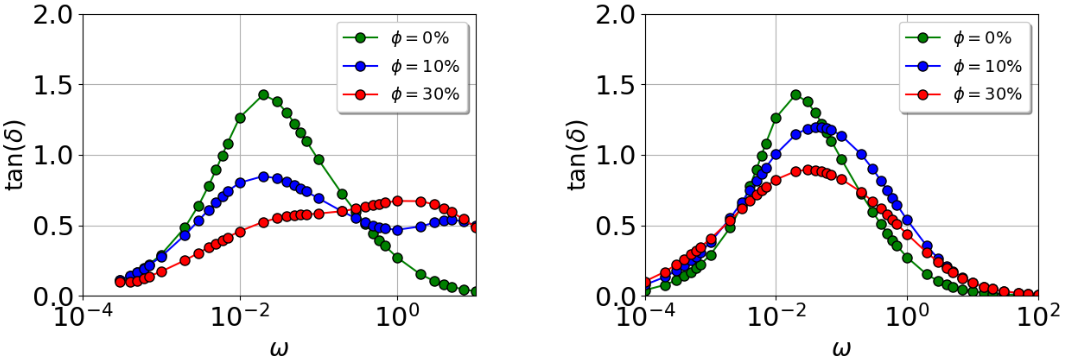

Figure 5.14: Simulated $\tan\delta$ vs. frequency ω. The system and the simulation parameters are the same as in Fig. 5.9. Left: $k_{FF} = 10.0$, $k_{PF} = 0.1$. Right: the same, but with an additional friction coefficient for filler nodes $\gamma_F = 15$.

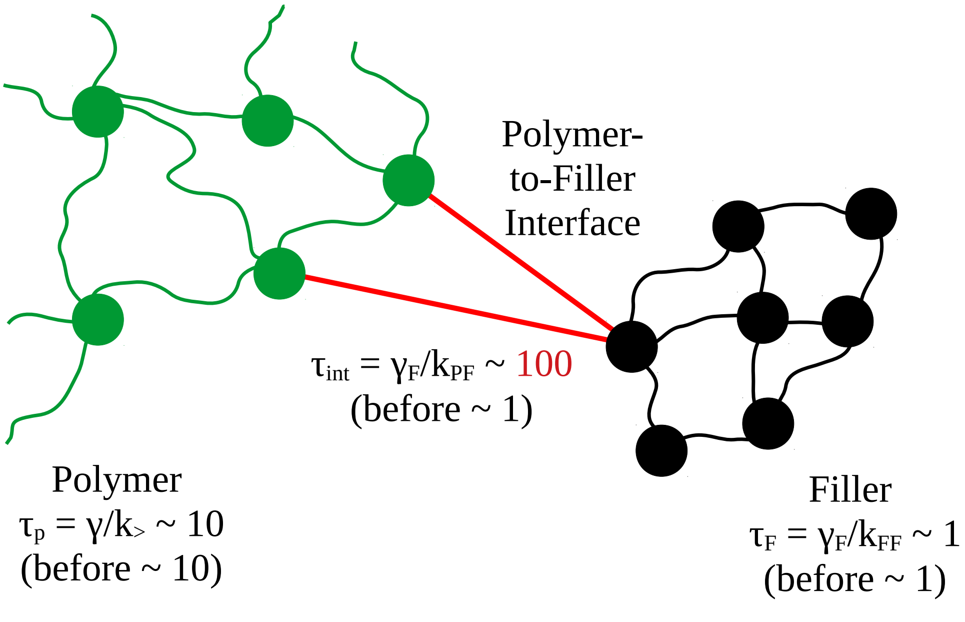

Figure 5.15: Relaxation times in different phases.

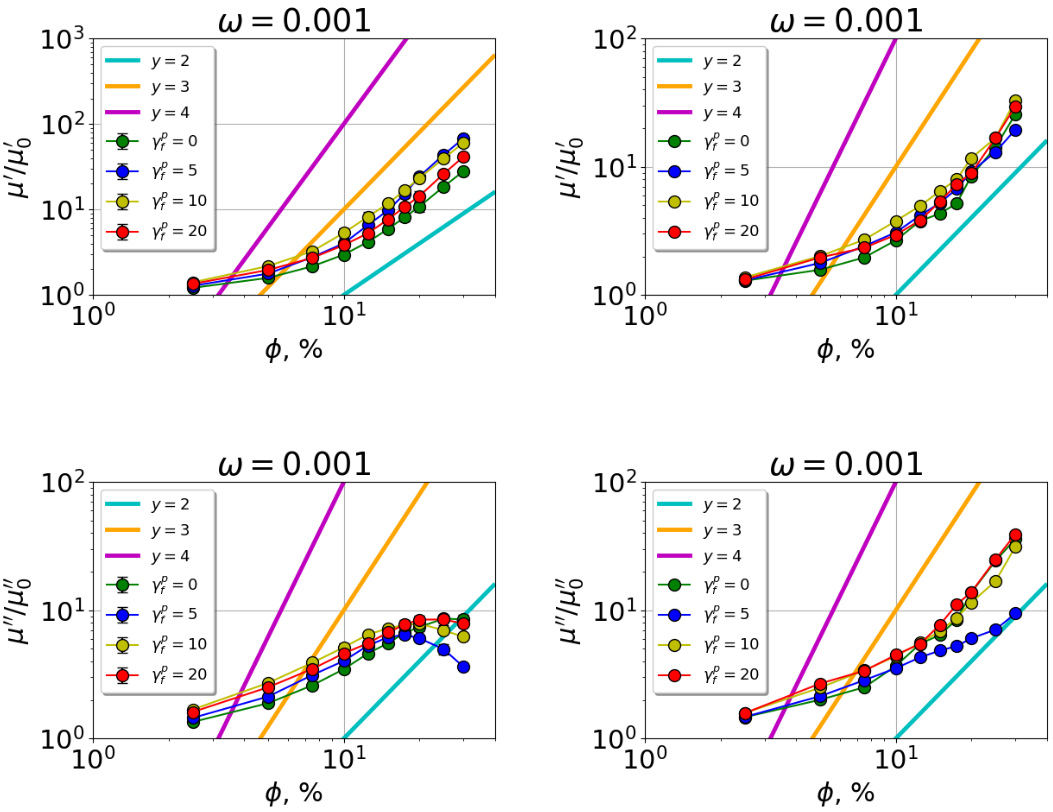

Figure 5.16: The storage and the loss moduli vs. filler volume content ϕ for the filled NR systems shown in the top row of Fig. 5.13. The strain amplitude is 1% and $\omega = 0.001$. Left: $k_{FF} = k_{PF} = 1$; right: $k_{FF} = 10$, $k_{PF} = 0.1$, $\gamma_F = 15$.

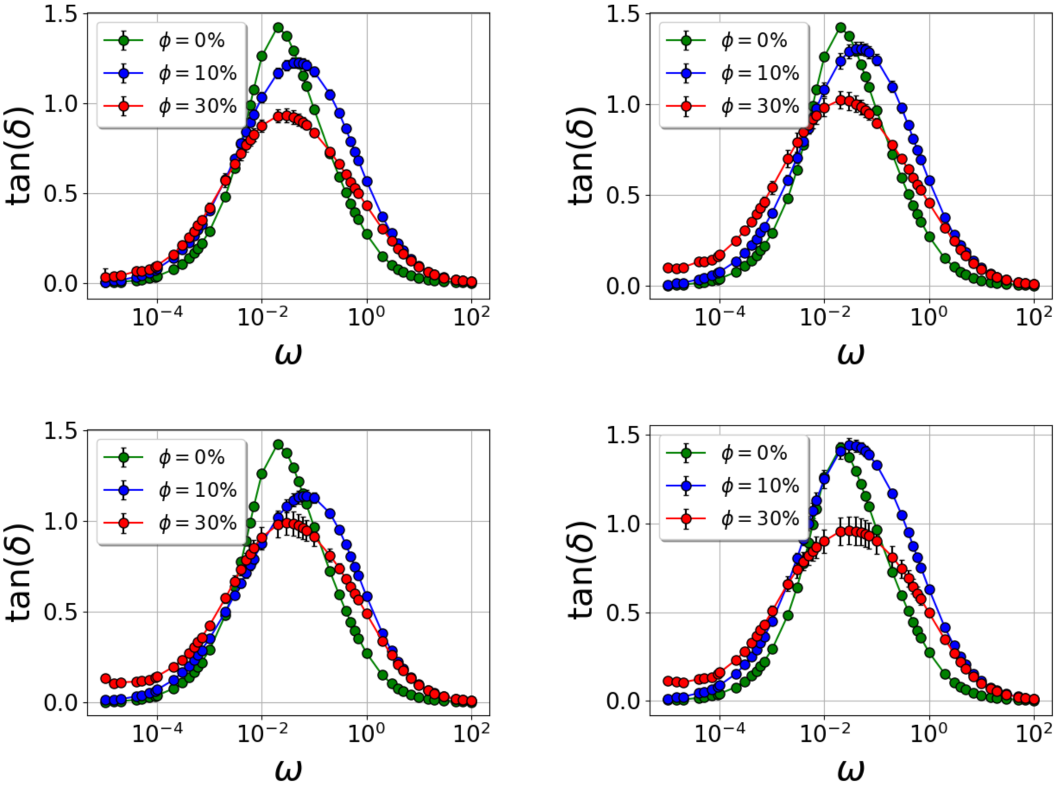

Figure 5.17: The loss tangent vs. frequency ω for filled NR systems with different filler dispersions and filler contents. $k_{PF} = 0.1$, $k_{FF} = 10$, $\gamma_f^d = 20 \text{ mJ/m}^2$. Top left panel: $u_0 = 1\%$, in all other panels $u_0 = 2\%$. In addition, top row: $\gamma_f^p = 0 \text{ mJ/m}^2$, bottom left: $\gamma_f^p = 10 \text{ mJ/m}^2$, bottom right: $\gamma_f^p = 20 \text{ mJ/m}^2$.

frequency at the peak and the relaxation time $\tau_2 = \eta/\mu_2$ (see also Section 2.4.1). In our model, friction is introduced via the friction coefficient γ, and the force constants are analogous to μ_2. The relaxation time in the model can be calculated via $\tau = \gamma/k$. If two significantly different force constants are combined with a single value of the friction coefficient, then two different values of the relaxation time are possible, which correspond to the two $\tan\delta$ peaks. On the one hand, the second peak was not present when $k_{FF} = k_{PF} = 1.0$. In this case, the relaxation time for filler nodes $\tau_F = \gamma/k_{FF}$ is 1. On the other hand, changes in the force constants involving filler do not affect the relaxation time in the polymer phase $\tau_P = \gamma/k_{PP}$ because k_{PP} remains the same. Hence, we require an additional friction coefficient for filler nodes, which changes the relaxation time in the polymer-filler interface. If $k_{FF} = 10$ and the filler friction coefficient $\gamma_F \approx 10$, the relaxation time in the filler phase is close to 1. On the right-hand side of Fig. 5.14, the loss tangents vs. ω for different filler contents are shown, when $k_{FF} = 10$, $k_{PF} = 0.1$ and $\gamma_F = 15$. All other simulation parameters are the same as above. Using the new parameter set increases the attendant peak heights for filled systems and shifts the peak positions to higher frequencies, but suppresses the second peak.

To study the effect of γ_F on the system's dynamics, we consider the respective

Table 5.5: Compilation of polymer-filler and filler-filler force constants and bond breaking distances.

Parameter	Symbol	Value	Comments
polymer - filler	k_{PF}	0.1	spring constant at P-F interface
	$k_{PF,weak}$	10^{-4}	spring constant after break
filler - filler	k_{FF}	10.0	spring constant at F-F interface
bond breaking	R_{PF}	$1.01\, r_{ij,o}$	P-F bond breaking separation
bond breaking	R_{FF}	$1.01\, r_{ij,o}$	F-F bond breaking separation
friction, NR	γ_F, NR	15	friction for filler nodes in NR systems
friction, SBR	γ_F, SBR	10^4	friction for filler nodes in SBR systems
friction	γ	1.0	friction for polymer nodes

relaxation time in each interface. In the polymer-polymer interface, we define the relaxation time as $\tau_P = \gamma/k_> = 0.1$. This relaxation time remains the same if we change k_{FF} and k_{PF}. In the filler-filler interface, the relaxation time $\tau_F \approx 1$, and it also doesn't change significantly. In the polymer-filler interface, when $k_{FF} = k_{PF} = 1$, the relaxation time $\tau_{PF} = \gamma/k_{PF} = 1$. If $k_{PF} = 0.1$ and $\gamma_F = 15$, then $\tau_{PF} = \gamma_F/k_{PF} \approx 100$. The different interfaces in the system together with the respective relaxation times are illustrated in Fig. 5.15. The previous set of force constants does not reflect the relaxation time in the polymer-filler interface, which is extremely long. In experimental systems, there exists a similar effect of the 'glassy layer'[2]. In this layer, the polymer in the direct vicinity of the filler surface has much less mobility and slower dynamics than in the bulk. Therefore, in order to obtain the behaviour of the mechanical moduli vs. filler volume content in good accord with experiments, we require an additional parameter increasing the relaxation time in the polymer-filler interface.

In the bottom right panel of Fig. 5.12, the simulated loss tangent as a function of filler volume content is shown, when $k_{FF} = 10$, $k_{PF} = 0.1$ and $\gamma_F = 15$. At low frequencies, the loss tangent increases with the filler content, in good qualitative agreement with the experiment. At high frequencies, $\tan\delta$ remains constant as the filler content approaches the percolation threshold and then drops. A comparison between the two sets of force constants in terms of the storage and loss moduli is presented in Fig. 5.16. The simulated systems are the same as in the top row of Fig. 5.13. On the left-hand side, the moduli correspond to $k_{FF} = k_{PF} = 1$. On the right-hand side, $k_{FF} = 10$, $k_{PF} = 0.1$ and $\gamma_F = 15$. The comparison shows that the storage modulus in the right panel of Fig. 5.16 is smaller, but the loss modulus is larger and exhibits a similar increase as the storage modulus for filler concentrations beyond the percolation threshold. This is not observed in the plots on the left. In both cases, the moduli for systems with different filler morphologies increase, except for $\gamma_f^p = 5$ mJ/m^2, which even drops in the left panel. The attendant TEM image for this system looks homogeneous with no filler agglomerates, which results in the

---

[2] The concept of the 'glassy layer' is also discussed in Section 2.2.

smaller loss modulus than for other systems, where filler flocculation takes place.

Notice, that in experimental systems at high temperatures (low frequencies) the order of the curves for systems with different filler contents is opposite to the one observed at the peak (see also the right panel of Fig. 5.9). Initially, when k_{FF} = k_{PF} = 1, the order of the curves at the peak is the same as at low frequencies, as shown in the left panel of Fig. 5.9. Changing the force constants values to k_{FF} = 10 and k_{PF} does not produce the loss tangent curves with the required order as well (see the left panel of Fig. 5.14). But introducing the new parameter γ_F allows to obtain the order of the loss tangent curves at low frequencies according to the experimental findings (the right panel of Fig. 5.14). Fig. 5.17 shows the loss tangent curves as functions of frequency ω for NR filled systems with different filler dispersions. The dispersive part of the filler surface energy is the same and equal to 20 mJ/m^2. In the top row γ_f^p = 0 mJ/m^2, in the bottom left panel γ_f^p = 10 mJ/m^2 and in the bottom right panel γ_f^p = 20 mJ/m^2. In addition, in the top left panel u_0 = 1% and in the rest of the panels u_0 = 2%. Changing the strain amplitude increases the loss tangent of the filled systems because, contrary to unfilled polymers, both the storage and the loss moduli are not constant due to the Payne effect. Nevertheless, the order of the curves in the range of low frequencies is opposite to the one observed at the peak for all presented systems. As discussed above, γ_F increases the relaxation time in the polymer-filler interface, and this effect is similar to a formation of 'glassy layers' in experimental systems. Based on the simulation results, the order of experimental loss tangent curves in the low frequency range, obtained for different filler concentrations, is governed by the relaxation time in the polymer-filler interface, which is extremely long. An increasing filler volume content ensures a large number of such interfaces in the system, which shifts above the respective $\tan\delta$ curve at low frequencies.

The values of k_{PF}, k_{FF} and γ_F for SBR filled systems were obtained based on the aforementioned approach. It was found that the same values of k_{FF} and k_{PF} can be used to provide a similar increase of μ' vs. ϕ. The value of γ_F, however, is significantly larger and close to 10^4. This is due to the difference in the respective $\tan\delta$ peak positions of pure polymers, where the experimental peak position of SBR is shifted to lower frequencies by 2 orders of magnitude in comparison to NR. This yields the respective relaxation time for SBR to be about 2 orders larger.

The final values of force constants, bond breaking distances and friction coefficients for filled systems are compiled in Table 5.5. All the simulation parameters used in both parts of the model, i.e., the MG and DMA, are collected in a table in Appendix C.

Chapter 6

Mechanical Properties of Filled Elastomers – Filled One Polymer Systems

In this chapter, mechanical properties of filled one polymer systems will be discussed. We will study how the mechanical properties depend on filler dispersion based on systems consisting of one polymer and one filler. Additionally, we will explore the effects of the filler volume content and the flocculation time on the dynamic moduli. The second part of this chapter is devoted to the polymer-filler interaction. We will discuss how the polymer-filler force constant k_{PF} can be tied to the polymer-filler interface tension γ_{pf}. This idea is illustrated by an example of the most commonly used fillers in the tire industry – carbon black and silica. We will look at the dispersion of these fillers in natural rubber and its impact on the dynamic moduli and relaxation processes.

6.1 Filler Morphology – Impact of Filler Surface Energy on Filler Dispersion

We start the discussion with the application of the MG algorithm to systems consisting of either NR or SBR plus filler. The morphology generation was performed in 20% filled systems, where the polymer surface tensions were fixed and the filler surface energy was varied. The obtained morphologies are shown in Fig. 6.1 for NR filled systems and in Fig. 6.2 for SBR filled systems. NR nodes are shown in green colour, SBR nodes – in yellow colour, while filler nodes are black. Note that for a better comparison between different cases, the morphologies in Figs. 6.1 – 6.2 show the respective systems after 1000 MC steps per node on average. For the calculation of dynamic moduli, however, the systems after 50 MC steps per node on average were used. In the top row of Figs. 6.1 and 6.2, the attendant wetting-envelope – work of adhesion plots are presented. Each morphology below the plot corresponds to a dot with the same number in the respective plot. As pointed out Section in 3.2.1, each loop corresponds to a constant value of ΔW_a, where ΔW_a is the main driving force for the filler agglomeration process. The curves labelled with

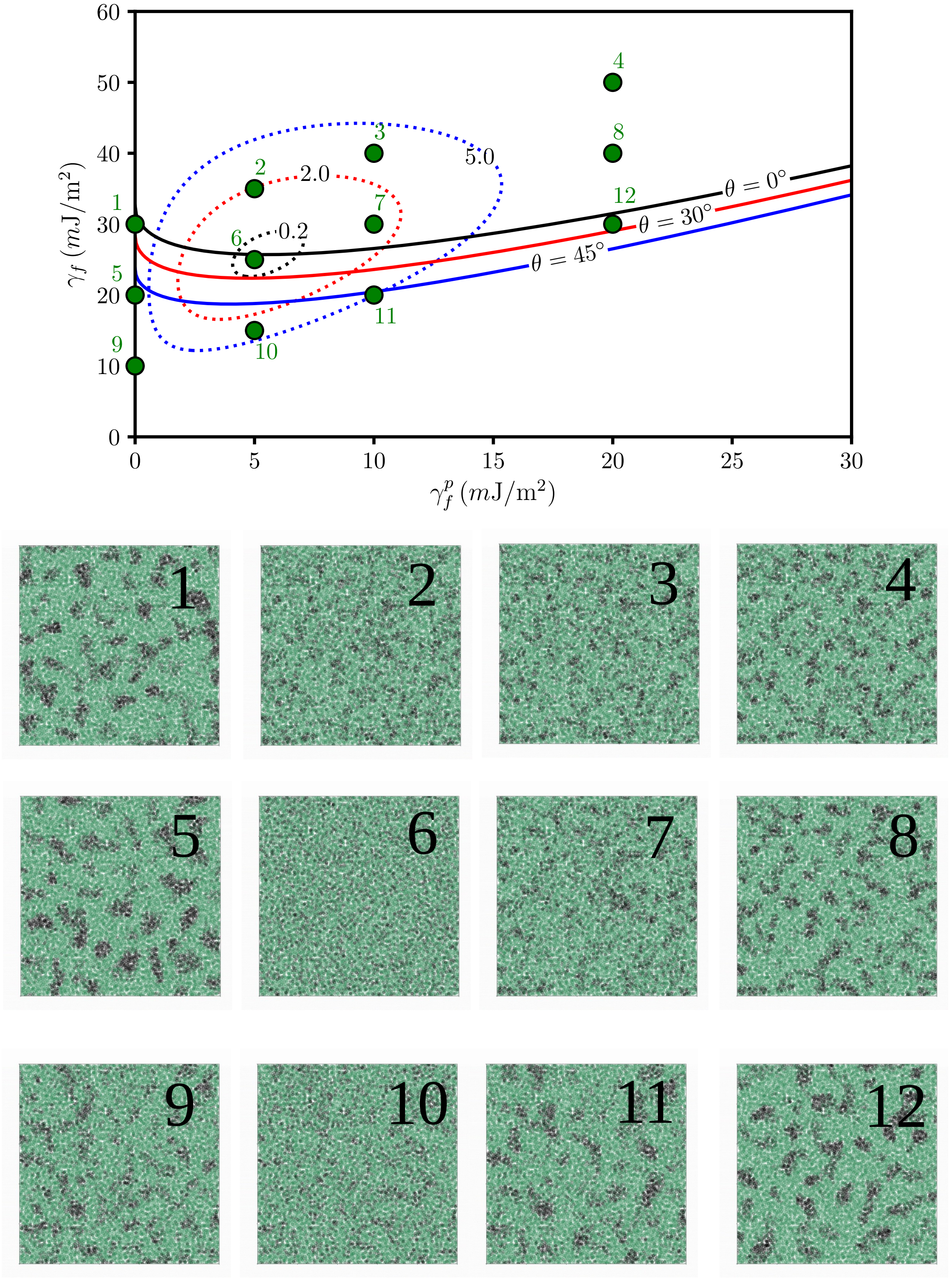

Figure 6.1: Top: the wetting-envelope – work of adhesion plot for NR filled systems characterized by different filler surface energy values. Bottom: TEM images corresponding to the systems shown as dots in the top plot.

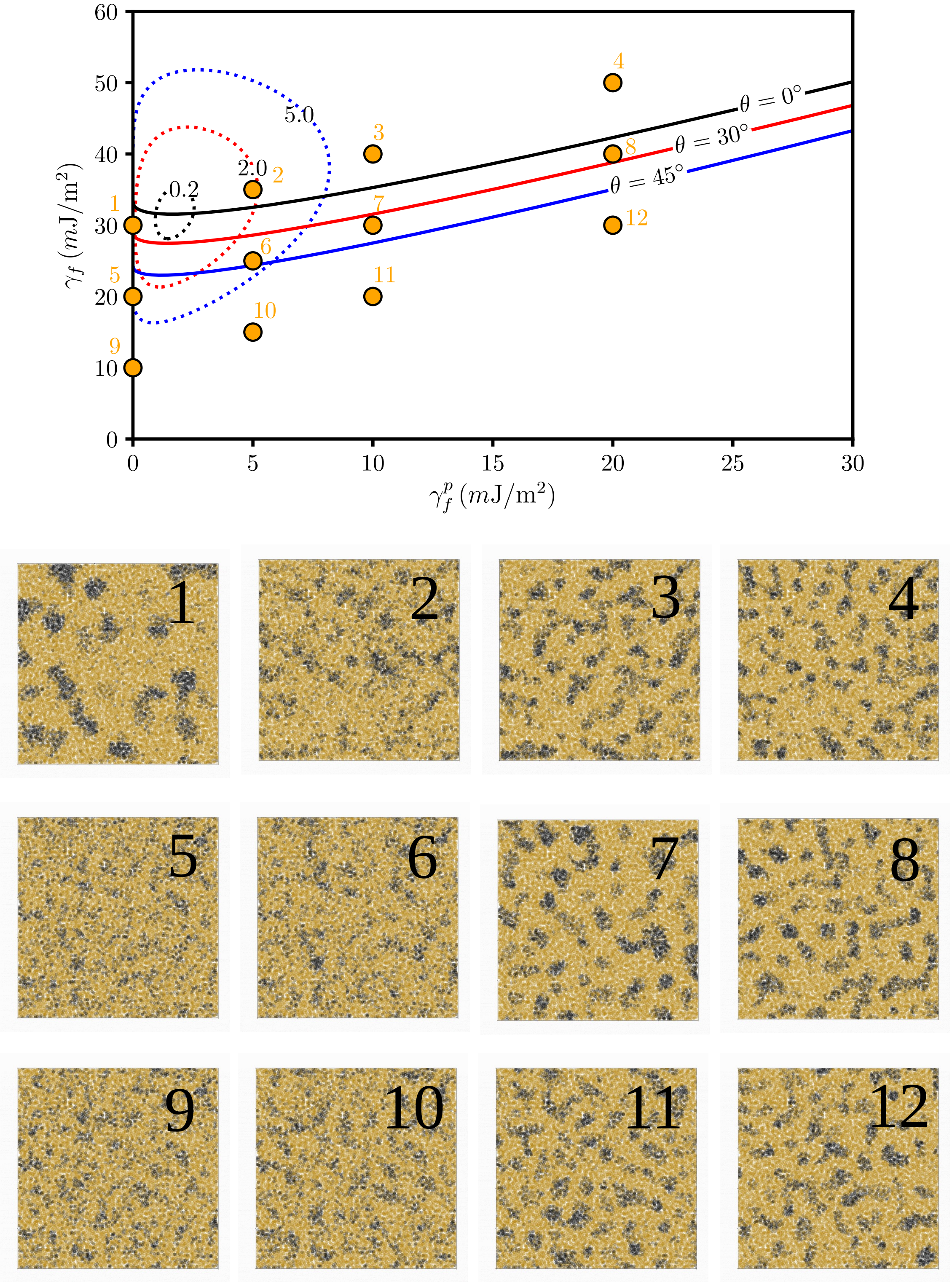

Figure 6.2: Top: the wetting-envelope – work of adhesion plot for SBR filled systems characterized by different filler surface energy values. Bottom: TEM images corresponding to the systems shown as dots in the top plot.

θ are obtained for a constant value of the contact angle. These loops and curves are drawn based on the solution of Eq. (3.5), therefore, depending on the polymer surface energy, they can look quite differently. The loops for SBR are shifted to $\gamma_p = 0$ mJ/m^2, and the curves with the same value of the contact angle are higher than for NR. For both polymers, a general trend for a filler during flocculation is similar, i.e., the largest filler agglomerates are observed for systems outside the largest loop, for instance systems Nrs. 1, 5 and 12 in Fig. 6.1 and systems 1 and 7 in Fig. 6.2. The system Nr. 6 in Fig. 6.1, which is inside the central loop in terms of its surface energy value, possesses the finest morphology. This overlap between the wetting-envelope – work of adhesion plots and the obtained filler morphologies shows how filler flocculation and wetting can be predicted based on the values of the polymer and the filler surface tensions.

6.2 Mechanical Properties – Impact of Filler Morphology on System's Dynamics

Next, we study the mechanical properties of the aforementioned filled systems. As an example, we consider filled NR systems and look at μ', μ'' and $\tan\delta$ as functions of different parameters. One of the most interesting questions in this context is how the filler morphology, defined via the filler surface energy and the polymer surface tension, affects the dynamic moduli of composites. In addition, we will study the effect of the filler content variation on the system's dynamics. Based on Fig. 5.17, we can select particular frequencies and strain amplitudes for studying the mechanical properties. One of the frequencies we use is $\omega = 0.001$, taken from the low frequency side of the $\tan\delta$ peak (or high temperature side due to the time-temperature superposition). These low frequencies/high temperatures would correspond to the normal working conditions of a tire and can be tied to rolling resistance. Ideally, the frequency should be still smaller, but this is not practical, since the computational time becomes prohibitively long. Thus, $\omega = 0.001$ is a compromise. Another frequency we consider is $\omega = 0.1$ because it is roughly where the $\tan\delta$ peak is – thus, this value is extremely useful for comparing and for getting information on wet grip. The strain amplitude u_0 in experiments can vary between 0.1 and 5%; in this work, most of the results are obtained at the intermediate strain $u_0 = 1\%$.

Note that the parameters for the polymer-filler and filler-filler interactions, used for the DMA simulations in this chapter, are compiled in Table 5.5.

6.2.1 Effect of Filler Surface Energy

The surface energy is a sum of two components, i.e., the dispersive part and the polar part, and both of them can be varied. Either, we can keep the dispersive part of the filler surface energy fixed and vary the polar part. Or we can as well keep the polar part constant and change the dispersive part. Based on the wetting-envelope – work of adhesion plot, these changes would correspond to moving parallel to $y = \gamma_f^d + \gamma_f^p$, where γ_f^d is constant, in the first case, or parallel to the y-axis in the second case. In both cases, we can tie the variations of filler morphology to the respective changes of μ', μ'' or $\tan\delta$.

The pink parallelogram in the top panel of Fig. 6.3 defines a set of systems, where γ_f^d is kept constant and equal to 20 mJ/m^2 and γ_f^p is varied between 0 and 20 mJ/m^2. The panels below show the attendant storage moduli, loss moduli and $\tan\delta$ (from top to bottom). On the left-hand side, the strain amplitude u_0 is varied, while on the right-hand side – the simulation frequency ω. The systems are characterized by the value of the polar part of the filler surface energy given in the plot legend. Note that all systems under study exhibit the Payne effect for both moduli. The onset of the Payne effect for the storage moduli starts at ≈ 1-2% strain, whereas for the loss modulus the onset is shifted to larger strains ≈ 3-4%. In addition, a drop in the loss modulus at small strain amplitudes can be observed, which is typical for experimental systems (see Fig. 2.18) and can be well reproduced by the model.

The results for the dynamic moduli can be compared with the respective filler morphologies presented in Fig. 6.1 (systems Nrs. 5-8). The filler Nr. 6 is inside the central ΔW_a-loop, and the respective system has the finest dispersion. In other systems, filler agglomerates are present, with the largest agglomerate size for the system Nr. 5 and the smallest – for the system 7. In terms of mechanical properties, the most dispersed system Nr. 6 yields the lowest dynamic moduli and $\tan\delta$. This is also reasonable from the experimental point of view, where large dynamic moduli are typically observed for highly flocculated systems (see, for instance, [125]). The fillers 5 and 8 are both outside the largest ΔW_a-loop, however the filler Nr. 8 is wetted by the polymer, while the wetting between the filler Nr. 5 and NR is low. In simulations, the system Nr. 8 exhibits the largest moduli and $\tan\delta$ plotted vs. frequency, while the largest filler agglomerates are found in the system Nr. 5. Note, that the respective loss tangent values increase for systems with a higher tendency for the filler to flocculate. In addition, the peak of the loss tangent plotted vs. frequency is shifted to higher frequencies, when the filler dispersion becomes more homogeneous. The dynamic moduli as functions of strain amplitude for different systems are close to each other and even overlap. The main reason for this subtle difference is the force constant values which are the same for all described systems. So far, the only difference between the aforementioned systems is in the filler distribution inside the polymer matrix. An extension of the model, introducing the polymer-filler spring constant being proportional to the interface tension between polymer and filler, will be discussed later in this chapter.

In Fig. 6.4 μ', μ'' and $\tan\delta$ are shown, where γ_f^d is varied between 10 and 30 mJ/m^2, and γ_f^p is fixed and equal to 10 mJ/m^2. The systems are filled with 20% filler and correspond to panels 3, 7 and 11 in Fig. 6.1. According to Fig. 6.1, the fillers Nrs. 3 and 7 are perfectly wetted by the polymer, whereas for the system 11 the wetting is poor due to the contact angle value $\theta = 45°$. In addition, the dot corresponding to the filler Nr. 7 is in the middle ΔW_a-loop, and the other two systems are inside the largest loop. In terms of mechanical properties, the system Nr. 11 can be characterized by the lowest values of the dynamic moduli. The other two systems, however, exhibit very close storage and loss moduli. Therefore, the loss tangent, as their ratio, hardly changes for different dispersive components of the filler surface energy. Overall, comparing systems with different γ_f^d and γ_f^p shows

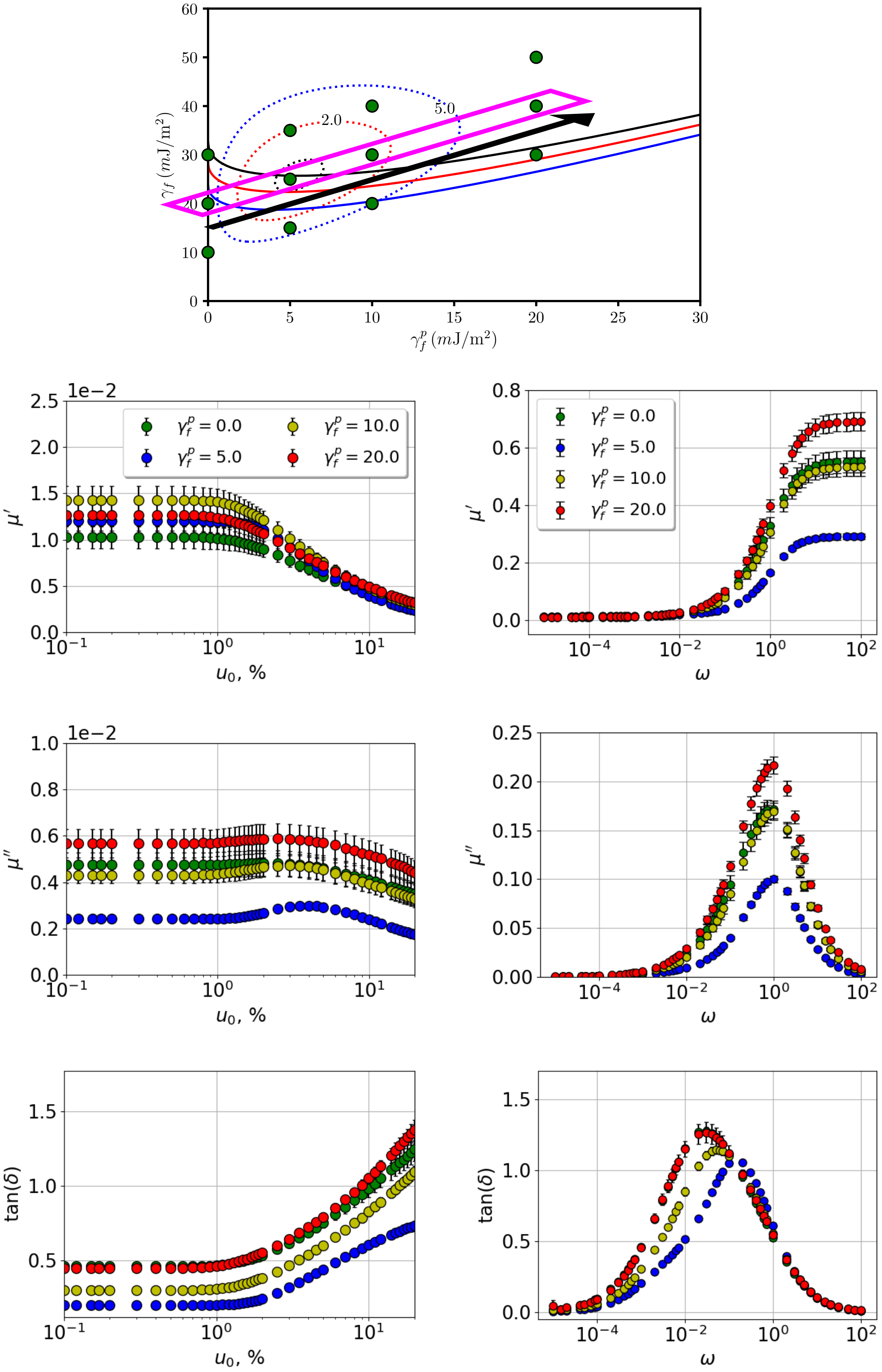

Figure 6.3: Top: variation of γ_f^p at $\gamma_f^d = 20$ mJ/m^2 (pink parallelogram) in the wetting-envelope – work of adhesion plot for NR filled systems. Bottom: the respective μ' (top row), μ'' (middle row) and $\tan\delta$ (bottom row) as functions of strain amplitude u_0 at $\omega = 0.001$ (left) or as functions of frequency ω at $u_0 = 1\%$ (right). The filler content ϕ is 20%.

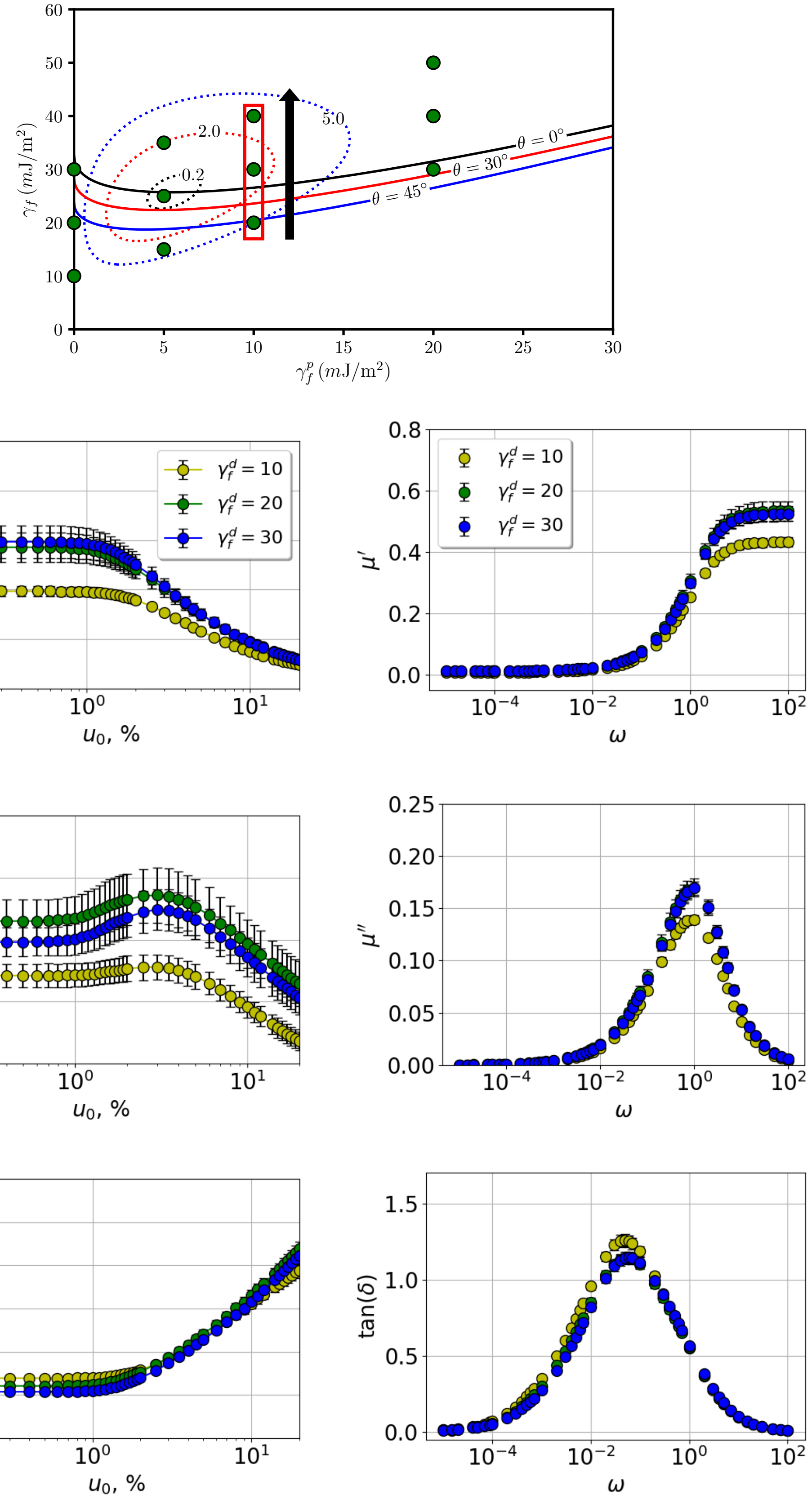

Figure 6.4: Top: variation of γ_f^d at $\gamma_f^p = 10\ \mathrm{mJ/m^2}$ (red box) in the wetting-envelope – work of adhesion plot for NR filled systems. Bottom: the respective μ' (top row), μ'' (middle row) and $\tan\delta$ (bottom row) as functions of strain amplitude u_0 at $\omega = 0.001$ (left) or as functions of frequency ω at $u_0 = 1\%$ (right). The filler content ϕ is 20%.

that both components of the filler surface energy can affect filler dispersion in the polymer. The effect of the filler type, which determines the filler polarity and thus γ_f^p, on the mechanical properties of filled systems was found to be considerably stronger than the impact of the particle size, which is related to γ_f^d.

6.2.2 Effect of Filler Volume Content

Experimental dynamic moduli increase with the filler volume content (see Figs. 2.15 and 2.18). Therefore, in simulations we can expect an increase of the dynamic moduli at higher filler contents. In Figs. 6.5 and 6.6, the dynamic moduli and the loss tangent are shown for a set of systems with different filler concentrations, i.e., 10, 20 and 25%. As we have already shown, filler dispersion strongly depends on the interface tension between polymer and filler. In Fig. 6.5 $\gamma_f^p = 5$ mJ/m^2, and this value corresponds to the system Nr. 6 in Fig. 6.1, which has the most homogeneous dispersion. Fig. 6.6 is obtained for the system with $\gamma_f^p = 20$ mJ/m^2, and this coincides with the system Nr. 8 in Fig. 6.1. It can be seen that the dynamic moduli for both systems increase with the filler volume content. As discussed in the previous section, the more dispersed system has smaller values of the moduli at the same filler content. The difference in the storage and loss moduli between various filler contents is also less for this system. The behaviour of the loss tangent is more complex. Generally, for the $\tan\delta$ as a function of strain amplitude, one can distinguish between two main regions. At strains $\leq 2\%$, the loss tangents for different filler concentrations are the same in the case of Fig. 6.6. For the system 6, $\tan\delta$ drops with the increasing filler content. The order of the curves then changes at strain amplitudes above 2% and becomes the same for both systems. In this region, the damping rises with the amount of filler in the system.

The simulated loss tangent as a function of frequency demonstrates several important properties. The most essential is that the dependence of $\tan\delta$ on the filler concentration is different with respect to filler dispersion. For the most dispersed system Nr. 6, the loss tangent at the peak rises with the filler content, and at lower frequencies the order of the curves is opposite to the one observed at the peak. The system with 10% filler exhibits a broader peak than the others, and the peak position is shifted to low frequencies. This is not observed for the system Nr. 8. Here the $\tan\delta$ value at the peak decreases with the increasing filler content, the order of the curves does not change and the peaks have similar widths. Overall, the loss tangent is a more complex value than the dynamic moduli. While the model can qualitatively predict the behaviour of the storage and loss moduli when varying the filler concentrations, it cannot simulate the changes in the loss tangent for all possible filler dispersions.

6.3 Effect of Flocculation Time

It is well known that during the filler flocculation the storage modulus of a filled rubber increases. As discussed in Section 2.6, the main reason for this increase is a formation of the filler network. In the left panel of Fig. 2.17, an example of flocculation curves is shown, where the change in the storage modulus is monitored as

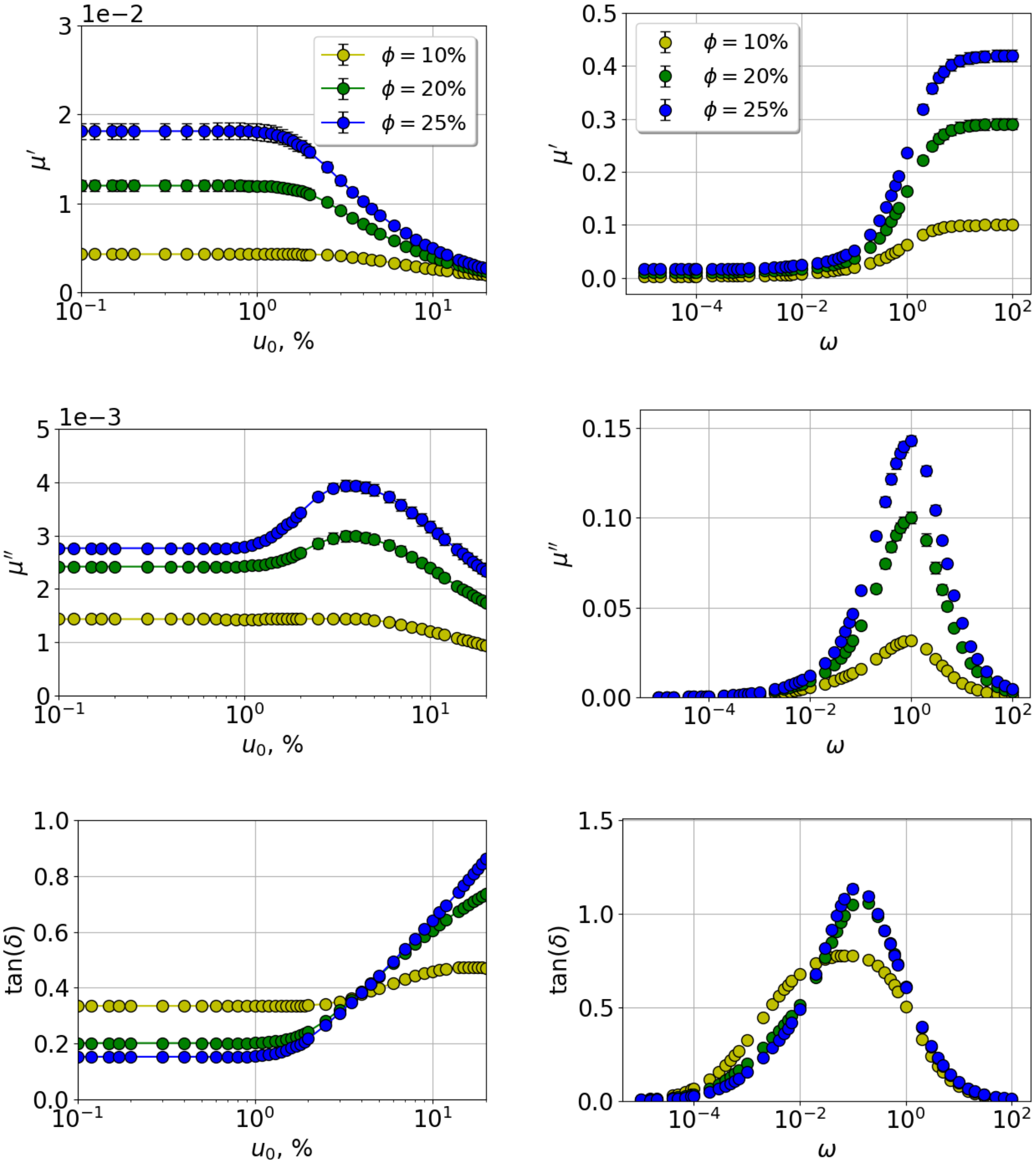

Figure 6.5: The μ' (top), μ'' (middle) and $\tan\delta$ (bottom) as functions of strain amplitude u_0 at $\omega = 0.001$ (left) or as functions of frequency ω at $u_0 = 1\%$ (right). The system corresponds to Nr. 6 in Fig. 6.1 ($\gamma_f^d = 20$ mJ/m^2, $\gamma_f^d = 5$ mJ/m^2), the filler content is varied and given in the legend.

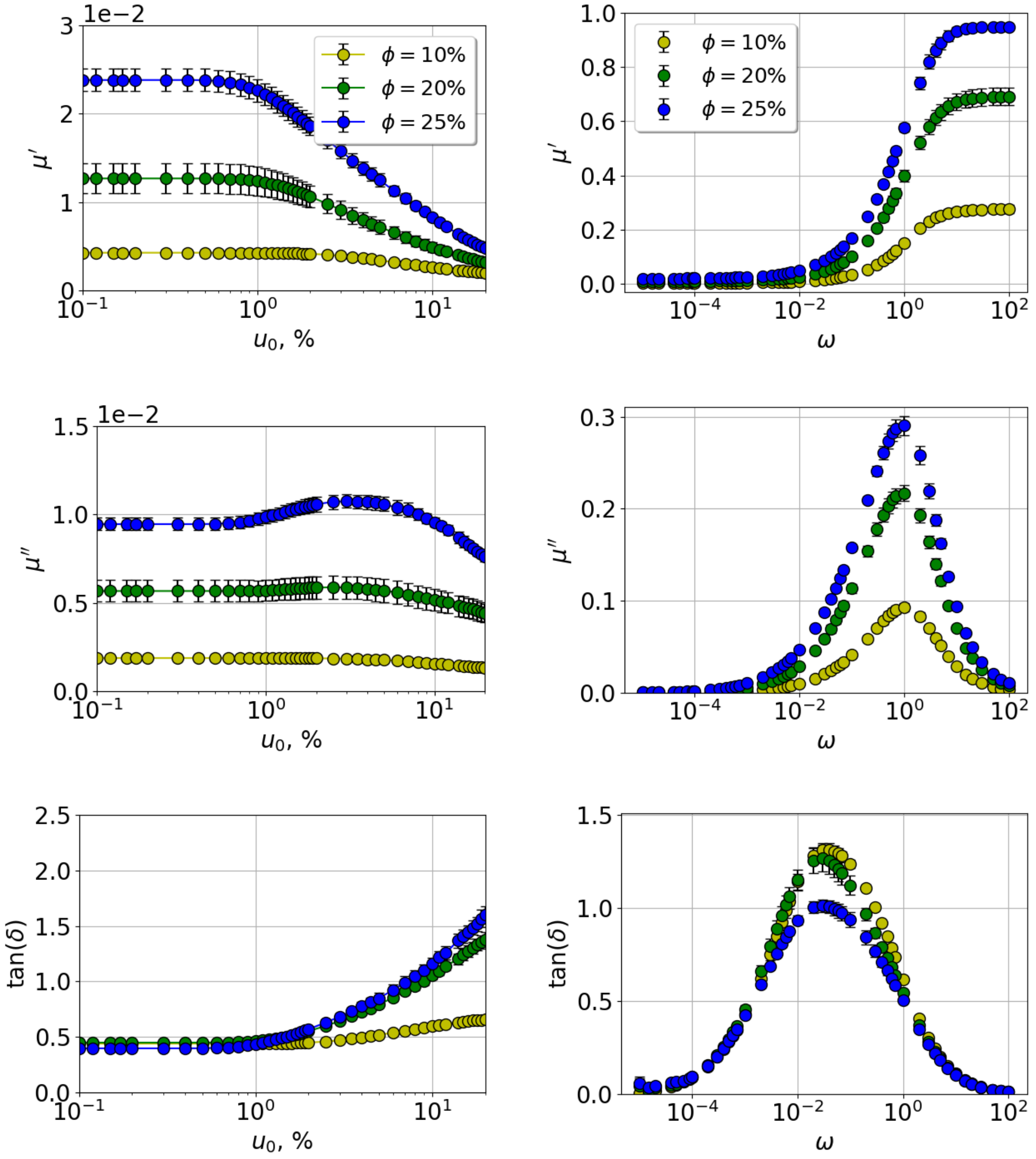

Figure 6.6: The μ' (top), μ'' (middle) and $\tan\delta$ (bottom) as functions of strain amplitude u_0 at $\omega = 0.001$ (left) or as functions of frequency ω at $u_0 = 1\%$ (right). The system corresponds to Nr. 8 in Fig. 6.1 ($\gamma_f^d = 20$ mJ/m^2, $\gamma_f^d = 20$ mJ/m^2), the filler content is varied and given in the legend.

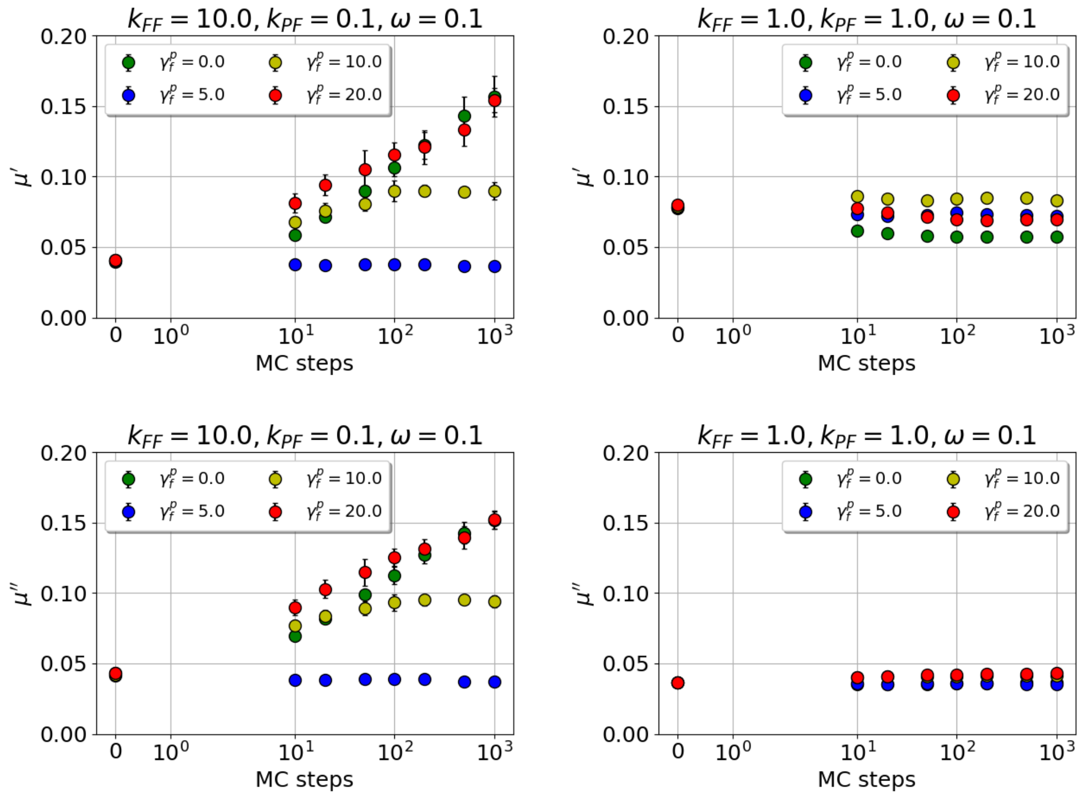

Figure 6.7: The μ' and μ'' vs. the number of MC steps per node on average for filled NR systems, where $\gamma_f^d = 20$ mJ/m^2 and γ_f^p is varied between 0 and 20 mJ/m^2. The strain amplitude u_0 is 1%, the frequency ω is 0.1. Left: $k_{FF} = 10$, $k_{PF} = 0.1$, $\gamma_F = 15$; right: $k_{FF} = k_{PF} = 1$.

a function of time. In experiments, such flocculation tests are frequently combined with the Payne effect measurements. Initially, the storage modulus, measured at different strain amplitudes, produces a typical Payne effect-curve. Then the strain is increased to large values, up to several hundreds percent, to ensure a complete breakdown of the filler network. After the external strain reduces, the filler network forms again, and the storage modulus at a small strain amplitude plotted vs. time yields a flocculation curve.

In our model, the filler flocculation is simulated by the morphology generator, and the number of MC steps can serve as a rough measure of time. Therefore, we can expect a dependence of the simulated dynamic moduli on the number of MC steps. In Fig 6.7 the simulated storage and loss moduli are presented as functions of the number of MC steps. The simulation frequency ω is the same in all panels and equal to 0.1. On the right-hand side $k_{FF} = 10.0$ and $k_{PF} = 0.1$, while on the left-hand side the force constants for the filler-filler and polymer-filler interactions are the same, i.e., $k_{FF} = k_{PF} = 1.0$. The systems have the same $\gamma_f^d = 20$ mJ/m^2 but different γ_f^p (between 0 and 20 mJ/m^2) and correspond to panels 5-8 in Fig. 6.1. How the dynamic moduli change with time strongly depends on the filler dispersion and the values of the force constants. The moduli do not change considerably with the number of MC steps, when $k_{FF} = k_{PF} = 1$. For the system Nr. 5 the storage modulus even drops. On the other hand, when the difference between the filler-filler and polymer-filler couplings is substantial, both moduli increase. The curves on the left-hand side of Fig.6.7 look similar to the experimental flocculation curves presented in Fig. 2.17. The only system that does not exhibit the moduli increase is the system Nr. 6 with $\gamma_f^p = 5$ mJ/m^2. This system has the most homogeneous dispersion, with no filler network being formed during the MC simulation. Consequently, the simulation time has no effect on μ' and μ''. It is worth mentioning that a similar trend is observed when $\omega = 0.001$ (not shown here). While at $k_{FF} = 10$ and $k_{PF} = 0.1$ the moduli depend on the number of MC steps, although differently than at $\omega = 0.1$, at $k_{FF} = k_{PF} = 1$ the loss modulus slightly increases, and the storage modulus drops with the increasing simulation time.

6.4 Polymer-Filler Interaction

This section deals with a discussion on how we can find a relation between the two parts of the model, i.e., the morphology generator and the shear simulation. Remember that in the morphology generation part, we use experimental interface tensions to model the filler flocculation. In the DMA part, the interactions between nodes are described in terms of force constants. The latter are chosen so that the model qualitatively reproduces the main experimental findings such as the Payne effect, a power law increase of μ' vs. ϕ or a drop of the $\tan\delta$ peak height at large filler contents. These force constants so far have no relation to the interface tensions between the components. Hence, using one set of force constants for all fillers ($k_{FF} = 10.0$, $k_{PF} = 0.1$) does not allow to distinguish between them, as shown in the previous section. The main idea discussed in this section is to tie the force constant of the polymer-filler interaction to the interface tension between polymer and filler, in order to make the choice of the force constants more experiment-based.

6.4.1 Force Constants from Surface Free Energies

Consider a mechanical work done by a spring between a polymer and a filler nodes

$$W = \int_{x'}^{x} F dx = \int_{x'}^{x} k_{PF}(x - x_0) dx \sim \frac{1}{2} k_{PF} d^2.$$

Here d is a characteristic distance. We assume that k_{PF} is the value that depends on the surface tensions of the components, while d is not significantly affected by the interface tension between polymer and filler. But how can this dependence look like? There are two main thermodynamic quantities which include the surface tensions – the work of adhesion W_a and the interface tension γ_{pf}. Note that according to the Dupré-Equation (A.6), the two quantities are related to each other, i.e.,

$$W_a = \gamma_f + \gamma_p - \gamma_{pf}.$$

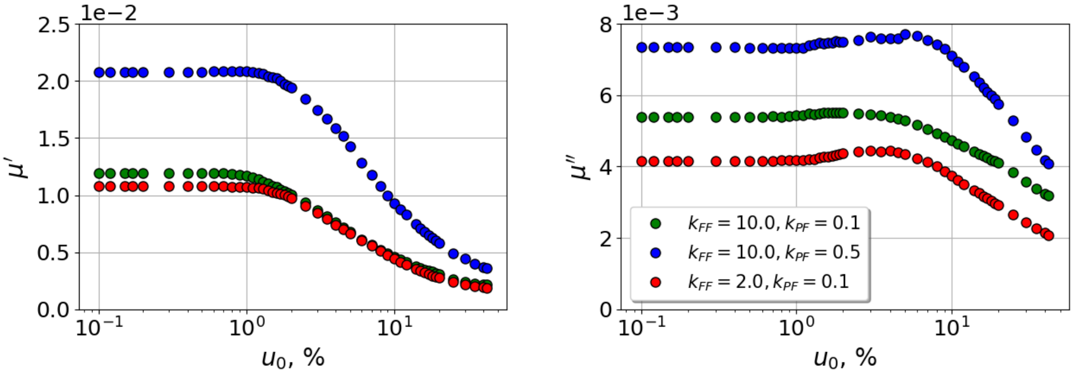

Figure 6.8: The storage (left) and the loss (right) moduli vs. strain amplitude u_0 for filled NR systems with $\phi = 20\%$ and for different combinations of k_{FF} and k_{PF}. The frequency ω is 0.001.

Using the OWRK theory (A.7), we can obtain

$$W_a = 2\left(\sqrt{\gamma_f^d \gamma_p^d} + \sqrt{\gamma_f^p \gamma_p^p}\right)$$

and

$$\gamma_{pf} = \gamma_f + \gamma_p - 2\left(\sqrt{\gamma_f^d \gamma_p^d} + \sqrt{\gamma_f^p \gamma_p^p}\right).$$

Our assumption is that either $k_{PF} \propto W_a$ or $k_{PF} \propto \gamma_{pf}$.

In Fig. 6.8 simulated dynamic moduli are presented for the 20% filled NR system ($\gamma_f^d = 20$ mJ/m^2, $\gamma_f^p = 0$ mJ/m^2) for various combinations of the force constants k_{PF} and k_{FF}. Changing k_{PF} by a factor of five from 0.1 to 0.5 leads to an increase in the storage modulus by a factor of two and in the loss modulus by a factor of 1.5. On the other hand, decreasing k_{FF} by the same factor from 10 to 2 does not affect considerably the storage modulus and results only in a small drop of the loss modulus. If our assumption about the proportionality between k_{PF} and either W_a or γ_{pf} is indeed true, then we can expect the amplitude of the dynamic moduli μ' and μ'' to be governed by W_a (or γ_{pf}). This can be checked based on experimental data combining measurements of the surface energies and the respective dynamic moduli.

At this point, we should briefly remark the following. Consider the storage modulus of a filled system as a sum of two contributions. The first one is due to the bulk polymer and the second is the result of filler networking (see also [39]):

$$\mu' = \mu'_{bulk\,poly} + \Delta\mu'. \tag{6.1}$$

Here $\Delta\mu'$ is the difference between the storage modulus of a filled elastomer at zero strain in comparison to its value at large strain, when the filler network is broken down. Although the first term may include a weak ϕ-dependence due to hydrodynamic reinforcement, the main effect of ϕ is concentrated in the second

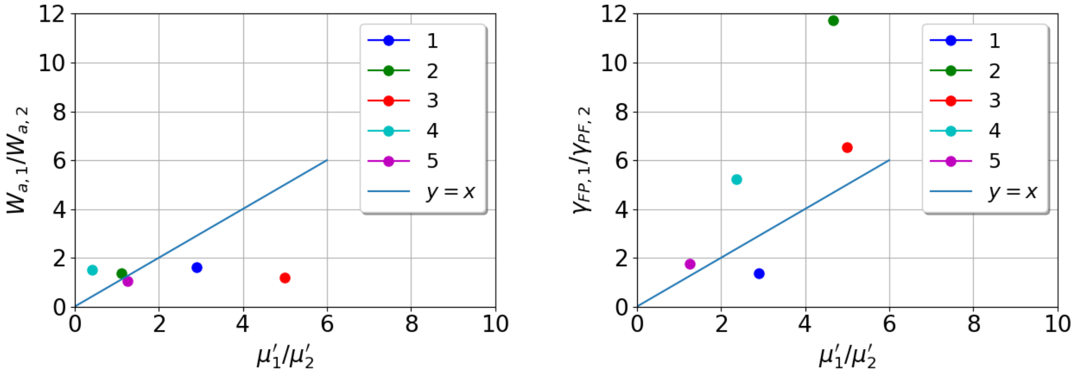

Figure 6.9: Left: the ratio of the works of adhesion vs. the ratio of experimental storage moduli. Right: the ratio of the interface tensions vs. the ratio of experimental storage moduli. The points are based on the data taken from [125] (1), [22] (2), [137] (3), [86] (4), [138] (5).

term and may be expressed as

$$\Delta\mu'(u=0) \sim \frac{\gamma}{R}\left[\frac{\phi}{\phi_c}\right]^Y, \tag{6.2}$$

where u is the strain amplitude, R is the aggregate size, ϕ is the filler volume fraction and ϕ_c is the filler volume content at the percolation threshold. The factor ϕ^Y with $Y \approx 3.5$ describes the structural filler reinforcement based on the notion of a fractal filler distribution in the polymer [7]. If we insert other typical values such as $\phi \approx 2\phi_c$, $\mu' \approx 10^7$ Pa and $R \sim 10^{-8}$ m into (6.2), we obtain for γ the values between 10 to 100 in units of $\mathrm{mJ/m^2}$, which is a typical range for both the interface tension and the work of adhesion. However, as we can see based on (6.2), not only γ may affect the storage modulus, but also R, ϕ, ϕ_c and probably other (unknown) quantities as well. Therefore, when comparing dynamic moduli for different systems, this dependence must also be taken into account.

We have collected experimental data from the literature for measurements of surface energies together with the storage modulus from either DMA or flocculation tests. For each example, we calculated the work of adhesion and the interface tension. Then we found the ratio of the largest and the lowest W_a and γ_{pf} and the ratio of the respective storage moduli. Note that we assume a linear proportionality between $W_a(\gamma_{pf})$ and μ', which implies that $W_a(\gamma_{pf}) = a\mu'$, where a is a constant. If we take two values μ_1' and μ_2' such that $\mu_1' = n\mu_2'$, with a proportionality coefficient n, then

$$W_{a,1} = a\mu_1' = n(a\mu_2') = nW_{a,2}$$

and

$$W_{a,1}/W_{a,2} = \mu_1'/\mu_2' = n. \tag{6.3}$$

The same is true for γ_{pf}. Based on (6.4), we conclude that

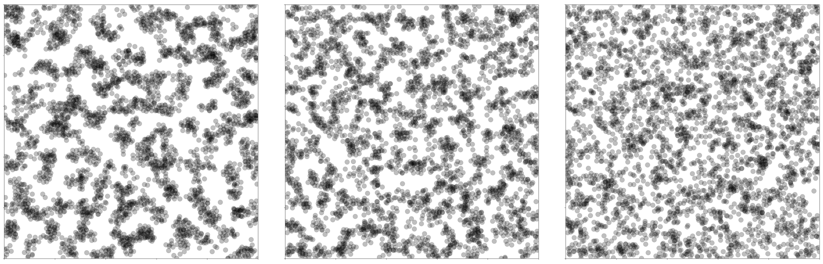

Figure 6.10: Simulated TEM images for filled NR systems. From left to right: CB ($\gamma^d = 30$ mJ/m^2, $\gamma^p = 0$ mJ/m^2), silica ($\gamma^d = 20$ mJ/m^2, $\gamma^p = 16$ mJ/m^2), silanized silica ($\gamma^d = 20$ mJ/m^2 $\gamma^p = 10$ mJ/m^2).

- If (6.4) is valid, the points should lie on the line $y = x$.
- If for different $x = \mu'_1/\mu'_2$ we get the same $y = W_{a,1}/W_{a,2}$, then there is no dependence between μ' and W_a.

In Fig. 6.9 two plots are shown, on the left-hand side a plot of $W_{a,1}/W_{a,2}$ as a function of μ'_1/μ'_2 and on the right-hand side a similar plot but for γ_{pf} instead of W_a. Each point represents one example from the literature. The following list compiles the examples in Fig. 6.9, using the notation of the respective study: Example (1) is Aerosil 200 and Aerosil R974 in EPDM (ethylene propylene diene monomer rubber) from [125]; example (2) Ultrasil VN3 and CB N330 in SBR from Ref. [22]; example (3) is untreated Ultrasil VN3 and Ultrasil VN3 modified with hexadecyltrimethoxysilane (C16) in SBR taken from [137]; example (4) is Ultrasil in two rubbers (S-SBR and M-S-SBR) denoted M0 and M3 from Ref. [86]; example (5) is conductive carbon black (CCB) in NR and carbon nanotubes (CNT) in ENR (epoxidized natural rubber) from Ref. [138]. Based on the left panel, changing μ'_1/μ'_2 does not result in changing of $W_{a,1}/W_{a,2}$, which implies that the storage modulus of the presented systems does not depend on the polymer-filler work of adhesion. Although in the right panel the scatter is considerable, most of the points lie close to the line $y = x$, so we can assume a linear dependence between the storage modulus and the interface tension. As shown in Fig. 6.8, the simulated storage modulus is largely governed by k_{PF}, so

$$k^j_{PF} \propto \gamma_{pf,j}. \tag{6.4}$$

At this point, it is worth mentioning that the dependence between k_{PF} and γ_{pf} is rather qualitative than quantitative because μ' depends on other quantities from (6.2). In order to quantitatively tie the force constants to the storage modulus, the former must include the effect of the aforementioned quantities as well.

6.4.2 Example of Different Fillers

The next step is to check our assumptions via simulation. We model three main types of fillers possessing different polarities, i.e., carbon black, silica and silanized silica, using different values of k_{PF} which are now proportional to γ_{pf}. As a polymer

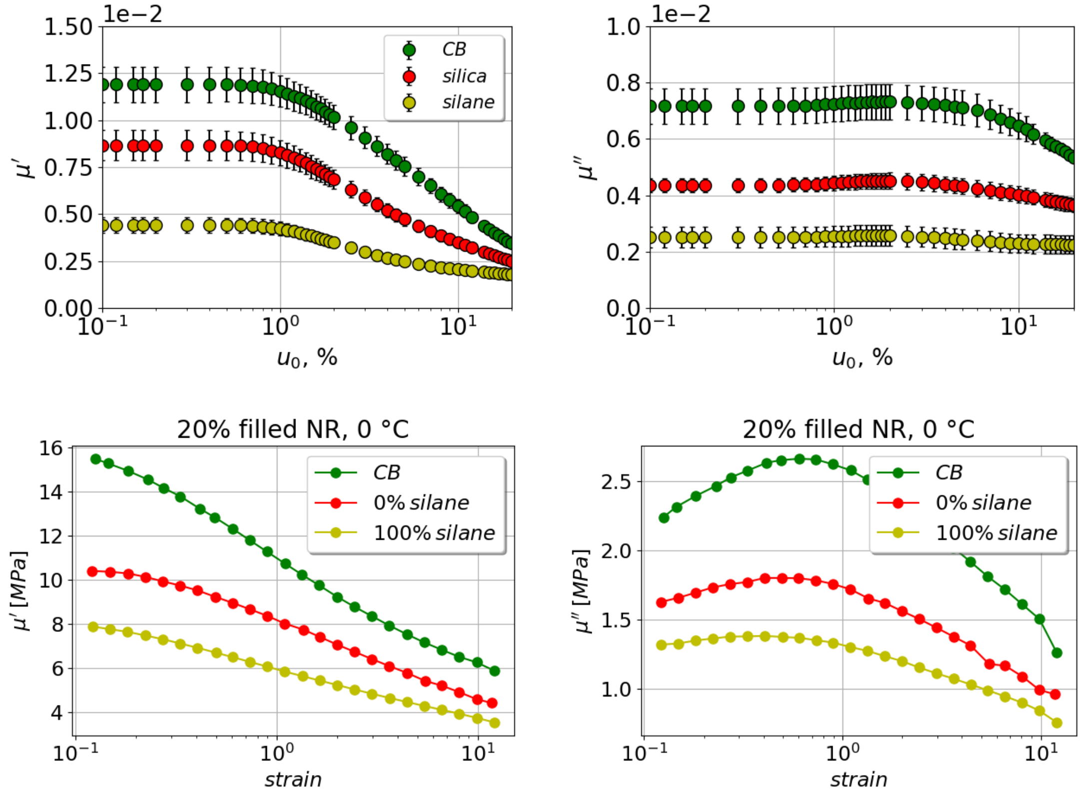

Figure 6.11: Top: the simulated μ' (left) and μ'' (right) vs. strain amplitude u_0 for filled NR systems. The fillers are CB, silica and silanized silica, ϕ is 20% and ω is 0.001. Bottom: the experimental μ' (left) and μ'' (right) vs. strain amplitude for NR filled with 20% CB, silica and silanized silica at 0°C.

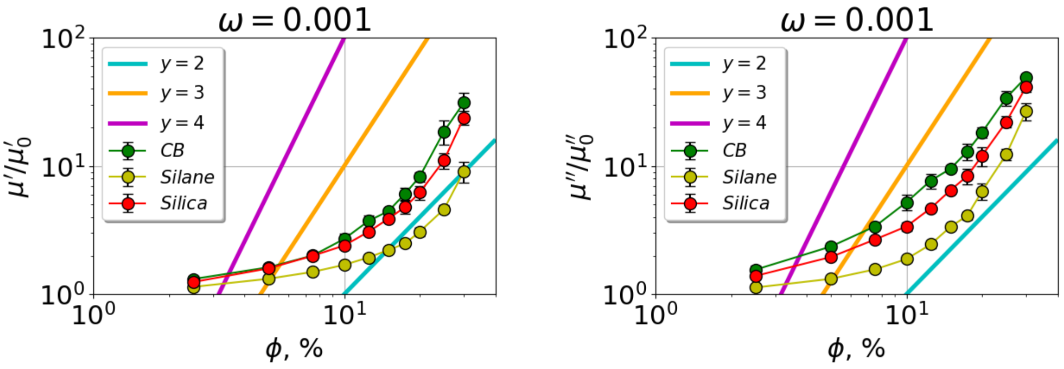

Figure 6.12: The μ' (left) and μ'' (right) vs. filler volume content ϕ for NR filled with CB, silica and silanized silica at $\omega = 0.001$ and $u_0 = 1\%$.

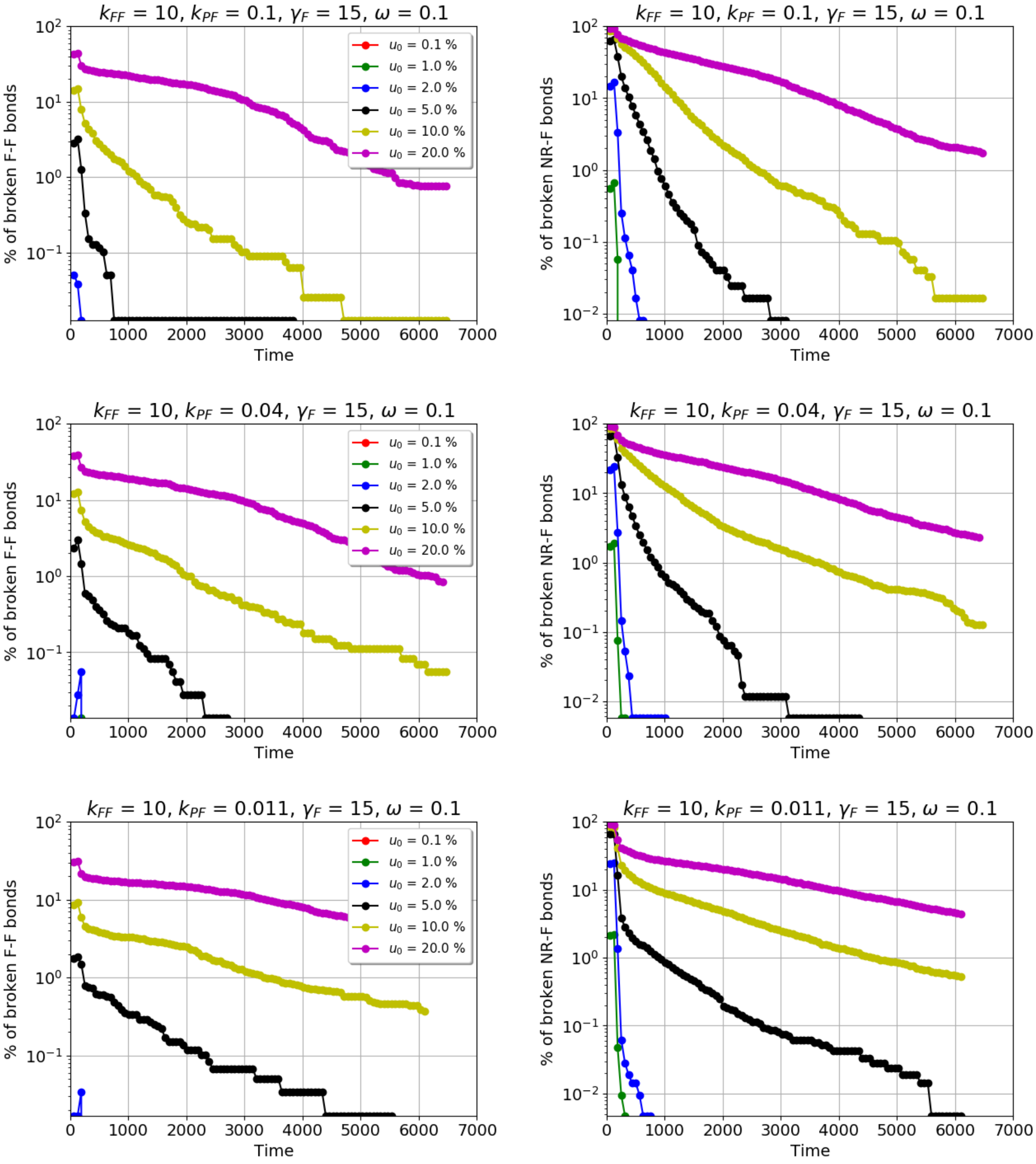

Figure 6.13: The number of reversibly broken bonds vs. simulation time at different strain amplitudes and $\omega = 0.1$. Top: CB ($k_{PF} = 0.1$), middle: silica ($k_{PF} = 0.04$), bottom: silanized silica ($k_{PF} = 0.011$). The left column corresponds to filler-filler bonds, the right column – to polymer-filler bonds.

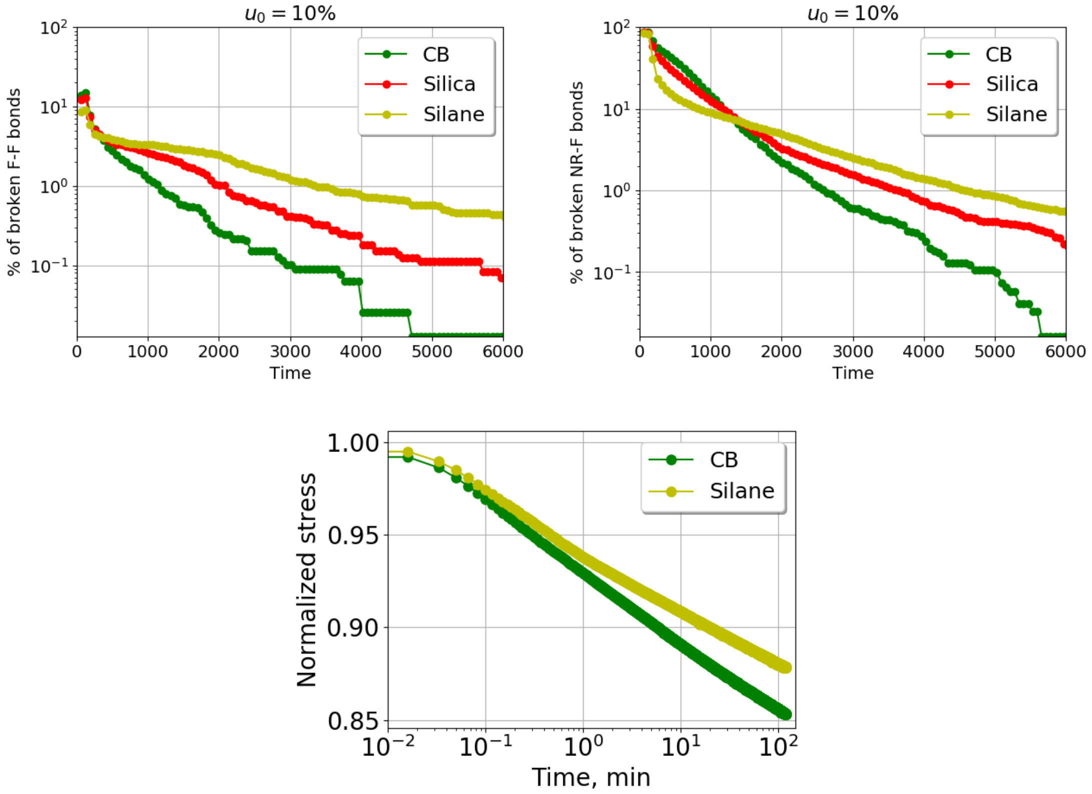

Figure 6.14: Top: the number of reversibly broken bonds vs. simulation time for NR systems with different fillers at $u_0 = 10\%$ and $\omega = 0.1$. The left panel corresponds to filler-filler bonds, the right – to polymer-filler bonds. Bottom: stress relaxation measurements for NR filled with CB and silanized silica.

we continue to use NR with $\gamma^d = 20.24$ mJ/m^2 and $\gamma^p = 5.46$ mJ/m^2. The values of the filler surface energies were taken from [125]. In this study, the authors found for carbon black N234 the dispersive part of the filler surface energy to be around 30 mJ/m^2, whereas the polar part was close to zero. But also CB N121 and N339 possess numerically similar surface free energies, according to Table 1 in the same reference. For silica the authors observed large contact angle hysteresis, so the resulting polar part of the surface tension for Ultrasil VN3 (precipitated silica) and Aerosil 200 (fumed silica) varies significantly for the advancing and receding contact angles (see Table A.1). The average values, however, are close to 20 mJ/m^2 for γ_f^d and 16 mJ/m^2 for γ_f^p [22]. The scatter was also significant for the silanized silica Coupsil 8113. Here we found 20 mJ/m^2 for γ_f^d and 10 mJ/m^2 for γ_f^p to be reasonable. For each pair 'NR-filler' we calculated the work of adhesion and the interface tension. Then we set the force constants k_{PF} to be proportional to the respective interface tensions. The system 'NR-CB' was chosen as a standard, for which $k_{PF} = 0.1$. The remaining k_{PF} were calculated according to Eq. (6.4), such that $k^j_{PF} = k^{NR-CB}_{PF} \frac{\gamma_j}{\gamma_{NR-CB}} = 0.1 \frac{\gamma_j}{\gamma_{NR-CB}}$. The values of W_a, γ_{pf} and k_{PF} are compiled in Table 6.1.

Fig. 6.10 illustrates morphologies obtained for NR systems with the different

Table 6.1: Surface tension, work of adhesion and interface tension values for NR ($\gamma^d = 20.24$ mJ/m^2, $\gamma^p = 5.46$ mJ/m^2) filled with carbon black, silica and silanized silica.

Filler	γ^d [mJ/m^2]	γ^p [mJ/m^2]	W_a	γ_{pf}	k_{PF}
CB	30.0	0.0	49.3	6.4	0.1
Silica	20.0	16.0	58.9	2.8	0.04
Silanized silica	20.0	10.0	55.0	0.7	0.01

fillers. Note that only filler nodes are shown. The frequency is 0.001, $\phi = 0.2$, $k_{FF} = 10$ and $k_{PF} \propto \gamma_{pf}$. In the row 'CB – silica – silanized silica', the agglomerate size decreases and the filler distribution becomes more homogeneous. Notice that the same sequence is obtained for γ_{pf}, i.e., large values of the interface tension promote filler flocculation. The respective dynamic moduli vs. strain amplitude for these systems are shown in Fig. 6.11. Changing k_{PF} leads to a separation between curves for different fillers, and the order of the curves corresponds to the sequence of the interface tension values. Although our initial assumption was made for μ' only, the loss modulus demonstrates the same order of curves, i.e., the dynamic moduli increase with the filler agglomerate size. Hence, (6.4) allows to differentiate fillers with different surface properties. Another example is Fig. 6.12, which shows in the top row the dynamic moduli as functions of filler volume content ϕ at $\omega = 0.001$. In the bottom row, experimental dynamic moduli at 0°C for the same systems are presented. Here we can differentiate the fillers as well, i.e., the smallest increase of the moduli at high filler volume contents is observed for silanized silica. The largest effect of the filler concentration is obtained for the CB filled system. Note that the order of the curves for these systems is in agreement with the experimental data for both moduli.

Another property ,which is affected by the interaction between polymer and filler, is the system's relaxation. The bond relaxation was studied in the following way. The first two shear cycles are performed as discussed above. The external deformation leads to reversible breaking of polymer-filler (PF) and filler-filler (FF) bonds. Then the strain amplitude is set to zero, and changes in the number of broken polymer-filler and filler-filler bonds with simulation time are monitored. Fig. 6.13 illustrates the ratios of broken PF and FF bonds with respect to the total number of bonds of each type vs. simulation time for NR filled with CB, silica or silanized silica. The attendant values of k_{PF} are given in the plot title. The frequency ω is 0.1, $k_{FF} = 10$, $\gamma_F = 15$. The measurements are performed at different strain amplitudes, which are listed in the legend of each plot. In general, the curves at different strains look similar, i.e., during the first two cycles the bonds break, and after the strain is set to zero, the number of open contacts reduces. Note that at small strains, e.g., at $u_0 = 0.1$-2%, the number of broken bonds is small, but it increases considerably at large strains. At the same strain, the number of open contacts is larger in the case of polymer-filler bonds. The time required for the complete recovery of bonds depends not only on the applied strain, but also on the filler type, i.e., the value of the polymer-filler spring constant directly affects the system's relaxation behaviour. The top row of Fig. 6.14 shows a comparison of the relaxation curves obtained for different fillers at $u_0 = 10\%$. The small k_{PF}, used for silanized silica, leads to the longest time required for bonds to close. This effect is observed not only for the polymer-filler contacts, but also for the filler-filler bonds, although k_{FF} remains unchanged. Hence, changing k_{PF} has an impact not only on the polymer-filler interactions but also on the filler-filler ones. Based on Fig.6.14, we can expect that in the row 'CB – silica – silanized silica', the two-component system consisting of CB and NR would relax faster than the silica filled one, and the latter – faster than the one with silanized silica. In the bottom row of Fig. 6.14, experimental curves are shown, which were obtained during stress relaxation measurements for NR filled with CB and silanized silica. In fact, the CB filled system relaxes faster, so our model can qualitatively predict the relaxation behaviour according to experiments.

It has been shown that by a proper choice of k_{PF}, the model can simulate the mechanical properties of systems with different fillers in qualitative agreement with experiment. Note that for a quantitative comparison with the experimental data, it is essential to have reliable experimental values of the surface energies as an input for the MG and as a measure of the polymer-filler interaction strength.

Chapter 7

Mechanical Properties of Filled Elastomers – Filled Binary Polymer Blends

In the previous chapter, we have shown that mechanical properties of filled one polymer systems strongly depend on various system parameters such as filler dispersion, filler content or flocculation time. In this chapter, we will look at the mechanical properties of filled binary polymer blends. The polymer blends under consideration are mixtures of NR, SBR and filler with different surface energy values at various concentrations. We start with the impact of the filler surface energy on filler dispersion in the mixture of polymers. Then we proceed with studying the effects of filler dispersion, filler content and blend ratio on the mechanical properties. The results presented in this chapter have also been published and can be found in [139].

7.1 Filler Morphology – Impact of Filler Surface Energy on Filler Dispersion

The impact of filler morphology was studied based on 50-NR/50-SBR polymer blends containing 20% filler. These volume fractions roughly correspond to 49 *phr* (parts per hundred rubber) NR and to 51 *phr* SBR. In the top row of Fig. 7.1, the wetting-envelope – work of adhesion plots for the two polymers are shown. On the left-hand side, NR is assumed to be the liquid, and on the right-hand side – SBR. The second polymer is shown as a dot, i.e., the green dot in the right panel is NR, and the yellow dot in the left panel corresponds to SBR. The black dots represent fillers. The solid lines are wetting envelopes showing the constant value of the contact angle θ. The dotted loops are the loops of constant ΔW_a, which is the main driving force for filler flocculation. Below the wetting envelope plots, the respective simulated TEMs are shown, where each panel matches a black dot with the same number. Here γ_f^d is varied between 10, 20 and 30, and γ_f^p is varied between 0, 5, 10 and 16. This corresponds to variations in the total value of the filler surface energy γ_f between 10 and 46. The TEMs are extracted after 50 MC steps per node on average, and $L = 50$ in the system units.

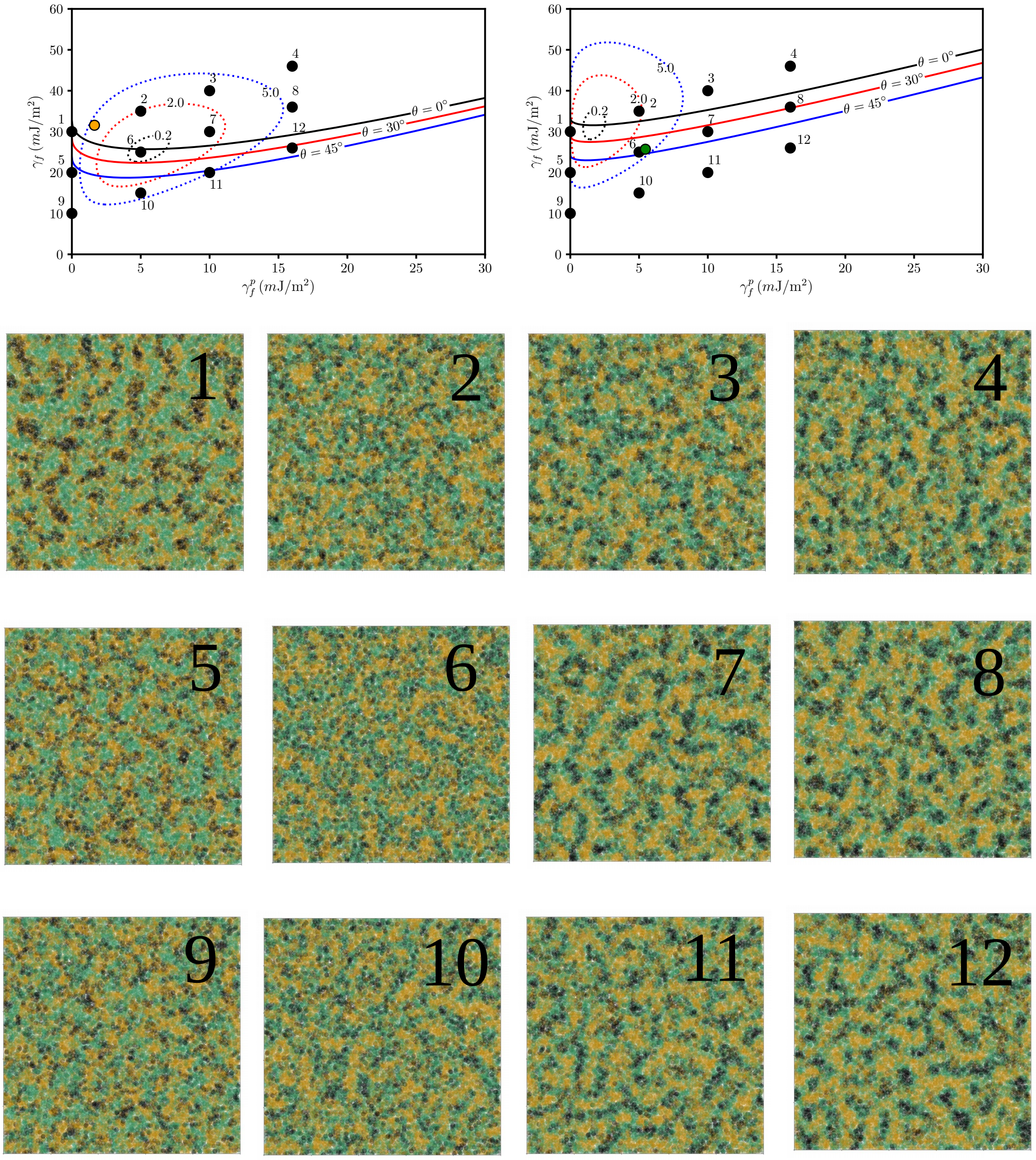

Figure 7.1: Top: Wetting-envelope – work of adhesion plots; left - NR as the liquid, right - SBR as the liquid. Bottom: TEM images corresponding to the systems shown as dots in the top panels.

Table 7.1: The surface energy values of the components.

Component	γ^d, mJ/m^2	γ^p, mJ/m^2	γ_{total}, mJ/m^2
Polymers			
NR	20.2	5.5	25.7
SBR	29.9	1.6	31.5
Fillers			
Nr. 1 (CB)	30.0	0.0	30.0
Nr. 8 (Silica)	20.0	16.0	36.0
Nr. 7 (Silane)	20.0	10.0	30.0
Nr. 6	20.0	5.0	25.0
Nr. 9	10.0	0.0	10.0

Table 7.2: The interface tensions and the values of the polymer-filler force constants k_{PF}.

Filler	NR		SBR	
	γ_{PF}, mJ/m^2	k_{PF}	γ_{PF}, mJ/m^2	k_{PF}
Nr. 1 (CB)	6.42	$1.0 \cdot 10^{-1}$	1.64	$2.6 \cdot 10^{-2}$
Nr. 8 (Silica)	2.80	$4.4 \cdot 10^{-2}$	8.39	$1.3 \cdot 10^{-1}$
Nr. 7 (Silane)	0.68	$1.1 \cdot 10^{-2}$	4.53	$7.1 \cdot 10^{-2}$
Nr. 6	0.01	$1.6 \cdot 10^{-4}$	1.90	$3.0 \cdot 10^{-2}$
Nr. 9	7.24	$1.1 \cdot 10^{-1}$	6.96	$1.1 \cdot 10^{-1}$

Based on TEMs presented in Fig. 7.1, we can draw several conclusions. In all presented cases, we can observe a micro-phase separation leading to the formation of domains consisting of either NR or SBR. NR/SBR blends are mostly immiscible, and a similar degree of the phase separation can be found in experiments [122, 135, 140]. The filler distribution depends on the relation between the polymer and the filler surface tensions. Based on the filler preferential concentration, we can determine several types of fillers. The filler Nr. 1, for instance, has a strong affinity to SBR due to its good wettability and low polarity. Consequently, its filler agglomerates can be found mainly in the SBR subphase. For highly polar fillers, the filler flocculation takes place predominantly in the NR subphase. For the fillers Nrs. 2 and 10, the value of $\gamma_f^p = 5$ mJ/m^2 is close to γ_p^p of NR, so the fillers concentrate in the NR subphase and do not form large agglomerates. In the limit case of the system Nr. 6, the filler is homogeneously dispersed in NR. The filler Nr. 9 can be characterized by the surface energy value that lies outside all the iso-ΔW_a loops and below all the iso-contact angle lines for both polymers; the filler in this case concentrates in the interface between NR and SBR. The size of filler agglomerates strongly depends on the position of the respective filler in the wetting envelope plot. Plots like in Fig. 7.1 can serve as guides for the selection of certain fillers. For example, Nr. 2 is a good choice for the blend, as it demonstrates high wettability and comparable ΔW_a for both polymers.

As mentioned in the previous chapter, three of the fillers presented in Fig. 7.1 correspond to the fillers commonly used in the tire industry. The filler Nr. 1 mimics

CB N234 (carbon black), Nr. 7 is close to Coupsil 8113 (silanized silica), and Nr. 8 represents Ultrasil VN3 (untreated precipitated silica). These fillers along with fillers Nrs. 6 and 9 were used to study the dynamic mechanical properties. The filler Nr. 6 was chosen due to its finest dispersion among morphologies in Fig. 7.1, while the filler Nr. 9 is of particular interest because it accumulates in the interface between the polymers. The surface tension values of the polymers and the fillers are collected in Table 7.1.

7.2 Mechanical Properties – Impact of Filler Morphology on System's Dynamics

To study the mechanical properties, we have to find the values of the force constants describing polymer-filler interactions for each system. Here we follow the approach described in Section 6.4.2. The value of γ_{CB-NR} is used as a standard, for which $k_{PF} = 0.1$. All other k_{PF} are calculated based on the value of the respective γ_{pf}. Table 7.2 contains the values of the interface tensions γ_{pf} and polymer-filler force constants k_{PF} for each pair 'polymer-filler'. Note that the pair 'SBR-Silica' has the largest k_{PF}, whereas the smallest k_{PF} was obtained for the pair 'NR-Nr.6' – the pair with the lowest value of the interface tension.

On the left-hand side of Fig. 7.2, the storage moduli (top row), the loss moduli (middle row) and the loss tangents (bottom row) for the filled blends are shown as functions of strain amplitude u_0 at $\omega = 0.001$. In all presented systems, we do observe the Payne effect as expected. Notice that the inflection point of the moduli hardly depends on the filler type. In [38], it was found that the inflection point of μ' in highly filled rubbers is related to the ratio between the gap spacing of neighbouring filler aggregates and the aggregate size. In our model we do not have significant variations in the distances between nodes; in addition, the aggregate size sets the unit of length. These model features lead to the uniformity in the positions of the inflection points. Apart from that, we can observe certain differences in the dynamic properties of the filled blends. For instance, the filler Nr. 6, which forms the system with the finest filler dispersion, exhibits the lowest values of both moduli. Comparing the plateau moduli for systems Nr. 7 and 8 shows that silanization leads to better dispersion and, consequently, to lower values of the dynamic moduli – the observation which is also well known from experiments [22, 141]. Notice that the system Nr. 9, characterized by the accumulation of filler in the NR-SBR interface, has a different shape of μ'. The value of μ'' lies significantly below than for the systems 1 (CB), 7 (silanized silica) and 8 (silica), which have the loss moduli close to their storage moduli. In [142], the authors studied the distribution of carbon black in the subphases formed by the polymers in NR/SBR blends. They found that the filler, depending on the mixing process, predominantly concentrates in either the SBR subphase or in the interface between NR and SBR. This corresponds to the situation shown in Fig. 7.1 for the fillers 1, 5 and 9, which have the polar parts of the surface energy close to those of CB. In addition, the authors found that the accumulation of filler in the polymer-polymer interface leads to an increased crack formation. This observation is supported by the magnitude of the Payne effect,

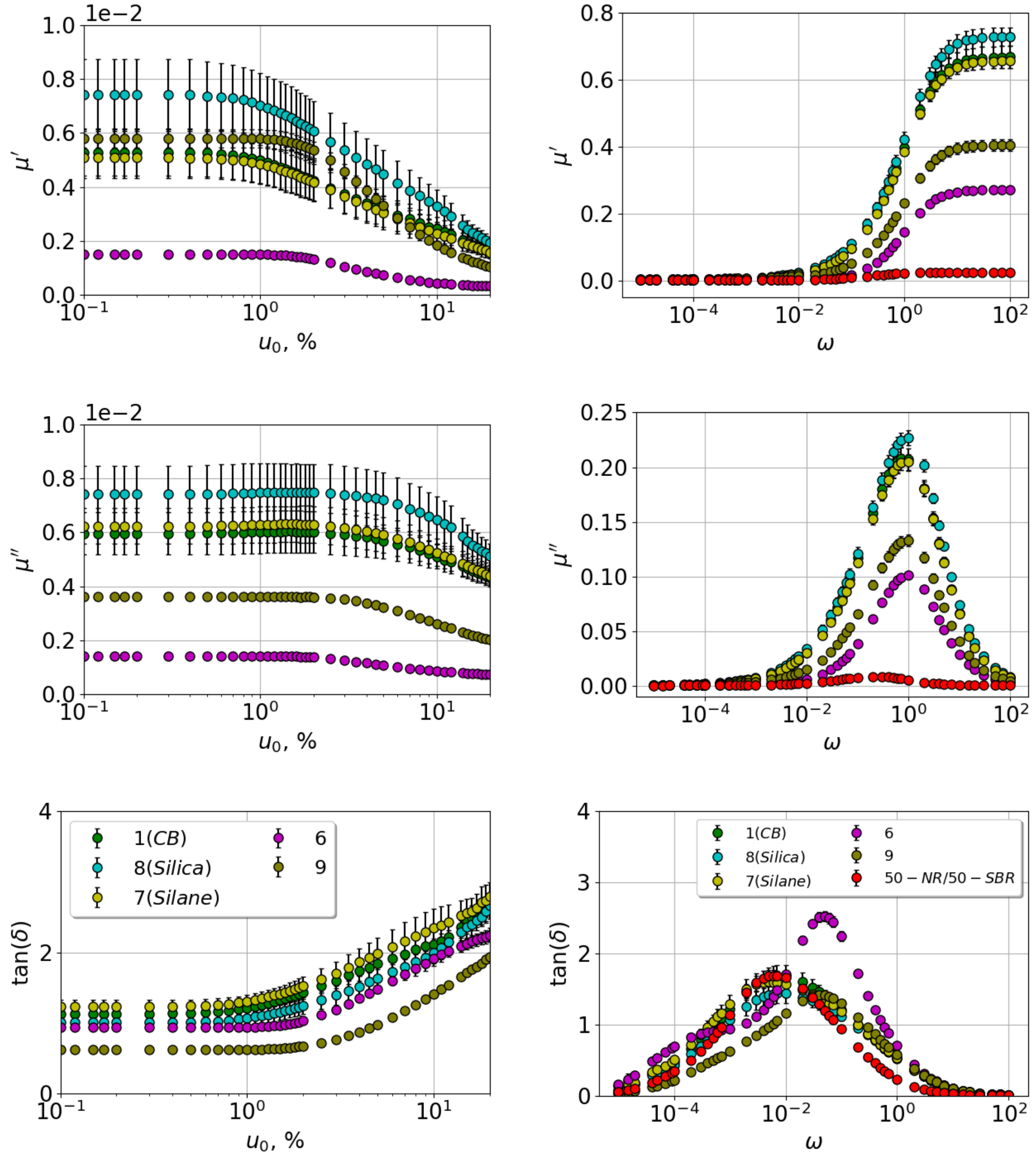

Figure 7.2: The simulated storage moduli μ' (top), loss moduli μ'' (middle) and $\tan\delta$ (bottom) vs. strain amplitude u_0 (left, $\omega = 0.001$) and frequency ω (right, $u_0 = 1\%$) The systems correspond to morphologies in Fig. 7.1.

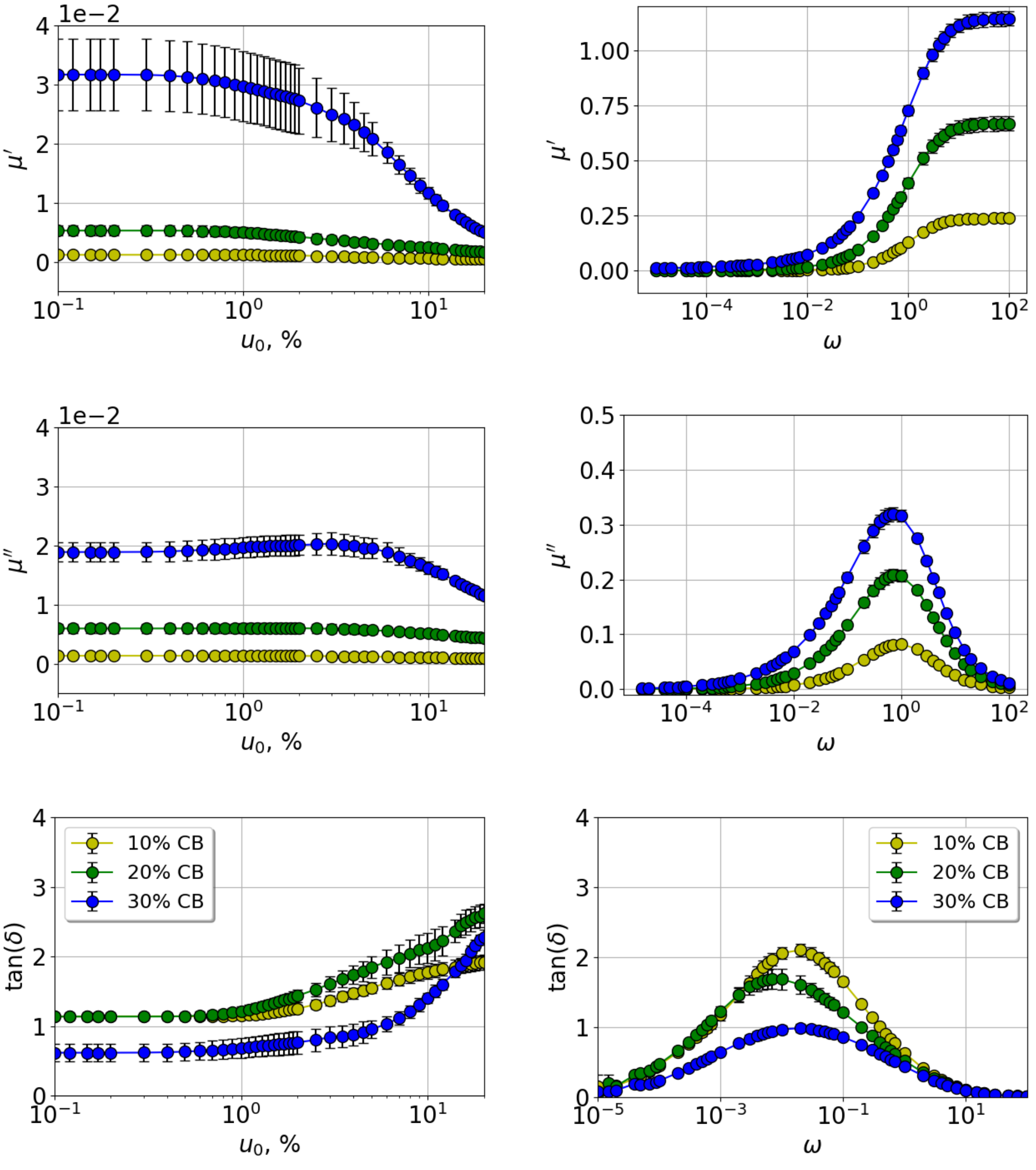

Figure 7.3: The simulated storage moduli μ' (top), loss moduli μ'' (middle) and $\tan\delta$ (bottom) for the 50-NR/50-SBR blend filled with different loadings (10, 20 and 30%) of carbon black vs. strain amplitude u_0 (left, $\omega = 0.001$) and frequency ω (right, $u_0 = 1\%$).

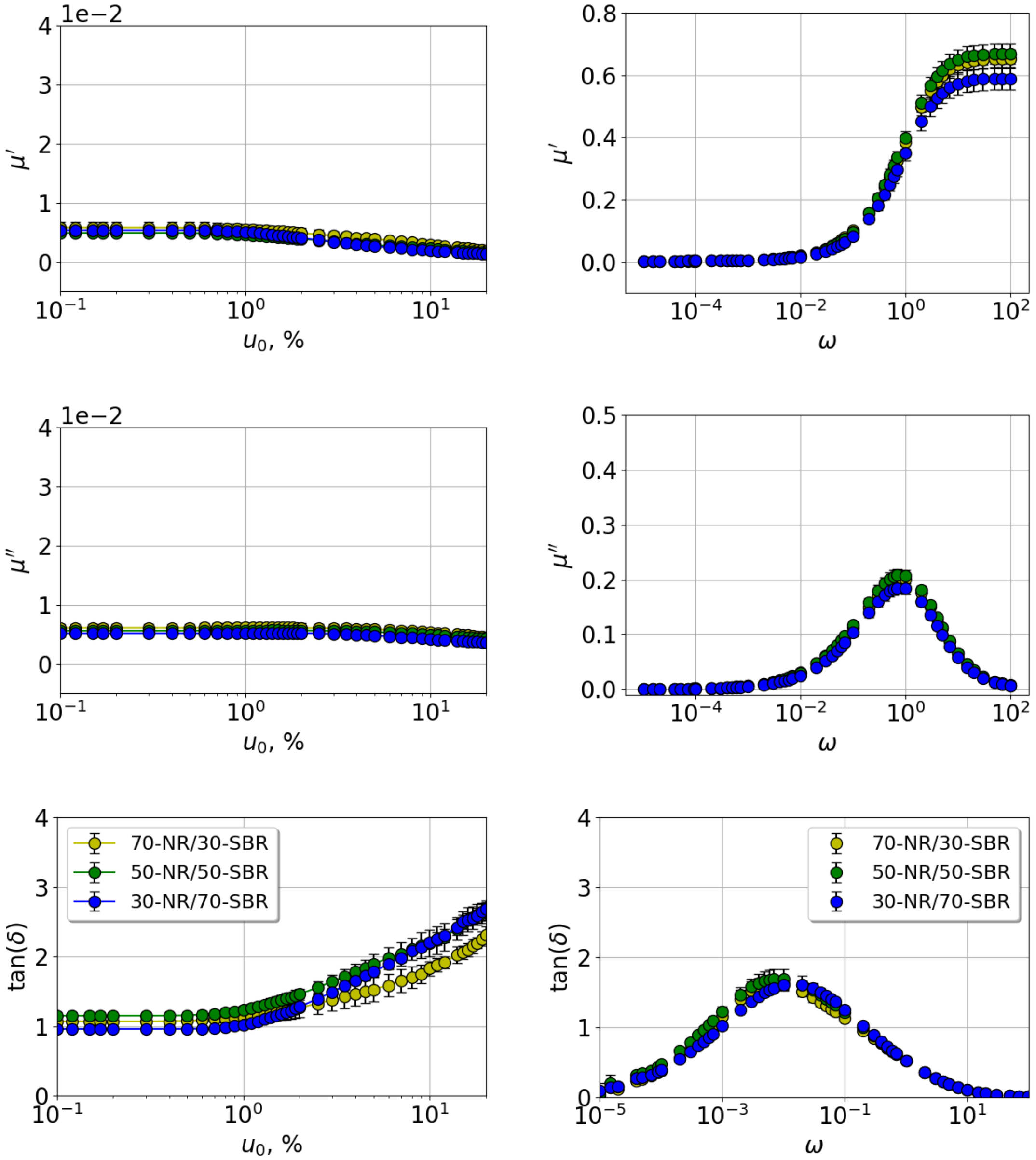

Figure 7.4: The simulated storage moduli μ' (top), loss moduli μ'' (middle) and $\tan\delta$ (bottom) for the NR-SBR blends filled with 20% carbon black vs. strain amplitude u_0 (left, $\omega = 0.001$) and frequency ω (right, $u_0 = 1\%$). The blend ratio is varied and given in the legend.

which is the largest for the system 9, i.e., in this case the loss of the material's strength under deformation is the most significant.

The panels on the right-hand side of Fig. 7.2 illustrate the storage moduli μ' (top row), the loss moduli μ'' (middle row) and the loss tangents (bottom row) for the aforementioned filled blends as functions of frequency ω at $u_0 = 1\%$. The shape of the curves is similar to what one finds in experiments, and the respective moduli for filled systems lie above the moduli for the unfilled blend. The loss tangent, as the ratio of the moduli, exhibits a more complicated behaviour. For all studied systems, one can observe the glass transition peak. As discussed above, when filler is added, the peak height drops, whereas the peak position does not significantly change. This behaviour can be reproduced by the model for filled systems containing one polymer, as shown in Fig. 5.17. For the filled blends this, however, is not observed. The position of the $\tan\delta$ peak for the blends filled with CB, silica or silanized silica does not change, while for the systems with fillers Nrs. 6 and 9 the peak position is shifted to higher frequencies. The height of the peaks for filled systems is comparable with the unfilled system, and is considerably larger in the case of the filler Nr. 6. In experimental systems, the order of the loss tangent curves for different filler contents at low frequencies is opposite to the one observed at the peak. Aside from the filler Nr. 9, this can be seen also for the simulated filled blends.

On the left-hand side of Fig. 7.3, the storage moduli (top), the loss moduli (middle) and the loss tangents (bottom) are shown as functions of strain amplitude u_0 at $\omega = 0.001$ for the 50-NR/50-SBR blends containing different loadings of carbon black, i.e., 10, 20 and 30%. In experiments, the amplitude of the Payne effect increases at larger filler contents, which is reproduced by the model for both moduli. The lowest $\tan\delta$ is obtained for the system with $\phi = 30\%$. At small strains, the loss tangents for the other two systems are close to each other, while at large strain amplitudes the highest value of the loss tangent was obtained for the system with 20% filler.

In the panels on the right-hand side of Fig. 7.3, the storage moduli (top), the loss moduli (middle) and the loss tangents (bottom) vs. frequency ω at $u_0 = 1\%$ are presented, when the volume content of CB is varied. The storage and the loss moduli increase with the filler content, as one would expect based on experimental findings, where larger moduli are found for highly filled systems [143, 144]. The positions of the peaks and the order of the $\tan\delta$ curves at the peak also correspond to experiments, i.e., the loss tangent drops for highly filled systems, whereas the peak position does not change. As the frequency decreases, the curve for 20% filler intersects the one for 10% CB, but the lowest value of the $\tan\delta$ throughout the whole frequency range was found for the 30% filled system.

In Fig. 7.4 the results are shown for the storage moduli (top), the loss moduli (middle) and $\tan\delta$ (bottom) vs. strain amplitude u_0 at $\omega = 0.001$ (left) and vs. frequency ω at $u_0 = 1\%$ (right). In the panels, the blend ratio is varied. We studied 70-NR/30-SBR, 50-NR/50-SBR and 30-NR/70-SBR blends, where $x_<^{interface} = 1.0$. In Fig. 5.7 the effect of the blend ratio variation was studied for unfilled blends based on the example of $\tan\delta$ for different $x_<^{interface}$. In that case, the variation of the blend ratio led to different positions and peak heights of the loss tangents. For instance, an increase in the NR content in a blend shifted the peak position to the peak position of pure NR. In addition, the loss tangent at the peak increased for higher SBR contents. Hence, the set of parameters used to describe the unfilled blends, i.e., $x_{<}^{interface}$, $k_{>}^{P_1P_2}$ and $k_{<}^{P_1P_2}$, allowed to distinguish between blends with different contents of NR and SBR. Adding filler, however, suppresses this behaviour, and the overall difference in the dynamic properties of filled blends with different blend ratios becomes minor.

Chapter 8

The Elusive Load-Bearing Path, Frequency Dependent Heterogeneity of Strain and Stress, and the Payne Effect Revisited

In the preceding two chapters we have modelled the mechanical properties of elastomer nanocomposites in general. In this chapter, we will look in detail at the different types of bonds and how their breaking is affected by strain amplitude, shear frequency, and other variables.

We start this chapter doing exactly this. Even though the initial motivation -finding and characterizing load-bearing network paths on the level of the bonds- had to be abandoned, the compiled information is useful and should not be omitted. In addition, we study what happens if open bonds do not return to their original closed state but to one with a significantly smaller force constant. This means that certain contacts may suffer irreversible 'damage' after experiencing high stress. Here the bonds in question are the filler-filler and the filler-polymer bonds.

Initiated by the aforementioned 'load-bearing path'-study, we made a discovery when we compared the stress and the strain in the various contacts – this time including the polymer subphase as well. At shear frequencies exceeding the typical relaxation rates of the bonds in the various contacts, we find that the global stress/strain and the local stress/strain are not very different. In addition, the local stress/strain is rather homogeneously distributed throughout the system quite independent of filler dispersion. This changes when the excitation frequency is small in the above sense, i.e., bonds are able to respond and relax. A pronounced redistribution of local stresses and strains in the various parts of composites occurs. In addition, the redistribution depends on filler dispersion. We emphasize that this information is beyond the well known static (or equilibrium) stress concentration in an elastic material in the vicinity of defects, e.g., particles or cavities. We suspect that the frequency dependent stress/strain concentration may have significant implications for long term 'damage' in the context of wear and that the extent of the damage can be influenced by how the filler is dispersed.

We also investigate the effect of not allowing filler-filler or filler-polymer bonds

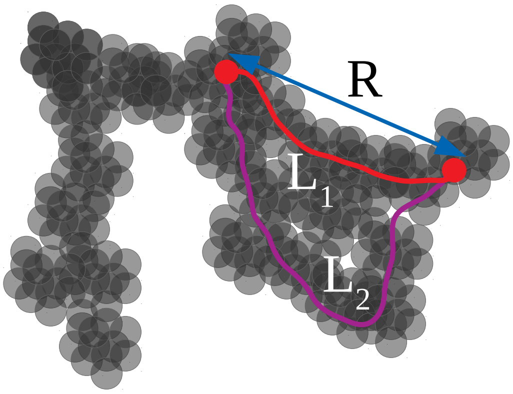

Figure 8.1: The filler network under deformation. The minimum, and therefore load-bearing, path L_1 is characterized by the end-to-end distance R. Only after L_1 breaks, L_2 becomes load-bearing.

to break at all. This in turn provides useful insight on the role of these contacts/interfaces in the Payne effect.

All the aforementioned studies are done based on two systems with significantly different filler dispersions, which we compare throughout the chapter. This comparison provides extremely useful information on the effect of filler dispersion not only on the Payne effect in filled elastomers, but also on the local strain and stress distributions.

8.1 Scaling Model

The goal of the scaling model, originally presented in [38], is to describe the amplitude and temperature dependence of the storage and loss moduli based on the filler properties and network structure. The key elements of the model are paths connecting particles in the filler network, as shown in Fig. 8.1. These paths can be characterized by a backbone length L and a respective end-to-end distance R. When external strain with the amplitude u is applied, a certain number of these paths bear the load, which can be described by a distribution function $H(L, R)$. The model assumes that the minimal paths are load-bearing. For instance, in Fig. 8.1 the load-bearing path is denoted as L_1. Only when this load-bearing path breaks under external deformation, the load will be redistributed, and L_2 will become load-bearing. The number of load-bearing paths is proportional to the number of contacts which will open when the paths are strained. The distribution of the minimum paths $h(L)$ is essential for calculating the storage modulus, i.e.,

$$\Delta\mu'(u) \propto h(L'),$$

where $\Delta\mu'(u)$ is the amplitude dependent part of the storage modulus and $h(L')$ is the distribution of the load-bearing paths in the strained system.

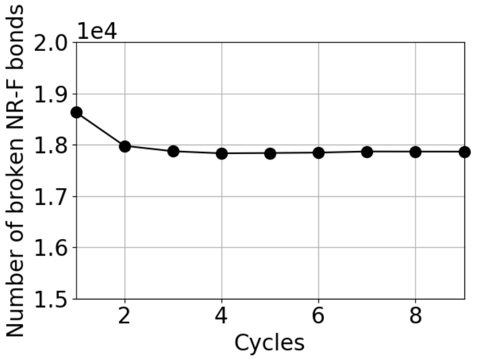

Figure 8.2: The number of broken polymer-filler bonds vs. the number of shear cycles for a filled NR system.

The temperature dependence of the Payne effect enters into the model via the activation energy, i.e., the energy difference between the closed and open bond-states. The activation energy is characteristic for the bond type, e.g., a hydrogen bond has the activation energy which is about 2.5 times larger than the van der Waals interaction of the polymer segment.

For the description of the loss modulus, one should consider the total dissipated energy per cycle, which in turn also depends on the chemical details of a filled elastomer such as filler volume fraction or sulphur content. Note that based on the model an equation for the loss tangent can also be derived [39].

Thus, according to the scaling model, the distribution function of the load-bearing paths is essential for the mechanical description of filled elastomer systems. If we can define the load-bearing paths in our simulation system and find their distribution function, then we will be able to check this assumption using our modelling approach.

8.2 Bond Breaking

In our model system, there are two types of bonds which can open and close reversibly, i.e., the filler-filler and the polymer-filler bonds. The fractions of breakable bonds depend on the filler volume content ϕ and the filler morphology. In 4.5, we mentioned that filled systems in comparison to unfilled ones demonstrate a different stress-strain behaviour during the first shear cycle (see Fig. 4.9). The additional loss in filled systems during first shear cycles is governed by a large number of broken polymer-filler and filler-filler contacts. Fig. 8.2 shows an example on how the number of broken polymer-filler bonds changes with the number of shear cycles in a filled NR system. During the first cycle this number is close to 1.87×10^4, then it decreases, and after the third cycle it does not considerably change. This is similar to the strain-stress behaviour of real systems, where loss during the first cycles is larger than during the following ones. Although this property is typical for filled elastomers, we cannot expect identical strain-stress curves for all filled systems. In the following sections, we will explore the effects of different parameters such as filler dispersion, strain amplitude, frequency and interaction strength on bond breaking.

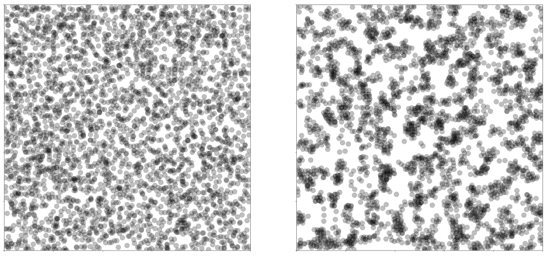

Figure 8.3: TEM images for filled NR systems with $\phi = 20\%$. Left: $\gamma_f^d = 20$ mJ/m^2, $\gamma_f^p = 5$ mJ/m^2, right: $\gamma_f^d = 20$ mJ/m^2 and $\gamma_f^p = 20$ mJ/m^2. The TEMs are extracted after 50 MC steps per node on average.

8.2.1 Effect of Filler Dispersion

For our study we choose two systems consisting of NR and filler with considerably different filler dispersions presented in Fig 8.3. The filler content ϕ in both cases is 20%. The value of γ_f^d is the same and equal to 20 mJ/m^2, while $\gamma_f^p = 5$ mJ/m^2 on the left-hand side (system 1) and $\gamma_f^p = 20$ mJ/m^2 on the right-hand side (system 2). While system 1 looks more homogeneous and dispersed, in the second case we can observe filler agglomeration taking place. As a result, the number of breakable bonds in the systems differs significantly. System 1 contains around eight times more polymer-filler than filler-filler bonds (22292 vs. 2822). In the second system the number of polymer-filler bonds is only about two times larger (16006 polymer-filler and 7370 filler-filler bonds). In order to study the effects of the filler network, it is reasonable to compare not the total number of broken bonds per cycle, but the relative number. The relative number of broken bonds is obtained in the following fashion. During each shear cycle, the broken bonds of both types are counted, then the average number per cycle is calculated. At the end, the average number is divided by the total number of bonds of the respective type in the system. Using this approach, we can compare the changes in the breaking statistics for the aforementioned systems with respect to different parameters. Unless stated otherwise, in the remainder of this chapter the plots on the left-hand side correspond to system 1 and on the right-hand side to system 2. In addition, the plots in the top row are obtained for filler-filler contacts, whereas the bottom row corresponds to polymer-filler bonds.

8.2.2 Effect of Interaction Strength

In Chapter 5 we studied the effect of the k_{PF} and k_{FF} variation on the dynamic moduli and $\tan\delta$. In Fig.8.4 the ratios of open filler-filler and polymer-filler contacts vs. strain amplitude are shown for the systems from Fig. 8.3 and for two different sets of spring constants. In the top row $k_{FF} = k_{PF} = 1$, and in this case, there is no difference between polymer-filler and filler-filler contacts in terms of their interaction strength. This is reflected in the number of broken bonds, as the ratio of the open filler-filler and polymer-filler contacts at the same u_0 is similar. Both the polymer-filler and the filler-filler bonds start to break at approximately 2-3%

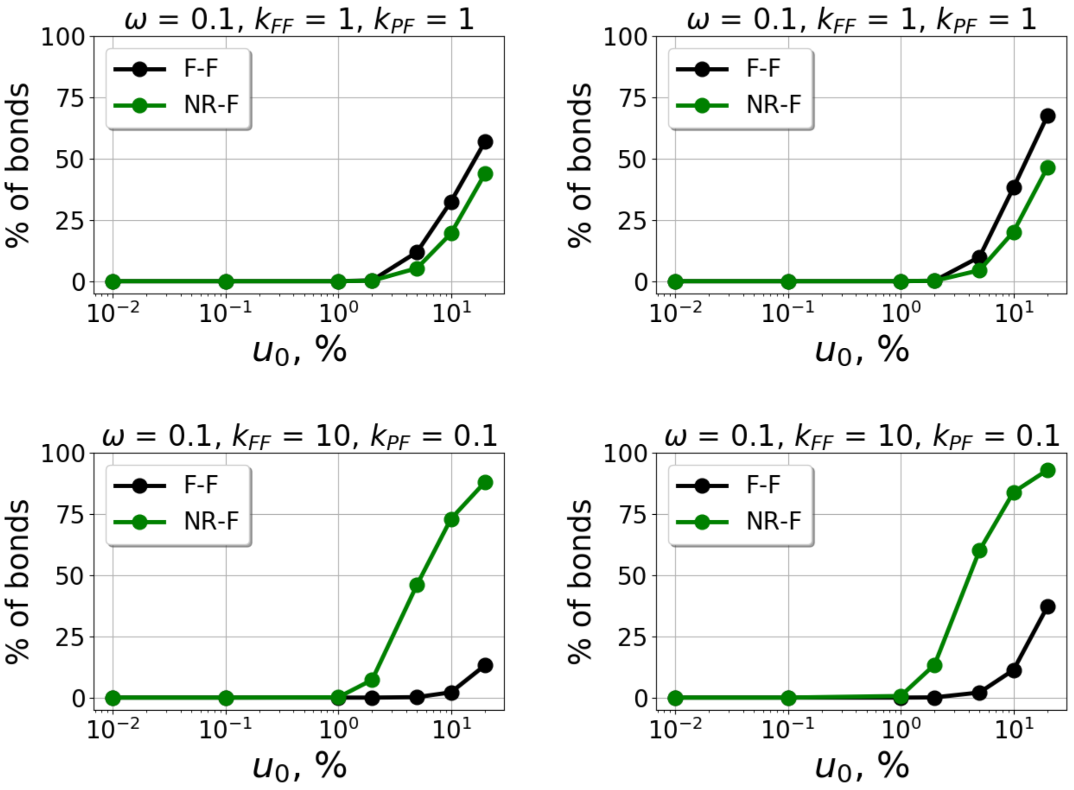

Figure 8.4: The ratios of broken filler-filler (black) and polymer-filler (green) bonds as functions of strain amplitude u_0. The frequency $\omega = 0.1$. Top: $k_{FF} = k_{PF} = 1$; bottom: $k_{FF} = 10$, $k_{PF} = 0.1$. The systems correspond to the TEMs presented in 8.3.

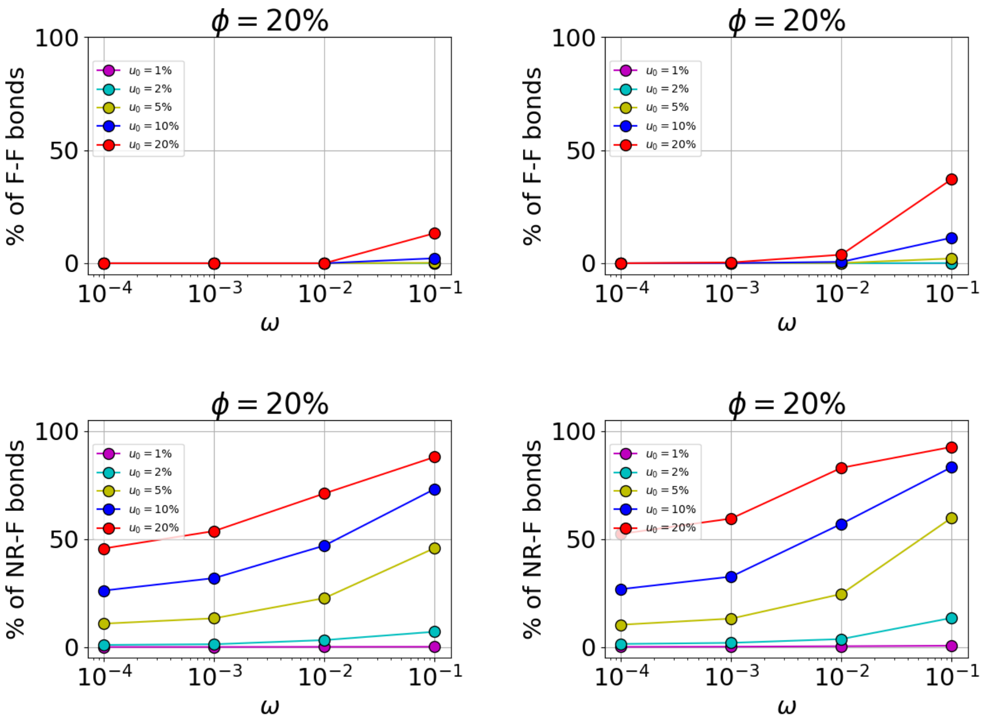

Figure 8.5: The relative number of broken bonds per shear cycle vs. simulation frequency ω at different strain amplitudes u_0 given in the legend.

strain. When k_{FF} increases and k_{PF} decreases by one order, the difference between the types of contacts becomes apparent. The polymer-filler bonds start to break earlier, and already at $u_0 = 1\%$ we can observe some bonds being broken. The number of broken polymer-filler bonds is quite substantial, and at 20% strain it is close to 90-95% of all polymer-filler bonds in the system. This is not surprising because these bonds have a weaker coupling strength and therefore break easier under external deformation. The filler-filler bonds due to a stronger coupling break at much larger strain amplitudes, and the number of open filler-filler contacts at 20% is about 13% on the left-hand side and 30% on the right-hand side. Here we can clearly see the effect of filler dispersion, i.e., the ratio of open contacts for system 2 is larger than the respective ratio for system 1. Based on these plots, we can assume that in system 2 the filer contacts and the filler network play an essential role in the load distribution. In system 1, filler aggregates do not form a filler network and the filler-filler contacts are less involved in the load bearing. As mentioned above, the number of broken contacts is directly related to the dissipated energy, so we can also expect that the loss modulus for system 2 is larger than the loss modulus for system 1.

In the remainder of this chapter, we use $k_{FF} = 10$ and $k_{PF} = 0.1$. The force constants for other types of interactions used to obtain the results are compiled in Table 5.5.

8.2.3 Effect of Frequency and Amplitude

Frequency and strain amplitude are the quantities which strongly affect the mechanical properties of filled elastomers. Therefore, we will look at the effect of these parameters on the bond breaking statistics.

Fig. 8.5 illustrates the relative number of broken filler-filler (top row) and polymer-filler (bottom row) bonds vs. simulation frequency ω at different strains. When the frequency increases, the relative number of both filler-filler and polymer-filler bonds broken during one shear cycle also rises. Typically, the simulation frequency defines how fast the deformation is applied to the system. At low frequencies, the system has enough time to change the system configuration in response to the applied strain, e.g., at frequencies up to 10^{-2} the filler-filler bonds do not break at all. At higher frequencies, these changes are constrained, therefore, the bonds break easier, and the largest number of broken bonds for both systems is obtained at $\omega = 0.1$. At the same frequency and strain amplitude, the number of broken bonds in system 2 is larger than in system 1. Again, in the first case, the filler-filler bonds break more often and play a more important role in the load distribution throughout the system. The relative number of broken polymer-filler bonds is also less in the case of the dispersed system. Note that in general the load bearing paths include not only direct filler contacts but also the adjacent polymer. Hence, the difference in the number of broken bonds between the two systems may be related to the formation of the filler network in system 2 and a more effective distribution of the load.

The next figure, Fig. 8.6, provides a comparison between the relative number of broken bonds vs. strain amplitude u_0 at different frequencies given in the legend. These plots support our previous conclusions. The polymer-filler bonds start to break at $u_0 \approx 1\%$, which roughly corresponds to an onset of the Payne effect in experimental systems. At high strain amplitudes, the number of broken bonds rises, especially at high frequencies. At the largest strain amplitude $u_0 = 20\%$, the number of broken polymer-filler bonds at the highest frequency $\omega = 0.1$ is close to 100%. The filler-filler bonds break at considerably higher strains, and the ratio of broken bonds is lower than for the polymer-filler bonds. The number of both filler-filler and polymer-filler bonds, which break during a shear cycle, is larger for system 2. In the bottom row of Fig. 8.6, the attendant loss moduli are presented. The loss modulus for system 2 is larger than the loss modulus for system 1 at the same frequency, which supports our assumption about the dissipated energy. The loss modulus as well as the ratio of broken bonds drop with the frequency, i.e., at high frequencies the bond breaking process contributes more to the dissipation of energy.

It is worth noting that the results for other filler contents under study ($\phi = 10$ and 30 %) are similar to the results shown here for $\phi = 20$ %.

8.2.4 Effect of Filler Content

In Fig 8.7 the relative number of broken bonds is shown as a function of filler content ϕ at $\omega = 0.1$ and various strain amplitudes given in the legend. While in some cases the number of broken polymer-filler bonds is nearly constant, in other

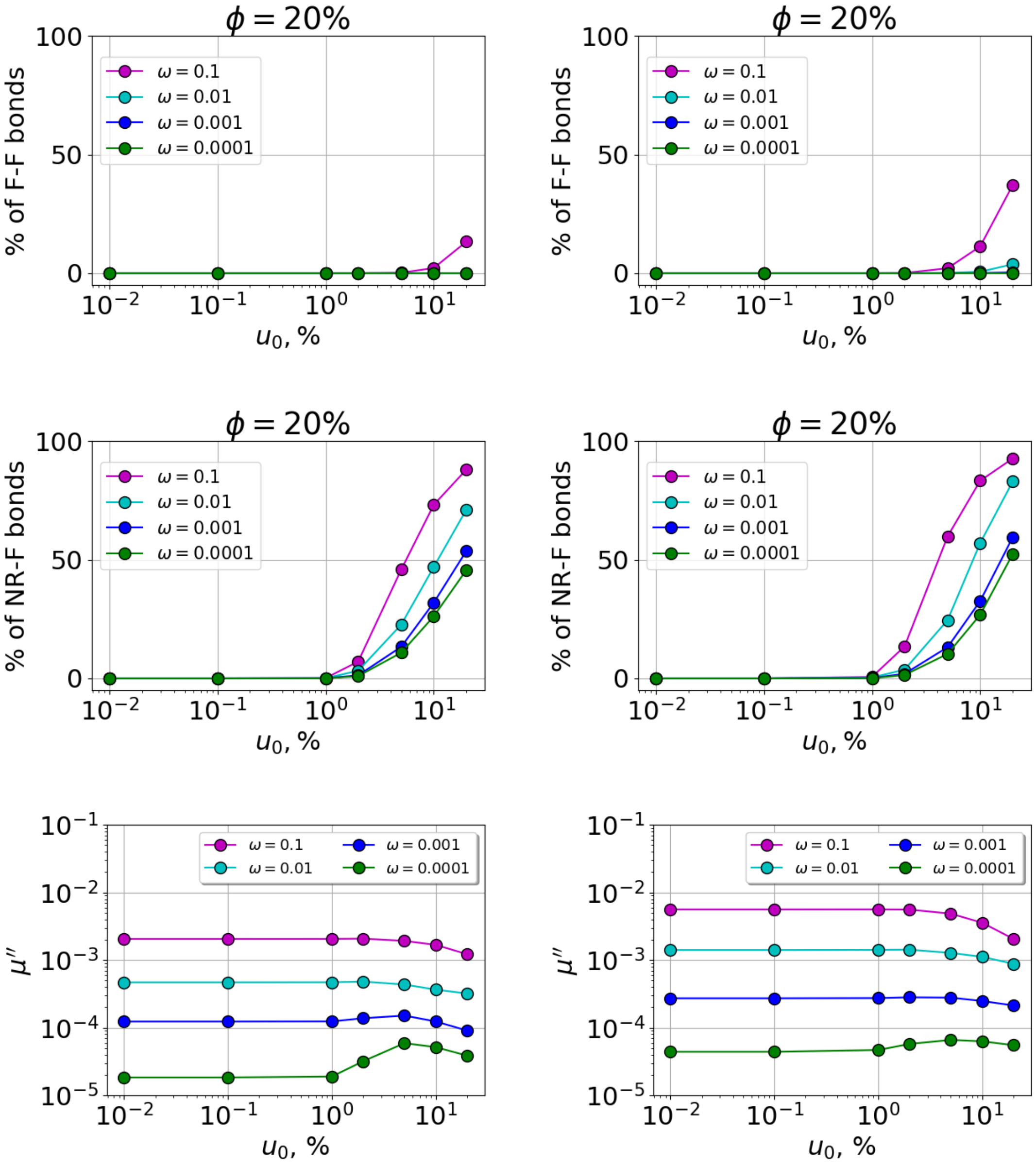

Figure 8.6: Top two rows: the relative numbers of broken bonds per shear cycle vs. strain amplitude u_0 at different frequencies ω given in the legend. Bottom row: the attendant loss moduli.

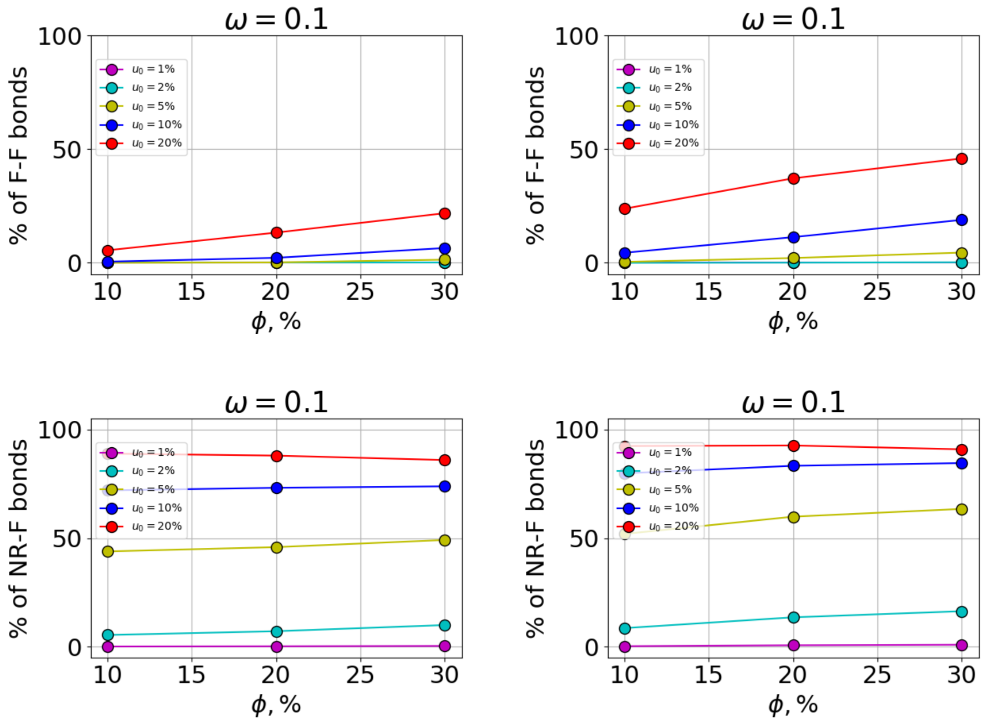

Figure 8.7: The relative number of broken bonds per shear cycle vs. filler content ϕ at different strain amplitudes u_0. The simulation frequency ω is 0.1.

cases it increases with the filler content as well as the number of broken filler-filler bonds. Obviously, the number of filler-filler and polymer-filler bonds increases with the filler content in general, but as we consider the relative number of broken bonds, this effect has already been taken into account. Note that the loss modulus is larger for systems with higher filler contents, i.e., the increasing ratio of broken bonds shows that the contribution of bond breaking to the loss increases with the filler content. At the same time, the importance of the friction loss reduces. Based on the plots, we can also assume that this contribution is larger for system 2 than for system 1. It is also worth mentioning that at lower frequencies, an increase in the ratio of broken polymer-filler bonds at higher filler contents is more pronounced.

8.2.5 Orientation Dependent Breaking

The reversible bond breaking of filler-filler and polymer-filler bonds is determined by the load distribution within the material, which is not homogeneous and depends on filler dispersion. Therefore, we can expect that the space orientation of breakable bonds affects how often they break. For instance, the relative elongation of bonds parallel to the strain direction should be larger than that for the bonds with another orientation. This idea is illustrated in the left panel of Fig. 8.8. The original system (blue edges) is deformed on the $xz-$plane, and the shear direction is diagonal to the x- and z-axes. In the deformed system (black dotted edges), the bonds parallel to the x-axis (red colour) do not significantly elongate and should rarely break. The

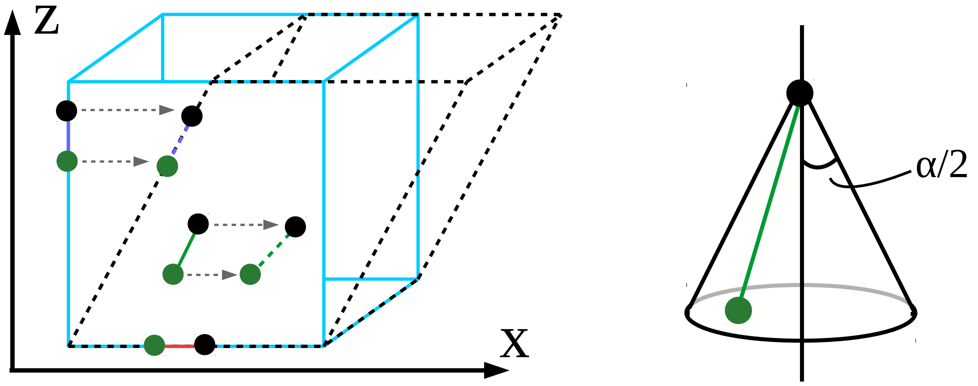

Figure 8.8: Left: the basic idea of orientation dependent bond breaking; right: a bond type is defined via a cone angle α.

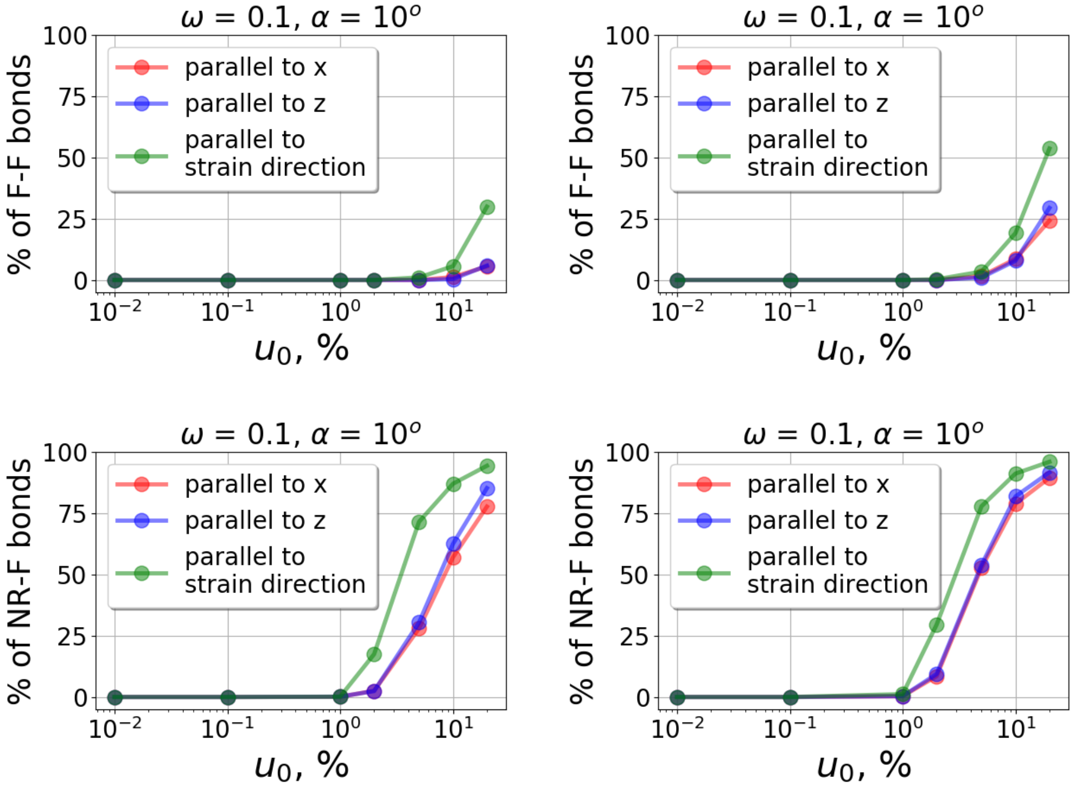

Figure 8.9: The relative number of broken bonds per shear cycle vs. strain amplitude u_0. The simulation frequency ω is 0.1, the cone angle $\alpha = 10°$. The different colours correspond to different bond orientations, the colour coding is the same as in the left panel of Fig. 8.8.

bonds parallel to the shear direction (green colour) experience the largest elongation, and node-to-node separations in this case often exceed the bond-breaking distance. The bonds parallel to the z-direction represent the case with an intermediate value of the expected elongation. The bond type is defined via a cone angle α, as presented in the right panel of Fig. 8.8. If the angle between a bond and the respective direction (x-, z-axes or strain direction) is less than α, then the bond is considered to have the attendant orientation type.

The simulation results for the orientation dependent breaking for the aforementioned two systems are shown in Fig. 8.9. The colour coding matches the one used in the left panel of Fig. 8.8. The relative number of broken filler-polymer bonds is larger than the number of broken filler-filler bonds, and for system 2 it is larger than for system 1. Note that the bond orientation strongly affects the bond breaking, i.e., bonds, which are parallel to the strain direction, break more often and start to break at lower strains than the other two types of bonds. This observation is independent of filler dispersion, as these bonds experience the largest elongation during shear. However, the difference in the relative number of broken bonds of different types is larger for the dispersed system. The bonds with an orientation parallel to either x- or z-axis do not exhibit much difference in their breaking behaviour. It is worth noting that at lower frequencies, the difference between the bond types decreases; the same happens if the cone angle α becomes larger. If α is large enough, no difference is observed because many bonds with different orientations are included into just one type, and the angles defining different bond types can overlap.

8.3 Breaking Visualization

Another feature of the model is the possibility to visualize internal strain and stress. This can provide insight to the distribution of the local strain (stress). The latter can be studied with respect to external deformation and filler morphology. The local strain for each pair of nodes i and j can be calculated via

$$u_{ij,local} = \frac{r_{ij} - r_{ij,equil}}{r_{ij,equil}}, \tag{8.1}$$

and the contribution of this pair to the local stress is

$$\sigma_{ij,local} = \frac{1}{2V}\frac{x_{ij}z_{ij}}{r_{ij}}F(r_{ij}). \tag{8.2}$$

Fig. 8.10 shows different cuts with $L = 20$ from the aforementioned systems, shown in Fig. 8.3, under applied shear deformation with $u_0 = 10\%$. In the background, the filler aggregates are shown. In the top row, the bonds with a positive value of the local strain $u_{ij,local}$ are illustrated, i.e., the bonds which are elongated during shear. The green colour corresponds to polymer-polymer (unbreakable) bonds, while the red colour combines filler-filler and polymer-filler bonds, which can break. In the bottom row, the bonds with a negative value of the local strain are shown, i.e., the bonds which are compressed during deformation. The breakable bonds have the dark blue colour and unbreakable contacts are shown in the

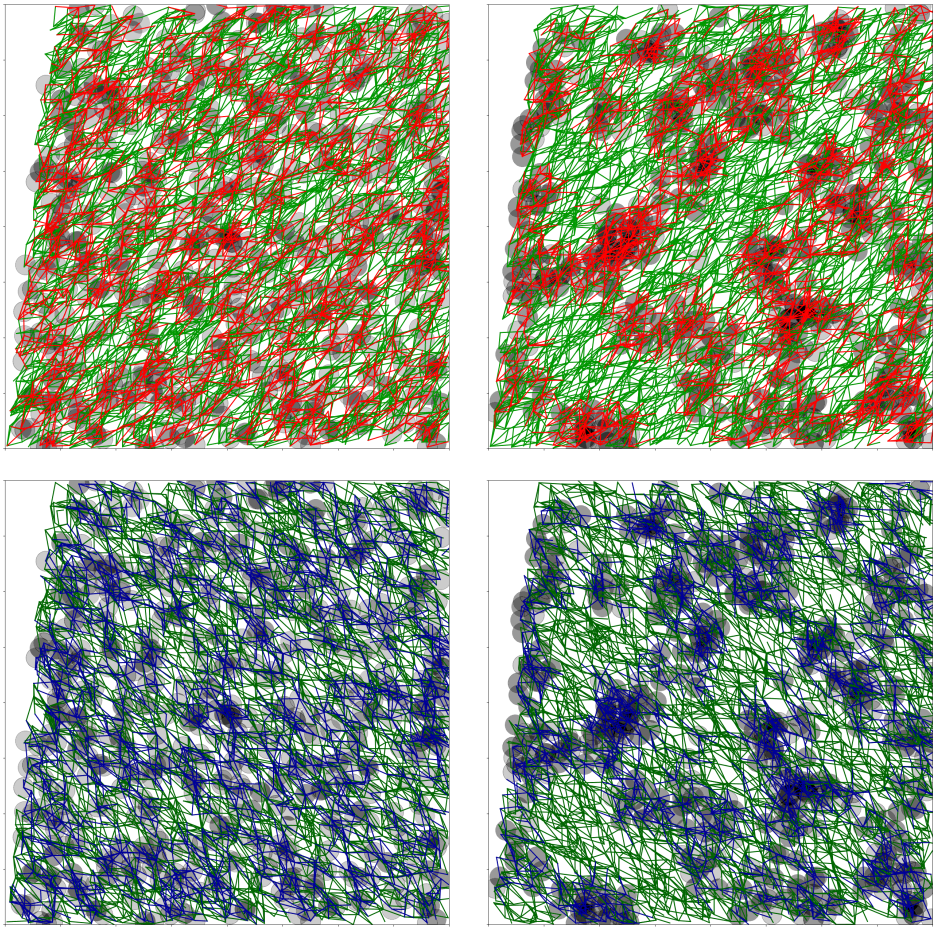

Figure 8.10: Top: bonds with a positive value of the local strain, i.e., the bonds which are elongated during shear deformation. Green colour – polymer-polymer (unbreakable) bonds, red – filler-filer and polymer-filler (breakable) bonds. Bottom: bonds with a negative value of the local strain, i.e., the bonds which are compressed during shear deformation. Dark green colour – polymer-polymer (unbreakable) bonds, blue – filler-filer and polymer-filler (breakable) bonds. All pictures are taken in the shear plane, $L = 20$.

dark green colour. In both systems, the elongated bonds have a specific orientation which is parallel to the direction of deformation. The compressed bonds are parallel to the compression direction, which is orthogonal to the direction of elongation. In general, the distribution and orientation of bonds in the systems resemble the respective filler morphologies.

Fig. 8.11 illustrates the bonds with the largest strain and stress in the top and bottom row, respectively. In each case, values of the local strain (or stress) are sorted in ascending order and the top 10% are plotted in the picture. The unbreakable bonds again have the green colour, but now we also distinguish between polymer-filler (blue) and filler-filler (red) bonds. In general, the strain and stress distributions depend on filler dispersion. For system 1 the pictures look more 'homogeneous', while in system 2 the most strain and stress are accumulated in the vicinity and

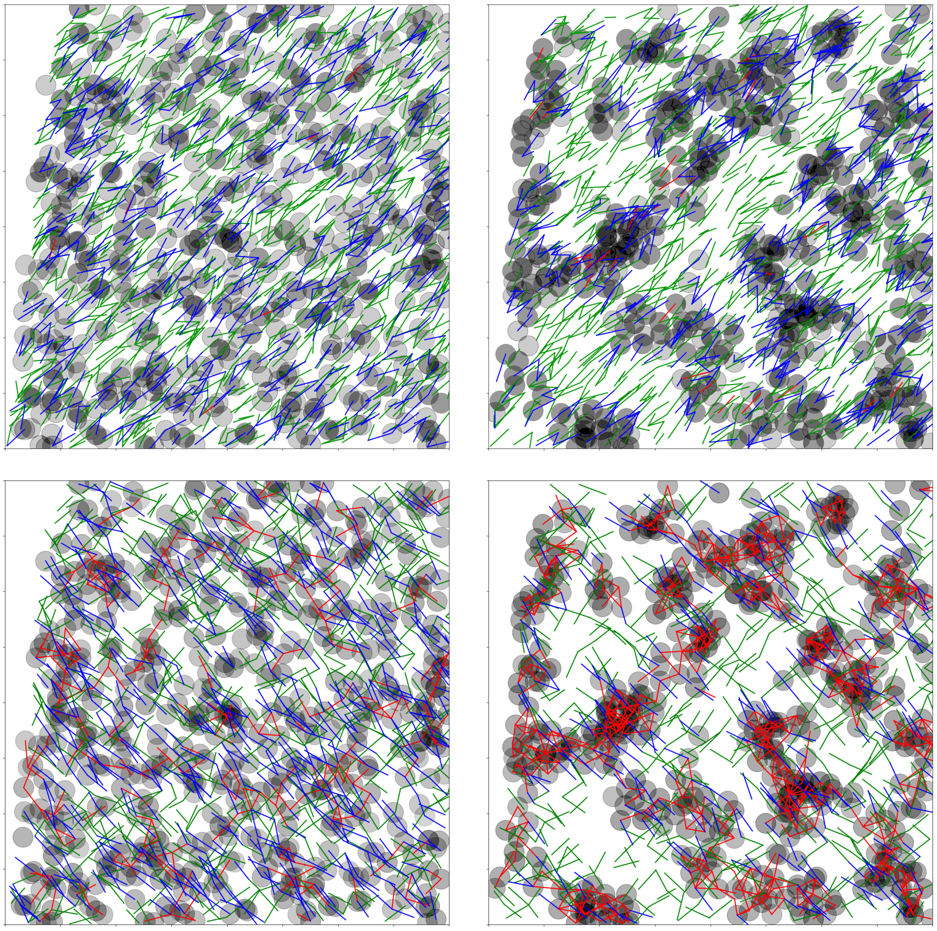

Figure 8.11: Top: bonds with a local strain value within top 10% during shear deformation. Bottom: bonds with a local stress value within top 10% during shear deformation. Green colour – polymer-polymer (unbreakable) bonds, red – filler-filer and blue – polymer-filler bonds. All pictures are taken in the shear plane, $L = 20$.

inside the filler agglomerates. In both cases, the bonds with the largest strain, i.e., which experience the largest elongation, are either polymer-polymer or polymer-filler. The main reason is that the values of the attendant force constants are smaller than for the filler-filler interaction. For system 2 not only the polymer-filler and filler-filler bonds, but also the polymer-polymer bonds are concentrated in the filler domains, forming 'cavities', i.e. regions in which the 'green bonds' are noticeably less dense, in the rubber phase, where the values of the local strain are much smaller.

For the stress distribution, the picture is entirely different, i.e., the contribution of filler-filler bonds to the microscopic stress is much larger than their contribution to the local strain. This is again due to the difference in the force constants, which define the force between two nodes in Eq. (8.2). The local stress is predominantly concentrated in the filler domains in the case of system 2, whereas the stress distribution for system 1 is more homogeneous. The cavities in the former case are even larger than for the local strain, which implies, that the contribution of filler

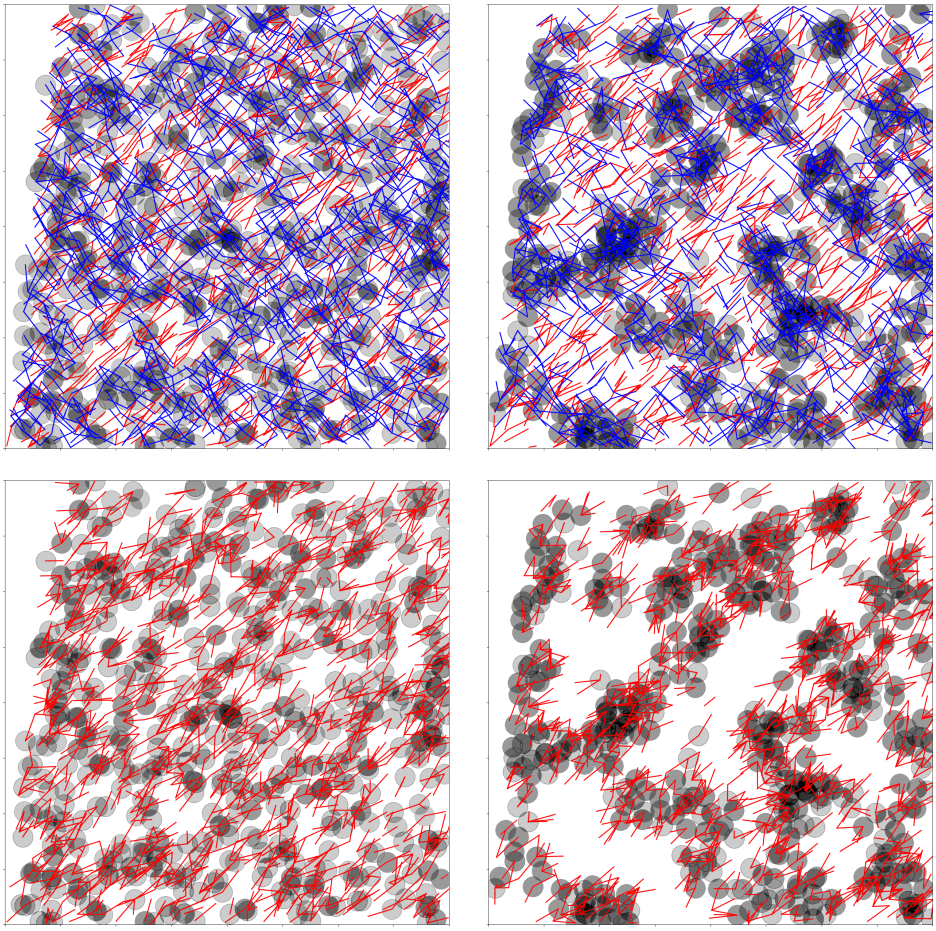

Figure 8.12: Top: bonds with the top 10% local strain (red) or the top 10% local stress (blue). Broken bonds are excluded. Bottom: filler-filler and polymer-filler bonds broken during a shear cycle.

domains to the local stress is more considerable than that of the rubber phase. As for a broken filler-filler bond $\sigma_{ij,local}$ is zero, only non-broken filler-filler bonds contributing to the local stress are shown in the picture.

In the top row of Fig. 8.12, the distribution of both the local strain and the local stress is shown, where broken bonds are excluded. These pictures show that the largest elongations are observed in the polymer phase, while the largest stress concentrates inside the filler agglomerates. The largest values of local strain are found in the polymer phase, because in the filler-filler and polymer-filler interfaces the bond elongation is limited by the bond breaking distances $R_{FR} = R_{FF} = 1.01\ r_{ij,0}$. Although the bonds inside filler agglomerates can break, they do not open during the shear cycle, according to the right panel of Fig. 8.12. This happens possibly due to a high concentration of bonds with large values of the force constants, which hinders breaking and makes these bonds in reality unbreakable. This is not observed on the left-hand side because the dispersed system does not have such filler domains, where the concentration of bonds with large values of force constants is significant.

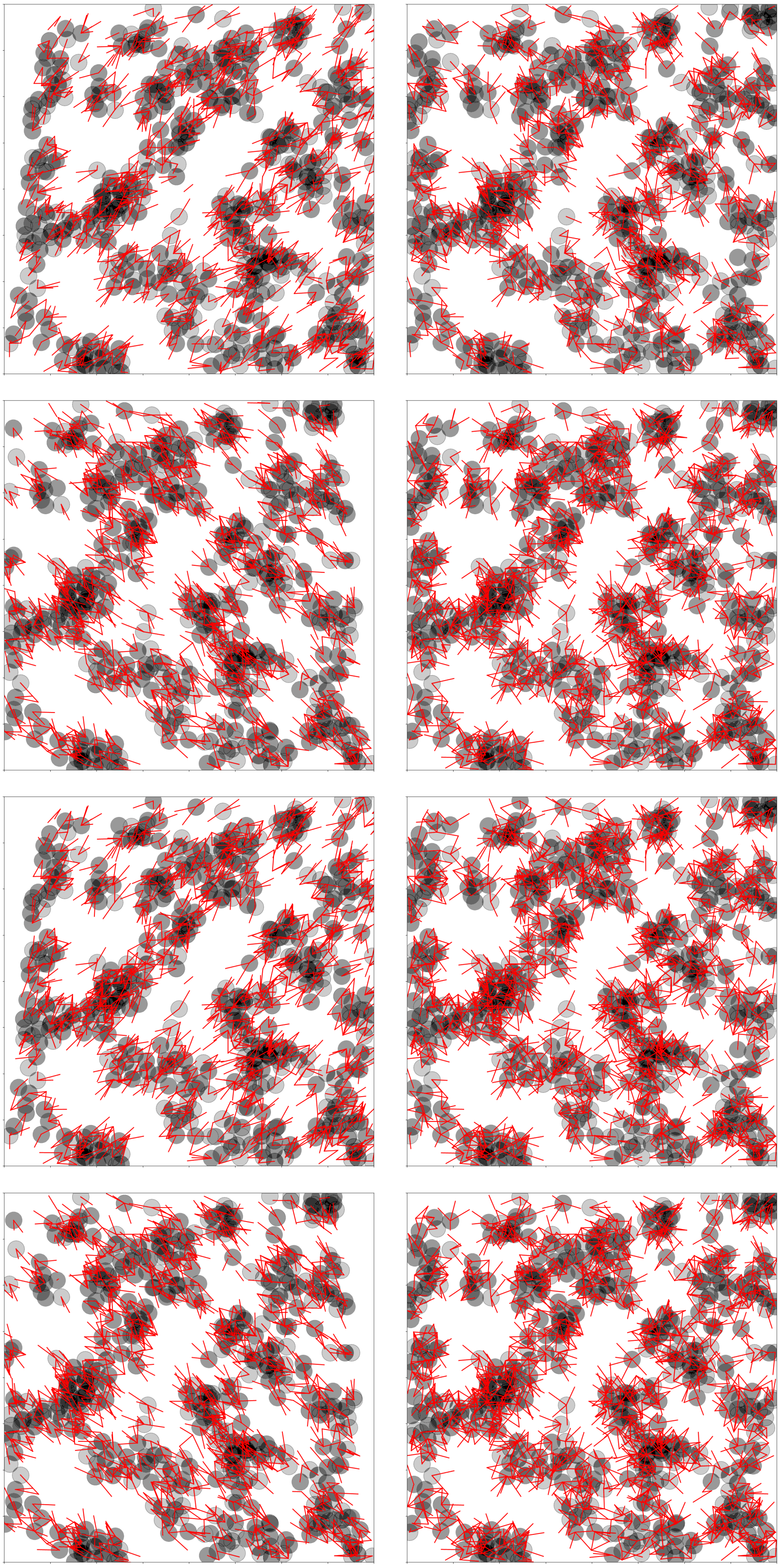

Figure 8.13: Broken polymer-filler and filler-filler bonds during first two shear cycles.

In the bottom row of Fig. 8.12, the broken filler-filler and polymer-filler bonds are shown. As broken bonds contribute directly to the energy dissipation, this type of representation allows to observe the loss distribution in the system. Note that according to the scaling model, when external deformation is applied, the load bearing paths break first. Based on the pictures in the bottom row of Fig. 8.12, we can monitor the positions of the broken bonds and how their number changes with the simulation time. In Fig. 8.13 snapshots from an animation are presented showing the broken polymer-filler and filler-filler bonds at $t = n \cdot \pi/2$, where $n = 1, 2, .., 8$. The shear direction on the left-hand side changes from top right to top left. The intermediate states with $t = m \cdot \pi$, where $m = 1, 2, 3, 4$, do not experience any deformation ($u_0 = 0$) and are shown on the right-hand side. After the first half of the first shear cycle, some bonds remain open even when $u_0 = 0$ (top right panel). The orientation of broken bonds corresponds to the shear direction, and when the deformation is zero, the bonds do not have any particular direction. After the first shear cycle is complete, the number of open bonds is larger than at $t = \pi$. As discussed above, the possibility for a bond to break depends on its relative orientation to the shear direction; as the shear direction changes, the bonds broken in the first and the second half of the cycle are different. However, during the second cycle, the number of broken bonds does not change significantly when $u_0 = 0$. The main difference is that the first shear cycle is performed on an undeformed material, while the second cycle – on the previously deformed one. This makes the first shear cycle special in terms of deformation. This behaviour is similar to the aforementioned Mullins effect in experimental systems. Overall, pictures like Fig. 8.12 and 8.13 may be helpful in finding and studying load bearing paths in the system.

8.4 Local Strain and Stress Distribution

The model provides the opportunity not only to qualitatively distinguish the local strain and stress, but also quantitatively describe the local strain and stress. One can study the local strain and stress distributions and how the local values deviate from the global deformation applied to the system. As large values of the local strain and stress often lead to cracks in a material, this study can provide important insights to the mechanisms of fatigue and damage in real systems. In addition, one can look at local strain and stress distributions with respect to different parameters, such as filler morphology, strain amplitude, frequency or shear cycle. In this section, we will describe possible sources of damage and will also discuss some selected results.

During deformation, the local strain can vary inside the material and according to the strain amplification idea may be considerably larger than the external strain. In Fig. 8.14 the ratios of the local strain to the global strain vs. strain amplitude are shown. On the left-hand side, the results for the system with $\gamma_f^p = 5$ mJ/m^2 are presented and on the right-hand side the plots are obtained for the system with $\gamma_f^p = 20$ mJ/m^2. The frequency ω is 0.1, which is near the glass transition peak of NR. In the top row, the value of the maximum local strain is given (elongation),

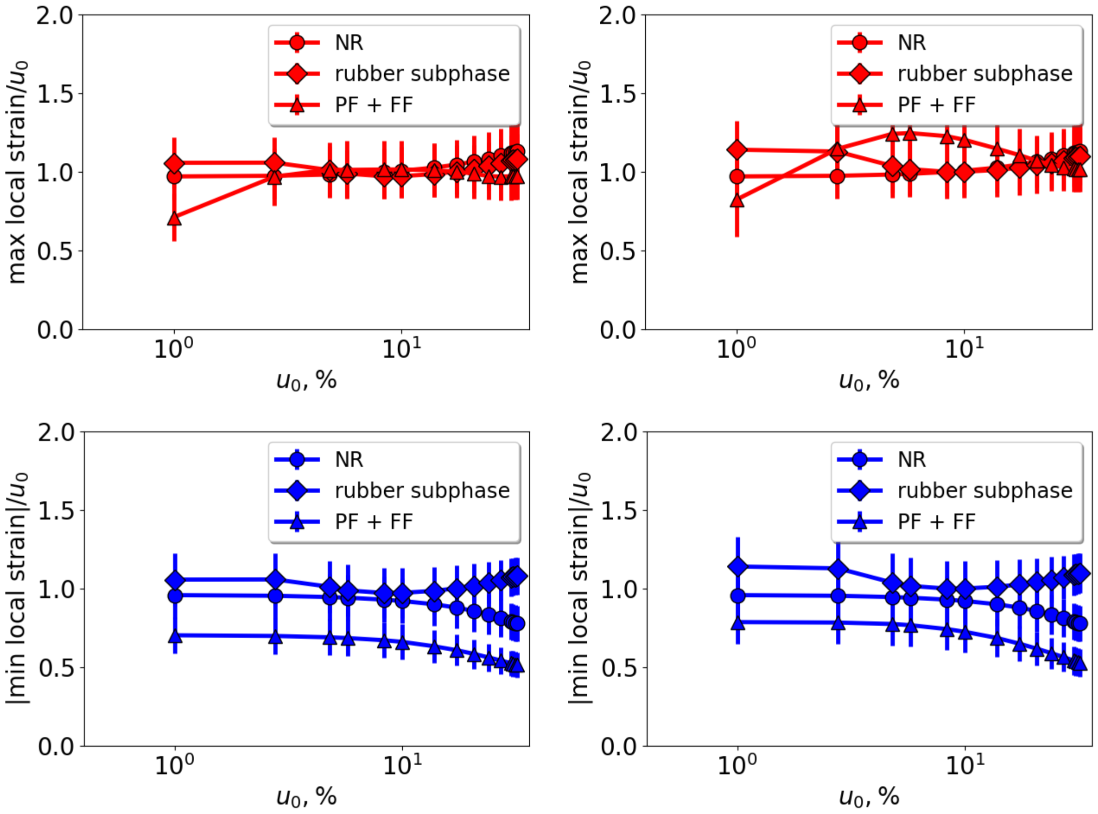

Figure 8.14: The ratios of the local maximal (elongation) in the top row or the absolute value of minimal (compression) strain in the bottom row to the global strain u_0 vs. u_0. The plots are done for the filled NR systems with 20% vol. filler ($\gamma_f^d = 20$ mJ/m^2) shown in Fig. 8.3. Left: $\gamma_f^p = 5$ mJ/m^2, right: $\gamma_f^p = 20$ mJ/m^2. The local strain values are shown for polymer-polymer bonds in the pure polymer ('NR'), polymer-polymer bonds in the filled system ('rubber subphase') and breakable bonds ('PF + FF'). The averages are calculated based on top/bottom 1% of bonds in each case. The frequency ω is 0.1.

while in the bottom row, the absolute value of the minimum local strain is shown (compression). In Fig. 8.14 one can also distinguish between different bond types in the system, e.g., polymer-polymer bonds in the filled system (rubber subphase) and breakable (polymer-filler and filler-filler) bonds. In addition, the results for pure NR are presented, which is used as a reference system. The values of the local elongation or compression are calculated based on 1% of bonds with either the highest or lowest value of the local strain, respectively. The error bars are obtained based on 5 subsystems, which are cut from the same larger system. Note that for breakable bonds, elongation is not a proper term because these bonds are broken for all local strains exceeding 1%; in this case we talk merely about a distance between two nodes. In general, the local strain is proportional to the global strain, making their ratio independent of the applied deformation. The ratio of the local strain to the global strain is close to one for all subphases, and large values of the standard deviations suppress the difference between the curves. In terms of compression, breakable bonds are the least deformed ones, while the strongest compression is observed in the rubber subphase of filled systems. It is worth noting that changing the ratio of bonds taken for the calculation of the values in Fig. 8.14 affects the ratio of the local strain to the deformation and the error. Taking 0.1% of bonds increases the ratio, while for 10% the ratio decreases to approximately 0.5.

Fig. 8.15 shows the ratios of the local strain to the global strain vs. global stress u_0 for the aforementioned systems at $\omega = 0.001$. In the top row, the curves for the elongation or maximal local strain are presented and in the bottom row – for the compression or minimal local strain. In comparison to the previous figure, showing the results at $\omega = 0.1$, in this case the respective ratios are up to 3-4 times larger. The comparison with the unfilled system shows that the rubber subphase in filled systems is subjected to larger elongations and compressions due to presence of filler. The breakable bonds are the least compressible, as they show the lowest values of the minimal local strain. While most curves do not change with u_0, and they are parallel to the x-axis, the maximal local strain for breakable bonds is about 0.5 at $u_0 = 1\%$ but increases for both systems with the strain amplitude. At this frequency, the respective values of the local strain (both maximal and minimal) for the flocculated system are also larger than for the dispersed one.

Fig. 8.16 complements Fig. 8.14 and presents the ratios of the maximal (top row) or minimal (bottom row) local stress to the average stress in the same systems as in Fig. 8.14 at the same frequency $\omega = 0.1$. The average stress is calculated as the total stress divided by the total number of bonds and, thus, represents the average 'energy density' supplied to the system. The error bars are calculated based on top or bottom 1% of the bonds in 5 subsystems with the same filler morphology for the maximal and minimal stress, respectively. Both the local and global stresses increase with the deformation, therefore their ratio is almost constant for all strain amplitudes. The largest values of both maximal and minimal local stress can be observed for the filler-filler bonds (FF). The maximal stress can be up to 50 times larger than the average stress in the system. The absolute value of the minimal local stress is at most 30 times larger than the average stress. The relative value of the local stress is close in both systems, i.e., it is not significantly affected by filler morphology. Rubber-rubber bonds in filled systems and in pure NR exhibit much

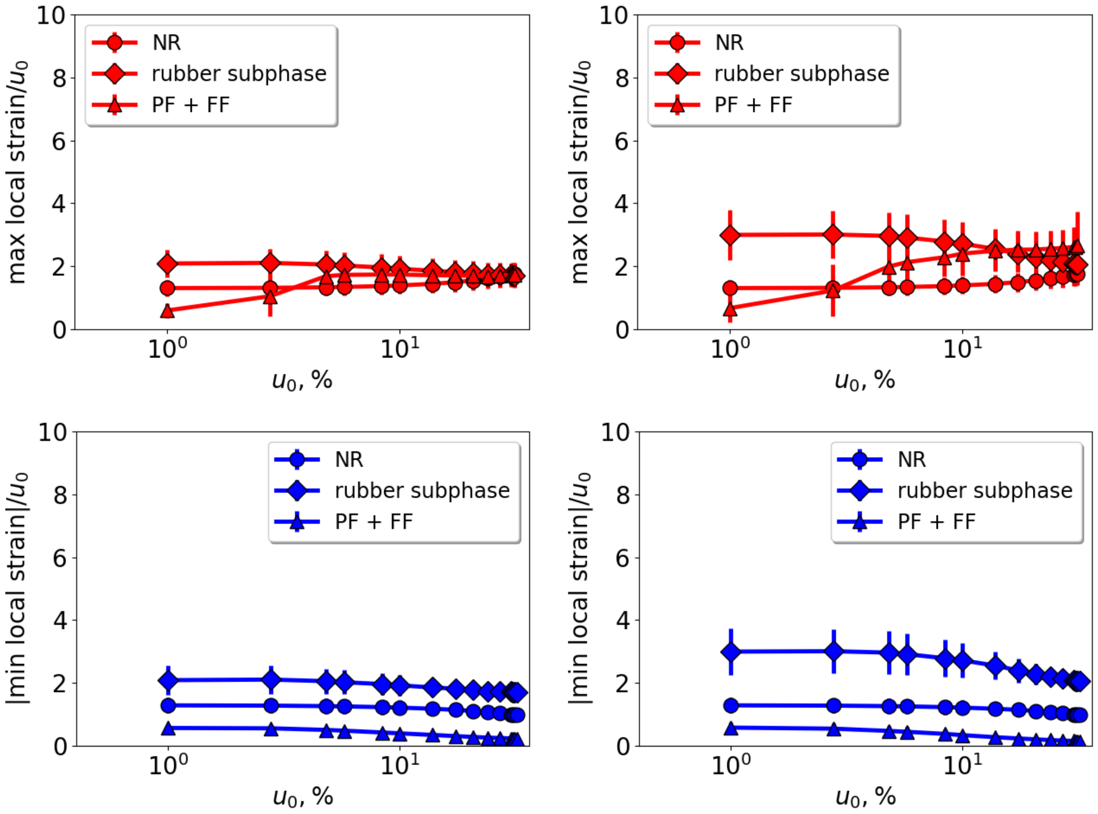

Figure 8.15: The ratios of the local maximal (elongation) in the top row or the absolute value of minimal (compression) strain in the bottom row to the global strain u_0 vs. u_0. The plots are done for the filled NR systems with 20% vol. filler ($\gamma_f^d = 20$ mJ/m^2) shown in Fig. 8.3. Left: $\gamma_f^p = 5$ mJ/m^2, right: $\gamma_f^p = 20$ mJ/m^2. The values of the local strain are shown for polymer-polymer bonds in the pure polymer ('NR'), polymer-polymer bonds in the filled system ('rubber subphase') and breakable bonds ('PF + FF'). The averages are calculated based on top/bottom 1% of bonds in each case. The frequency ω is 0.001.

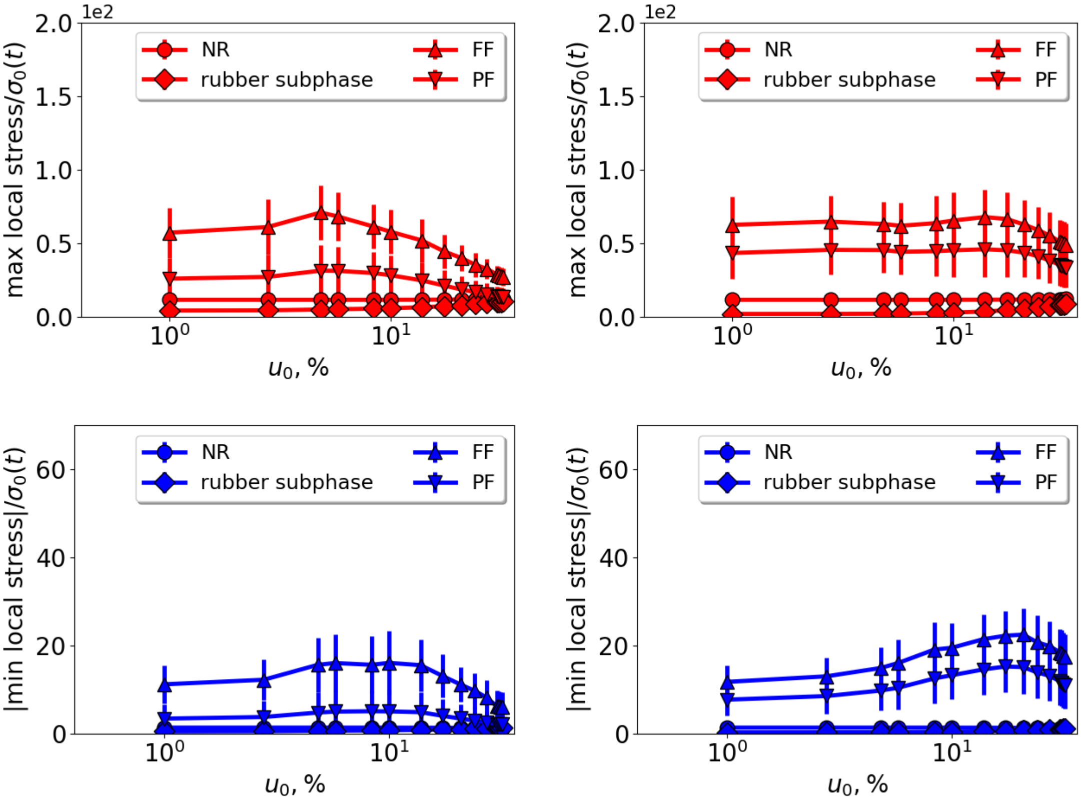

Figure 8.16: The ratios of the local maximal stress in the top row or the absolute value of minimal stress in the bottom row to the global stress σ_0 vs. u_0. The plots are done for the filled NR systems with 20% vol. filler ($\gamma_f^d = 20$ mJ/m^2) shown in Fig. 8.3. Left: $\gamma_f^p = 5$ mJ/m^2, right: $\gamma_f^p = 20$ mJ/m^2. The values of the local stress are shown for all types of bonds, i.e., polymer-polymer bonds in the pure polymer ('NR'), polymer-polymer bonds in the filled system ('rubber subphase') polymer-filler ('PF') and filler-filler ('FF') bonds. The averages are calculated based on top/bottom 1% of bonds in each case. The frequency ω is 0.1.

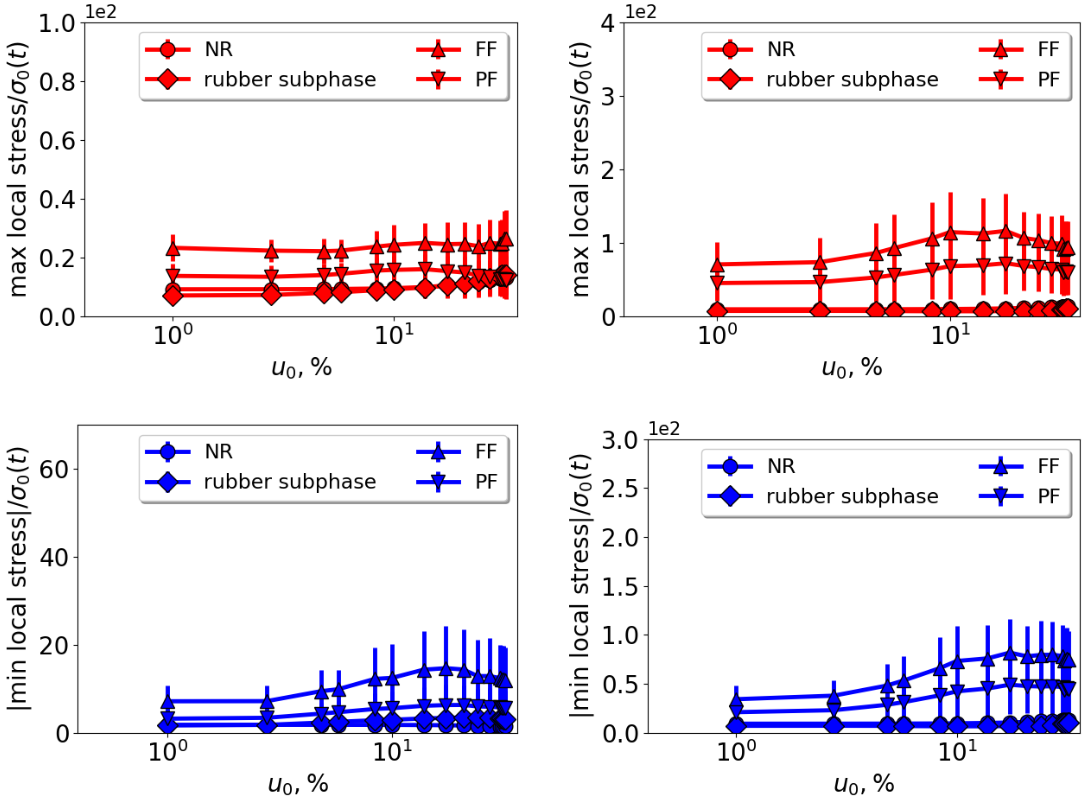

Figure 8.17: The ratios of the local maximal stress in the top row or the absolute value of minimal stress in the bottom row to the global stress σ_0 vs. u_0. The plots are done for the filled NR systems with 20% vol. filler ($\gamma_f^d = 20$ mJ/m^2) shown in Fig. 8.3. Left: $\gamma_f^p = 5$ mJ/m^2, right: $\gamma_f^p = 20$ mJ/m^2. The values of the local stress are shown for all types of bonds, i.e., polymer-polymer bonds in the pure polymer ('NR'), polymer-polymer bonds in the filled system ('rubber subphase') polymer-filler ('PF') and filler-filler ('FF') bonds. The averages are calculated based on top/bottom 1% of bonds in each case. The frequency ω is 0.001.

smaller stress than filler-filler and polymer-filler bonds, i,e., the stress propagates in the system mainly via filler-filler and polymer-filler bonds. This is probably expected due to the values of the force constants used for the stress calculation in (8.2). A large value of k_{FF} ensures a considerable relative contribution of filler-filler bonds to the total stress, while the contributions of other bonds are smaller.

The next Fig. 8.17 shows the ratios of the maximal (top) and minimal (bottom) local stress to the average stress at $\omega = 0.001$. The plots are similar to those shown in the previous figure. As at $\omega = 0.1$, the largest relative local stress is observed for the filler-filler bonds. The main difference to Fig. 8.16 is the effect of filler dispersion, which becomes apparent at $\omega = 0.001$. The relative value of the maximal local stress in the dispersed system (left) is about 5 times smaller than in the flocculated system (right). A similar ratio can be observed for the values of the minimal local stress. It is worth noting that increasing the number of bonds taken for the calculation of the average to 10% decreases the obtained local stress.

If, however, only top/bottom 0.1% bonds are considered, the obtained values rise significantly. Combining Figs. 8.14 – 8.17 leads to the conclusion that there are areas in the system where the local strain and stress are considerably larger than the applied deformation and the average stress, respectively. The number of such areas is small with respect to the total number of bonds, mainly it is 0.1-1% of all bonds which experience the significantly larger strain or stress. If we assume that damage is initiated in exactly those areas, then failure of a material starts in a small number of areas where locally the strain and stress are large. As the material approaches fatigue, the stress concentration areas begin to initiate microscopic cracks. The number and the size of the cracks will increase until the material fails.

Comparing Figs. 8.14 – 8.17 shows that the effect of filler dispersion on the local strain/stress strongly depends on frequency. At $\omega = 0.1$, there are little differences between the two morphologies. When $\omega = 0.001$, improving the filler dispersion decreases the local strain in the rubber subphase roughly by a factor of two and the local stress in the filler-filler interface – by a factor of five.

Fig. 8.18 shows the difference of two histograms obtained during the fifth and the first shear cycles vs. the local strain value at different global strain amplitudes given in the legend. On the y-axis the respective number of bonds is plotted. Two columns correspond to the above systems with different filler dispersions presented in Fig. 8.3. The top row shows the distribution for the polymer subphase of the filled system, while the bottom row presents the results for the breakable subphase. The breakable subphase includes polymer-filler and filler-filler bonds. The black lines at 1% strain in the bottom row divide the figures in two parts, beyond these lines the bonds are considered to be broken. Generally, the distributions for the rubber subphase at all strains are more symmetric than for breakable bonds. At high strain amplitudes, e.g., $u_0 = 10$ and 30 %, the width of the strain distribution increases from the first to the fifth cycle, i.e., the local compression and elongation become larger. During the first shear cycle, however, there are more bonds with the local strain close to zero. The width of the local strain distribution increases with the deformation amplitude, which complements the results shown in the Figs. 8.14 – 8.15. The distribution of breakable bonds is highly asymmetric, and the distances between nodes increase between the shear cycles. Contrary to the positive strain side of the plot, on the compression side the distribution is close to zero below approximately -20%.

It is worth noting that at $\omega = 0.001$, the deformation during different shear cycles yields similar distributions. The difference of the local strain histograms in this case is symmetric about the y-axis, while the absolute values are close to zero.

Obtaining similar histograms for the stress distribution is more complicated than for the strain distribution due to several reasons. Firstly, because stress is a microscopic value, the width of the distribution is much smaller. Secondly, for broken filler-filler bonds the stress is equal to zero. If there are many broken bonds in the system, the height of the central bin is considerable and often much larger than the height of other bins. Moreover, the comparison between different shear cycles did not show significant differences between the two, so the subtraction of the histograms in this case was close to zero. Therefore, here we limit ourselves to considering only examples of stress histograms obtained at different strain ampli-

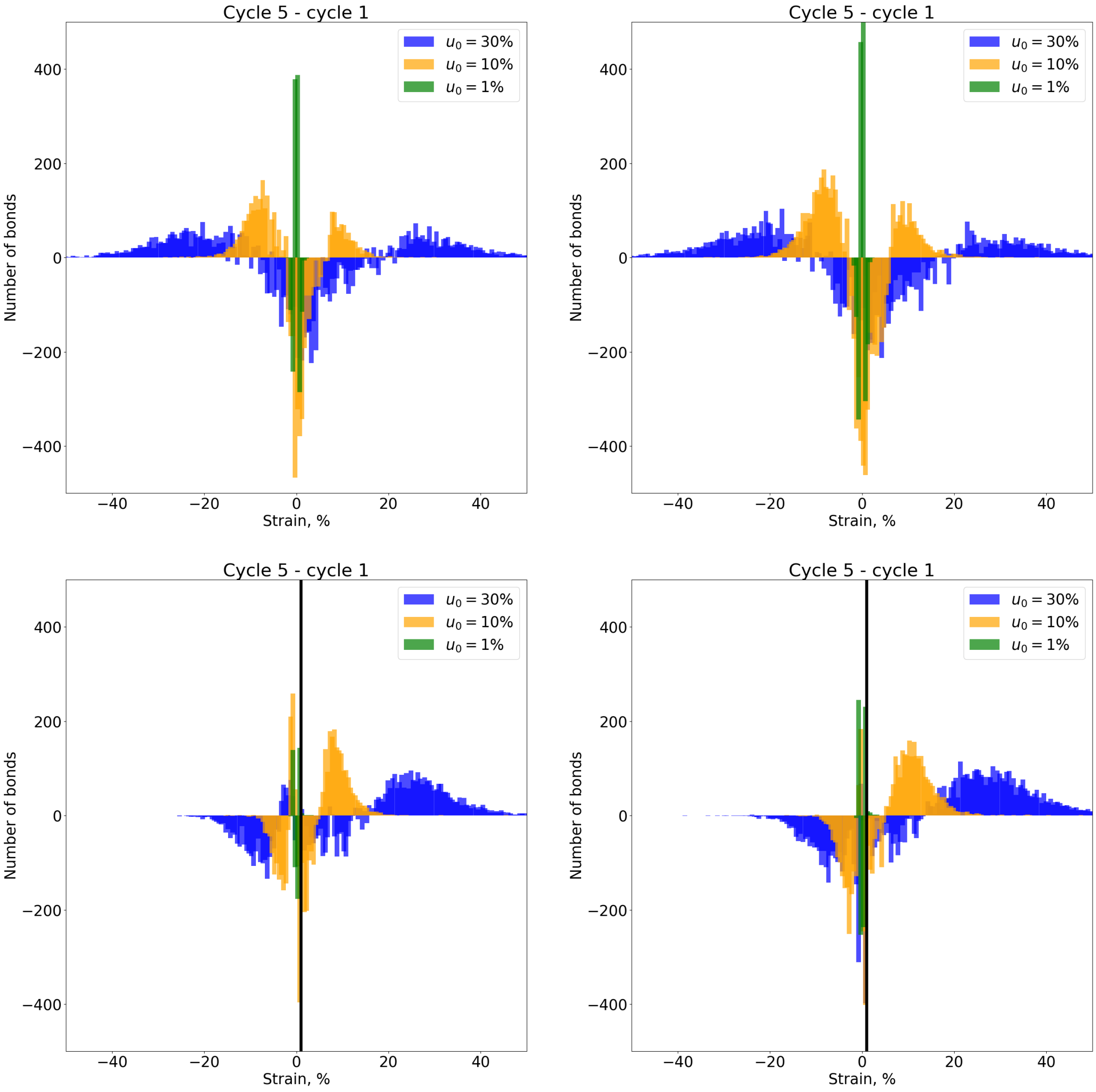

Figure 8.18: The difference of histograms obtained during the 5th and 1st shear cycles vs. the local strain value at different strain amplitudes given in the legend. Top: the polymer subphase, bottom: breakable bonds. The black lines in the bottom row are plotted at 1% of the local strain; all bonds with the local strain beyond this line are broken. The frequency ω is 0.1. The systems are filled NR shown in Fig. 8.3, left: $\gamma_f^p = 5$ mJ/m^2, right: $\gamma_f^p = 20$ mJ/m^2.

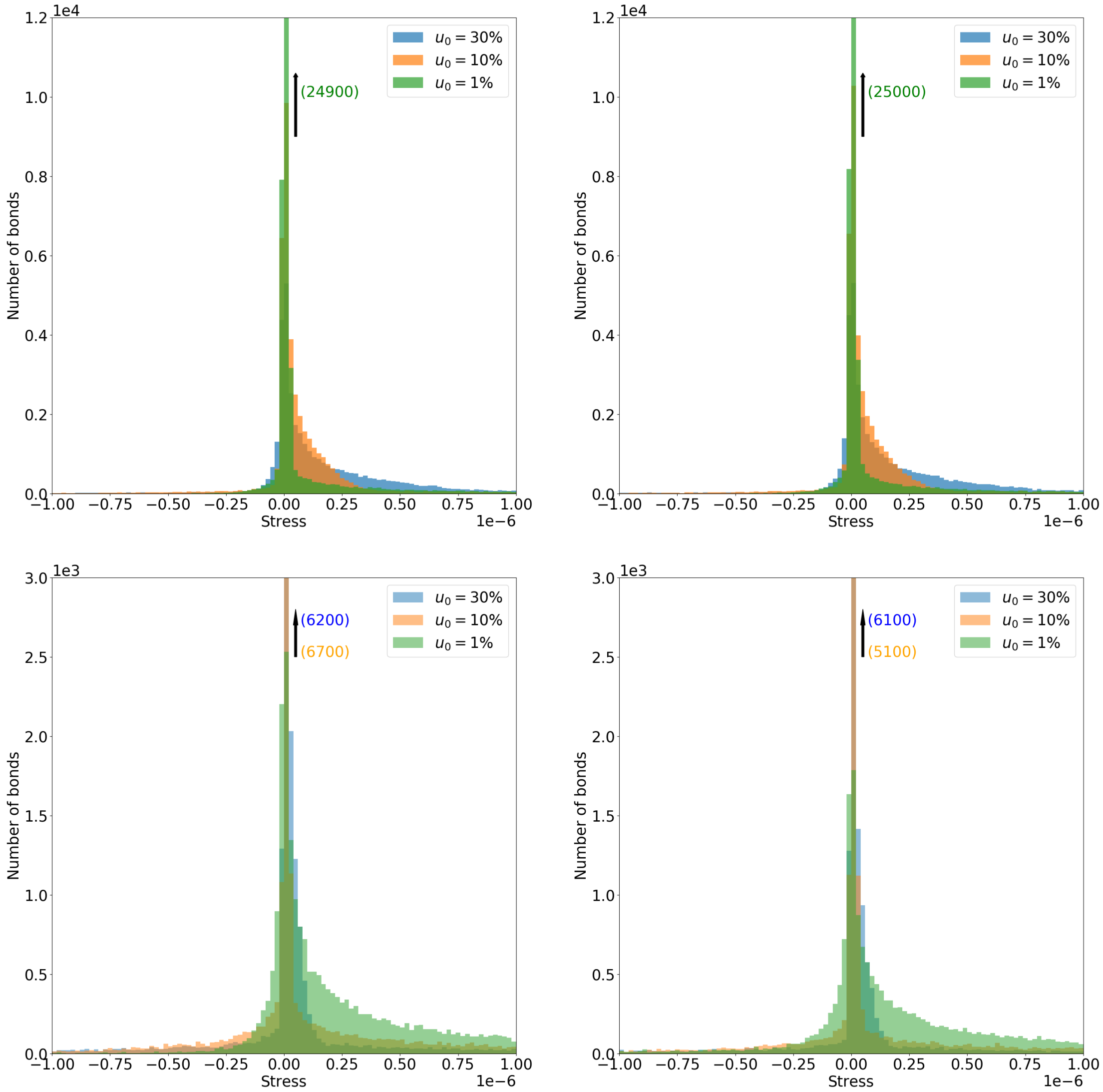

Figure 8.19: Histograms obtained during the first shear cycle vs. the local stress at different global strain amplitudes given in the legend. Top: the polymer subphase, bottom: breakable bonds. The systems are filled NR shown in Fig. 8.3, left: $\gamma_f^p = 5$ mJ/m^2, right: $\gamma_f^p = 20$ mJ/m^2.

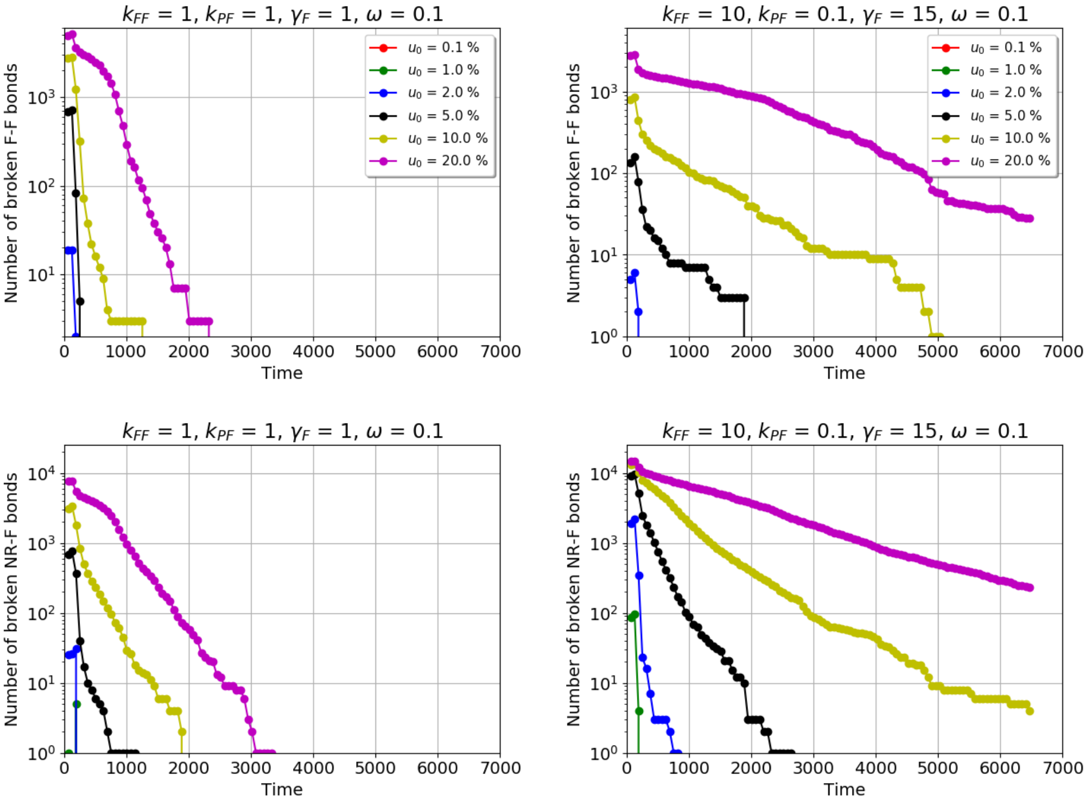

Figure 8.20: The number of open contacts vs. simulation time at different strain amplitudes given in the legend. Left: $k_{FF} = k_{PF} = 1$, right: $k_{FF} = 10$, $k_{PF} = 0.1$, $\gamma_F = 15$. Top: filler-filler bonds, bottom: polymer-filler bonds. In addition, the system is 20% filled NR with $\gamma_f^d = 20$ mJ/m^2, $\gamma_f^p = 20$ mJ/m^2 (the right panel of Fig. 8.3) at $\omega = 0.1$.

tudes.

Fig. 8.19 shows the histograms of the local stress at different global strain amplitudes given in the legend. On the y-axis, the respective number of bonds is plotted. The plots on the left-hand side correspond to the system with $\gamma_f^p = 5$ mJ/m^2 and on the right-hand side – to $\gamma_f^p = 20$ mJ/m^2. The top row is obtained for the polymer subphase of the respective filled system, and in the bottom row the results for breakable bonds are shown. Overall, the stress distributions are asymmetric for all presented cases, i.e., there are more bonds with a positive value of the local stress than with a negative value. This property is demonstrated by both polymer and breakable subphases. However, the latter can also be well distinguished based on the behaviour at different strain amplitudes. While in the polymer subphase the width of the distribution increases with the global strain value, it is opposite for the breakable bonds. The height of the central bin is also different depending on the strain amplitude and the bond type. Whereas in the polymer the height of the central bin drops with the deformation, in the breakable subphase it increases. When external strain increases, the internal stress rises and more and more filler-filler bonds break. For these bonds, the stress is equal or close to zero, therefore the height of the central bin becomes larger, and the values, that the microscopic stress can reach, are limited. In the rubber phase, the bonds cannot break, therefore larger deformations lead to increasing values of the local stress. At 1% strain, the local stress for most rubber-rubber bonds is close to zero.

8.5 Relaxation

The next example we consider in this chapter is the relaxation behaviour for a system with different values of k_{PF} and k_{FF}. As we have already shown in Fig. 6.13, filler dispersion can significantly affect the system relaxation, and due to similarity of the results here we consider only the NR filled system with $\gamma_f^p = 20$ mJ/m^2 shown in the right panel of Fig. 8.3.

In Fig. 8.20 two cases are presented, where in the left column $k_{PF} = k_{FF} = 1$ and in the right column $k_{FF} = 10$, $k_{PF} = 0.1$ and $\gamma_F = 15$. The procedure for obtaining these plots is the same as described in the discussion of Fig. 6.13. The top row shows the number of open filler-filler bonds, whereas the bottom row presents the plots for the broken polymer-filler bonds. Generally, the relaxation behaviour for different types of bonds is similar at various strain amplitudes and slows drastically when the force constants change. In addition, the number of broken polymer-filler bonds increases, while the number of open filler-filler bonds drops, which is in agreement with the results shown in Fig. 6.13. For instance, the polymer-filler interaction is weaker and the respective bonds break more often. For the same set of spring constants, the slowest relaxation is observed at the largest strain amplitude. In both cases, the polymer-filler bonds close slower than the filler-filler ones. On the other hand, the total number of polymer-filler bonds is significantly larger than the number of filler-filler bonds, which may affect the relaxation time.

It is worth mentioning that an attempt was made to simulate stress relaxation experiments, but the model was not capable of reproducing the experimental findings typical for such measurements.

8.6 The Payne Effect in Filled Elastomer Systems

In this section, we will study the Payne effect in filled systems for two main cases. In the first case, we mimic breaking of a relatively strong chemical bond with the subsequent formation of a much weaker physical bond. After a bond breaks once, it closes again with a spring having a weaker spring constant. For the filler-filler interaction, based on the difference in the bond energies, we assume that $k_{FF,\text{after break}} = 0.01 k_{FF}$ is reasonable, whereas for the polymer-filler interaction we set $k_{PF,\text{ after break}} = 0.1 k_{PF}$. In the second case, we make some types of bonds unbreakable in order to study the respective contributions of different bond types to the magnitude of the Payne effect.

In Fig. 8.21 the storage μ' (left) and loss μ'' (right) moduli vs. strain amplitude u_0 are presented for the systems from Fig. 8.3. The blue and green curves are obtained for the system with $\gamma_f^p = 20$ mJ/m^2 (right panel of Fig. 8.3), and red and yellow curves – for the system with $\gamma_f^p = 5$ mJ/m^2 (left panel of Fig. 8.3). The

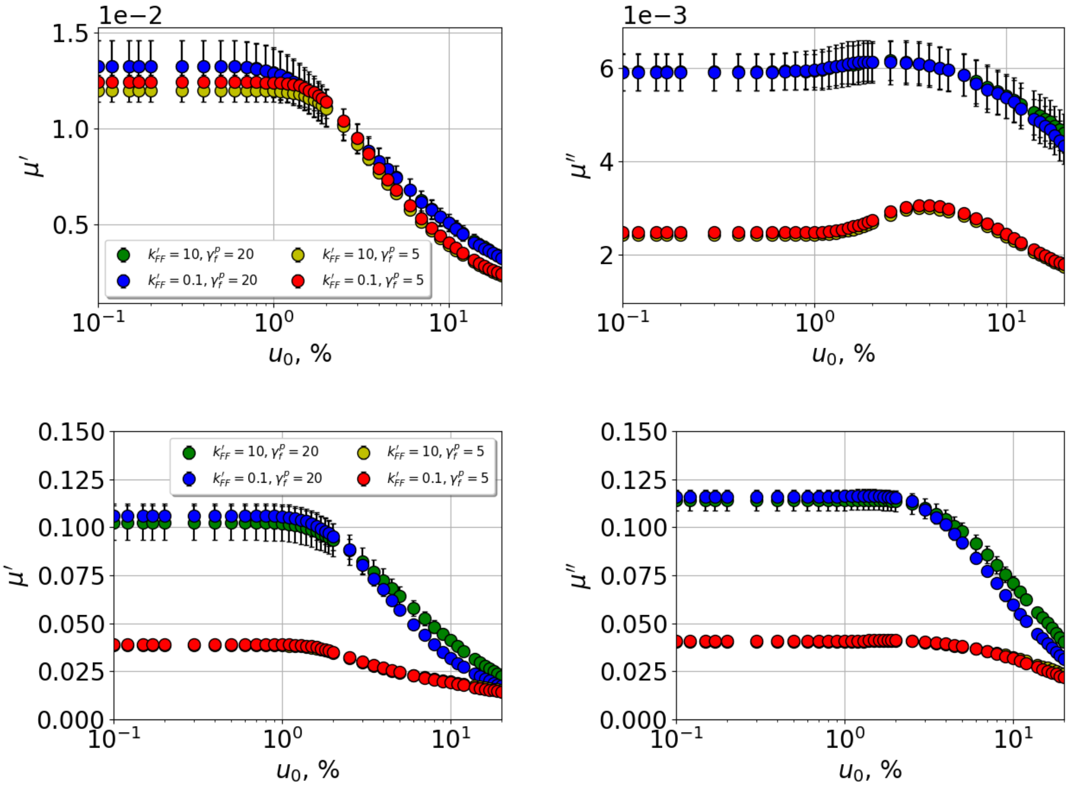

Figure 8.21: The storage μ' (left) and loss μ'' (right) moduli vs. strain amplitude u_0 for filled NR systems from Fig. 8.3. Top: $\omega = 0.001$, bottom: $\omega = 0.1$. The value of the filler-filler force constant after the break k' is varied between 10 (the same as before the break) and 0.1.

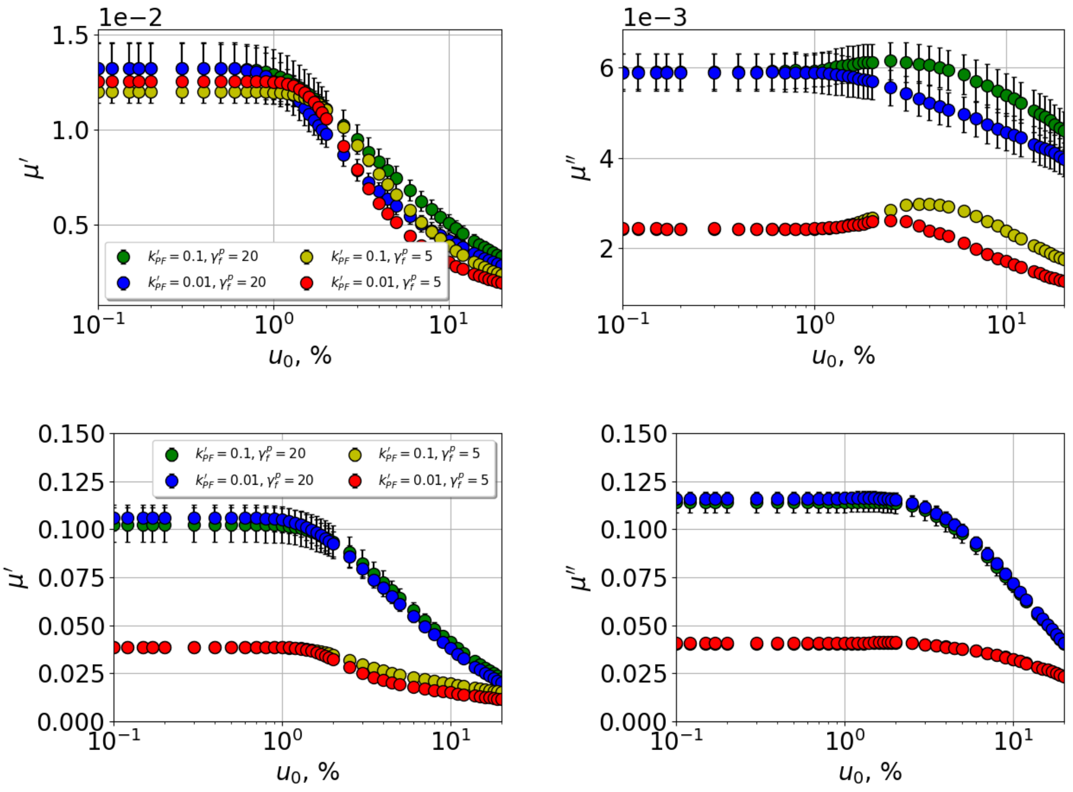

Figure 8.22: The storage μ' (left) and loss μ'' (right) moduli vs. strain amplitude u_0 for filled NR systems from Fig. 8.3. Top: $\omega = 0.001$, bottom: $\omega = 0.1$. The value of the polymer-filler force constant after the break k' is varied between 0.1 (the same as before the break) and 0.01.

colour coding remains unchanged in the remainder of this section. The top row corresponds to $\omega = 0.001$, and the bottom row – to $\omega = 0.1$. Here we vary the value of k_{FF} after the break, i.e., after a filler-filler bond reversibly opens it closes again with a weaker spring constant $k'_{FF} = 0.01k_{FF} = 0.1$. The attendant curves for the dynamic moduli (blue and red) are then compared with the ones obtained for the case when no alterations in k_{FF} are made (green and yellow). Note that the respective storage modulus at $\omega = 0.1$ and the loss moduli at both frequencies for the system with the fine dispersion lie below the curves for the system with $\gamma_f^p = 20$ mJ/m^2. However, the difference between the results for various k'_{FF}-values after the break appears to be minor. For the dispersed system the difference in the moduli values is within the error bars, while for the flocculated system at $\omega = 0.1$ and $u_0 > 3\%$ the moduli are slightly smaller when $k'_{FF} = 0.1$. This result is probably expected because the number of performed shear cycles in the simulation is small. In real systems, any dramatic changes in the dynamic moduli during the first deformation cycles are also uncommon due to quality standards ensuring nearly constant performance throughout the life cycle of products.

In the next Fig. 8.22, the alterations are made in the value of the polymer-filler force constant after the break k'_{PF}. At $\omega = 0.1$, for both systems no considerable changes are observed between the cases when $k'_{PF} = 0.1k_{PF}$ (blue and red) and $k'_{PF} = k_{PF}$ (green and yellow). The dynamic moduli for the flocculated system are about two times larger than the moduli for the dispersed system. At $\omega = 0.001$, the storage moduli for these two systems are close to each other, and both drop in the range of the onset of the Payne effect, when k'_{PF} is reduced. The loss modulus for the dispersed system is about three times smaller than for the flocculated system. When $k'_{PF} = 0.1k_{PF}$, the height of the loss modulus peak decreases for both systems, and for the system with $\gamma_f^p = 20$ mJ/m^2 the peak completely vanishes. Hence, the height of the loss modulus peak at $\omega = 0.001$ depends on the polymer-filler coupling strength k_{PF}.

In Fig. 8.23 the blue curve for $\gamma_f^p = 20$ mJ/m^2 and the red curve for $\gamma_f^p = 5$ mJ/m^2 are obtained when filler-filler bonds in the system are unbreakable. They are compared with the case when no alterations are made (the green curve for $\gamma_f^p = 20$ mJ/m^2 and the yellow curve for $\gamma_f^p = 5$ mJ/m^2). As above, in the top row $\omega = 0.001$ and in the bottom row $\omega = 0.1$. At the low frequency, only subtle differences within the error bars can be observed for both systems. At the high frequency, however, the magnitude of the Payne effect is significantly reduced for both moduli. The loss modulus is more affected and becomes almost independent of the strain amplitude. This drop of the Payne effect magnitude is also considerably larger in the flocculated system than in the dispersed one. The finding leads us to the conclusion that the contribution of the filler-filler contacts to the magnitude of the Payne effect depends not only on frequency but also on filler dispersion.

The aforementioned effect was found not only for the filler-filler bonds but also for the polymer-filler bonds. In Fig. 8.24 the blue ($\gamma_f^p = 20$ mJ/m^2) and red ($\gamma_f^p = 5$ mJ/m^2) curves show the dynamic moduli when the polymer-filler bonds in the system are unbreakable. The green ($\gamma_f^p = 20$ mJ/m^2) and yellow ($\gamma_f^p = 5$ mJ/m^2) curves show the dynamic moduli for breakable polymer-filler bonds. In the top row $\omega = 0.001$, and in the bottom row $\omega = 0.1$. At the high frequency ω

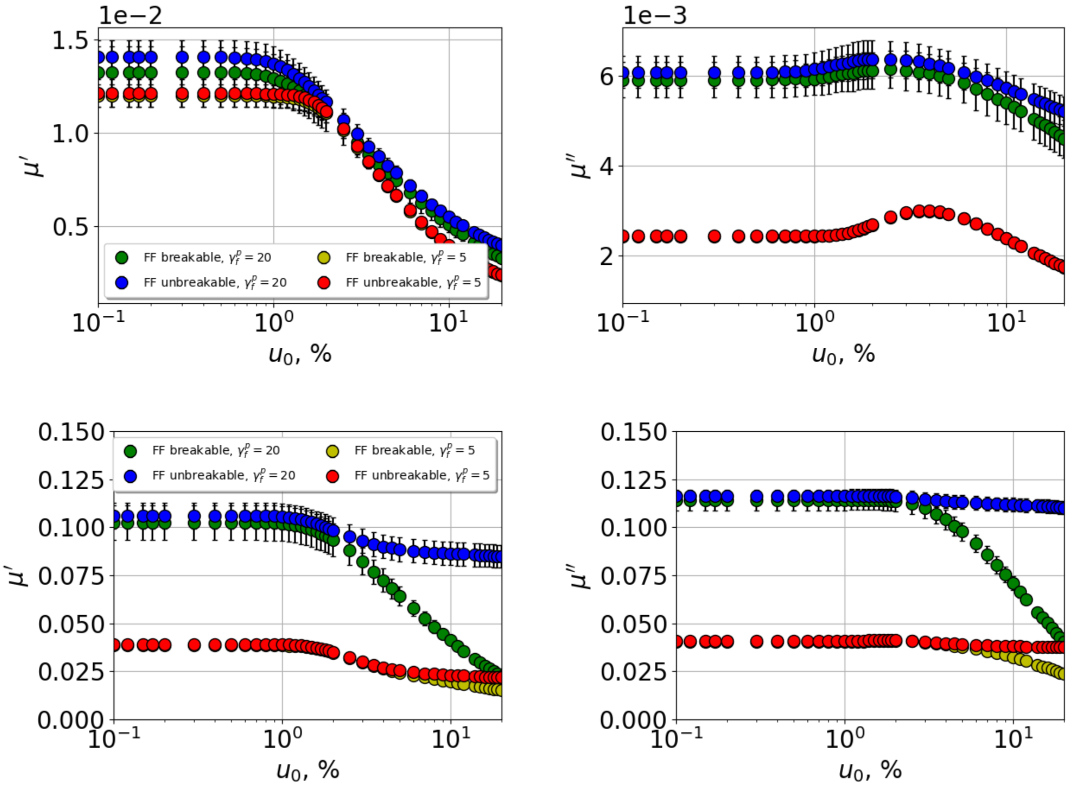

Figure 8.23: The storage μ' (left) and loss μ'' (right) moduli vs. strain amplitude u_0 for filled NR systems from Fig. 8.3. Top: $\omega = 0.001$, bottom: $\omega = 0.1$. Green and yellow: filler-filler bonds are breakable; blue and red: filler-filler bonds are unbreakable.

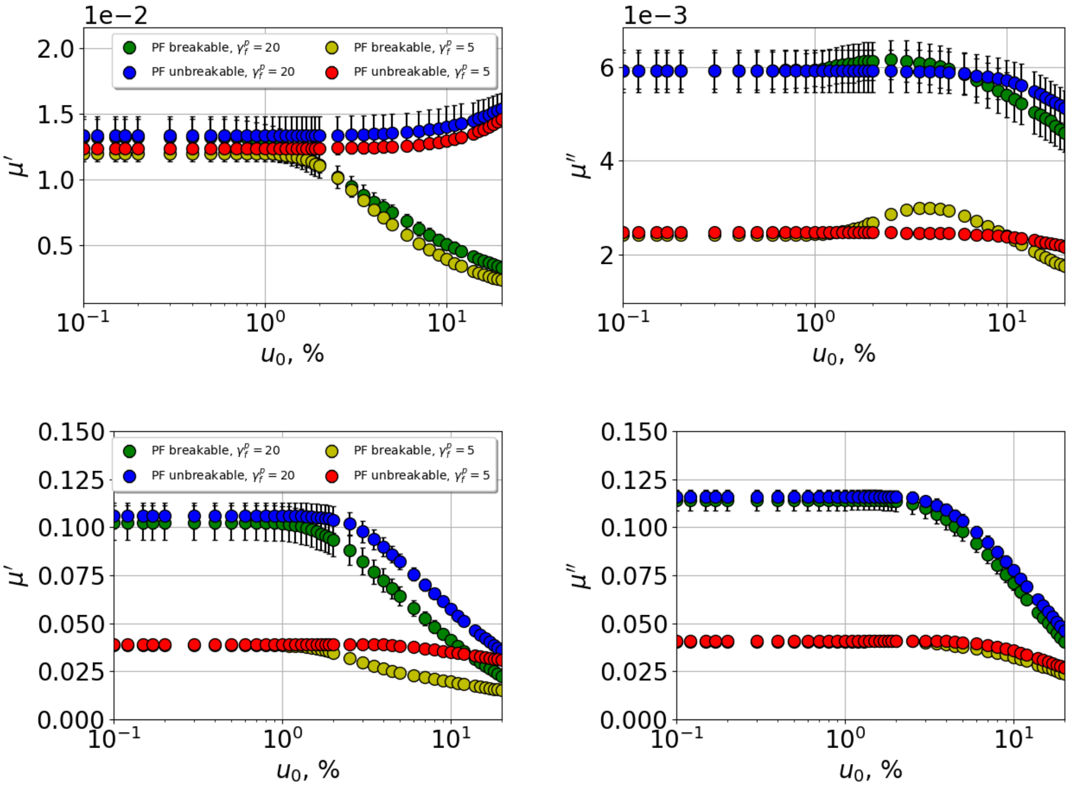

Figure 8.24: The storage μ' (left) and loss μ'' (right) moduli vs. strain amplitude u_0 for filled NR systems from Fig. 8.3. Top: $\omega = 0.001$, bottom: $\omega = 0.1$. Green and yellow: polymer-filler bonds are breakable; blue and red: polymer-filler bonds are unbreakable.

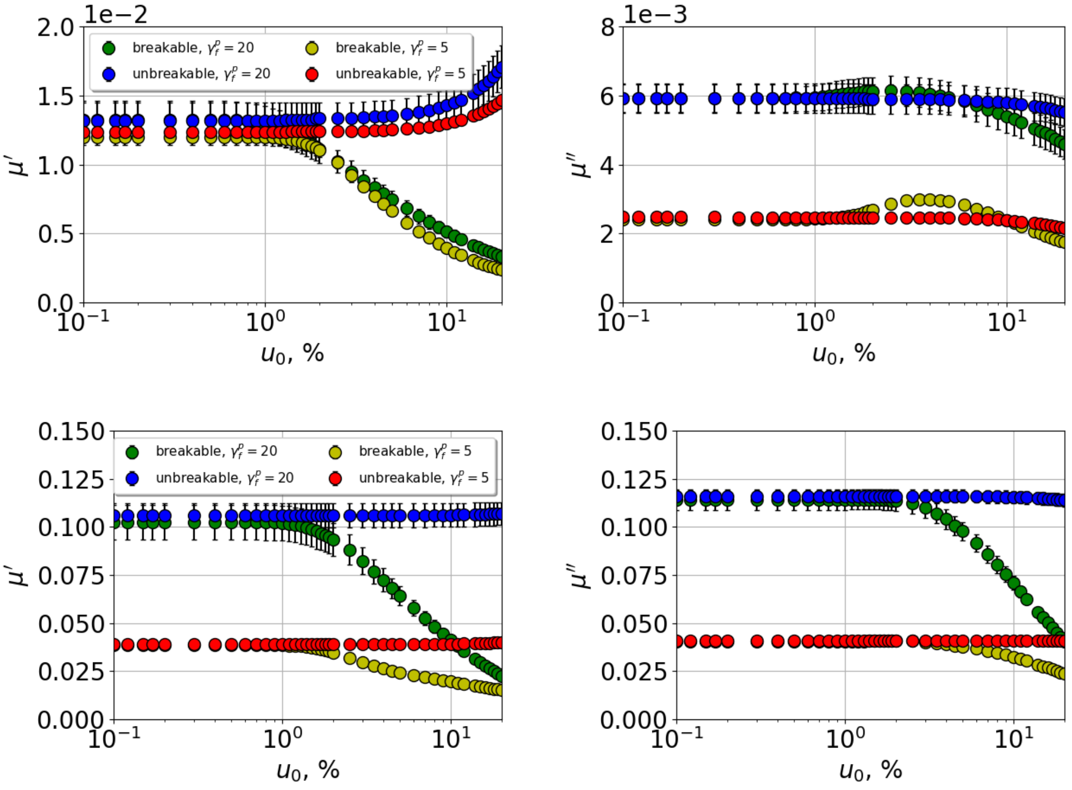

Figure 8.25: The storage μ' (left) and loss μ'' (right) moduli vs. strain amplitude u_0 for filled NR systems from Fig. 8.3. Top: $\omega = 0.001$, bottom: $\omega = 0.1$. Green and yellow: filler-filler and polymer-filler bonds are breakable; blue and red: all bonds are unbreakable.

= 0.1, in the bottom row the difference between the two cases can be mainly seen in the value of the storage modulus, where the Payne effect magnitude drops for both systems. The loss modulus is unaffected by this change, and in this case, the difference remains small. At the low frequency, one can observe an absence of the Payne effect for the storage modulus in both systems, i.e., μ' is constant within the strain amplitude range. The loss modulus also becomes nearly independent of strain. While the values of the moduli at small strains do not change, as the strain amplitude increases, the difference between the moduli for systems with breakable and unbreakable polymer-filler bonds becomes larger. We found as well that the μ''-peak disappears; this effect is more noticeable in the dispersed system, where the contribution of the polymer-filler bonds to the magnitude of the Payne effect is more significant than that of the filler-filler bonds.

In Fig. 8.25 the dynamic moduli vs. strain amplitude are shown when PF and FF bonds are breakable (the green curve for $\gamma_f^p = 20$ mJ/m^2 and the yellow one for $\gamma_f^p = 5$ mJ/m^2) and when all the bonds are unbreakable (the blue curve for $\gamma_f^p = 20$ mJ/m^2 and the red one for $\gamma_f^p = 5$ mJ/m^2). In the latter case, no Payne effect can be expected, as all bonds in the system resemble unbreakable polymer-polymer bonds with different interactions strengths. And this is exactly what happens with the dynamic moduli in Fig. 8.25. Both the storage and the loss moduli are independent of the applied strain. The systems with unbreakable bonds are close in their characteristics to unfilled polymer systems in the sense that they do not exhibit the Payne effect which is typical for filled elastomers.

The model provides useful insights to the sources of the Payne effect in filled elastomer systems. The Payne effect, which is caused by dissipation processes in the filler network, has a complex nature. It has been a long-standing question whether the Payne effect is due to filler-filler or polymer-filler bonds. As shown above, this question does not have a simple answer. The contributions of filler-filler and polymer-filler contacts to the magnitude of the Payne effect depend not only on filler dispersion, but also on frequency. At frequencies significantly below the glass transition, the contribution of the filler-filler bonds dominates. As the frequency decreases, the dissipation from polymer-filler contacts overcomes the contribution due to filler-filler bonds and becomes essential for the Payne effect.

Chapter 9

Conclusion

The main goal of this work was the development of a modelling approach relating filler dispersion in filled elastomers, based on the experimental surface energies of individual components, to the mechanical properties of elastomer composites. The approach combined two models. The first one was an extension of previous work [19–21], which presents a coarse-grained model to filler flocculation based on the Metropolis Monte Carlo simulation. Filler flocculation is a process, which leads to re-agglomeration of initially well dispersed filler particles in the post-mixing stages [10–17]. This algorithm, called the morphology generator, minimizes the free enthalpy of the system, and the interactions between different components are described via the experimental interface free energies. The second model performed shearing of the systems obtained via the morphology generator to obtain the storage and loss moduli as well as their ratio – $\tan\delta$. This simulation mimics the dynamic mechanical analysis, or DMA, which is widely used in laboratories to measure the mechanical performance of tire materials. One of the most important effects in this context is the so-called Payne effect, i.e., the pronounced decrease of the complex modulus with increasing strain amplitude in filled elastomers under cyclic loading [32–36]. A long standing question, which was addressed here, is the relative importance of polymer-filler vs. filler-filler interactions in this context [37]. Generally, the model provides a connection between the chemical composition, characterized by the experimental surface free energies, and the mechanical properties of the material and can serve for a laboratory prediction of material performance parameters. In this work, we concentrated on the dispersion in the range from primary particles to the filler network on the scale of up to several μm. The main focus was on natural rubber (NR), styrene butadiene rubber (SBR) and fillers with different surface energies as well as on their combinations.

In Chapter 3, the morphology generator algorithm (MG) was discussed. In addition, the concepts of wetting-envelope – work of adhesion plots and simulated transmission electron micrographs (TEM) were introduced. The main result of this chapter was the generalization of the previous morphology generator. The original cubic lattice was replaced by a neighbour list allowing a variable number of neighbouring nodes. Nodes are volume elements, whose entirety is the material sample, representing polymer or filler particles. These particles are the smallest unbreakable filler entities. Neighbouring nodes share a common interface. Here the number of neighbours a node has is close to the number of neighbours a molecule has in a liquid. This ensures the isotropy of the elastomer material. The new MG was tested, compared to the previous one and parameters, like the number of neighbours a node can have, were optimized. Typically, the MG operates on systems consisting of roughly 10^6 nodes. Due to the local nature of the site-exchange Monte Carlo steps, the number of steps can, albeit roughly, be compared to time.

The output of the MG, i.e., a neighbour list representing the system morphology at this 'time', becomes the input of the DMA modelling. This was discussed in Chapter 4. The main result of this chapter was an algorithm, which converts the neighbour list to an attendant network of nodes linked via viscous springs. A dynamically changing shear profile drives the network and the nodes in it. The trajectories of the latter were obtained by solving the force equilibrium subject to shear-adapted boundary conditions. Test runs yielded stress-strain behaviour in good accord with real experiments on linear (unfilled) as well as non-linear (filled) systems. Due to the increase in computational effort compared to the MG, in particular when the shear frequency is low, the DMA system size was reduced to about 10^4 nodes. Final results were averages over, usually, five independent systems of this size.

The main objective of Chapter 5 was to find the parameters for both parts of the model, i.e., the MG and the DMA. The parameters for the MG part were adjusted based on the comparison of the simulated morphologies to experimental TEM images. The size of agglomerates and their connectivity depended to a large extent on the simulation time. If the simulation time was too long, the loss of connectivity between filler agglomerates was observed. Therefore, comparing the agglomerate size in the simulated and experimental TEMs was essential for determining a proper number of MC steps in the MG. For the parametrization of the DMA part, it was found that two force constants with substantially different force constants are required to model loss tangents of unfilled polymers. These force constants were distributed randomly in the system. By a proper choice of the force constant values and their ratios, this approach allowed to simulate the heights of pure NR and SBR peaks, as well as the separation between them. Unfilled blends can be modelled using mixing rules, where the force constants in the polymer interface are combinations of the force constants for pure polymers. The ratio between the 'weak' and 'strong' spring constants in the interface had a significant impact on the $\tan\delta$ peak heights for unfilled blends. When filler is added, there is a certain filler concentration, called the percolation threshold, at which the filler network forms. The filler network formation leads to significant changes in the mechanical properties of filled elastomers. The force constants for the polymer-filler and the filler-filler interactions were chosen so that the power law increase of the simulated storage modulus as a function of filler volume content reproduces the experimental one beyond the percolation threshold. Also, the effects of the bond breaking distances and the filler morphology on the dynamic moduli of filled systems were studied. In order to obtain the $\tan\delta$ curves for different filler contents at low frequencies in accord with experiments, the relaxation time in the polymer-filler interface must be significantly increased. Experimentally, this situation would correspond to a formation of a polymer layer with less mobility and slower dynamics than in the bulk. An important result in this context was the discovery that the long relaxation time in the polymer-filler interface has an impact on the loss tangent in the low frequency range – the range of particular importance in terms of rolling resistance. The force constants for SBR filled systems were found to be close to those used for NR filled elastomers.

The next three chapters were applications of the MG/DMA modelling tool.

Chapter 6 was devoted to filled systems, consisting of a polymer and a filler. The main objective of the chapter was to study the effects of different parameters such as filler morphology, filler volume content and flocculation time on mechanical properties of filled systems consisting of one polymer plus filler. We varied gradually the dispersive and polar parts of the filler surface energy and looked at the dynamic moduli and $\tan\delta$ as functions of either strain amplitude or frequency. It was found that the filler polarity, determined by the filler type, has a more significant effect on the dynamic moduli and the Payne effect than the filler size. The latter can in turn be related to the dispersive contribution of the filler surface energy. The impact of the filler content variation depended on the filler type, but in general, and in accord with experiments, the magnitude of the Payne effect increased with the filler concentration. Generally, the dynamic moduli increased with the number of MC steps, which roughly corresponds to flocculation time. The plotted curves were similar to experimental ones obtained in flocculation tests. In that chapter, we also proposed an approach for a more experiment-based choice of the polymer-filler force constants. Each polymer-filler force constant was set to be proportional to the interface tension of the respective pair 'polymer-filler'. Based on this approach, we considered an example of three fillers widely used in the tire industry, i.e., carbon black, silica and silanized silica in NR. We studied the filler dispersion, the Payne effect and the relaxation behaviour in these systems. The order of the Payne effect-curves corresponded to the experimental one. The magnitude of the Payne effect increased with the agglomerate size, i.e., finer dispersion leads to better performance. The carbon black filled system exhibited the fastest relaxation, while the system with silanized silica – the slowest. This finding was also supported by stress relaxation experiments.

In Chapter 7, the main focus was on the mechanical properties of filled polymer blends consisting of NR, SBR and a filler. We studied the filler distribution and enrichment of polymer subphases by different fillers depending on their surface energy. The filler morphology had a strong impact on the dynamic moduli of filled blends. The magnitude of the Payne effect was the smallest for the system with the finest dispersion and increased for the conventional fillers, i.e., carbon black, silica and silanized silica. The dynamic moduli of the 50-NR/50-SBR blend filled with carbon black increased with the filler volume content. Adding of filler, however, suppressed the difference in the mechanical properties between blends with various blend ratios.

In the last Chapter 8, we studied bond breaking, the Payne effect and local strain and stress in two filled NR systems with substantially different filler dispersions. The main objective was to study the bond breaking in order to separate the contributions of the polymer-filler and filler-filler bonds to the Payne effect. Another question was to determine how much local strain and stress in some areas of the system, i.e., different interfaces or the polymer subphase, differ from the average stress or applied strain. The latter can provide information on possible mechanisms of damage initiation and fatigue. An ultimate goal was to determine and visualize the load bearing paths in the system. It was found that the ratio of the broken polymer-filler and filler-filler bonds depends on filler dispersion and the force constant values describing the interaction strength between nodes. The ratio of broken bonds increased with frequency, strain amplitude and filler volume content. The ratio of broken filler-filler bonds was smaller for the dispersed system. The bond orientation affected the probability for a bond to break; the largest ratio of broken bonds was found for the bonds parallel to the strain direction. The largest local stress concentrated in the filler domains, while the largest local strain – in the polymer phase. For a small fraction of bonds (0.1 - 1%) the local stress significantly exceeded the average stress, and the local strain was considerably larger than the applied strain. If damage starts in areas with substantial strain/stress, the number of such areas should be small, and the initiation of permanent damage is a relatively rare event. This effect also depended on frequency; at low frequencies the system had enough time to redistribute the load, and the respective local stress and strain were larger. The local strain and stress distributions were also studied using histograms at different strains and shear cycles. The values of the polymer-filler and filler-filler force constants after the first break hardly had an effect on the dynamic moduli. Making certain types of bonds unbreakable, however, led to a reduction of the magnitude of the Payne effect. The effect of the filler-filler bonds was stronger at the higher frequency, and the effect due to the polymer-filler bonds – at the lower frequency. Thus, the contributions of the polymer-filler and filler-filler contacts to the Payne effect were different and depended on frequency. At frequencies near the glass transition, the contribution of the filler-filler bonds dominates, so the filler-filler bonds play a more important role in grip properties of the material. As frequency dropped, the dissipation from polymer-filler contacts increased and eventually overcame the contribution of the filler-filler bonds, i.e., the polymer-filler contacts are more important for rolling resistance.

Overall, the presented model can be used as a tool for the development of novel elastomer composites with desired mechanical properties. The model is capable of reproducing a series of important experimental findings and can be easily extended to more than three components. The model also allows to study macroscopic material properties in relation to the internal dynamics and relaxation – the information which otherwise is nearly impossible to obtain. However, the predictive power of the model strongly depends on its input, i.e., the quality of experimental surface tensions. Unfortunately, most of the currently available data for the dispersive and polar parts of filler and, in part also, polymer surface tensions are quite inaccurate. Much of what this model can accomplish in the future will depend on improving these measurements to an accuracy of 10% and better.

Appendix A

Surface Free Energies

In this chapter, we will explain the terms 'surface tension' and 'surface energies'. In addition, the main experimental techniques for measuring surface energies will be discussed.

A.1 Surface Tension and Surface Energies

In materials science, the terms surface free energy and surface tension are often used interchangeably, although, the term 'surface tension' refers only to liquids, while the term 'surface free energy' is more general and can be used when referring to solids. The molecules on the surface of a material have different energy compared to molecules in the bulk of the material, and exactly this excess of energy is called the surface energy. On the other hand, we can define the surface energy as the work required to create two surfaces by cutting a bulk sample.

At a constant pressure P and a temperature T, the Gibbs free energy G is the quantity which is commonly used to thermodynamically describe a system [145]. According to the first law of thermodynamics, we find for the internal energy of the system

$$dE = dq - dw + \sum_i \mu_i dN_i. \tag{A.1}$$

Here q is the heat, w is the work done by the system, μ_i is the chemical potential and N_i is the number of moles of the i-th component. The work done by the system can be split into two components, i.e., expansion of the system and extension of the surface

$$dw = PdV - \gamma dA. \tag{A.2}$$

Here γ is the surface tension or the force per unit length required to extend the surface A. Using $G = H - TS$, $H = E + PV$ and $dq = TdS$, where H is the enthalpy and S is the entropy, we find for the free enthalpy

$$dG = VdP - SdT + \gamma dA + \sum_i \mu_i dN_i. \tag{A.3}$$

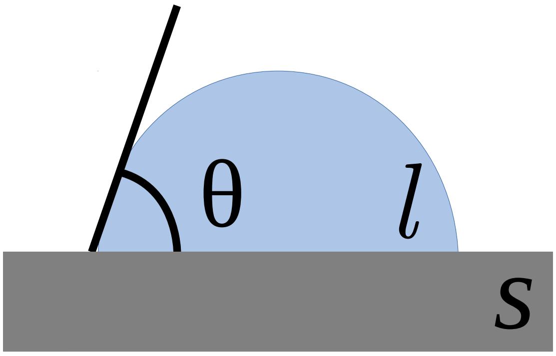

Figure A.1: A drop of a liquid l (sessile drop) on a smooth solid substrate s. The contact angle θ is defined between the interface of the liquid with its vapour and the surface of the solid.

The surface tension is then

$$\gamma = \frac{\partial G}{\partial A}\Big|_{P,T,N_{j\neq i}}. \tag{A.4}$$

The surface tension is thus the change in the Gibbs free energy of the system corresponding to the unit increase in the surface area. In the case of liquids, it is equal to the surface free energy, which is defined as the change in the Gibbs free energy of the surface associated with a unit increase in the surface area. For a solid, due to stretching, both quantities are not necessarily equal.

A.2 Contact Angle and Interface Tension

The surface energy is an essential quantity in studying the wetting phenomena of liquids on solids. A measure of the wettability is a contact angle – the angle between a liquid-vapour interface and a solid surface, shown in Fig A.1. The surface energy can be related to the contact angle via the Young equation

$$\gamma_s - \gamma_{sl} = \gamma_l \cos\theta. \tag{A.5}$$

Here γ is the surface energy and the subscripts s and l correspond to the solid substrate and the probe liquid, respectively; γ_{sl} is the interface tension or interfacial energy between the solid and liquid phases; θ is the contact angle. The situation when $\theta = 0°$ is called perfect wetting; in this case the adhesion, or the interaction between the liquid and the solid, is stronger than the cohesion, i.e., the interaction between the liquid molecules or between the solid molecules. When $\theta = 180°$, the cohesive forces are stronger than the adhesive ones, and no wetting is observed. The values of the contact angle between 0° and 90° yield wetting of the surface being favourable and correspond to high wettability. Generally, the Young equation assumes the equilibrium state and that the solid surface is smooth and homogeneous.

When a solid and a liquid surfaces are put together, the attractive solid-liquid interaction reduces the interface tension by the solid-liquid work of adhesion W_a. This is expressed in the Dupré equation

$$W_a^{sl} = \gamma_s + \gamma_l - \gamma_{sl}. \tag{A.6}$$

There exist several approaches to deriving the interface tension based on the surface energies of a liquid and a solid. One of the most common ones is the approach of Owens, Wendt, Rabel und Kaelble, also known as the OWRK theory [146],

$$\gamma_j \equiv \gamma_{sl} = \gamma_s + \gamma_l - 2\Big(\sqrt{\gamma_s^d \gamma_l^d} + \sqrt{\gamma_s^p \gamma_l^p}\Big). \tag{A.7}$$

The interface energies γ_s and γ_l consist of the dispersive and polar parts, i.e, $\gamma_s = \gamma_s^d + \gamma_s^p$ and $\gamma_l = \gamma_l^d + \gamma_l^p$. The dispersive part is due to the London dispersion forces, while the polar component includes Keesom, Debye and acid-base interactions.

The approach of Fowkes [147] is typically used for hydrocarbons, such as alkanes and other non-polar compounds because it doesn't consider any polar interactions. The interface tension in this approach is given by $\gamma_{12} = \gamma_1 + \gamma_2$ - $2\sqrt{\gamma_1^d \gamma_2^d}$.

The work of Wu [148] concentrates specifically on polymers. He follows the OWRK approach and splits the surface tensions into two components describing dispersive and polar interactions. However, he uses a harmonic mean for both terms. The resulting interface tension is then given by $\gamma_{12} = \gamma_1 + \gamma_2$ - $4\Big(\frac{\gamma_1^d \gamma_2^d}{\gamma_1^d + \gamma_2^d} - \frac{\gamma_1^p \gamma_2^p}{\gamma_1^p + \gamma_2^p}\Big)$. Although better results for polymers can be obtained with the approach of Wu, the OWRK approach is widely used in both experimental [22, 122, 125, 146] and theoretical [18, 20, 21, 31] contexts. Therefore, the relation of the OWRK theory for the interface tension is used throughout this work.

A typical experimental approach to measuring the surface energy of a solid is the following. The interface tension expressed according to the OWRK theory (A.7) is combined with the Young equation (A.5), giving

$$\sqrt{\gamma_s^d \gamma_l^d} + \sqrt{\gamma_s^p \gamma_l^p} = \gamma_l \frac{\cos\theta + 1}{2}. \tag{A.8}$$

Dividing by $\sqrt{\gamma_l^d}$, we obtain

$$\underbrace{\sqrt{\gamma_s^d}}_{\text{b}} + \underbrace{\sqrt{\gamma_s^p}}_{\text{m}} \underbrace{\sqrt{\frac{\gamma_l^p}{\gamma_l^d}}}_{\text{x}} = \underbrace{\frac{\gamma_l}{\sqrt{\gamma_l^d}} \frac{\cos\theta + 1}{2}}_{\text{y}} \tag{A.9}$$

This is a linear equation, where x includes only the surface tension of a liquid and y contains the contact angle. The intercept b and the slope of the line m are defined by the dispersive and polar components of a solid, respectively. This equation is typically used in experiments to define the surface energy of a solid, if the surface tension of a liquid and the contact angle between the solid and the liquid are known. The idea of the method is shown in Fig. A.2. A set of test liquids defines the points on the x-axis, the values of x vary typically between 0 for non-polar liquids and (commonly) ≈ 1.5 for water ($\gamma^d = 26.4$ mJ/m^2, $\gamma^p =$

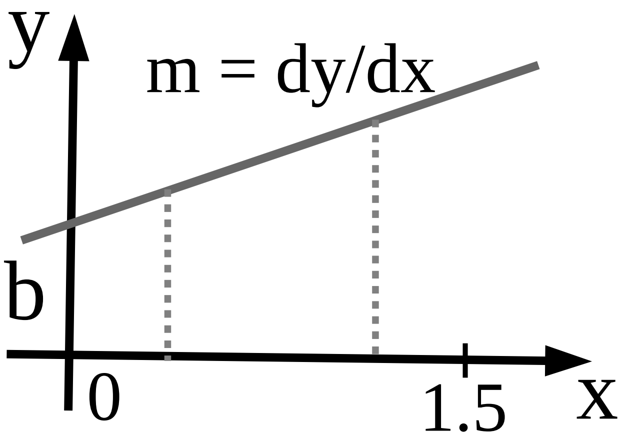

Figure A.2: The experimental approach to finding the surface energy of a solid. A set of test liquids gives the value of $x = \sqrt{\frac{\gamma_l^p}{\gamma_l^d}}$, the contact angle values are contained in $y = \frac{1+\cos\theta}{2} \cdot \frac{\gamma_l}{\sqrt{\gamma_l^d}}$. The surface energy of the solid is calculated from the intercept $b = \sqrt{\gamma_s^d}$ and the slope $m = \sqrt{\gamma_s^p}$.

46.4 mJ/m^2). Note that liquids with substantially different polarities have to be used, otherwise it may lead to large deviations in the measurements of the surface energy of a solid. Generally, the test liquids must be chosen with care in order to avoid (as much as this is possible) too small contact angles, since this will reduce the sensitivity of the method with respect to the dispersive part of γ_s or too large contact angles, since this can cause gravitational distortion of the drop or it can also mean that contact angle hysteresis becomes pronounced. In addition, the test liquids should not react with the substrate, vaporize too quickly, or simply diffuse into the substrate, etc.

A.3 Experimental Techniques

Various experimental techniques are in use to obtain the surface tensions of different materials. The most popular techniques include the sessile drop and the Wilhelmy plate method. The former is used for solids, while the latter is mainly relevant for liquids. The main idea of these methods is to measure the contact angle θ; the surface free energy is then obtained from the Young equation (see Eq. A.5).

A method based on an entirely different approach is the inverse gas chromatography, which is also widely used in the rubber science for measurements of the surface energies of filler particles and their interactions with rubbers [149–152]. Another interesting application of this method is measurements of the surface energies of popular process oils used in the rubber industry, such as MES (mildly extracted solvate) or TDAE (treated distillate aromatic extract) [153].

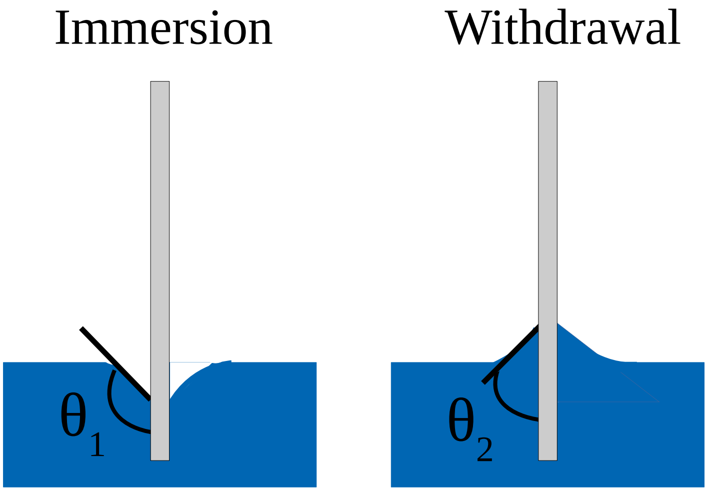

Figure A.3: Wilhelmy dynamic contact angle measurements. The advancing θ_1 and receding θ_2 contact angles are obtained during immersion and withdrawal of the plate, respectively.

A.3.1 Sessile Drop

In the sessile drop method, a droplet of a liquid with a known value of the surface tension is placed on a solid substrate. By measuring the contact angle formed by the liquid on the solid, the surface energy of the solid sample can be calculated. The contact angle is measured with a contact angle goniometer or tensiometer, which allows visual analysis of the drop shape, either by eye or by image analysis software. As the droplet is static, the contact angle obtained by this method is referred to as static as well. The sessile drop method is one of the most commonly used methods for determination of surface energies of polymers, as uncured rubber samples cannot be melted [22, 86, 125, 154, 155]. The technique can also be used for determining the surface energies of fillers, e.g., by coating an adhesive plate with the filler powder [138, 156]. The general approach is then the one discussed above when the contact angle values are measured using a set of test liquids. To obtain smooth and nonpenetrable powder compacts, some additional preparations may be required [137, 157].

A.3.2 Wilhelmy Method

In the Wilhelmy method, a thin plate usually made from platinum or glass is used, which is called a Wilhelmy plate. This plate is immersed into and withdrawn out of a test liquid during the dynamic measurements. The magnitude of the capillary force F acting on the plate is then measured, and this force is proportional to the wetted perimeter l and the surface tension of the liquid γ

$$F = \gamma l \cos\theta.$$

Table A.1: Surface energies in mJ/m^2 obtained from the advancing and receding contact angle measurements taken from [125].

Filler	Advancing contact angle			Receding contact angle		
	γ_s^d	γ_s^p	γ_s	γ_s^d	γ_s^p	γ_s
Ultrasil VN3 pulv.	21.5	5.5	27.0	17.9	29.7	47.6
Ultrasil VN3 gran.	20.2	11.9	32.1	17.7	30.0	47.8
Aerosil 200	26.3	0.5	26.7	17.0	33.9	51.0
Coupsil 8113 pulv.	27.5	0.0	27.5	17.0	33.5	50.5
CB N339	22.0	0.0	22.0	31.3	0.0	31.3
CB N990	18.2	0.0	18.2	19.1	23.9	43.0

Here θ is the contact angle. Hence, for a series of test liquids the contact angles with the solid can be measured and the surface energy of the solid can be calculated.

The dynamic Wilhelmy method yields two different values of the contact angle [125]. Fig. A.3 shows a schematic picture of the Wilhelmy dynamic contact angle measurements. The advancing contact angle is calculated during the immersion of the plate, and the receding contact angle is obtained during the withdrawal out of the liquid. The difference between them is called contact angle hysteresis. One of the reasons of the contact angle hysteresis is the nature of dynamic measurements, which are far from equilibrium. The value of the equilibrium or static contact angle lies inside the hysteresis.

High contact angle hysteresis can be observed when measuring contact angles of powders. In this case, the Wilhelmy plate is covered with the studied powder and the excess is blown away by a stream of nitrogen. Note, that the Young equation assumes that the solid surface is perfectly smooth and homogeneous. This, however, is rarely true for powder materials. The plate covered by a powder material possesses roughness and heterogeneity of particle layers, which results in very large contact angle hysteresis. An example of such measurements made on powder fillers is presented in Table A.1. Note that for some fillers, the values of the surface energies based on the advancing and receding contact angles differ considerably. The sessile drop method, however, often cannot be used at all due to drainage of the drop into the porous particle layer for hydrophilic powders [125].

A.3.3 Inverse Gas Chromatography

The inverse gas chromatography method can be used to determine the surface properties and the dispersive part of the surface energy of solid materials. In addition, different properties of polymers and nanomaterials can be studied such as enthalpy and entropy of sorption, work of co/adhesion, surface heterogeneity and glass transition temperature [158]. The extensive work on measuring surface energies of different fillers and studying their effect on reinforcement was done by Wang [24–26, 159, 160].

When defining the surface energies of fillers, the filler is used as the stationary phase and the solute injected is called a probe. At infinite dilution, information can be obtained regarding the solute adsorption on the filler surface and, consequently, filler-probe interaction [25]. The stationary phase in the chromatographic measurements is usually put inside special tubes called columns. Once the probe is injected, it vaporizes and moves in a column with a flow of a carrier gas. As the latter, frequently noble gases or nitrogen are used, which ensures the absence of interaction between the gas and the probe, as well as between the gas and the stationary phase. The time required for a solute to pass through a chromatography column is called retention time, and it depends on the adsorption strength between the filler and the solute. The volume of a carrier gas required for a probe to pass through the column is called a retention volume and is proportional to the retention time.

The procedures for calculating the dispersive and polar components of the solid surface energy can be different. Here we follow [25], which contains an example of such a procedure.

Studies have shown that for a series of homologous n-alkanes adsorbed on silicas and other solids at zero coverage, the free energies of adsorption change linearly with the number of carbon atoms. The free energy of adsorption corresponding to one methylene group can be calculated via

$$\Delta G_{CH2} = -RT \ln \frac{V_{N(n)}}{V_{N(n+1)}},$$

where $V_{N(n)}$ and $V_{N(n+1)}$ are the retention volumes of n-alkanes with n and $(n+1)$ carbon atoms, respectively.

Since it is assumed that no polar interactions take place between alkanes and solid surfaces, ΔG_{CH2} can be used to estimate the dispersive interaction between a $-\mathrm{CH_2}-$ group and an adsorbent. In the absence of polar interactions, the work of adhesion is given by the dispersive components of the solid and the liquid

$$W_a = 2\sqrt{\gamma_l^d \gamma_s^d}.$$

For alkanes $\gamma_l = \gamma_l^d$. The work of adhesion is related to the free-energy increment of adsorption associated with a $-\mathrm{CH_2}-$ group, and

$$W_a = \frac{\Delta G_{CH2}}{Na} = 2\sqrt{\gamma_{CH2} \gamma_s^d}.$$

Here N is Avogadro's number and a is the area covered by a $-\mathrm{CH_2}-$ group (0.06 nm^2). The quantity γ_{CH2} is the surface tension of a surface constituted of closely packed $-\mathrm{CH_2}-$ groups and is given by

$$\gamma_{CH2} = 35.6 + 0.058(20 - T), \text{in mJ/m}^2 \tag{A.10}$$

where T is the experimental temperature.

Thus, by injecting a series of n-alkanes as probes, the dispersive component of silica surface energy can be found from the free energy of adsorption.

Table A.2: Comparison of the dispersive component γ_d in mJ/m^2 of the surface energy for different fillers obtained via Wilhelmy method and IGC.

Filler	Wilhelmy method [125]	IGC [26]
CB N234	29.5	226.9
CB N330	26.4[22]	196.9
CB N339	27.0	232.4
CB N990	26.8	71.8
Ultrasil VN3	19.4	34.3
Aerosil 200	20.0	44.3

The interaction of polar probes with solid surfaces also includes a specific or polar component. In this case, the work of adhesion can be expressed by the sum of two terms corresponding to the dispersive and polar interactions

$$W_a = W_a^d + W_a^p.$$

In practice, one obtains a linear relationship between the free energy of adsorption of a series of alkanes and the surface area of their molecules, and this line provides a reference. The points for polar probes lie above this reference straight line. In this case

$$-\Delta G^0 = NaW_a^{d-ref} + NaW_a^p,$$

where NaW_a^{d-ref} gives the free energy of adsorption of an alkane with a surface area identical to that of the given polar probe. Thus, at a given surface area of a polar molecule, the difference between the experimental points corresponding to the polar probe and the reference line gives the value of the polar free energy of adsorption. The surface area a can be calculated from the liquid density and molecular weight.

Though this approach is mainly empirical, it provides the opportunity to compare the surface polarities of different fillers on a unified scale.

A general problem of the methods described in this chapter is that the surface energies obtained via different techniques can differ by an order of magnitude. A comparison of the dispersive component of the filler surface energy calculated from the Wilhelmy method and the inverse gas chromatography is shown in Table A.2. While for different types of silica the dispersive components obtained via IGC are about 2 times larger, in the case of carbon blacks the values can differ by an order of magnitude. One of the reasons might be higher temperatures at that IGC measurements are carried out. This, however, doesn't explain such a difference in the values for different fillers. Another possible reason is a presence of high energy sites on the surface of carbon blacks. The surface energies obtained by contact angle measurements represent the mean energy of the wide range of available surface sites. The IGC method provides the values of γ_s^d at a molecular level, as the probe concentration is small and molecules can adsorb on the highest energy sites. In addition, the availability of those sites is better in IGC than in the macroscopic techniques because before the actual measurements the columns are held at high temperatures for several hours [161].

Appendix B

Theory of Elasticity

In this chapter, we give a general introduction to the elasticity theory and the definitions of strain and stress tensors. The theoretical description is mainly based on [68, 162–164].

B.1 Strain Tensor

A deformation applied to a body can be described by a vector displacement $\vec{u}$, which is defined as the difference between the position of a point in the undeformed body $\vec{r}$ and the position of the same point in the deformed body $\vec{r}\,'$:

$$\vec{u} = \vec{r}\,' - \vec{r}. \tag{B.1}$$

The distance between two points, which before the deformation are located at $\vec{r}$ and $\vec{r} + d\vec{r}$, is given by[68]

$$dr = \sqrt{dx_1^2 + dx_2^2 + dx_3^2}$$

or, using the usual summation convention for repeated subscripts, we get

$$dr = \sqrt{dx_i^2}.$$

After the deformation, the distance is equal to

$$dr' = \sqrt{dx_1'^2 + dx_2'^2 + dx_3'^2},$$

or

$$dr' = \sqrt{dx_i'^2}.$$

Using (B.1), we get

$$\begin{aligned}
dr'^2 &= (dx_i + du_i)^2 \\
&= \Big(dx_i + \frac{\partial u_i}{\partial x_k} dx_k\Big)^2 \\
&= dx_i^2 + \underbrace{2\,\frac{\partial u_i}{\partial x_k} dx_i dx_k}_{\text{i} \leftrightarrow \text{k}} + \underbrace{\frac{\partial u_i}{\partial x_k}\frac{\partial u_i}{\partial x_l} dx_k dx_l}_{\text{i} \leftrightarrow \text{l}} \\
&= dl^2 + 2\Big(\frac{\partial u_k}{\partial x_i} dx_i dx_k + \frac{1}{2}\frac{\partial u_l}{\partial x_k}\frac{\partial u_l}{\partial x_i} dx_i dx_k\Big).
\end{aligned}$$

$$dr'^2 = dr^2 + 2u_{ik} dx_i dx_k.$$

Here u_{ik} is the strain tensor:

$$u_{ik} = \frac{1}{2}\Big(\frac{\partial u_i}{\partial x_k} + \frac{\partial u_k}{\partial x_i} + \frac{\partial u_l}{\partial x_k}\frac{\partial u_l}{\partial x_i}\Big). \tag{B.2}$$

The most significant properties of the strain tensor are:

- The strain tensor is symmetric, i.e. $u_{ik} = u_{ki}$
- At small strains $\frac{\partial u_l}{\partial x_k}\frac{\partial u_l}{\partial x_i} \ll \frac{\partial u_i}{\partial x_k} + \frac{\partial u_k}{\partial x_i}$, and the strain tensor may be approximated by

$$u_{ik} \approx \frac{1}{2}\Big(\frac{\partial u_i}{\partial x_k} + \frac{\partial u_k}{\partial x_i}\Big). \tag{B.3}$$

B.2 Stress Tensor

We consider a body of a volume V in mechanical equilibrium. Under deformation, internal forces called stresses are generated, which try to restore the body to its equilibrium state. The net force acting on the entire volume of the body is given by [68]

$$\int \vec{f} dV,$$

where $\vec{f}$ is a force density. The total force can be described by

$$F_\alpha = \int f_\alpha dV,$$

where F_α is the α-component of the total force acting on the volume V. The stress tensor is then can be expressed via

$$f_\beta = \frac{\partial \sigma_{\beta\gamma}}{\partial x_\gamma}. \tag{B.4}$$

At mechanical equilibrium, the net force for an arbitrary volume is equal to zero, which is only possible if the force density $\vec{f}$ is zero everywhere. This yields the equilibrium conditions of the deformed elastic body

$$\frac{\partial \sigma_{\beta\gamma}}{\partial x_\gamma} = 0. \tag{B.5}$$

Like the strain tensor u_{ik}, the stress tensor $\sigma_{\beta\gamma}$ is also symmetric:

$$\sigma_{\beta\gamma} = \sigma_{\gamma\beta}. \tag{B.6}$$

Based on its definition, it is clear that the stress tensor is a macroscopic quantity. In our model, however, we require a microscopic quantity. To derive the microscopic stress tensor, we start from the integration of the multiplication f_β and x_α

$$\int_V dV x_\alpha \frac{\partial \sigma_{\beta\gamma}}{\partial x_\gamma} = \int_V x_\alpha f_\beta. \tag{B.7}$$

We apply the Gauss's theorem to convert the volume integral on the left-hand side of B.7 to a surface integral. We also use here the symmetry property of the stress tensor to approximate the volume integral by its mean value ($\bar{\sigma}_{\alpha\beta}$)

$$\begin{aligned} \int_V dV x_\alpha \frac{\partial \sigma_{\beta\gamma}}{\partial x_\gamma} &= \int_V dV \frac{\partial}{\partial x_\gamma}(x_\alpha \sigma_{\beta\gamma}) - \int_V dV \underbrace{\frac{\partial x_\alpha}{\partial x_\gamma}}_{=\,\delta_{\alpha\gamma}} \sigma_{\beta\gamma} \\ &= \int_A dA\, n_\gamma x_\alpha \sigma_{\beta\gamma} - \underbrace{\int_V dV \sigma_{\beta\alpha}}_{\approx\, V\bar{\sigma}_{\alpha\beta}}, \end{aligned} \tag{B.8}$$

$$n_\gamma \sigma_{\gamma\beta} = P_\beta. \tag{B.9}$$

Here n_γ is the component of a surface unit vector pointing away from the surface and P_β is the β-component of the force area density (pressure) acting on the surface. By rewriting, we obtain

$$\int_A dA\, x_\alpha P_\beta \propto \sum_i \dot{x}^i_\alpha \dot{x}^i_\beta. \tag{B.10}$$

The superscripts denote the particles, while the subscripts refer to the vector components.

If we assume the shear process being a sequence of static states, we can neglect the terms depending on the velocities, which leads to

$$\begin{aligned} \bar{\sigma}_{\alpha\beta} &\approx -\frac{1}{V} \int dV x_\alpha f_\beta \\ &\approx -\frac{1}{V} \sum_i x^i_\alpha F^i_\beta \\ &\approx -\frac{1}{2V} \sum_{\substack{i,j \\ i\neq j}} \frac{x^{ij}_\alpha x^{ij}_\beta}{r^{ij}} F^{ij}, \end{aligned} \tag{B.11}$$

where $x^{ij}_\alpha = x^i_\alpha - x^j_\alpha$ is the distance between particles i and j in the α-direction, $r^{ij} = |\vec{x}^i - \vec{x}^j|$ is the total distance between i and j and F^{ij} is the magnitude of the total force between i and j. This form of the stress tensor demonstrates immediately the symmetry property. In addition, it is more convenient for calculating the stress in simulations because it requires the distances between particles and not their absolute coordinates.

B.3 Work in the Deformed Body

The definition of mechanical work (force times distance) yields

$$\begin{aligned}
W_{loss} &= -\int_V dV \int d(u_\beta) f_\beta \\
&= \int_V dV \int d(u_\beta) \frac{\partial \sigma_{\beta\gamma}}{\partial x_\gamma} \\
&= \int_V dV \int d(u_{\alpha\beta}) \sigma_{\alpha\beta} \\
&= \frac{1}{2} \int_V dV \int d\Big(\frac{\partial u_\alpha}{\partial x_\beta} + \frac{\partial u_\beta}{\partial x_\alpha}\Big) \sigma_{\alpha\beta}.
\end{aligned}$$

The minus sign implies that the work is dissipated by the system. During simulation, a cubic volume with the side length L is sheared on the xz-plane by $u(t)$ in the x-direction. Then

$$\frac{\partial u_\alpha}{\partial x_\beta} = \begin{cases} 2\frac{u(t)}{L}, & \text{if } \alpha = x, \beta = z \\ 0, & \text{else.} \end{cases} \tag{B.12}$$

Due to the shear direction, only σ_{xz} component of the stress tensor is relevant, and the components σ_{xy} and σ_{yz} can be neglected. Using (B.12), we obtain for the dissipated work

$$\begin{aligned}
W_{loss} &= \frac{1}{L} \int_V dV \int d(u(t)) \sigma_{xz}(t) \\
&= \frac{1}{L} \int_V dV \int dt \frac{d(u(t))}{dt} \sigma_{xz}(t) \\
&= \frac{1}{L} \int_V dV \int dt\, \dot{u}(t) \sigma_{xz}(t).
\end{aligned} \tag{B.13}$$

During DMA measurements, both strain and stress can be expressed via sine functions, i.e, $u = u_0 \sin(\omega t)$ and $\sigma = \sigma_0 \sin(\omega t + \delta)$. Consider the dissipated work per volume in the time interval $[0,\ t_0]$:

$$\begin{aligned}
w_{loss} &= \frac{W_{loss}}{V} \\
&= \int_0^{t_0} \sigma_{xz} \frac{du}{dt} dt \\
&= \int_0^{t_0} \sigma_0 \sin(\omega t + \delta)\, u_0 \omega \cos(\omega t) dt \\
&= \frac{\sigma_0 u_0}{4} \Big(\cos\delta + 2\omega t_0 \sin\delta - \cos(\delta + 2\omega t_0) \Big).
\end{aligned} \tag{B.14}$$

The storage μ' and the loss μ'' moduli are given by (see also (2.11) - (2.12))

$$\mu' = \frac{\sigma_0}{u_0} \cos(\delta),$$

$$\mu'' = \frac{\sigma_0}{u_0} \sin(\delta).$$

Integrating over one period $t_0 = 2\pi/\omega$ yields

$$\begin{aligned}
w_{loss}(t_0 = 2\pi/\omega) &= \frac{\sigma_0 u_0}{4} \Big(\cos\delta + 4\pi \sin\delta - \cos(\delta + 4\pi) \Big) \\
&= u_0^2 \pi \mu''.
\end{aligned} \tag{B.15}$$

Thus, the loss modulus is proportional to the work per volume dissipated by the system during one shear cycle and can be calculated via numerical integration of the area under the curve in the $\sigma - u$ plane.

Appendix C

Simulation Parameters

In this chapter, the notations and the values of the simulation parameters are complied into one table. The table consists of several sections. In the first section, the parameters used for the Monte Carlo morphology generator are listed. They are followed by the values of the surface tensions of the components. The third section presents the parameters used for the DMA simulation, with the values of the force constants combined into a separate subsection.

Table C.1: Simulation parameters

Parameter	Symbol	Value	Comments
Monte Carlo Morphology Generator			
Diameter of the node	d	1.0	Sets the unit of length. The distance between nodes is also equal to d
Lattice type		randomized FCC	FCC randomized via a random displacement
Random displacement	δr	$\delta r_{max} = 0.3\ d$	Chosen according to the uniform distribution
Simulation box length	L	≈ 100	
Number of nodes	n	$1.372{\cdot}10^6$	Corresponds to a FCC lattice with $L \approx 100$
Number of MC steps	n_{steps}	1000 n	Mimics roughly a flocculation time
Number of neighbours	n_{nn}	12 in FCC	Depends on the lattice
Cutoff radius	r_{cut}	1.3	Chosen so that $\mathrm{n}_{nn} \approx 12$ in case of the randomized FCC
Blend ratio NR/SBR	x	50/50, 30/70, 70/30	
Filler content	ϕ	0.0 - 30.0 % vol.	
Temperature	T	0.57021	Corresponds to $\mathrm{T}_{exp} = 140$ °C
Surface tensions			
Surface tensions	γ^d, γ^p		Dispersive and polar parts
NR		$\gamma^d = 9.69$, $\gamma^p = 2.61$	From experiment ($\gamma^d = 20.24$ and $\gamma^p = 5.46\ mJ/m^2$)
SBR		$\gamma^d = 14.31$, $\gamma^p = 0.78$	From experiment ($\gamma^d = 29.91$ and $\gamma^p = 1.64\ mJ/m^2$)
filler		$\gamma^d = 4.8$ - 14.4, $\gamma^p =$ 0.0 - 9.6	Mimics different fillers (experimentally correspond to $\gamma^d = 10$ - 30, $\gamma^p = 0$ - 20 mJ/m^2)
Shear Simulation			
Simulation box length	L	20.0	Cut from the original morphology with L $\approx$ 100
Number of nodes	n	1.1 - $1.3{\cdot}10^4$	Corresponds to the randomized FCC lattice with L = 20.0
Number of neighbours	n_{nn}	≈ 12	Taken from the MC simulation
Number of steps	n_{steps}	$3{\cdot}10^5$	
Strain amplitude	u_0	0.1 - 40 %	

Frequency	ω	10^{-6} - 10^{2}	
Time step	Δt	$5{\cdot}10^{-4}$ for $\omega = 0.2$	Depends on ω, so that $\omega \Delta t n_{steps} \approx 10\ \pi$
Friction coefficient	γ	1.0	
Friction coefficient for filler nodes	γ_F	15.0	
Force constants			
Force constant	k		Depends on the interaction. Weak and strong spring constants and the ratio between them are set by the experimental $\tan\delta$ for pure polymers
NR-NR, weak	$k_<^{NR-NR}$	10^{-3}	Weak spring constant for NR-NR interaction
NR-NR, strong	$k_>^{NR-NR}$	0.2	Strong spring constant for NR-NR interaction
Fraction of weak springs for NR	$x_<^{NR}$	0.7	$x_<^{NR} + x_>^{NR} = 1.0$
SBR-SBR, weak	$k_<^{SBR-SBR}$	10^{-5}	Weak spring constant for SBR-SBR interaction
SBR-SBR, strong	$k_>^{SBR-SBR}$	0.1	Strong spring constant for SBR-SBR interaction
Fraction of weak springs for SBR	$x_<^{SBR}$	0.56	$x_<^{SBR} + x_>^{SBR} = 1.0$
NR-SBR, weak	$k_<^{NR-SBR}$	10^{-4}	Weak spring constant for NR-SBR interaction $k_<^{NR-SBR} = \sqrt{k_<^{NR-NR} k_<^{SBR-SBR}}$
NR-SBR, strong	$k_>^{NR-SBR}$	0.1414	Strong spring constant for NR-SBR interaction $k_>^{NR-SBR} = \sqrt{k_>^{NR-NR} k_>^{SBR-SBR}}$
Fraction of weak springs for NR-SBR interface	$x_<^{\text{interface}}$	0, 0.5, 1	$x_<^{\text{interface}} + x_>^{\text{interface}} = 1.0$
Filler-NR	k_{NR-F}	$1.6{\cdot}10^{-4}$ - $1.1{\cdot}10^{-1}$	$k_{NR-F} \propto \gamma_{pf}$
Filler-SBR	k_{SBR-F}	$3{\cdot}10^{-2}$ - $1.3{\cdot}10^{-1}$	$k_{SBR-F} \propto \gamma_{pf}$
Filler-filler	k_{FF}	10.0	

Bond-breaking distance, F-NR	R_{NR-F}	$1.01r_{ij}$	Depends on the distance between nodes and corresponds to the local strain equal to 1%
Bond-breaking distance, F-SBR	R_{SBR-F}	$1.01r_{ij}$	Depends on the distance between nodes and corresponds to the local strain equal to 1%
Bond-breaking distance, F-F	R_{FF}	$1.01r_{ij}$	Depends on the distance between nodes and corresponds to the local strain equal to 1%

List of Figures

List of Tables

Bibliography

[1] Long, J. C. The History of Rubber—A Survey of Sources about the History of Rubber. *Rubber Chemistry and Technology*, 74(3):493–508, July 2001. DOI: `10.5254/1.3547648`.

[2] Liu, J., Zhang, L., Cao, D., Shen, J., and Gao, Y. COMPUTATIONAL SIMULATION OF ELASTOMER NANOCOMPOSITES: CURRENT PROGRESS AND FUTURE CHALLENGES. *Rubber Chemistry and Technology*, 85(3):450–481, September 2012. DOI: `10.5254/rct.12.87966`.

[3] Dannenberg, E. M. The Effects of Surface Chemical Interactions on the Properties of Filler-Reinforced Rubbers. *Rubber Chemistry and Technology*, 48(3):410–444, July 1975. DOI: `10.5254/1.3547460`.

[4] Wang, M.-J. and Morris, M. *Rubber reinforcement with particulate fillers*. Hanser Publications, 2021.

[5] Jancar, J., Douglas, J., Starr, F., Kumar, S., Cassagnau, P., Lesser, A., Sternstein, S., and Buehler, M. Current issues in research on structure–property relationships in polymer nanocomposites. *Polymer*, 51(15):3321–3343, 2010. DOI: `https://doi.org/10.1016/j.polymer.2010.04.074`.

[6] Heinrich, G., Klüppel, M., and Vilgis, T. A. Reinforcement of elastomers. *Current Opinion in Solid State and Materials Science*, 6(3):195–203, 2002. DOI: `https://doi.org/10.1016/S1359-0286(02)00030-X`.

[7] Vilgis, T., Heinrich, G., and Klüppel, M. *Reinforcement of polymer nanocomposites*. Cambridge University Press, 2009.

[8] Maiti, M., Bhattacharya, M., and Bhowmick, A. K. Elastomer Nanocomposites. *Rubber Chemistry and Technology*, 81(3):384–469, July 2008. DOI: `10.5254/1.3548215`.

[9] Tjong, S. and Mai, Y.-W. *Physical properties and applications of polymer nanocomposites*. Woodhead Publishing, October 2010.

[10] Robertson, C. G. Flocculation in elastomeric polymers containing nanoparticles: jamming and the new concept of fictive dynamic strain. *Rubber Chemistry and Technology*, 88(3):463–474, 2015. DOI: `10.5254/rct.15.85950`.

[11] Mihara, S., Datta, R. N., and Noordermeer, J. W. M. Flocculation in silica reinforced rubber compounds. *Rubber Chemistry and Technology*, 82(5):524–540, 2009. DOI: `10.5254/1.3548262`.

[12] Tunnicliffe, L. B., Kadlcak, J., Morris, M. D., Shi, Y., Thomas, A. G., and Busfield, J. J. C. Flocculation and viscoelastic behaviour in carbon black-filled natural rubber. *Macromolecular Materials and Engineering*, 299(12):1474–1483, 2014. DOI: `10.1002/mame.201400117`.

[13] Kadlcak, J., Kuřitka, I., Tunnicliffe, L., and Cermak, R. *Quantification of the filler flocculation process in natural rubber melts*. In 2015. DOI: `10.1201/b18701-98`.

[14] Robertson, C. G., Lin, C. J., Bogoslovov, R. B., Rackaitis, M., Sadhukhan, P., Quinn, J. D., and Roland, C. M. Flocculation, reinforcement, and glass transition effects in silica-filled styrene-butadiene rubber. *Rubber Chemistry and Technology*, 84(4):507–519, 2011. DOI: `10.5254/1.3601885`.

[15] Lin, C. J., Hergenrother, W. L., Alexanian, E., and Böhm, G. G. A. On the filler flocculation in silica-filled rubbers Part I. Quantifying and tracking the filler flocculation and polymer-filler interactions in the unvulcanized rubber compounds. *Rubber Chemistry and Technology*, 75(5):865–890, 2002. DOI: `10.5254/1.3547689`.

[16] Kaewsakul, W., Sahakaro, K., Dierkes, W. K., and Noordermeer, J. W. Factors influencing the flocculation process in silica-reinforced natural rubber compounds. *Journal of Elastomers & Plastics*, 48(5):426–441, 2016. DOI: `10.1177/0095244315580456`.

[17] Böhm, G. G. A. and Nguyen, M. N. Flocculation of carbon black in filled rubber compounds. i. flocculation occurring in unvulcanized compounds during annealing at elevated temperatures. *Journal of Applied Polymer Science*, 55(7):1041–1050, 1995. DOI: `https://doi.org/10.1002/app.1995.070550707`.

[18] Stöckelhuber, K. W., Wießner, S., Das, A., and Heinrich, G. Filler flocculation in polymers – a simplified model derived from thermodynamics and game theory. *Soft Matter*, 13(20):3701–3709, 2017. DOI: `10.1039/C6SM02694J`.

[19] Gundlach, N. *Modeling Filler Flocculation in Elastomers – an Approach Based on Surface Free Energies and Monte Carlo Simulation*. PhD thesis, Bergische Universität Wuppertal, 2019.

[20] Gundlach, N. and Hentschke, R. Modelling filler dispersion in elastomers: relating filler morphology to interface free energies via SAXS and TEM simulation studies. *Polymers*, 10(4):446, 2018. DOI: `10.3390/polym10040446`.

[21] Gundlach, N., Hentschke, R., and Karimi-Varzaneh, H. A. Filler flocculation in elastomer blends - An approach based on measured surface tensions and Monte Carlo simulation. *Soft Materials*, 17(3):283–296, 2019. DOI: `10.1080/1539445X.2019.1568261`.

[22] Stöckelhuber, K. W., Svistkov, A. S., Pelevin, A. G., and Heinrich, G. Impact of filler surface modification on large scale mechanics of styrene butadiene/silica rubber composites. *Macromolecules*, 44(11):4366–4381, 2011. DOI: `10.1021/ma1026077`.

[23] Natarajan, B., Li, Y., Deng, H., Brinson, L. C., and Schadler, L. S. Effect of interfacial energetics on dispersion and glass transition temperature in polymer nanocomposites. *Macromolecules*, 46(7):2833–2841, 2013. DOI: `10.1021/ma302281b`.

[24] Wolff, S. and Wang, M.-J. Filler—elastomer interactions. Part IV. The effect of the surface energies of fillers on elastomer reinforcement. *Rubber Chemistry and Technology*, 65(2):329–342, 1992. DOI: `10.5254/1.3538615`.

[25] Wang, M.-J., Wolff, S., and Donnet, J.-B. Filler-elastomer interactions. Part I: silica surface energies and interactions with model compounds. *Rubber Chemistry and Technology*, 64(4):559–576, 1991. DOI: `10.5254/1.3538573`.

[26] Wang, M.-J., Wolff, S., and Donnet, J.-B. Filler—elastomer interactions. Part III. Carbon-black-surface energies and interactions with elastomer analogs. *Rubber Chemistry and Technology*, 64(5):714–736, 1991. DOI: `10.5254/1.3538585`.

[27] Menard, K. P. *Dynamic mechanical analysis: a practical introduction.* CRC Press, 2001.

[28] Menard, K. P. and Bilyeu, B. W. *Dynamic mechanical analysis of polymers and rubbers.* In *Encyclopedia of Analytical Chemistry.* American Cancer Society, 2008. DOI: `https://doi.org/10.1002/9780470027318.a2007.pub2`.

[29] Alig, I., Skipa, T., Lellinger, D., and Pötschke, P. Destruction and formation of a carbon nanotube network in polymer melts: rheology and conductivity spectroscopy. *Polymer*, 49(16):3524–3532, 2008. DOI: `https://doi.org/10.1016/j.polymer.2008.05.037`.

[30] Rasa, A. J. Applying dynamic mechanical analysis to research & development for viscoelastic damping materials, 2014.

[31] Wang, M.-J. Effect of polymer-filler and filler-filler interactions on dynamic properties of filled vulcanizates. *Rubber Chemistry and Technology*, 71(3):520–589, 1998. DOI: `10.5254/1.3538492`.

[32] Payne, A. and Whittaker, R. Reinforcement of rubber with carbon black. *Composites*, 1(4):203–214, 1970.

[33] Ouyang, G. Modulus, hysteresis and the payne effect. *Kautschuk Gummi Kunststoffe*, 59:332–342, June 2006.

[34] Ouyang, G. Network junction model for carbon black reinforcement. *Kautschuk Gummi Kunststoffe*, 59:454–458, September 2006.

[35] Heinrich, G. and Klüppel, M. *Recent advances in the theory of filler networking in elastomers.* In *Filled Elastomers Drug Delivery Systems.* Springer Berlin Heidelberg, 2002, pages 1–44. DOI: `10.1007/3-540-45362-8_1`.

[36] Maier, P. G. and Goeritz, D. Molecular interpretation of the payne effect. *Kautschuk Gummi Kunststoffe*, 49(1):18–21, 1996.

[37] Warasitthinon, N., Genix, A.-C., Sztucki, M., Oberdisse, J., and Robertson, C. G. THE PAYNE EFFECT: PRIMARILY POLYMER-RELATED OR FILLER-RELATED PHENOMENON? *Rubber Chemistry and Technology*, 92(4):599–611, October 2019. DOI: `10.5254/rct.19.80441`.

[38] Hentschke, R. The Payne effect revisited. *eXPRESS Polymer Letters*, 11(4):278–292, 2017. DOI: `10.3144/expresspolymlett.2017.28`.

[39] Hentschke, R. Macroscopic mechanical properties of elastomer nano-composites via molecular and analytical modelling. *Soft Materials*, 16(4):315–326, 2018. DOI: `10.1080/1539445X.2018.1518243`.

[40] Oberth, A. E. Principle of Strength Reinforcement in Filled Rubbers. *Rubber Chemistry and Technology*, 40(5):1337–1363, November 1967. DOI: `10.5254/1.3539147`.

[41] Pavlov, A. S. and Khalatur, P. G. Fully atomistic molecular dynamics simulation of nanosilica-filled crosslinked polybutadiene. *Chemical Physics Letters*, 653:90–95, 2016. DOI: `https://doi.org/10.1016/j.cplett.2016.04.061`.

[42] Lauke, B. and Morozov, I. A. Modeling of structure evolution of filled elastomers under uniaxial elongation. *International Journal for Multiscale Computational Engineering*, 7(4):251–261, 2009.

[43] Raos, G., Moreno, M., and Elli, S. Computational experiments on filled rubber viscoelasticity what is the role of particle-particle interactions? *Macromolecules*, 39(19):6744–6751, 2006. DOI: `10.1021/ma061008h`.

[44] Sodhani, D. and Reese, S. Finite element based micro-mechanical modeling of interphase in filler reinforced elastomers. *Soft Materials*, 12(sup1):S152–S161, 2014. DOI: `10.1080/1539445X.2014.959596`.

[45] Long, D. and Sotta, P. Nonlinear and plastic behavior of soft thermoplastic and filled elastomers studied by dissipative particle dynamics. *Macromolecules*, 39(18):6282–6297, 2006. DOI: `10.1021/ma061306e`.

[46] Merabia, S., Sotta, P., and Long, D. R. A microscopic model for the reinforcement and the nonlinear behavior of filled elastomers and thermoplastic elastomers (Payne and Mullins effects). *Macromolecules*, 41(21):8252–8266, 2008. DOI: `10.1021/ma8014728`.

[47] Papon, A., Guy, T. C. L., Saalwaechter, K., Oberdisse, J., Merabia, S., Long, D., Sotta, P., Frielinghaus, H., Radulescu, A., Deme, B., et al. Studying model samples to understand mechanical properties of filled elastomers. *Kautschuk Gummi Kunststoffe*, 66(9):52–58, 2013.

[48] Li, Z., Liu, J., Zhang, Z., Gao, Y., Liu, L., Zhang, L., and Yuan, B. Molecular dynamics simulation of the viscoelasticity of polymer nanocomposites under oscillatory shear: effect of interfacial chemical coupling. *RSC Adv.*, 8(15):8141–8151, 2018. DOI: `10.1039/C7RA13415K`.

[49] Termonia, Y. Molecular modeling of particle reinforcement in elastomers: effect of particle radius and volume fraction. *Polymer*, 51(19):4448–4451, 2010. DOI: `https://doi.org/10.1016/j.polymer.2010.07.029`.

[50] Rendek, M. and Lion, A. Strain induced transient effects of filler reinforced elastomers with respect to the Payne-effect: experiments and constitutive modelling. *ZAMM - Journal of Applied Mathematics and Mechanics / Zeitschrift für Angewandte Mathematik und Mechanik*, 90(5):436–458, 2010. DOI: `https://doi.org/10.1002/zamm.200900362`.

[51] Wang, W., Hou, G., Zheng, Z., Wang, L., Liu, J., Wu, Y., Zhang, L., and Lyulin, A. V. Designing polymer nanocomposites with a semi-interpenetrating or interpenetrating network structure: toward enhanced mechanical properties. *Phys. Chem. Chem. Phys.*, 19(24):15808–15820, 2017. DOI: `10.1039/C7CP01453H`.

[52] Shen, J., Liu, J., Gao, Y., Li, X., and Zhang, L. Elucidating and tuning the strain-induced non-linear behavior of polymer nanocomposites: a detailed molecular dynamics simulation study. *Soft Matter*, 10(28):5099–5113, 2014. DOI: `10.1039/C4SM00233D`.

[53] Davris, T., Mermet-Guyennet, M. R. B., Bonn, D., and Lyulin, A. V. Filler size effects on reinforcement in elastomer-based nanocomposites: experimental and simulational insights into physical mechanisms. *Macromolecules*, 49(18):7077–7087, 2016. DOI: `10.1021/acs.macromol.6b00844`.

[54] Chen, Y., Li, Z., Wen, S., Yang, Q., Zhang, L., Zhong, C., and Liu, L. Molecular simulation study of role of polymer–particle interactions in the strain-dependent viscoelasticity of elastomers (Payne effect). *The Journal of Chemical Physics*, 141(10):104901, 2014. DOI: `10.1063/1.4894502`.

[55] Wang, L., Zheng, Z., Davris, T., Li, F., Liu, J., Wu, Y., Zhang, L., and Lyulin, A. V. Influence of morphology on the mechanical properties of polymer nanocomposites filled with uniform or patchy nanoparticles. *Langmuir*, 32(33):8473–8483, 2016. DOI: `10.1021/acs.langmuir.6b01049`.

[56] Breneman, C. M., Brinson, L. C., Schadler, L. S., Natarajan, B., Krein, M., Wu, K., Morkowchuk, L., Li, Y., Deng, H., and Xu, H. Stalking the materials genome: a data-driven approach to the virtual design of nanostructured polymers. *Advanced Functional Materials*, 23(46):5746–5752, 2013. DOI: `https://doi.org/10.1002/adfm.201301744`.

[57] Xi, H. and Hentschke, R. Dynamic moduli of filled elastomers – a coarse grained computer model. *European Polymer Journal*, 48(10):1777–1786, 2012. DOI: `https://doi.org/10.1016/j.eurpolymj.2012.07.005`.

[58] Xi, H. and Hentschke, R. The influence of structure on mechanical properties of filler networks via coarse-grained modeling. *Macromolecular Theory and Simulations*, 23(6):373–382, 2014. DOI: `10.1002/mats.201400009`.

[59] Hager, J. *Modellierung dynamischer Module von Silica gefüllten Elastomeren auf der Basis molekularer Simulationen*. PhD thesis, Bergische Universität Wuppertal, 2015.

[60] Meyer, J., Hentschke, R., Hager, J., Hojdis, N., and Karimi, A. A nanomechanical instability as primary contribution to rolling resistance. *Scientific Reports*, 7:11275, December 2017. DOI: `10.1038/s41598-017-11728-6`.

[61] Meyer, J. *Molekulare Modellierung der mechanischen Eigenschaften von elastomeren Nano-Kompositen.* PhD thesis, Bergische Universität Wuppertal, 2018.

[62] Wrana, C. *Introduction to Polymer Physics - 100 Years Synthetic Rubber, Creating the Way the World Moves Today.* Lanxess AG, 2009.

[63] Wrana, C. *Polymerphysik: eine physikalische Beschreibung von Elastomeren und ihren anwendungsrelevanten Eigenschaften.* Springer, 2014.

[64] Strobl, G. R. *The physics of polymers concepts for understanding their structures and behavior; with 295 figures and 2 tables.* Springer, 2007.

[65] Rubinstein, M. and Colby, R. H. *Polymer Physics.* OUP Oxford, New York, London, 2003.

[66] De, S. K. and White, J. R. *Rubber Technologist's Handbook.* iSmithers Rapra Publishing, Shrewsbury, 2001.

[67] Gent, A. N. *Engineering with Rubber - How to Design Rubber Components.* Carl Hanser Verlag GmbH Co KG, 2012.

[68] Hentschke, R. *Classical Mechanics - Including an Introduction to the Theory of Elasticity.* Springer, Berlin, Heidelberg, 1st edition, 2016.

[69] Kim, D. Y., Park, J. W., Lee, D. Y., and Seo, K. H. Correlation between the crosslink characteristics and mechanical properties of natural rubber compound via accelerators and reinforcement. *Polymers*, 12(9), 2020. DOI: `10.3390/polym12092020`.

[70] Coran, A. Chapter 7 - Vulcanization. In J. E. Mark, B. Erman, and C. M. Roland, editors, *The Science and Technology of Rubber (Fourth Edition)*, pages 337–381. Academic Press, 2013. DOI: `https://doi.org/10.1016/B978-0-12-394584-6.00007-8`.

[71] Lechner, M. D., Gehrke, K., Nordmeier, E. H., and Schmitt, B. J. *Makromolekulare Chemie: ein Lehrbuch für Chemiker, Physiker, Materialwissenschaftler und Verfahrenstechniker.* Springer Spektrum, 2014.

[72] Nikiel, L., Wampler, W., Neilsen, J., and Hershberger, N. How carbon black affects electrical properties. *Rubber & Plastics News*:12–18, March 2009.

[73] Lacayo-Pineda, J. *Filler dispersion and filler networks.* In *Encyclopedia of Polymeric Nanomaterials.* S. Kobayashi and K. Müllen, editors. Springer Berlin Heidelberg, 2015, pages 771–776. DOI: `10.1007/978-3-642-29648-2_291`.

[74] Silva, L. F. M. d., Andreas, Ö., and Adams, R. D. *Handbook of adhesion technology.* Springer, 2011.

[75] Thomas, S. and Maria, H. J. *Progress in rubber nanocomposites.* Woodhead Publishing, 2017.

[76] Fukahori, Y. New progress in the theory and model of carbon black reinforcement of elastomers. *Journal of Applied Polymer Science*, 95(1):60–67, 2005. DOI: `https://doi.org/10.1002/app.20802`.

[77] Berriot, J., Montes, H., Lequeux, F., Long, D., and Sotta, P. Evidence for the shift of the glass transition near the particles in silica-filled elastomers. *Macromolecules*, 35(26):9756–9762, 2002. DOI: `10.1021/ma0212700`.

[78] Dequidt, A., Long, D. R., Sotta, P., and Sanséau, O. Mechanical properties of thin confined polymer films close to the glass transition in the linear regime of deformation: theory and simulations. *The European Physical Journal E*, 35(7):61, 2012. DOI: `10.1140/epje/i2012-12061-6`.

[79] Guy, L., Daudey, S., Cochet, P., and Bomal, Y. New insights in the dynamic properties of precipitated silica filled rubber using a new high surface silica. *Kautschuk Gummi Kunststoffe*, 62:383–391, July 2009.

[80] Huang, M., Tunnicliffe, L. B., Thomas, A. G., and Busfield, J. J. The glass transition, segmental relaxations and viscoelastic behaviour of particulate-reinforced natural rubber. *European Polymer Journal*, 67:232–241, 2015. DOI: `10.1016/j.eurpolymj.2015.03.024`.

[81] Herd, C. R., Mcdonald, G. C., and Hess, W. M. Morphology of carbon-black aggregates: fractal versus euclidean geometry. *Rubber Chemistry and Technology*, 65(1):107–129, 1992. DOI: `10.5254/1.3538594`.

[82] Hyde, E. D. E. R., Seyfaee, A., Neville, F., and Moreno-Atanasio, R. Colloidal silica particle synthesis and future industrial manufacturing pathways: a review. *Industrial & Engineering Chemistry Research*, 55(33):8891–8913, 2016. DOI: `10.1021/acs.iecr.6b01839`.

[83] Sugino, Y. and Kawaguchi, M. Fumed and precipitated hydrophilic silica suspension gels in mineral oil: stability and rheological properties. *Gels*, 3(3):32, 2017. DOI: `10.3390/gels3030032`.

[84] Mihara, S. *Reactive processing of silica-reinforced tire rubber : new insight into the time- and temperature-dependence of silica rubber interaction*. PhD thesis, University of Twente, May 2009. DOI: `10.3990/1.9789036528399`.

[85] Le, H. H., Ilisch, S., Heidenreich, D., Wutzler, A., and Radusch, H.-J. Kinetics of the phase selective localization of silica in rubber blends. *Polymer Composites*, 31(10):1701–1711, 2010. DOI: `10.1002/pc.20960`.

[86] Qu, L., Wang, L., Xie, X., Yu, G., and Bu, S. Contribution of silica–rubber interactions on the viscoelastic behaviors of modified solution polymerized styrene butadiene rubbers (m-s-sbrs) filled with silica. *RSC Adv.*, 4(109):64354–64363, 2014. DOI: `10.1039/c4ra09492a`.

[87] Bouty, A., Petitjean, L., Degrandcourt, C., Gummel, J., Kwaśniewski, P., Meneau, F., Boué, F., Couty, M., and Jestin, J. Nanofiller structure and reinforcement in model silica/rubber composites: a quantitative correlation driven by interfacial agents. *Macromolecules*, 47(15):5365–5378, 2014. DOI: `10.1021/ma500582p`.

[88] Ladouce, L., Bomal, Y., Flanckn, L., and Labarre, D. Dynamic mechanical properties of precipitated silica filled rubber: influence of morphology and coupling agent. *ACS Rubber Division Meeting, Dallas, Texas*, April 2000.

[89] Arridge, R. G. C. *Mechanics of polymers*. Clarendon Press, 1975.

[90] Meyers, M. A. and Chawla, K. K. *Mechanical behavior of materials: processing, characterization, theory and mechanical properties*. Prentice Hall, 1999.

[91] Williams, M. L., Landel, R. F., and Ferry, J. D. The temperature dependence of relaxation mechanisms in amorphous polymers and other glass-forming liquids. *Journal of the American Chemical Society*, 77(14):3701–3707, 1955. DOI: `10.1021/ja01619a008`.

[92] Bourbigot, S., Duquesne, S., and Jama, C. Polymer nanocomposites: how to reach low flammability? *Macromolecular Symposia*, 233(1):180–190, 2006. DOI: `https://doi.org/10.1002/masy.200690016`.

[93] Mahi, H., Wilhelm, M., and Rodrigue, D. A rheological criterion to determine the percolation threshold in polymer nano-composites. *Rheologica Acta*, 53:869–882, October 2014. DOI: `10.1007/s00397-014-0804-0`.

[94] Baxter, S. C. and Robinson, C. T. Pseudo-percolation: critical volume fractions and mechanical percolation in polymer nanocomposites. *Composites Science and Technology*, 71(10):1273–1279, 2011. DOI: `https://doi.org/10.1016/j.compscitech.2011.04.010`.

[95] Kadlcak, J., Tunnicliffe, L., Busfield, J., Lacayo, J., Cermak, R., and Kuřitka, I. Evaluation of carbon black flocculation in natural rubber melts. In May 2014.

[96] Payne, A. R. The dynamic properties of carbon black-loaded natural rubber vulcanizates. part i. *Journal of Applied Polymer Science*, 6(19):57–63, 1962. DOI: `10.1002/app.1962.070061906`.

[97] Payne, A. R. Dynamic properties of heat-treated butyl vulcanizates. *Journal of Applied Polymer Science*, 7(3):873–885, 1963. DOI: `10.1002/app.1963.070070307`.

[98] Payne, A. R. Strainwork dependence of filler-loaded vulcanizates. *Journal of Applied Polymer Science*, 8(6):2661–2686, 1964. DOI: `10.1002/app.1964.070080614`.

[99] Payne, A. R. Effect of dispersion on the dynamic properties of filler-loaded rubbers. *Journal of Applied Polymer Science*, 9(6):2273–2284, 1965. DOI: `10.1002/app.1965.070090619`.

[100] Payne, A. R. The dynamic properties of carbon black-loaded natural rubber vulcanizates. part i. *Rubber Chemistry and Technology*, 36(2):432–443, 1963. DOI: `10.5254/1.3539570`.

[101] Payne, A. R., Whittaker, R. E., and Smith, J. F. Effect of vulcanization on the low-strain dynamic properties of filled rubbers. *Journal of Applied Polymer Science*, 16(5):1191–1212, 1972. DOI: `10.1002/app.1972.070160513`.

[102] Medalia, A. I. Elastic modulus of vulcanizates as related to carbon black structure. *Rubber Chemistry and Technology*, 46(4):877–896, 1973. DOI: `10.5254/1.3547416`.

[103] Medalia, A. I. Filler aggregates and their effect on reinforcement. *Rubber Chemistry and Technology*, 47(2):411–433, 1974. DOI: `10.5254/1.3540450`.

[104] Voet, A. and Cook, F. R. Mild stress softening and dynamic properties of rubber vulcanizates. *Rubber Chemistry and Technology*, 40(5):1364–1372, 1967. DOI: `10.5254/1.3539148`.

[105] Mukhopadhyay, K. and Tripathy, D. Strain dependent dynamic mechanical properties of silica filled ethylene vinyl acetate rubber. *Journal of Elastomers & Plastics*, 24(3):203–220, 1992. DOI: `10.1177/009524439202400305`.

[106] Einstein, A. Eine neue Bestimmung der Moleküldimensionen. *Annalen der Physik*, 324(2):289–306, 1906. DOI: `https://doi.org/10.1002/andp.19063240204`.

[107] Smallwood, H. M. Limiting law of the reinforcement of rubber. *Journal of Applied Physics*, 15(11):758–766, 1944. DOI: `10.1063/1.1707385`.

[108] Domurath, J., Saphiannikova, M., and Heinrich, G. The concept of hydrodynamic amplification in filled elastomers. *Kautschuk Gummi Kunststoffe*, 70:40–43, January 2017.

[109] Bischoff, A., Klüppel, M., and Schuster, R. H. Mechanical behavior at low strain of microgel containing elastomers. *Polymer Bulletin*, 40(2):283–290, February 1998. DOI: `10.1007/s002890050253`.

[110] Lin, C.-R. and Lee, Y.-D. Strain-dependent dynamic properties of filled rubber network systems. *Macromolecular Theory and Simulations*, 5(6):1075–1104, 1996. DOI: `10.1002/mats.1996.040050605`.

[111] Kraus, G. Mechanical losses in carbon-black-filled rubbers. *Journal of Applied Polymer Science: Applied Polymer Symposium*, 39:75–92, 1984.

[112] Huber, G. and Vilgis, T. Universal properties of filled rubbers: mechanisms for reinforcement on different length scales. *Kautschuk Gummi Kunststoffe*, 52:102–107, 1999.

[113] Sternstein, S. S. and Zhu, A.-J. Reinforcement mechanism of nanofilled polymer melts as elucidated by nonlinear viscoelastic behavior. *Macromolecules*, 35(19):7262–7273, 2002. DOI: `10.1021/ma020482u`.

[114] Montes, H., Lequeux, F., and Berriot, J. Influence of the glass transition temperature gradient on the nonlinear viscoelastic behavior in reinforced elastomers. *Macromolecules*, 36(21):8107–8118, 2003. DOI: `10.1021/ma0344590`.

[115] Mullins, L. Softening of Rubber by Deformation. *Rubber Chemistry and Technology*, 42(1):339–362, March 1969. DOI: `10.5254/1.3539210`.

[116] Mullins, L. and Tobin, N. R. Theoretical Model for the Elastic Behavior of Filler-Reinforced Vulcanized Rubbers. *Rubber Chemistry and Technology*, 30(2):555–571, March 1957. DOI: `10.5254/1.3542705`.

[117] Govindjee, S. and Simo, J. A micro-mechanically based continuum damage model for carbon black-filled rubbers incorporating Mullins' effect. *Journal of the Mechanics and Physics of Solids*, 39(1):87–112, 1991. DOI: `https://doi.org/10.1016/0022-5096(91)90032-J`.

[118] Harwood, J. A. C., Mullins, L., and Payne, A. R. Stress softening in natural rubber vulcanizates. part II. Stress softening effects in pure gum and filler loaded rubbers. *Journal of Applied Polymer Science*, 9(9):3011–3021, 1965. DOI: `https://doi.org/10.1002/app.1965.070090907`.

[119] Klüppel, M. and Schramm, J. A generalized tube model of rubber elasticity and stress softening of filler reinforced elastomer systems. *Macromolecular Theory and Simulations*, 9(9):742–754, 2000. DOI: `https://doi.org/10.1002/1521-3919(20001201)9:9<742::AID-MATS742>3.0.CO;2-4`.

[120] Hess, W. M. and McDonald, G. C. Improved Particle Size Measurements on Pigments for Rubber. *Rubber Chemistry and Technology*, 56(5):892–917, November 1983. DOI: `10.5254/1.3538171`.

[121] Allen, M. P. and Tildesley, D. J. *Computer Simulation of Liquids*. Oxford University Press, 2nd edition, 2017.

[122] Klat, D., Karimi-Varzaneh, H. A., and Lacayo-Pineda, J. Phase morphology of NR/SBR blends: effect of curing temperature and curing time. *Polymers*, 10(5):510, 2018. DOI: `10.3390/polym10050510`.

[123] Natarajan, B., Li, Y., Deng, H., Brinson, L. C., and Schadler, L. S. Effect of interfacial energetics on dispersion and glass transition temperature in polymer nanocomposites. *Macromolecules*, 46(7):2833–2841, 2013. DOI: `10.1021/ma302281b`.

[124] Adamson, A. W. and Gast, A. P. *Physical chemistry of surfaces*. Wiley, 1997.

[125] Stöckelhuber, K. W., Das, A., Jurk, R., and Heinrich, G. Contribution of physico-chemical properties of interfaces on dispersibility, adhesion and flocculation of filler particles in rubber. *Polymer*, 51(9):1954–1963, 2010. DOI: `10.1016/j.polymer.2010.03.013`.

[126] Mihara, S., Datta, R. N., Dierkes, W. K., Noordermeer, J. W. M., Amino, N., Ishikawa, Y., Nishitsuji, S., and Takenaka, M. Ultra small-angle X-ray scattering study of flocculation in silica-filled rubber. *Rubber Chemistry and Technology*, 87(2):348–359, June 2014. DOI: `10.5254/rct.13.88958`.

[127] Hentschke, R. *A nano-mechanical model for energy dissipation in filler networks*. In June 2013, pages 299–304.

[128] Hentschke, R., Hager, J., and Hojdis, N. W. Molecular modeling approach to the prediction of mechanical properties of silica-reinforced rubbers. *Journal of Applied Polymer Science*, 131(18):40806, 2014. DOI: `https://doi.org/10.1002/app.40806`.

[129] Viktorova, M., Hentschke, R., Fleck, F., Prange, C., and Karimi-Varzaneh, H. A. Mesoscopic model for the simulation of dynamic mechanical properties of filled elastomers: model construction and parameterization. *ACS Applied Polymer Materials*, 2(12):5521–5532, 2020. DOI: `10.1021/acsapm.0c00868`.

[130] Hager, J., Hentschke, R., Hojdis, N., and Karimi-Varzaneh, H. A. Computer simulation of particle-particle interaction in a model polymer nanocomposite. *Macromolecules*, 48(24):9039–9049, 2020. DOI: `10.1021/acs.macromol.5b01864`.

[131] Meyer, J., Hentschke, R., Hager, J., Hojdis, N. W., and Karimi-Varzaneh, H. A. Molecular simulation of viscous dissipation due to cyclic deformation of a silica–silica contact in filled rubber. *Macromolecules*, 50(17):6679–6689, 2017. DOI: `10.1021/acs.macromol.7b00947`.

[132] Lees, A. W. and Edwards, S. F. The computer study of transport processes under extreme conditions. *Journal of Physics C Solid State Physics*, 5:1921–1928, 1972. DOI: `10.1088/0022-3719/5/15/006`.

[133] Leach, A. R. *Molecular modelling principles and applications*. Prentice Hall, 2001.

[134] Klüppel, M. *The role of disorder in filler reinforcement of elastomers on various length scales*. In *Filler-Reinforced Elastomers Scanning Force Microscopy*. B. Capella, M. Geuss, M. Klüppel, M. Munz, E. Schulz, and H. Sturm, editors. Springer Berlin Heidelberg, 2003, pages 1–86. DOI: `10.1007/b11054`.

[135] Klat, D., Kępas-Suwara, A., Lacayo-Pineda, J., and Cook, S. Morphology and nanomechanical characteristics of NR/SBR blends. *Rubber Chemistry and Technology*, 91(1):151–166, January 2018. DOI: `10.5254/rct-18-82612`.

[136] Hiemenz, P. C. and Lodge, T. P. *Polymer chemistry*. CRC Press, 2007.

[137] Mahtabani, A., Alimardani, M., and Razzaghi-Kashani, M. Further evidence of filler–filler mechanical engagement in rubber compounds filled with silica treated by long-chain silane. *Rubber Chemistry and Technology*, 90(3):508–520, 2017. DOI: `10.5254/rct.16.83739`.

[138] Nakaramontri, Y., Kummerloewe, C., Vennemann, N., Wisunthorn, S., Pichaiyut, S., and Nakason, C. Effect of bis(triethoxysilylpropyl) tetrasulfide (TESPT) on properties of carbon nanotubes and conductive carbon black hybrid filler filled natural rubber nanocomposites. *Express Polymer Letters*, 12(10):867–884, 2018. DOI: `10.3144/expresspolymlett.2018.75`.

[139] Viktorova, M., Hentschke, R., Fleck, F., Taherian, F., and Karimi-Varzaneh, H. A. A mesoscopic model for the simulation of dynamic mechanical properties of filled elastomers: filled binary polymer blends. *Computational Materials Science*, 212:111597, 2022. DOI: `https://doi.org/10.1016/j.commatsci.2022.111597`.

[140] Noguchi, F., Akabori, K., Yamamoto, Y., Kawazura, T., and Kawahara, S. Tear energy and strain-induced crystallization of natural rubber/styrene-butadiene rubber blend. *Journal of Physics: Conference Series*, 184, August 2009. DOI: `10.1088/1742-6596/184/1/012020`.

[141] Gauthier, C., Reynaud, E., Vassoille, R., and Ladouce-Stelandre, L. Analysis of the non-linear viscoelastic behaviour of silica filled styrene butadiene rubber. *Polymer*, 45:2761–2771, April 2004. DOI: `10.1016/j.polymer.2003.12.081`.

[142] Wunde, M. and Klueppel, M. Impact of mixing procedure on phase morphology and fracture mechanical properties of carbon black-filled nr/sbr blends. *Continuum Mechanics and Thermodynamics*, 29:pages 1135–1148, September 2017. DOI: `10.1007/s00161-017-0562-1`.

[143] Gandhi, K. and Salovey, R. Dynamic mechanical behavior of copolymers containing carbon black. *Polymer Engineering & Science*, 28(24):1628–1636, 1988. DOI: `https://doi.org/10.1002/pen.760282409`.

[144] Yurekli, K., Krishnamoorti, R., Tse, M. F., McElrath, K. O., Tsou, A. H., and Wang, H.-C. Structure and dynamics of carbon black-filled elastomers. *Journal of Polymer Science Part B: Polymer Physics*, 39(2):256–275, 2001. DOI: `https://doi.org/10.1002/1099-0488(20010115)39:2<256::AID-POLB80>3.0.CO;2-Z`.

[145] Cherry, B. *Polymer Surfaces.* Cambridge Solid State Science Series. Cambridge University Press, 1981.

[146] Owens, D. K. and Wendt, R. C. Estimation of the surface free energy of polymers. *Journal of Applied Polymer Science*, 13(8):1741–1747, 1969. DOI: `10.1002/app.1969.070130815`.

[147] Fowkes, F. M. Attractive forces at interfaces. *Industrial & Engineering Chemistry*, 56(12):40–52, 1964. DOI: `10.1021/ie50660a008`.

[148] Wu, S. Calculation of interfacial tension in polymer systems. *Journal of Polymer Science Part C: Polymer Symposia*, 34(1):19–30, 1971. DOI: `https://doi.org/10.1002/polc.5070340105`.

[149] Strzemiecka, B., Voelkel, A., Donate-Robles, J., and Martín-Martínez, J. M. Estimation of polyurethane-carbon black interactions by means of inverse gas chromatography. *Journal of Chromatography A*, 1314:249–254, 2013. DOI: `10.1016/j.chroma.2013.09.040`.

[150] Calvet, R., Confetto, S. D., Balard, H., Brendlé, E., and Donnet, J.-B. Study of the interaction polybutadiene/fillers using inverse gas chromatography. *Journal of Chromatography A*, 1253:164–170, 2012. DOI: `10.1016/j.chroma.2012.07.002`.

[151] Kimura, M., Nakamura, K., and Tsutsumi, K. Surface free energies of silica fillers and their relation to the adsorption of poly(ethylene terephthalate). *Journal of Colloid and Interface Science*, 279(2):509–514, 2004. DOI: `https://doi.org/10.1016/j.jcis.2004.06.093`.

[152] Balard, H. and Brendlé, E. Carbon black using inverse gas chromatography techniques: study of the batch to batch stability of the surface properties. *Kautschuk Gummi Kunststoffe*, 55:464–469, 2002.

[153] Hamieh, T., Abbasian, A., and Farshchi, N. New methods to characterize the surface and interface acid–base properties of some hydrocarbons by inverse gas chromatography. *Chromatographia*, 2020. DOI: `10.1007/s10337-020-03878-z`.

[154] Luo, Y., Wang, R., Zhao, S., Chen, Y., Su, H., Zhang, L., Chan, T. W., and Wu, S. Experimental study and molecular dynamics simulation of dynamic properties and interfacial bonding characteristics of graphene/solution-polymerized styrene-butadiene rubber composites. *RSC Advances*, 6(63):58077–58087, 2016. DOI: `10.1039/c6ra08417f`.

[155] Mi, X., Wei, F., Zeng, L., Zhong, L., Zhang, J., Zhang, D., and Luo, Y. Incorporation of hyperbranched polyamide-functionalized graphene oxide into epoxy for improving interfacial and mechanical properties. *Polymer International*, 68(8):1492–1501, 2019. DOI: `10.1002/pi.5855`.

[156] Nakaramontri, Y., Kummerlöwe, C., Vennemann, N., Wisunthorn, S., Pichaiyut, S., and Nakason, C. Electron tunneling in carbon nanotubes and carbon black hybrid filler-filled natural rubber composites: influence of non-rubber components. *Polymer Composites*, 39(S2):E1237–E1250, 2018. DOI: `10.1002/pc.24821`.

[157] Alimardani, M., Razzaghi-Kashani, M., Karimi, R., and Mahtabani, A. Contribution of mechanical engagement and energetic interaction in reinforcement of SBR-silane–treated silica composites. *Rubber Chemistry and Technology*, 89(2):292–305, 2016. DOI: `10.5254/rct.15.84854`.

[158] Mohammadi-Jam, S. and Waters, K. Inverse gas chromatography applications: a review. *Advances in Colloid and Interface Science*, 212:21–44, 2014. DOI: `https://doi.org/10.1016/j.cis.2014.07.002`.

[159] Wang, M.-J. and Wolff, S. Filler-elastomer interactions. Part VI. Characterization of carbon blacks by inverse gas chromatography at finite concentration. *Rubber Chemistry and Technology*, 65(5):890–907, 1992. DOI: `10.5254/1.3538649`.

[160] Wang, M.-J. and Wolff, S. Filler-elastomer interactions. Part V. Investigation of the surface energies of silane-modified silicas. *Rubber Chemistry and Technology*, 65(4):715–735, 1992. DOI: `10.5254/1.3538637`.

[161] Pérez-Mendoza, M., Almazán-Almazán, M., Méndez-Liñán, L., Domingo-García, M., and López-Garzón, F. Evaluation of the dispersive component of the surface energy of active carbons as determined by inverse gas chromatography at zero surface coverage. *Journal of Chromatography A*, 1214(1):121–127, 2008. DOI: `https://doi.org/10.1016/j.chroma.2008.10.070`.

[162] Landau, L. D. and Lifschitz, E. M. *Theory of elasticity*. Pergamon Press, 1970.

[163] Meyer, J. *Ein corse-grained Modell für die Simulation dynamisch-mechanischer Eigenschaften gefüllter Elastomernetzwerke*. Master's thesis, Bergische Universität Wuppertal, 2014.

[164] Viktorova, M. *Calculation of elastic constants from displacement fluctuations in Lennard-Jones systems*. Master's thesis, Bergische Universität Wuppertal, 2018.

Index